Sheffield Hallam University

A Sheffield Hallam University thesis

Computer Simulation of Rod-Sphere Mixtures

Dmytro Antypov

A thesis submitted in partial fulfilment of the requirements

of Sheffield Hallam University for the degree of

Doctor of Philosophy

February 2003

Abstract

Results are presented from a series of simulations undertaken to investigate the effect of adding small spherical particles to a fluid of rods which would otherwise represent a liquid crystalline (LC) substance.

Firstly, a bulk mixture of Hard Gaussian Overlap particles with an aspect ratio of 3:1 and hard spheres with diameters equal to the breadth of the rods is simulated at various sphere concentrations. Both mixing-demixing and isotropic-nematic transition are studied using Monte Carlo techniques.

Secondly, the effect of adding Lennard-Jones particles to an LC system modelled using the well established Gay-Berne potential is investigated. These rod-sphere mixtures are simulated using both the original set of interaction parameters and a modified version of the rod-sphere potential proposed in this work. The subject of interest is the internal structure of the binary mixture and its dependence on density, temperature, concentration and various parameters characterising the intermolecular interactions. Both the mixing-demixing behaviour and the transitions between the isotropic and any LC phases have been studied for four systems which differ in the interaction potential between unlike particles. A range of contrasting microphase separated structures including bicontinuous, cubic, and micelle-like arrangement have been observed in bulk.

Thirdly, the four types of mixtures previously studied in bulk are subjected to a static magnetic field. A variety of novel phases are observed for the cases of positive and negative anisotropy in the magnetic susceptibility. These include a lamellar structure, in which layers of rods are separated by layers of spheres, and a configuration with a self-assembling hexagonal array of spheres.

Finally, two new models are presented to study liquid crystal mixtures in the presence of curved substrates. These are implemented for the cases of convex and concave spherical surfaces. The simulation results obtained in these geometries indicate segregation of spheres at the topological defect of the director field induced by the surface.

Acknowledgements

Advanced Studies

As part of the course of study a number of postgraduate Research Method and Research Study Units within the MRI at Sheffield Hallam University were completed.

A number of relevant external courses and conferences were participated in. These were, along with any work presented at them, in chronological order:

- CCP5 Summer School for Methods in Molecular Simulation, UMIST, Manchester (July 2000)

- Complex Fluids 2000 international conference, SHU, Sheffield (September 2000)

- Materials Chemistry Forum "Molecular Topology in Liquid Crystals" (September 2001). Poster presentation, *"Simulation of rod-sphere mixtures"*

- CCP5 Annual Conference, University of Warwick (September 2001). Poster presentation, *"Simulation of rod-sphere mixtures"*

- IOP Complex Fluids Group Winter School, University of Warwick (December 2001)

- BLCS Annual Meeting, University College London (March 2002). Oral presentation, *"The role of attractive potentials in binary rod-sphere mixtures"*

- Liquid Crystal Colloids IOP Workshop, SHU, Sheffield (April 2002). Oral presentation, *"The microphase formation in rod-sphere mixtures"*

- 19th International Liquid Crystal Conference, Edinburgh (July 2002). Poster presentation, *"The role of attractive potentials in binary rod-sphere mixtures"*

Contents

Chapter 1

Introduction

Liquid crystalline phenomena are observed in a wide range of areas in the physical and biological sciences. Ranging from such technological applications as liquid crystal displays (LCDs), and the wide-spread use of surfactants in the cleaning industry, through to the importance of self-assembly in a large number of biological processes, mesogenic behaviour is clearly a worthwhile topic for investigation.

Although many thousands of examples of liquid crystals (LCs) and their mixtures have been synthesised and studied, there is still a poor understanding of the interactions, at a molecular level, that drive many of the processes of self-organisation. It is also self-evident that a thorough understanding of these driving forces would open up enormous technological possibilities in the fields of micro-engineered devices and bio-medical applications [1]. Numerous novel high-tech applications of LC self-assembling systems, for example, as light modulators, as photoconductors, as polarised light emitting materials and as intelligent lubricants are in development [2]. Finally, it is relevant to note that it is the local supramolecular order, created by self-organising LC systems, that is responsible for the unique properties of living cell membranes [3].

It is, of course, important to realise that the complicated nature of LC systems means that experimental techniques can sometimes be of limited success in providing un-

1

derstanding of the origins of various phenomena. Also, the assumptions inherent in many theoretical treatments can make them too far removed from the real situation to provide useful information. It is here that computer simulation can come into its own - essentially lying in between the realms of theory and experiment, simulation can be of great use in gaining insight into phenomena which are difficult to access using other techniques [4].

1.1 Aims and Objectives

The motivation for this work was provided by previous simulations of two-component liquid crystal mixtures, in particular, mixtures of relatively similar molecule types which were found to undergo a degree of substrate-induced demixing [5]. This encouraged us to extend the project to cover mixtures of more extreme particle types. The work described in this thesis, therefore, relates to computer simulations performed with the aim of promoting greater understanding of the mechanisms and nature of LC behaviour in the presence of non-mesogenic additives. Specifically, attention has been focused on the phase behaviour of the Gay-Berne model [6] in the presence of additive Lennard-Jones particles.

The aims of this work initially were defined as follows:

- to combine existing computer codes and develop new variants in order to model and characterise the bulk phase behaviour of mesogens diluted with small spherical additive particles;

- to use the results of these bulk simulations to plan and perform an extensive programme of simulations in a confined geometry, paying particular attention to the effects of differential adsorption on bulk and surface region structure;

- to investigate the migration of volatile additive molecules towards orientationally disordered regions, and their effect in healing defects in the director field;

- to improve understanding of dilute liquid crystals in bulk, in the presence of substrates and around defect structures.

The next Section reviews the overall structure of this thesis describing the work undertaken to meet the aims stated above.

1.2 Outline of Thesis

Aside from this introduction, this thesis is organised as follows.

In Chapter 2, an introduction to liquid crystals in given, concentrating on the types of molecules which exhibit such phases and details of the structures involved. It also reviews relevant LC theoretical models, particular attention being paid to rod-sphere system studies.

Chapter 3 considers experimental approaches used in the study of LC systems. Attention is focused on studies which are relevant to the results presented within this report, although some effort has been made to give a wider consideration of experiments performed on LC mixtures.

Chapter 4 reviews simulation techniques and models of LC systems. A detailed description is given of the Gay-Berne potential and a review is presented of some literature results from simulations of pure and mixed systems performed using this model.

Chapter 5 presents some of our preliminary simulation results. These include simulations of the original Gay-Berne fluid using the Molecular Dynamics (MD) approach and simulations of Hard Gaussian Overlap (HGO) particles of the same aspect ratio using Monte Carlo (MC) techniques. Then, mixtures of these HGOs and small hard spheres are studied at different concentration ratios in order to build an approximate system phase diagram.

In Chapter 6, the Gay-Berne type of model of a rod-sphere system being used

here is described, followed by the results of a series of simulations of bulk mixtures performed in order to determine the effect of the rod-sphere interaction on the phase diagram. Four types of mixture are studied.

Guided by these results, some of these mixtures are then investigated in Chapter 7 in the presence of an applied field. The effect of the field on the structural properties of the systems is studied.

Chapter 8 presents results from simulations of rod-sphere mixtures in the presence of curved substrates. The two cases of convex and concave spherical surfaces are considered, these being used to represent, respectively, colloid-LC and Polymer Dispersed LC systems.

Finally, Chapter 9 summarises the main results of this thesis and presents conclusions and suggestions for future work. A bibliography is included.

Chapter 2

Theoretical Approaches used in

the Study of LCs

This Chapter describes the classification of different types of liquid crystals and explains methods of their theoretical study.

2.1 Liquid Crystals

The term liquid crystals (LCs) refers to materials which exhibit intermediate properties between those in liquid and crystalline states. It is a matter of common knowledge that matter exists in three states: solid, liquid, and gas. How, therefore, can the LC state be classified? These three states of aggregation refer to the mechanical properties of matter such as volume and shape. In these terms, a gas is compressible and does not maintain its shape (it flows and expands in a vacuum). A liquid, by comparison, is incompressible while still being fluid. And finally, a solid maintains its shape and volume and resists external shears. Importantly, none of these characteristics refer in any way to the internal structure of the matter. On referring to the microscopic structure of the matter we can state that a crystalline phase is characterised by a periodic lattice whereas an isotropic liquid phase pos-

sesses only short range order. So, the term *phase* refers to the internal structure of the matter, while *state of aggregation* corresponds to its mechanical properties. The majority of liquids are isotropic and the majority of solids have crystalline structure, but there are some exceptions. There are a lot of examples of solids with amorphous structure (like glasses). These amorphous phases form because their constituent molecules, due to their large size, low mobility or some specific properties, become quenched in liquid-like configurations. In the case of LCs, the molecules are small enough to have high mobility but they have another feature. They are essentially anisotropic in shape (disc-like or rod-like) and they develop orientational order while the material is still in the liquid state. A classic example of this sort of substance is *p*-azoxyanisole (PAA) with the molecular formula: From a steric point of view,

$$CH_3-O \left\langle\bigcirc\right\rangle- \underset{\underset{O}{\downarrow}}{N=N} \left\langle\bigcirc\right\rangle- O-CH_3$$
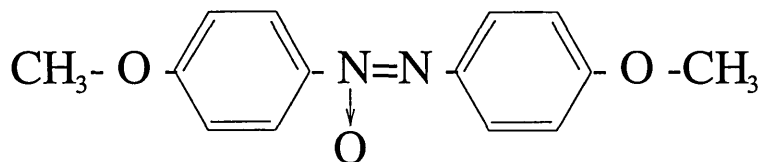
Figure 2.1: Typical mesogen: *p*-azoxyanisole (PAA).

this molecule is a rigid rod of length ~ 20Å and width ~ 5 Å [7]. The molecules which form LC materials are called *mesogens*, and a LC phase is often termed a *mesophase*. For the sake of completeness, let us mention all of the different classes of molecule which form LCs. There are four of them:

- small organic molecules, either rod-like or disc-like.

- main-chain and side-chain polymers which are composed of rigid mesogenic parts attached in consecutive or parallel fashion.

- amphiphilic compounds - compounds of two or more components, one of which is an amphiphile (e.g. containing a polar head group attached to one or more long hydrocarbon chains) [8].

- rods in a liquid substrate - suspensions of synthetic polypeptides or other rigid polymers, glass or plastic fibres floating in water, etc.

We will be particularly interested in the first type of mesogens.

2.2 Classification of LCs

Liquid crystals can be classified into two main categories: *thermotropic* LCs, and *lyotropic* LCs. These two types of LC are distinguished by the mechanisms that drive their self-organisation. Thermotropic LCs form different mesophases with variation in temperature, while lyotropic LCs do so by changes in concentration. Thermotropic liquid crystals can be classified into two types: *enantiotropic* liquid crystals, which can be changed into the LC state from either lowering the temperature of a liquid or raising of the temperature of a solid, and *monotropic* LCs, which can only be changed into the LC state from either an increase in the temperature of a solid or a decrease in the temperature of a liquid, but not both. In general, thermotropic mesophases occur because of anisotropic dispersion forces between the molecules and because of packing interactions. In contrast to thermotropic mesophases, lyotropic ones occur as a result of solvent-induced aggregation of the constituent mesogens into micellar structures [8].

Thermotropic mesophases have been found to be produced by two distinct types of molecular shape, rod-like - called *calamitic LCs* - which were the first to be discovered, and disc-like - called *discotic LCs* - which have been discovered only relatively recently [9]. The observed phases vary depending upon the shape of molecule being used, and upon the chemical details of the molecular structure.

Since the work described within this report is concerned with thermotropic calamitics, a brief description of the observed phases follows. There are two types of calamitic LC phase: *nematic*, in which there is orientational order such that the long axes of the molecules are aligned in a preferential direction but there is no translational order; and *smectic*, in which the molecules are arranged in regularly spaced layers or planes, such that there is a density wave running through the material, but only have short ranged positional order within these layers. Therefore, smectic phases

show a degree of translational order not present in the nematic phase (Fig. 2.2). When the molecules that make up a nematic LC are *chiral* (i.e. they are not sym-
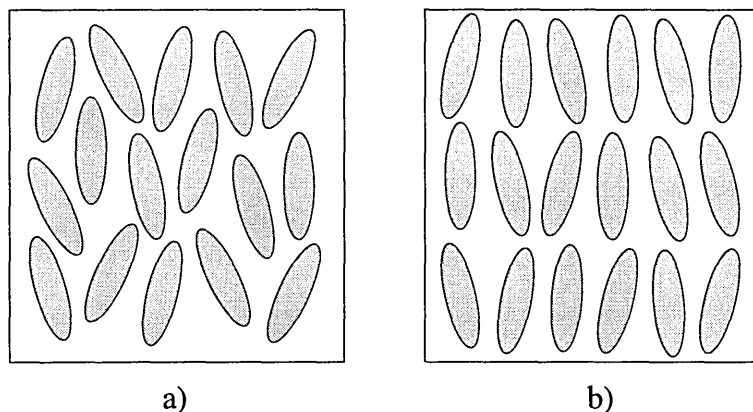
Figure 2.2: Schematics of nematic (a) and smectic A (b) LC phases.

metrical under reflection) the *chiral nematic* (or *cholesteric*) phase will form instead of the normal nematic. In this phase, the molecules prefer to lie next to each other in a slightly skewed orientation. This leads to the formation of a structure which can be visualised as a stack of very thin 2-D nematic-like layers with the director in each layer twisted with respect to those above and below. Thus a helical director configuration develops, in which the director rotates through the material. As with chiral nematics, there are chiral forms of the smectic phases. There are also several further smectic phases, classified in terms of the degree of ordering within the layers, the presence of any tilt and correlations between the layers [7]. In thermotropic systems, different mesophases are formed by changing the degree order in the sample by varying the temperature: the lower the temperature, the greater the order in the system. According to this rule LC phases are expected to appear in the sequence [10] shown in Fig. 2.3. This sequence is given only as a guide and does not
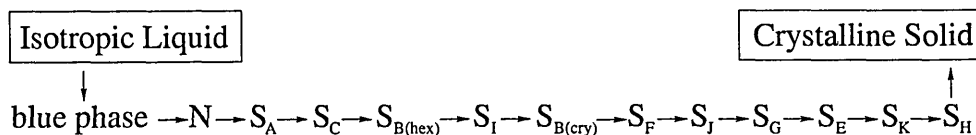
Figure 2.3: Sequence of LC phases.

include phases observed for some specific types of LCs (for example, flexoelectrics). The classification of the various smectic phases observed experimentally corresponds to both the arrangement of molecules within each smectic layer and any correlations between the arrangement in neighbouring layers. For example, a S_A phase has the highest symmetry and there are no long-range correlations within the layers; in a S_C phase, molecules are tilted in respect to the director; in a S_B phase, the molecules form a hexagonal pattern within a single smectic layer and so on. The only type of smectic phase exhibited by the Gay-Berne model (Subsection 4.2.3) which is studied within this work is the S_B phase. Note that no single compound has yet been found for which the complete sequence shown in Fig. 2.3 may be observed. In most pure mesogenic materials only a small subset of these phases exists, though they form in the order predicted by this sequence. The preceding statement is not always true for mixtures, however; for such systems there are some examples of a strong enhancement of the smectic phase region, resulting in the appearance of reentrant nematic regions on the phase diagrams [11]. Studies of binary mixtures of 6OCB and 8OCB also exhibit nematic reentrance as a function of temperature, pressure and concentration [12]. These examples indicate that the mixing of two or more components can dramatically change the properties of the resultant fluid.

The large number of LC phase transitions provides numerous examples for much of the theoretical work on critical phenomena. Since many mesophase transitions are either weakly discontinuous (first order transitions) or continuous (second order transitions), they display behaviour associated with critical points, including strong fluctuations and diverging susceptibilities. One of the most significant findings of theory is that, in the vicinity of such a transition, the microscopic details of the system become unimportant in describing the details of the transition [10]. Instead, the range of the interactions, the dimensionality of the system, and symmetry of the order parameter determine the behaviour of the system close to a transition point.

2.3   Descriptions of Ordering in LC Systems

In LC phases, molecules are aligned along a preferred axis called the *director*. To quantify the degree order in the system, an order parameter is defined. The nematic order parameter S is given as follows:

$$S = \langle P_2(\cos\theta) \rangle = \frac{\langle 3\cos^2\theta - 1 \rangle}{2}, \tag{2.1}$$

where θ is the angle between the director and the long axis of each molecule and P_2 is the second order Legendre polynomial. The angled brackets denote an average over all of the molecules in the sample. In an isotropic liquid, the average of the cosine terms is one third and, therefore, the order parameter is equal to zero. For a perfectly aligned system, the order parameter saturates to one. Typically, the value for the order parameter of a thermotropic LC ranges between 0.3 and 0.9 and depends on temperature. This dependence is illustrated schematically in Fig. 2.4, where T_{NI}
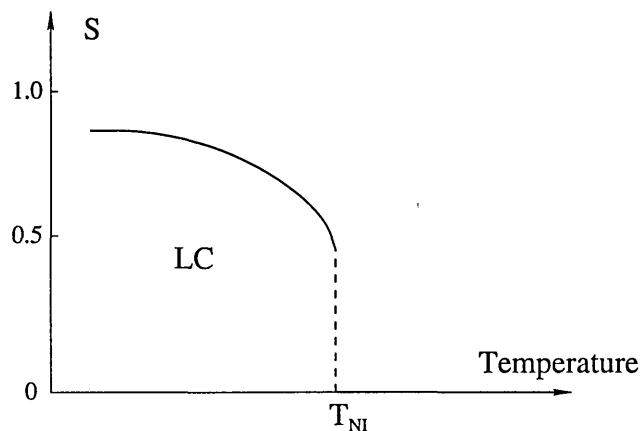
Figure 2.4:   Schematic dependence of the nematic order parameter, S, on temperature.

denotes the nematic-isotropic transition temperature. Above this temperature the isotropic liquid phase is stable, whereas below T_{NI} the liquid crystal phase forms. The transition between nematic and isotropic phases is weakly first order [13].

The nematic order parameter, S, does not provide us with complete information about the alignment of the molecules in the system. In general, the orientation of each molecule is determined by three independent coordinates - the set of Euler

angles $(\theta_i, \phi_i, \psi_i)$. To characterise the orientational order in a system on microscopic level, we could use the function $f(\theta, \phi, \psi)$ that gives the probability of finding a molecule with given orientation. It is usually assumed that the ordered phase symmetry is not lower than the symmetry of the constituent molecules [10], and orientational order is described using scalar or tensor quantities. For example, biaxial mesophases (i.e., biaxial nematic, smectic C, etc.) are characterised by the symmetric tensor order parameter with zero trace. If the molecules have cylindrical symmetry (f is independent of ψ) and the LC phase is cylindrically symmetric too (f is independent of ϕ), the distribution function f depends only on θ. In this case the scalar nematic order parameter (2.1) is used to describe the orientational order in the system.

Taking into account the symmetry of the nematic phase, we can expand the function $f(\theta)$ under even Legendre polynomials:

$$f(\cos\theta) = \sum_{n(even)} \frac{2n+1}{2} \langle P_n(\cos\theta)\rangle P_n(\cos\theta), \qquad (2.2)$$

where $\langle P_n(\cos\theta)\rangle$ are coefficients of the expansion:

$$\langle P_n(\cos\theta)\rangle = 2\pi \int f(\theta)P_n(\cos\theta)\sin\theta d\theta. \qquad (2.3)$$

Equation (2.2) can be used to approximate the distribution function $f(\theta)$ using the experimental values of $\langle P_2 \rangle$ and $\langle P_4 \rangle$. The higher terms do not make significant contribution and, since they are quite difficult to measure, are often omitted [14].

The nematic phase does not possess long range translational order so ordering in the system is described in terms of orientational but not spatial variables. In order to explore spatial ordering in LC phases, it is convenient to consider various distribution functions. The radial distribution function $g(r)$ provides structural information about the system. It is defined as the probability of finding a pair of molecules a distance r apart, relative to the probability expected for a completely random distribution at the same density. In calculating $g(r)$ in computer simulation we actually calculate the number of neighbouring molecules found in a series of concentric spherical shells centred on a certain molecule. If, instead, we calculate

the number of molecules found in thin slices oriented perpendicular to the sample director, we will evaluate the parallel distribution function, $g_\parallel(r_\parallel)$, where $r_\parallel = (\mathbf{r} \cdot \hat{\mathbf{n}})$. In a smectic A or B phase, this will show how the molecules are distributed in layers perpendicular to the director. The perpendicular distribution function, $g_\perp(r_\perp)$, where $r_\perp = \sqrt{r^2 - r_\parallel^2}$, shows how many molecules (subject to normalisation) reside inside cylindrical shells around a certain molecule. It can be used to infer in-plane structure in smectic phases.

The microscopic definition of the nematic order parameter given by equation (2.1) includes some assumptions about molecular properties that are often rather approximate. Experimentally, the order and, as a consequence, anisotropy in the sample expresses itself through changes in all macroscopic tensor properties. For instance, the diamagnetic susceptibility tensor $\chi_{\alpha\beta}$ for an isotropic liquid:
$$\begin{bmatrix} \chi & 0 & 0 \\ 0 & \chi & 0 \\ 0 & 0 & \chi \end{bmatrix}$$

is different from that of a uniaxial nematic phase:
$$\begin{bmatrix} \chi_\perp & 0 & 0 \\ 0 & \chi_\perp & 0 \\ 0 & 0 & \chi_\parallel \end{bmatrix}$$

(where the director is taken to be parallel to z-axis). The *macroscopic* tensor order parameter $Q_{\alpha\beta}$, that vanishes in the isotropic phase, is defined as

$$Q_{\alpha\beta} = G \begin{bmatrix} \frac{1}{3}(\chi_\perp - \chi_\parallel) & 0 & 0 \\ 0 & \frac{1}{3}(\chi_\perp - \chi_\parallel) & 0 \\ 0 & 0 & \frac{2}{3}(\chi_\parallel - \chi_\perp) \end{bmatrix}, \qquad (2.4)$$

where G is a normalisation constant chosen to set $Q_{zz} = 1$ in a perfectly aligned system. For relatively simple systems and in theoretical approaches the macroscopic order parameter is found to be in a good agreement with the microscopic one. It was shown by Saupe and Maier in their NMR experiments that for PAA (Fig. 2.1) the difference between the parallel and perpendicular components of the diamagnetic susceptibility tensor is proportional to the microscopic order parameter S(T) [15].

2.4 Review of Theoretical Descriptions of LC Phase Behaviour

The statistical mechanics of LCs is exceptionally difficult, and even for the simplest physical models no exact solution has been worked out. The vast majority of mesogens are rod-like in shape and in 1949, in his seminal work, Onsager [16] showed that a system of hard rods develops orientational order above a certain number density. Onsager used a mean field type approximation and made a number of assumptions: rods can not interpenetrate (steric repulsion); volume fraction is much less than one (sparse system); rods are very long. Within these limits, it was successfully shown that the system undergoes a first order phase transition from the isotropic to the nematic phase. This was the first evidence that attractive forces are not necessary for a system to show spontaneous alignment. However, apart from the assumptions made above, this model differs from actual observations on thermotropic systems in many respects (the transition density is too low, the jump in density at the transition is too abrupt and the order parameter at the threshold is too high [7]). Like all models involving only infinite repulsive forces, the system is "athermal", i.e. independent of temperature.

Another mean-field calculation for the dense hard-rod system was performed by Flory in 1956 [17]. He described a rod as a set of points inscribed on a lattice, the number of points in each rod playing the role of elongation. This approach proved to be useful for treating dense, highly ordered system, but neither Flory nor Onsager calculations can be entirely reliable over the whole range of density.

Maier and Saupe [18] developed a theory which takes into account attractive intermolecular interactions, using a lattice model with nearest neighbour interactions. Solving the problem with a mean-field approximation, they predicted a strongly first order transition to occur between the isotropic and nematic phases, at a temperature dependent upon the intermolecular potential. In particular the order parameter for the nematic phase was found to be much smaller than that predicted by Onsager

and a lot closer to those observed experimentally.

A relatively simple but powerful tool for the theoretical study of anisotropic systems is Landau theory. It is based on the assumption that the free energy can be expanded in a power series of a suitable order parameter, where only those terms compatible with the symmetry of the system are included. It is also possible to include in the expansion spatial variations of the order parameter; this introduces a new dimension not considered in mean-field theories [10]. Landau theory was first applied to LCs by de Gennes in 1971, with a result that this type of treatment of nematic LCs is now known as the Landau-de Gennes theory [19]. Subsequently, the de Gennes approach was extended and generalised to enable treatment of various systems and phase transitions. For example, there are generalised Landau-de Gennes theories for uniaxial and biaxial nematic LCs [20] and for the nematic-smectic-A tricritical phase transition in a binary mixture of LCs [21].

Continuum theories of LC phases are used to study flow properties, topological defects, responses to electric and magnetic fields, etc. These theories normally assume that the fluid is incompressible and at a constant temperature. The director is defined at each point of space and represents the direction of preferred orientation of the molecules in the immediate neighbourhood. The foundations of continuum theory were laid out in the 1920's by Oseen and Zocher [22] who developed a successful static theory. Thirty years later, Frank [23] reexamined Oseen's treatment and presented it as a theory of curvature elasticity. Dynamical theories that describe the mechanical behaviour of the nematic state were subsequently proposed by Ericksen [24] and Leslie [25].

2.5 Theoretical Studies of Rod-Sphere Mixtures

Most of the models of LC behaviour described above may be classified as mesoscopic, which means that a structural unit of the model represents a large number of molecules. In a mixture of two or more species, however, a majority of the pro-

cesses of interest occurs on a molecular scale so that microscopic details are essential. Mesoscopic models can still be applied to composite systems in which phenomena of interest occur on the mesoscopic scale (i.e. emulsions), or if there is a big difference in the sizes of the species, so one of them can be treated mesoscopically. Classical examples of such systems can be colloid-LC and colloid-polymer mixtures. A colloid is considered as a spherical particle of radius R suspended in a continuum medium. The liquid crystal is represented as a director field $\hat{\mathbf{n}}(\mathbf{r})$, where the unit vector $\hat{\mathbf{n}}$ points in the direction of the average alignment of molecules in the vicinity of point $\mathbf{r}$. Provided that changes in the director field are on a much larger scale than the molecular size, the free energy density f_d due to bulk elastic deformation of the nematic can be expressed as a sum of the energies of splay, twist and bend of the director field. The Frank elastic constants associated with these deformations are often of the same order of magnitude and the one-constant approximation of Frank elastic energy is employed [26]:

$$f_d = \frac{1}{2}K\left[(div\,\hat{\mathbf{n}})^2 + (curl\,\hat{\mathbf{n}})^2\right] \tag{2.5}$$

For homeotropic boundary conditions, where the director has to be perpendicular to the surface of the colloid, a topological mismatch is created between the director fields near the colloid and at large distances. A deviation from uniform field $\hat{\mathbf{n}}$ is penalised by the surface energy [27]

$$F_S = -\frac{1}{2}W\int(\hat{\mathbf{n}}\cdot\hat{\nu})^2 dS, \tag{2.6}$$

where W is the anchoring energy and $\hat{\nu}$ is the surface normal. If $WR/K \gg 1$, where R is the colloid radius, the anchoring is strong and there are two possibilities: the liquid crystal can form a quadrupolar Saturn ring structure (Fig. 2.5(a)) or a dipolar structure with a satellite defect (Fig. 2.5(b)). The theoretical comparison of the energy of both structures critically depends on the core energies of the disclination ring and the point defect. In experiment, the structure formed appears, to a large extent, to be determined by the system history (e.g. the cooling regime employed) [27].

If $WR/K \ll 1$ the anchoring is weak and the bulk elasticity prevails over the surface energy. The director field in this case is only slightly distorted as shown in Fig. 2.5(c)

a)   b)   c)
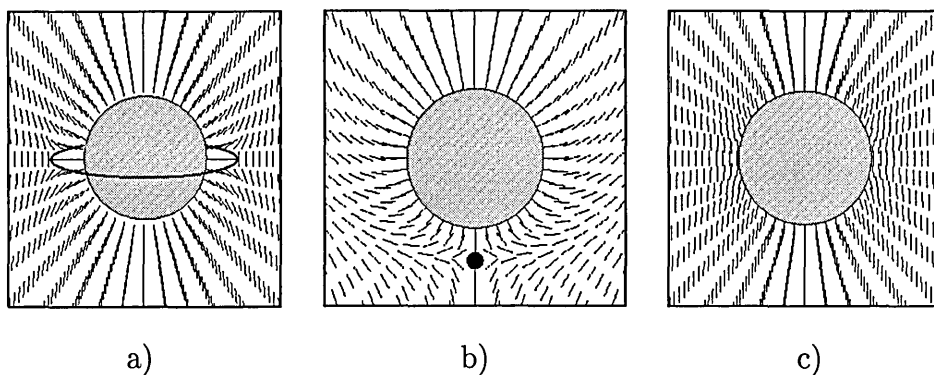
Figure 2.5: The calculated director field around a single spherical particle in a uniform nematic matrix: (a) the quadrupolar defect or Saturn ring, (b) the dipolar structure with a satellite point defect, (c) no topological singularities in the case of weak anchoring (from [27])

Since the pioneering work of Asakura and Oosawa [28], complex colloidal systems have been of great interest to theoretical physicists. It is known that two colloidal particles in a suspension of rod-like molecules experience an effective attraction due to the depletion effect. If the radius of the colloid is R and the length of the rod is L, there is a depletion zone of thickness $L/2$ around the colloid in which a reduced number of possible orientations is available to the rod, so reducing its entropy. When two colloids approach each other, their depletion zones overlap and more volume becomes available for the rods. Since this increases the rods' entropy here is a resultant attractive force between the colloids. The depletion potential between two colloids separated by distance h in the limit $R \gg L$ has the form [29]

$$U_{depletion}(h) = -\frac{\pi}{6} k_B T \phi R L^2 \left(1 - \frac{h}{L}\right)^3, \qquad (2.7)$$

where ϕ is the number density of the rods. If R and L are comparable this approach overestimates the potential and, in general, its exact analytical form is not available. Nevertheless, a numerical solution of the form

$$U_{YJM}(h, R/L) = -k_B T \phi R L^2 K(h/L, R/L), \qquad (2.8)$$

also known as YJM model, was proposed by Yaman, Jeppesen, and Marques [30]. Here, the function $K(h/L, R/L)$ was computed to fit the simulation data. Despite the numerical nature of this solution it only considers rod density to first order

and the rods are assumed to be noninteracting needles. Since the rods do not interact they are always in the isotropic phase. The phase diagram of a mixture of hard spheres and noninteracting needles therefore only has mixed and demixed regions [31].

In order to study the behaviour of LC phases, a number of systems have been studied with rods being treated as hard parallel spherocylinders [32–34]. The order parameter in such a mixture is always equal to one and while it is possible to observe the demixing behaviour there is no isotropic-nematic transition. Mixtures of spheres of diameter d and parallel spherocylinders of the same diameter with length l was studied using density functional theory by Koda et $al.$ [32] for l/d ratios 5, 7, 10, and 20. It was shown that the addition of small spheres induces a smectic A phase due to microphase separation between the spheres and the parallel spherocylinders. The stability of this layered structure was found to grow with increasing rod length. Figure 2.6 shows the stability boundaries for the system with $l/d = 20$. If the length
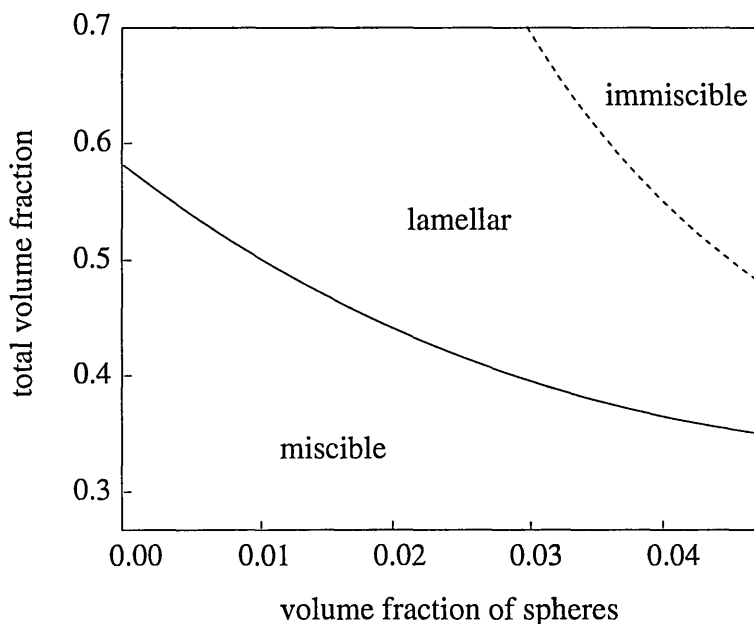
Figure 2.6: Stability boundaries for a mixture of parallel spherocylinders ($l/d = 20$) and spheres of the same diameter. The full line indicates the theoretical prediction of the volume fraction at which the system becomes unstable with respect to lamellar fluctuations. The dashed line indicates instability with respect to demixing into two macroscopically distinct phases (from [33]).

of the rod is decreased the region of lamellar phase becomes narrower and moves to higher total volume fractions (more shorter rods are required to obtain the lamellar phase at the same volume fraction of spheres). At an aspect ratio of 5 the stability boundary of lamellar phase is nearly horizontal which makes it difficult for theoretical analysis to predict the phase diagram for even smaller aspect ratios. The effect of sphere diameter on the phase diagram of the mixture was also studied [33]. It was found that decreasing the sphere size increases the stability of the layered phase whereas adding spheres with diameters essentially larger than the spherocylinder's diameter dramatically alters the phase diagram. For example, adding spheres of diameter $6d$ to spherocylinders with aspect ratio $l/d = 10$ stabilises the nematic and not the smectic phase. The layered phase is formed to persist at low volume fraction of spheres but here the large spheres fit into the spherocylinder layers rather than into the gaps between them [33].

The effect of depletion-driven demixing separately in both isotropic and perfectly aligned binary mixture of hard rods with the same length but different diameters was studied by van Roij and Mulder [34] using second virial coefficient approximation of the Helmholts free energy. It was shown that the demixing spinodal was thermodynamically stable with respect to the isotropic-nematic transition, if the diameter ratio was larger than about 5.

A theoretical approach formulated first by Rosenfeld [35] and then developed by Perera and co-workers [36], has brought new perspectives into the study of hard particle mixtures. In this theory, the Helmholtz excess free energy is written in terms of a series of weighted densities, and the weights are related to such geometrical properties of the components as volume, surface area, and mean radii. This approach may be used to study entropy driven demixing for the general case of isotropic binary mixtures of convex bodies. In particular, within this approximation, demixing is forbidden for binary mixtures of two dimensional fluids, regardless the shape of the components [37]. In $3D$, prolate or oblate particles are expected to demix more easily than spherical ones. In the case of rod-sphere mixtures, the fluid-fluid demixing is explicitly forbidden if the breadth of the rods and diameter of the spheres are

equal. The theory, however, does not consider demixing being preempted by an orientational transition of the rods, which is associated with a significant entropy change [38].

As the undertaken literature review shows, there is no theory capable of describing both mixing-demixing and the isotropic-nematic transition. Moreover, the theoretical predictions seem to work better for long and thin rods while real liquid crystal molecules have aspect ratios less than 5. Importantly, non-steric interactions have not been incorporated into any of the theoretical models described above. Therefore, computer simulation can be a useful tool for studying mixtures of rods with moderate aspect ratios and small spheres.

Chapter 3

Experimental Approaches used in the Study of LCs

3.1 Experimental Techniques

A large number of experimental methods are employed to study the dynamic and static properties of LCs. This Chapter gives an overview of some of them with an emphasis being given to the methods used in experiments on rod-sphere systems, and particularly those methods which recover structural properties.

3.1.1 LC Microscopy

LCs were first discovered and then found their practical application due to their specific optical properties. This is why different optical techniques are the most often used tools for experimental analysis of LCs.

LCs are found to be *birefringent*, i.e. they have two indices of refraction. For a nematic phase, the index of refraction $n_\parallel$ for light polarised parallel to the director differs from the index $n_\perp$ for light polarised perpendicular to the director. When light enters a birefringent material, it is broken into fast (called the *ordinary* ray)

and slow (called the *extraordinary* ray) components. These two components travel at different velocities and when they are recombined, as they exit the sample, the polarization state is found to have changed because of the resultant phase difference. This property is exploited for phase characterisation by placing a sample between crossed-polarisers under a microscope. Figure 3.1(a) shows the typical pattern observed for a nematic phase, with dark areas indicating whether the director is parallel or perpendicular to the light propagation. If the birefringence of the sample

(a)   (b)   (c)
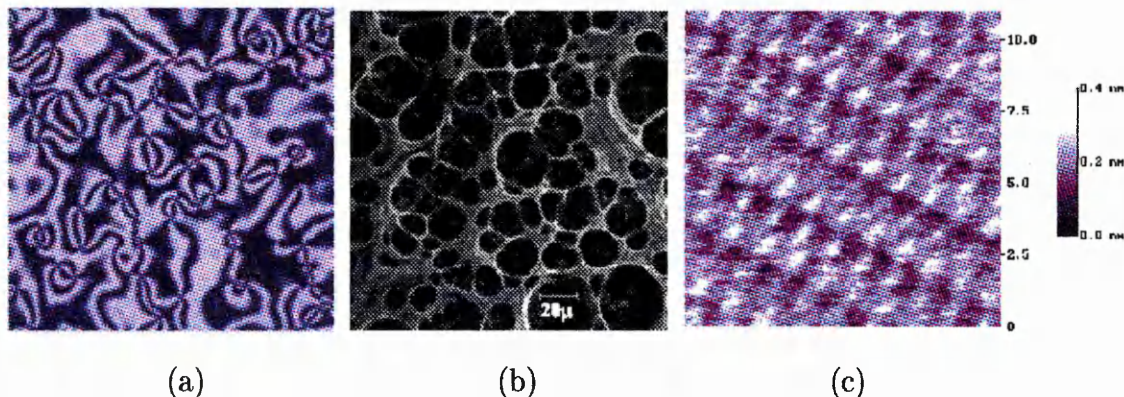
Figure 3.1: (a) polarization microscope image of nematic phase [40]; (b) confocal image of cellular structure of colloid-LC composite [41]; (c) STM image of 8CB molecules on MoS_2 [42].

is wavelength dependent, patterns of colours can be seen as well.

There are some advanced techniques as Confocal Microscopy and Scanning Tunneling Microscopy (STM) which can provide three-dimensional high-resolution images. Examples of such images of sizes $150\mu \times 150\mu$ and $11nm \times 11nm$ are shown in Fig. 3.1(b) and (c) respectively. The illumination in a confocal microscope is focused on one volume element at a time. Then a pinhole placed in front of the detector rejects the out-of-focus information, so that only the region that is in focus is detected. This technique gives sharp, blur-free images with resolution of order $10nm$. STM imaging is widely used to study the structure of matter at the nanoscale, revealing details of the size of a single atom. The principle of this technique is based on the tunnelling (without physical contact) current between a metallic tip, which is sharpened to a single atom point, and a conducting material. The magnitude of the tunneling current is extremely sensitive to the gap distance between the tip and

the sample. As the tip is raster scanned across the surface, atomic information of the surface can, therefore, be recovered from the resultant tunnelling map.

3.1.2 DSC

Differential Scanning Calorimetry (DSC) is a useful tool which complements optical methods in the study of LC phase transitions. As a matter of fact, not all phase transitions lead to changes in the optical properties of LC materials, and not all changes in optical properties are caused by phase changes. DSC can reveal the occurrence of phase transitions but cannot be used to characterise the types of phase present.

DSC instruments measure the energy change in a sample as it is heated or cooled at a constant rate. Typically, a DSC instrument consists of two pans, one containing the sample and one empty, each with its own heater and thermocouple. The instrument records the difference in energy required to keep the pans at the same temperature as that temperature is slowly raised or lowered. If the sample undergoes, for example, a nematic to isotropic transition at a certain temperature some heat is required to "melt" the sample and, therefore, more energy is needed from the heater to maintain the required heating rate. This results in a sharp peak in the energy difference recorded and, thus, indicates the transition point.

3.1.3 Other Techniques

Information about the structure of an LC sample can be obtained from experiments on scattering of various sorts of radiation. This includes light scattering, X-ray diffraction, polarised Raman spectroscopy, small angle neutron scattering (SANS) and so on. All of these methods are based on the fact that a beam of radiation changes its properties while passing through the sample and so can provide information on the sample's structure. The higher the frequency of the radiation the higher the resolution of the method. Thus light scattering is used to study supramolecular

structures while X-ray diffraction can reveal periodic features in the structure of materials at a molecular scale [43]. SANS can look even in even more detail and is used to investigate molecular conformations and orientations as well as to build up radial distribution functions [44].

A number of spectroscopic methods are employed to study orientational order in LC phases. The classical method of measuring the second rank order tensor (of which $\langle P_2 \rangle$ is the unique component for a cylindrically symmetric phase) is nuclear magnetic resonance (NMR). NMR is a phenomenon which occurs when nuclei with nonzero spin are immersed in strong static magnetic field and exposed to a second, perpendicular to the first, oscillating magnetic field. The spins rotate at the Larmor frequency in the static magnetic field and "flip" if the oscillating field has the same frequency. This changes the magnitude of the magnetization vector and can, therefore, be recorded.

Electron spin resonance, fluorescence depolarisation and polarised Raman spectroscopy techniques are now also widely used, since they can provide both the $\langle P_2 \rangle$ and $\langle P_4 \rangle$ order parameters [44]. Magnetic susceptibility measurements and optical birefringence can also give information about order in a sample but, since they operate with macroscopic properties, integral characteristics are evaluated.

Methods like dynamic light scattering and slow neutron scattering are employed to study dynamic properties of LC phases. "Guest-Host" techniques which use deuterated molecules or fluorescent dye molecules have also found application especially in the study of biological systems.

3.2 Experimental Studies of Rod-Sphere Systems

Several experimental studies of rod-sphere systems have been performed using colloid-LC composites. The phase ordering of colloids suspended in a thermotropic LC has been studied by Terentjev *et al.* [39] using confocal microscopy and DSC. This

showed that colloidal particles, rather than being homogeneously dispersed in a nematic phase, tend to aggregate to reduce the orientational elastic energy. Spherical PMMA particles in 5CB were aggregated to form thin interfaces surrounding large volumes of pure nematic liquid, thus forming an open cellular structure (see Fig. 3.1(b)). In this study, small steric PMMA particles dispersed in a LC matrix were found to pack at cell interfaces, below T_{NI}, but mix reversibly with the mesogens when the system was heated above T_{NI}. The low temperature material was found to have a remarkably high elastic modulus ($G' > 0.1$ MPa), which varied approximately linearly with particle concentration. Subsequently, Petrov conducted DSC measurements of PMMA/5CB mixtures [41] investigating the transition kinetics and the effect of particle size on the mechanical properties of these composites. Two separate first order phase transitions were observed near T_{NI}. The first was an ordinary isotropic-nematic transition, while the second, which took place at lower temperature, was associated with structural rearrangement of the rods and spheres in the system [41]. It was found that smaller particles produced more rigid structures well below the transition temperature, whereas the storage module was independent of particle size in the vicinity of T_{NI}. Poon and coworkers carried out experimental studies of the optical properties of colloid-LC composites [45]. Over a wide range of particle concentrations and across the full temperature range of the nematic phase, strong electro-optical switching was observed for 5CB and a series of other commercially available LC mixtures. The analysis of observed electro-optical responses suggested that the local viscosity (controlling molecular reorientation) was decoupled from the (much higher) bulk viscosity. Contrast ratio, viewing angle characteristics, switching time and optical hysteresis were also found to depend strongly on particle density [45].

The structure of colloid-LC systems have also been studied by Poulin and coworkers [46, 47]. An inverted nematic emulsion composed of water droplets dispersed in a thermotropic LC was used [46] to demonstrate the effect of the anchoring of LC molecules at the surfaces of droplets. The anchoring was controlled by using various amphiphilic compounds which were observed to accumulate at the water-LC inter-

face. Molecular surfactants were used to induce strong homeotropic anchoring, while a PVA polymer was used to induce strong planar anchoring. The amphiphilic compound also prevented small water droplets, generated by vigorous shaking of the sample, from coalescing. The resultant structures were observed through crossed polarisers with optical microscopy to map the distortions of the director field. An isolated water droplet in a nematic film formed a dipolar defect, whereas a quadrupolar defect was found in an homeotropically aligning LC. For planar anchoring, a pair of topological point defects, known as boojums, was observed. In order to minimize the orientational elastic energy, water droplets formed linear chains when the anchoring was normal. When the anchoring was planar, the droplets formed more compact but still anisotropic clusters. In this case the lines of water droplets were not parallel to the director but made an angle of about 30° to it [46].

Highly ordered arrays of macroscopic chains (several millimetres long) were found to be formed [47] in a binary mixture consisting of isotropic fluid (silicon oil) and LC (E7). This system has the phase diagram shown in Fig. 3.2. Rapid cooling from
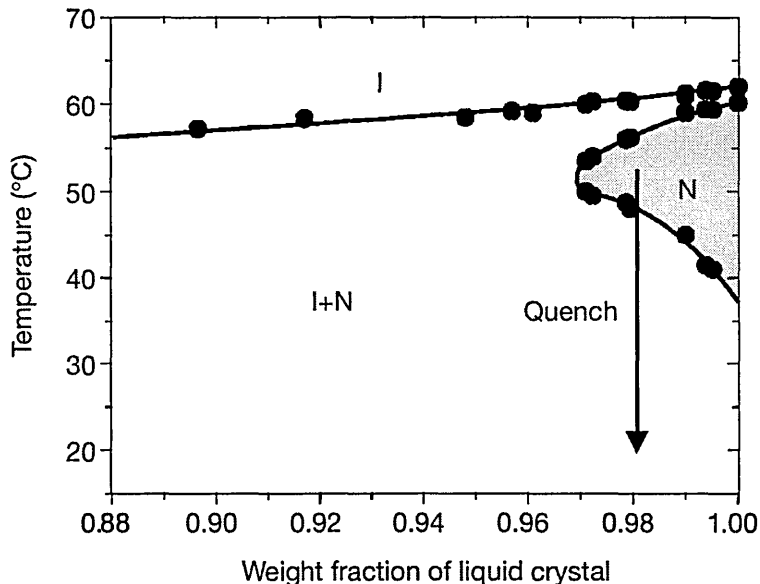
Figure 3.2: Phase diagram of the mixture of liquid crystal and silicone oil. The figure shows the isotropic phase (I), equilibrium between an isotropic and a nematic phase (N+I), and the nematic phase (N).

a mixed state induced microphase separation which developed through the initial

formation and subsequent growth of small monodisperse colloidal droplets. It was found that the size and spatial organization of the droplets were controlled by the orientational elasticity of the LC phase.

The group of Prof. Tanako has studied microemulsions of water in 5CB in the presence of the surfactant DDAB [48]. When 5CB is in the isotropic phase, this system was found to behave the same way as a conventional water-in-oil microemulsion. When nematic order developed below the transition temperature, the inverse micelles dispersed in the nematic were found to distort long-range orientational order. The inverse micelles composed of water and surfactant molecules were only about $4nm$ in diameter, i.e. of the order of the length of a LC molecule. As a result of strong homeotropic anchoring, the LC became ordered around the droplets, but the phase formed did not exhibit the strong light scattering generally associated with bulk nematic. Therefore, this optically transparent phase was called "transparent nematic" (TN). As shown in Fig. 3.3, the TN phase can be distinguished in experiment by DSC and dynamic light scattering. The DSC scans showed two distinct
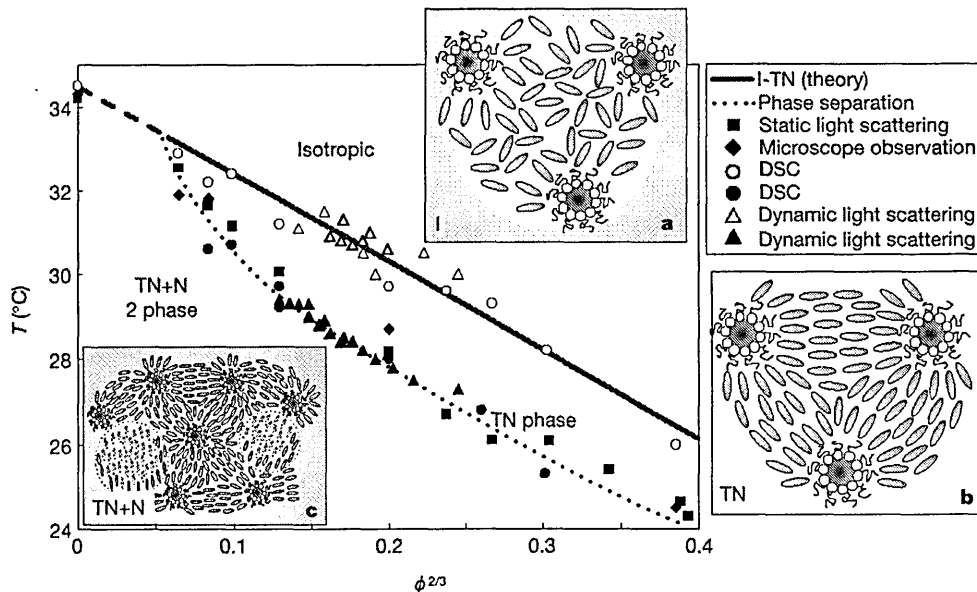
Figure 3.3: Phase diagram from [48]. The three insets show schematic diagrams of the states of the microemulsion (a) in the isotropic phase, (b) in the "transparent nematic" phase, and (c) after phase separation.

peaks, indicating the existence of two first order transitions. The first peak was as-

signed to the I-N transition because it becomes the I-N transition peak in the limit of pure 5CB. The second peak was associated with phase separation in which pure nematic droplets developed in coexistence with the TN phase.

A number of experimental studies of rod-sphere system of colloidal rod-like and sphere-like particles have also been performed recently [49–51]. The phase behaviour of suspensions of Tobacco Mosaic Virus (TMV) and polyethylene oxide spheres was studied by Adams and Fraden using optical microscopy [49]. The phase diagram of the mixture was found to comprise six regions, each representing a distinct morphology. Rod-like drops of TMV, hexagonal domains, different kinds of lamellar structures, and a homogeneous gel-like state were observed as the concentration of TMV was increased. This phase behaviour gave qualitative agreement with theoretical predictions for depletion interactions in rod-sphere mixtures (Section 2.5). To reduce the effect of electrostatic repulsion between the rods, suspensions of fd virus and polystyrene spheres of different sizes were studied with some salt added [50]. The phase diagram of this system (Fig. 3.4) resembles that predicted by theory for spheres
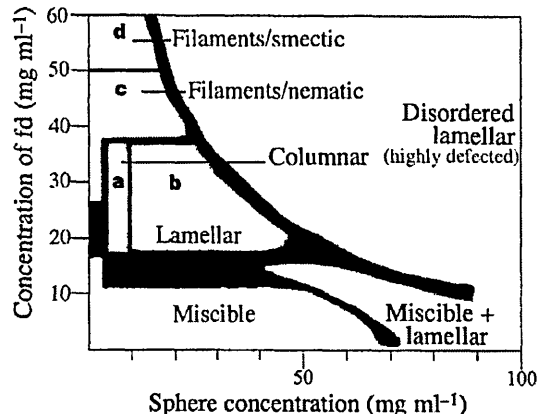
Figure 3.4: Phase diagram for fd and 100-nm diameter polystyrene spheres from [50].

and parallel spherocylinders (Fig. 2.6) as well as incorporates isotropic-nematic and nematic-smectic transitions for the rods. Figure 3.5 illustrates photographs and diagrams of the observed phases. The micrographs shown cannot clearly resolve single particles, so the drawings of an approximate representation of the structure are given. While phase diagrams of identical topology were observed for polystyrene
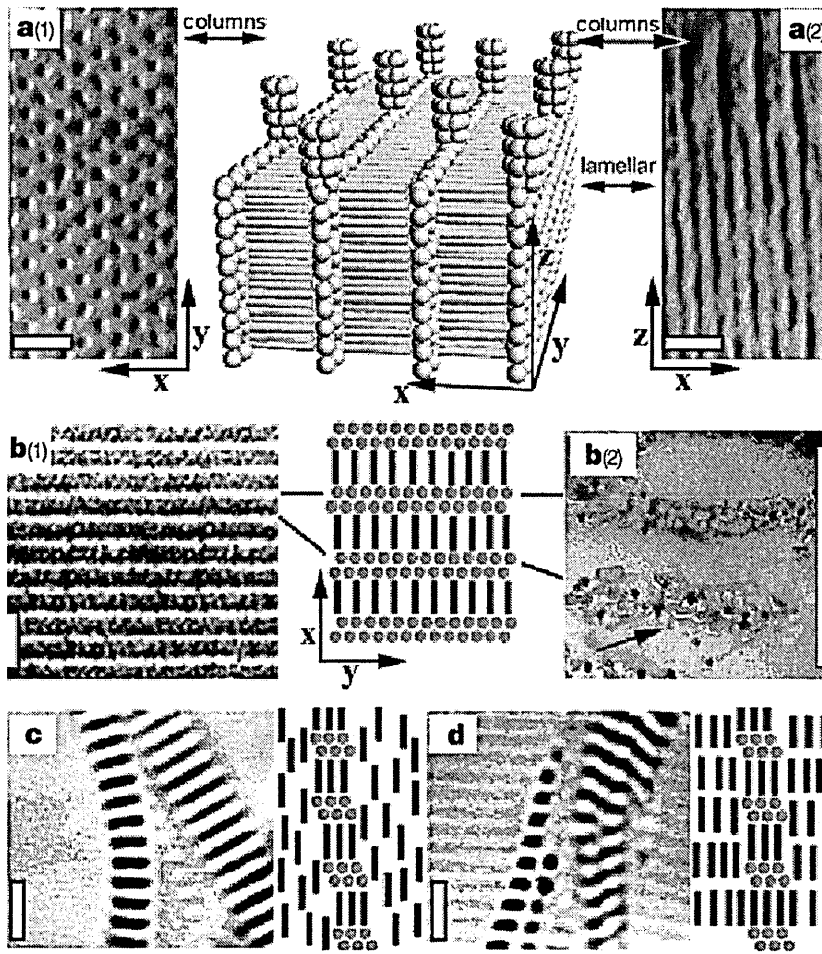
Figure 3.5: Photographs and diagrams of regions of the phase diagram shown in Fig. 3.4. Length bars are $3\mu m$.

spheres ranging from 22 to $120nm$ diameter, for spheres of size greater than $200nm$ the lamellar phase was not found. When low concentrations of $300-nm$-diameter PS spheres were added to fd nematics, rapid association of the spheres into chain-like structures was observed. At higher concentrations, the spheres packed into a cubic array with a lattice constant of one rod length, which suggests effective "rod-sphere" attraction in the system.

Lekkerkerker and co-workers studied mixtures of colloidal rods and spheres using fluorescence confocal microscopy [51]. Silica spheres $370 \pm 8nm$ in diameter and silica coated boehmite rods of length $230 \pm 90nm$ and $9 \pm 2nm$ in diameter were used in these experiments. At different volume fractions, the particles were dispersed

in dimethylformamide (DMF) with added salt (*LiCl*), and sphere aggregation and subsequent crystallisation was observed for some of these systems. This process was found to be controlled by a surprisingly low limiting rod concentration. In the studied systems, the aggregation of the spheres at $1 - 5\%$ volume fraction was observed at rod volume fractions around 0.3%. Although both rods and spheres could not to be taken as hard bodies, the depletion interactions were considered as the main reason for the sphere aggregation.

An interesting set of results for a rod-sphere system at molecular scale were obtained by Cheung *et al.* [52]. They studied a 10% mixture of n-octadecane (spheres) in Merck Phase 5 (rods) in the vicinity of the isotropic-nematic transition temperature using a deuterium NMR method. According to molecular field theory the field-induced orientational order in the isotropic phase of a nematogenic mixture should diverge as the nematic phase is approached. As soon as the biphasic region, in which nematic and isotropic phases coexist, is entered, the pretransitional divergence is predicted to be quenched, the field-induced order decreasing slightly with decreasing temperature. However, the authors' experimental findings showed that the divergence of the field-induced order was not quenched immediately on entering the biphasic region. This disagreement between theory and experiment was explained by the presence of concentration gradients within the sample; a method for the elimination of such gradients was demonstrated.

Chapter 4

Computer Simulation of LCs

In this Chapter, a computer simulation approach to LC study is presented. First, the major methods of simulations are considered together with their theoretical background. Then a review of LC models and some examples of their implementation are given.

4.1 Methods of Computer Simulation

Computer simulation of LCs provides a direct route from the microscopic details of a system to macroscopic properties of practical interest. It aims to predict the properties of real materials and test theories based upon model systems, by providing essentially exact results for problems in statistical mechanics which otherwise would be solved by approximate methods, or might be quite intractable [4]. In computer simulations we operate with a system containing several hundreds or thousands of molecules, the aim being to represent a real macrosystem of 10^{23} molecules or so. To simulate bulk behaviour, the small idealised system is replicated periodically through space. A number of assumptions are made about the system and an appropriate computational technique is applied to study the properties of interest. A detailed analysis of the methods used in such computer simulations is given in Chapter 5.

There are two main simulation methods for modelling molecular liquids, namely Monte Carlo (MC) and Molecular Dynamics (MD). Both methods yield essentially exact results for the behaviour of the model system in the chosen statistical ensemble. MC uses random numbers to generate a series of configurations of the system and then accepts each with an appropriate probability. MD uses the forces between molecules to solve Newton's equations of motion (to an acceptable degree of accuracy using finite difference methods) to determine the evolution of the system with time. For this reason, MD is advantageous as it allows dynamical information to be obtained, whereas MC is conceptually easier and normally computationally cheaper. MC also allows any sort of move to be attempted (not necessarily realistic) and, through careful choice of moves, certain systems can be brought to equilibrium with greater ease. This Chapter presents the basics of the both methods.

4.1.1 Molecular Dynamics

Molecular dynamics is a method which solves the classical equations of motion for a system of N molecules with potential energy U. If we consider a system of molecules with Cartesian coordinates $\mathbf{r_i}$, then the equations of translational motion are

$$\frac{d^2}{dt^2}(m_i \mathbf{r_i}) = \mathbf{F}_i, \tag{4.1}$$

where m_i is the mass of molecule i and

$$\mathbf{F}_i = -\nabla_{\mathbf{r_i}} U \tag{4.2}$$

is the total force acting upon molecule i. If the molecules are not spherically symmetric they can also rotate as a result of their interactions. This rotation has to be taken into account through equations of rotational motion that are similar to equation (4.1). The angular acceleration of the molecule, β_i, and the total torque acting upon it, τ_i, are connected by

$$\hat{I}_i \beta_i = \tau_i, \tag{4.3}$$

where $\hat{I}_i$ is the second rank tensor of inertia. This equation, applicable to molecules of arbitrary shape, can be simplified for symmetric rod-like molecules. For a linear

molecule, only the force $\mathbf{g}_i$ which rotates the molecule needs to be considered. If the orientation of a linear molecule is defined by the unit vector $\hat{\mathbf{u}}_i$, the torque can be written as:

$$\tau_i = \hat{\mathbf{u}}_i \times \mathbf{g}_i. \tag{4.4}$$

However, the vector $\mathbf{g}_i$ can always be replaced by its component perpendicular to the molecular axis, such that,

$$\tau_i = \hat{\mathbf{u}}_i \times \mathbf{g}^\perp, \tag{4.5}$$

where

$$\mathbf{g}_i^\perp = \mathbf{g}_i - (\mathbf{g}_i \cdot \hat{\mathbf{u}}_i)\mathbf{u}. \tag{4.6}$$

The algorithm for rotational motion presented in App. A introduces an extra force which constrains the length of vector $\hat{\mathbf{u}}_i$. For a linear molecule, the angular velocity vector, ω_i, is perpendicular to vector $\hat{\mathbf{u}}_i$ and

$$\dot{\hat{\mathbf{u}}}_i = [\omega_i \times \hat{\mathbf{u}}_i]. \tag{4.7}$$

This allows us to rewrite equation 4.3 as follows

$$\frac{d^2}{dt^2}(I_i\hat{\mathbf{u}}_i) = \mathbf{g}_i^\perp. \tag{4.8}$$

This resembles equation (4.1) with the difference that vector $\hat{\mathbf{u}}_i$ has to be constrained on the unit sphere.

A number of different numerical methods can be used to solve the system of 6N second order differential equations of motion [4]. However, there seems little advantage of considering techniques other than the Verlet-like algorithms which were especially designed for numerical solution of this type of differential equations. These algorithms are simple to program, exactly reversible in time and, given conservative forces, guaranteed to conserve linear momentum. They have also shown excellent energy conserving properties and are relatively stable with increasing time step. The Velocity Verlet algorithm implemented in this work is discussed in Subsection 5.2.1.

Whatever the MD algorithm used to solve the equations of motion, the structure of an MD programme is always as follows:

1. Setting of the initial configuration of the system

2. Calculation of the forces and update of the molecular positions and velocities

3. Calculation of instantaneous properties

4. ········· Return to step 2 ·········

5. Calculation of time average properties

The number of repetitions of the loop $2-3-4$ multiplied by the time step defines the total time of simulation run.

4.1.2 Monte Carlo

The term Monte Carlo has come into use to designate numerical methods in which stochastic elements are introduced, in contrast to the deterministic MD approach. While MD explores the configuration space by following a time evolving trajectory, the MC is an importance-sampling technique for generating states of the system in a particular statistical ensemble. Each molecular configuration is defined by a unique set of coordinates. These include the positions of all the particles, $\{\mathbf{r}_i\}$, as well as their orientational coordinates, $\{\Omega_i\}$, if the particles are not spherically symmetric. The MC method generates a sequence (a Markov chain) of molecular configurations each new arrangement being generated by making random changes to the previous one. A new configuration is accepted or rejected according to a criterion which ensures that, in the limit of an infinite number of transitions, a given configuration occurs with a probability proportional to its Boltzmann factor. Properties of interest are then calculated as an ensemble average over all states of the system. A more detailed analysis of this method applied to the constant NVT and NPT ensembles now follows.

The canonical or constant NVT ensemble is a set of systems each consisting of N particles confined in a fixed volume V and at a fixed temperature T. The probability

of finding a certain configuration, m, is proportional to the Boltzmann factor of the potential energy, U_m,

$$\rho_{NVT} = \frac{1}{Z_{NVT}} \exp\left(-\frac{U_m}{k_B T}\right), \tag{4.9}$$

where Z_{NVT} is the sum of the Boltzmann factors for all possible configurations of the system:

$$Z_{NVT} = \int \exp\left(-\frac{U(\mathbf{r}_i, \Omega_i)}{k_B T}\right) d\mathbf{r}_i d\Omega_i. \tag{4.10}$$

If the potential energy is assumed to be independent of velocity (no dissipative forces in the system), the statistical average of an observable $A(\mathbf{r}_i)$ can be written as

$$\langle A \rangle = \int \rho_{NVT}(\mathbf{r}_i, \Omega_i) A(\mathbf{r}_i, \Omega_i) d\mathbf{r}_i d\Omega_i \tag{4.11}$$

While this integral is calculated over the whole configuration space, $\{\mathbf{r}_i, \Omega_i\}$, the distribution of $\rho_{NVT}(\mathbf{r}_i, \Omega_i)$ is very inhomogeneous and tends to be zero in the major of $\{\mathbf{r}_i, \Omega_i\}$: significant contributions to the average $\langle A \rangle$ are made, therefore, by those configurations with high values of $\rho_{NVT}(\mathbf{r}_i, \Omega_i)$. The MC method uses the importance sampling technique to estimate the average $\langle A \rangle$ by concentrating the computational efforts on the most likely configurations of the system.

Let $\Gamma = \{\Gamma_1, \Gamma_2, ...\}$ be a set of all possible configurations of the system. A Markov chain is a series of trials which satisfies two conditions:

- the outcome of each trial belongs to a finite set of outcomes Γ

- the choice of each new state depends only on the state that immediately precedes it.

The stochastic matrix π is defined as the transition matrix, with the element π_{mn} being the probability of moving from state m to state n. If the vector $\mathbf{p} = \{\rho_1, \rho_2, ...\}$ contains the probabilities of finding the system in state Γ_1, Γ_2, etc., then, at equilibrium, it satisfies the eigenvalue equation

$$\mathbf{p}\pi = \mathbf{p},$$
$$\sum_m \rho_m \pi_{mn} = \rho_n. \tag{4.12}$$

The sum of the probabilities of moving to any state n from the set Γ (including state m) has also to satisfy

$$\sum_n \pi_{mn} = 1. \tag{4.13}$$

The assumption normally made about the elements of the transition matrix is that

$$\frac{\pi_{mn}}{\pi_{nm}} = \frac{\rho_n}{\rho_m} \tag{4.14}$$

This so-called "microscopic reversibility" condition narrows the scope of searching for solutions to equations (4.12) and (4.13). The first such solution was suggested by Metropolis *et al.* [53] in 1953. In this, for a given probability vector **p** the stochastic matrix can be defined as:

$$\pi_{mn} = \begin{cases} \alpha_{mn} & \rho_n \geq \rho_m & m \neq n \\ \alpha_{mn}(\rho_n/\rho_m) & \rho_n < \rho_m & m \neq n \\ 1 - \sum_{m \neq n} \pi_{mn} & & m = n \end{cases} \tag{4.15}$$

where α is a symmetrical stochastic matrix, often called the underlying matrix of the Markov chain.

When performing simulations in the canonical ensemble, we assume that the probability vector **p** is given by the Boltzmann factors 4.9. The state space Γ is then explored according to the following scheme

- Generate a new configuration n by a random change of the existing configuration m (MC move or trial)

- Calculate energy change $\Delta U_{mn} = U_m - U_n$

- Calculate $\chi_{mn} = \min\left(1, \exp\left(-\frac{\Delta U_{mn}}{k_B T}\right)\right)$

- Generate a random number ψ on [0,1]

- Accept new state m if $\psi \leq \chi_{mn}$

The probability α_{mn} is incorporated in choosing the move and if $\Delta U_{mn} \leq 0$ it can be accepted automatically. If the move is uphill in energy, i.e. $\Delta U_{mn} > 0$, then $\rho_n < \rho_m$, and the move is accepted with probability $\frac{\rho_n}{\rho_m} = \exp\left(-\frac{\Delta U_{mn}}{k_B T}\right)$.

The underlying stochastic matrix α is determined by the MC move being used. For instance, at every MC step, we can select in random particle j and give it a small displacement $\delta \mathbf{r}_j$. Let new coordinates of the particle be

$$
\begin{aligned}
x_j^n &= x_j^m + (2\psi_1 - 1)\Delta r_{max} \\
y_j^n &= y_j^m + (2\psi_2 - 1)\Delta r_{max} \\
z_j^n &= z_j^m + (2\psi_3 - 1)\Delta r_{max}
\end{aligned}
\tag{4.16}
$$

where ψ_1, ψ_2, ψ_3 are random numbers on [0,1]. In this case, all possible new configurations differ from configuration m only by the position of particle j within $\delta \mathbf{r}_j$. The rest of state space Γ is not available for this particular move, giving zero elements α_{mn} in row m. On the computer there are a large but finite number of new configurations, N_{new}, and all of these states can be selected with an equal probability $\alpha_{mn} = \frac{1}{N_{new}}$. The fact that state n can be chosen with the same probability following a trial move from state m, as m can be a move from state n, then satisfies the requirements of microscopic reversibility.

It is also possible to generalise the Metropolis solution to other statistical ensembles, by means of an appropriate modification to the probability vector $\mathbf{p}$ designed to ensure that the correct thermodynamic distribution of states is given. For example, in the isothermal-isobaric (constant NPT) ensemble, the configuration integral is given by

$$
Z_{NPT} = \int \exp\left(-\frac{PV}{k_B T}\right) dV \int \exp\left(-\frac{U(\mathbf{r}_i, \Omega_i)}{k_B T}\right) d\mathbf{r}_i d\Omega_i.
\tag{4.17}
$$

This means that a particular configuration m is adopted with probability

$$
\rho_{NPT} = \frac{1}{Z_{NPT}} \exp\left(-\frac{U_m + PV_m}{k_B T} + N \log V_m\right),
\tag{4.18}
$$

and a trial move to state n can be accepted with probability given by

$$
\chi_{mn} = \min\left(1, \exp\left(-\frac{\Delta U_{mn} + P(V_n - V_m) - N k_B \log(V_n/V_m)}{k_B T}\right)\right).
\tag{4.19}
$$

4.2 Models of LCs

The methods described in the previous Sections can be applied to a number of different models. Here, a model implies a theoretical description of the system which incorporates information about its intrinsic properties (such as interaction potentials, for example). It can have some special and sometimes unrealistic features and demand an application of a specific method to study the properties of interest.

Simulation of LCs is a particulary challenging task. Firstly, the molecules are complex, having flexible or semi-flexible structures and often possess complicated electronic charge distributions, making them computationally expensive to model realistically. Secondly, LC phenomena occur over relatively large time and length scales, that require lengthy simulations of large systems [54].

For these reasons, a great deal of powerful CPU time is required, and it is not surprising that early attempts to simulate mesogens in the 1970s [55, 56] suffered greatly from insufficient computer time preventing any definite conclusions from being drawn. It was not until the 1980s that there was sufficient computer power for mesogenic phases to be definitely observed.

There are four types of models in LC simulation:

- lattice models

- hard nonspherical models

- soft nonspherical models

- realistic atom-atom potential models

Brief descriptions of these are given in the following with special attention being paid to binary mixtures.

4.2.1 Lattice Models

Lattice models represent a LC as a set of classical spin vectors, located on the sites of a cubic lattice. In the Lebwohl and Lasher lattice model [57] spins are allowed to rotate on their lattice sites, interacting with their nearest neighbours via the potential:

$$U_{ij} = -\epsilon \frac{3\cos^2 \alpha_{ij} - 1}{2}, \qquad (4.20)$$

where ϵ is a positive coupling constant, α_{ij} is the angle between neighbouring spins i and j. The spins should not be taken to represent individual molecules in a LC. Rather each site represents a small region of the LC sample, with the spin denoting the locally-averaged nematic orientation within that region [54]. Simulation results [58] indicate that the Lebwohl-Lasher lattice model exhibits an isotropic-nematic transition in good agreement with Landau-de Gennes theory. There are some alternative lattice models that differ in terms of the type of lattice and interaction potential used. Adding extra terms to the potential energy (4.20) allows the Lebwohl-Lasher model to be used to simulate a LC in an external field, in confined geometry, etc. To simulate a rod-sphere mixture the Lebwohl-Lasher model was extended by Hashim and Luckhurst [59]. The spheres were represented as vacancies in their model. While nematogenic solvent molecules interacted via potential 4.20, the spherical solute molecules had no anisotropic interaction with them neither they interacted with each other. This system exhibit phase behaviour similar to that of LC-oil mixture shown in Fig. 3.2. The main features here are decreasing of the transition temperature with increasing concentrations of spheres and presence of a re-entrant biphasic regime at low concentrations of spheres.

4.2.2 Hard Particle Models

A hard particle model implies that each particle has an infinitely repulsive core within which no penetration is possible. Such a model contains no attractive forces,

and is expressed mathematically, for a sphere, as,

$$U^{HS}(\mathbf{r_{ij}}) = \begin{cases} 0 & (r > \sigma) \\ \infty & (r \leq \sigma) \end{cases} \tag{4.21}$$

where σ is the diameter of the molecule. The simplicity of equation (4.21) makes this class of model particularly simple to simulate using the Monte Carlo technique. The first simulations of hard particle systems were surprisingly effective at reproducing features of the liquid state, showing that the main driving forces behind liquid structure are excluded volume effects. Simulations of LCs performed using hard particles have shown that a primary cause of mesogenic behaviour is the degree of shape anisotropy. That said, attractive interactions can certainly affect the phase behaviour drastically.

To simulate calamitic LCs hard ellipsoids and spherocylinders are usually used. An ellipsoid is one of the simplest shapes to be studied. It is simply a sphere subjected to elongation or compression. By defining semi-axes to be a, b and c, if a = b = c we have a sphere, a $\neq$ b = c is an axially symmetric molecule (ellipsoid of revolution) and a $\neq$ b $\neq$ c a general biaxial molecule. When defining the shape of an axially symmetric molecule a factor e is used as a measure of elongation or axial ratio ($e = a/b$). If e is less than 1, the molecule is discotic and if e is greater than 1, the molecule is calamitic. Frenkel and co-workers [61–63] explored the phase diagram of the hard ellipsoid system, considering a whole range of axial ratios from infinitely thin discs through hard spheres up to various lengths of rod-like molecules. It was found that the degree of anisotropy of the molecules determines the degree of stability of the nematic phase. A nematic phase was observed for $e = 1/2.75$ and 3, no nematic was seen for less extreme ratios. For $e \approx 1$ a plastic crystal phase was observed. More extreme shapes, $e = 1/10, 1/5, 5$ and 10 have been studied [54] and in each case a spontaneous ordering to the nematic phase was observed as the system underwent uniform compression. It was also noticed that upon transformation from discotic to calamitic (e to $1/e$) the phase diagram is almost symmetrical.

It was suggested by Frenkel [63] that a hard-core system composed of ellipsoids can not exhibit smectic phases, that can be observed in systems of spherocylinders. A

spherocylinder is a cylinder of length L and diameter D with hemispherical end caps of diameter D. The overall length to breadth ratio is given by $\gamma = (L+D)/D$. The first simulations using this model [64] considered a system of parallel spherocylinders with $\gamma = 5$, thus even at the lowest densities, the system possessed a nematic order. The most striking result of this work was that the system displayed a stable smectic phase, the range of which was increased with the non-sphericity of the particles. More recent work [65] has examined the effect of the orientational degrees of freedom of the system by removing the parallel constraint for a $\gamma = 5$ system, and later for other aspect ratios [66]. It was shown that for $\gamma < 3$ only isotropic and crystalline phases can occur, and that for larger γ stable nematic and smectic phases are present. The complete phase diagram of a pure spherocylinder fluid was mapped by Bolhuis and Frenkel [67].

There are some more examples of hard-core models. To simulate discotic LCs coin-like particles and spheres from which the top and bottom have been removed are employed [54]. Prolate chain-like particles composed of hard spheres with either rigid or semi-flexible bonds have also been used in calamitic LC simulations [68].

Hard particle modelling is widely used in the simulation of LC mixtures. The very first simulations of binary mixtures of hard parallel spherocylinders with different lengths were presented by Stroobants [69]. The behaviour of these mixtures differs markedly, quantitatively as well as qualitatively, from the phase behaviour of the separate monodisperse components. In particular, it was observed that the mixture favours columnar order over smectic order.

Hard ellipsoid rod-plate mixtures were studied by Camp and Allen [70] using Onsager theory and constant-pressure Gibbs ensemble Monte Carlo simulation. Four distinct phases for mixtures of uniaxial ellipsoids with elongations e and $1/e$ were observed: isotropic, uniaxial nematic (N_+ and N_-), and biaxial nematic [71]. Koda and Ikeda [32] conducted constant pressure Monte Carlo simulation of parallel hard spherocylinders and hard spheres. They found that the smectic layer periodicity was stretched when the spheres were added to the smectic-A phase of the spherocylin-

ders. Recent simulations of binary mixtures of hard spheres and spherocylinders [33] have revealed that adding spheres smaller then the rod length decreases the total volume fraction needed for the formation of a layered phase. Small spheres, therefore, effectively stabilise the layered phase; the opposite is true for large spheres. It was shown by comparison of computer simulation results with experiments and theory that entropy driven microphase separation takes place in mixtures of parallel rods and spheres [33].

4.2.3 Soft Particle Models

Despite the inherent problems of simulating mesogens, a surprising number of features have been reproduced using hard core models. However, realistic interactions between molecules are known to have both attractive and repulsive components. This is mimicked in so-called soft particle models in which the potential comprises an attractive tail at large intermolecular separations and a short range repulsive core. The best known example of such a potential is the Lennard-Jones pair potential:

$$U^{LJ}(\mathbf{r_{ij}}) = 4\epsilon_0 \left(\left(\frac{\sigma_0}{r_{ij}} \right)^{12} - \left(\frac{\sigma_0}{r_{ij}} \right)^6 \right). \tag{4.22}$$

This potential has a long-range attractive tail of the form $- \left(\frac{1}{r} \right)^6$, a negative well of depth ϵ_0 and a steeply rising repulsive wall of the form $\left(\frac{1}{r} \right)^{12}$ at distances less than $r_{ij} \sim \sigma_0$. The exponent 6 is used to model the Van der Waals interactions between non-polar molecules, whereas the exponent 12 does not have any explicit theoretical basis. It is chosen mainly to reduce the computational costs while maintaining a reasonable fit to realistic interatomic potentials [4].

For the purposes of modelling an anisotropic molecule, several Lennard-Jones potentials would have to be used for each molecule. Such simulations of LC phases were successfully performed, for example, by Paolini et al. [72]. They employed a system of molecules composed of a few (11) atoms, constrained to form a linear molecule, and in mutual interaction via a continuous repulsive site-site potential of
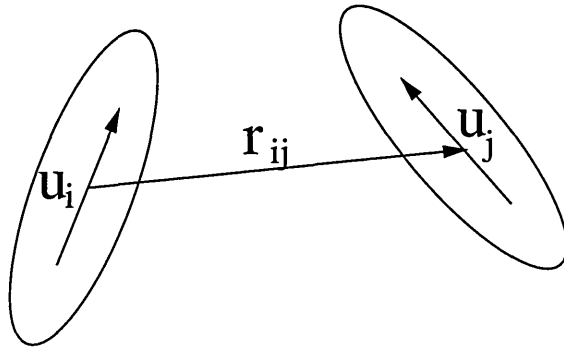
Figure 4.1: Schematic diagrams of orientations and separation of the particles.

the form $\left(\frac{1}{r}\right)^{12}$. It was found that such a model was capable of exhibiting nematic and smectic liquid-crystal phases.

The idea of using an anisotropic site-site potential to represent an intermolecular interaction was first proposed by Corner [73]. His work was based upon a numerical fit to a multi-site Lennard-Jones based potential with orientationally dependent range and energy parameters. A similar approach was made by Berne and Pechukas [74], but they considered the angular dependence of σ determined by the overlap of two Gaussian ellipsoidal functions. The Berne-Pechukas potential takes the Lennard-Jones form which has orientation dependent parameters:

$$U^{BP}(\hat{\mathbf{r}}_{ij}, \hat{\mathbf{u}}_i, \hat{\mathbf{u}}_j) = 4\epsilon(\hat{\mathbf{u}}_i, \hat{\mathbf{u}}_j) \left[\left(\frac{\sigma(\hat{\mathbf{r}}_{ij}, \hat{\mathbf{u}}_i, \hat{\mathbf{u}}_j)}{r_{ij}} \right)^{12} - \left(\frac{\sigma(\hat{\mathbf{r}}_{ij}, \hat{\mathbf{u}}_i, \hat{\mathbf{u}}_j)}{r_{ij}} \right)^{6} \right], \qquad (4.23)$$

where $\hat{\mathbf{u}}_i$ and $\hat{\mathbf{u}}_j$ are unit vectors describing the orientation of the molecules (Fig 4.1). The energy parameter is given by

$$\epsilon(\hat{\mathbf{u}}_i, \hat{\mathbf{u}}_j) = \epsilon_0 \left[1 - \chi^2 \left(\hat{\mathbf{u}}_i . \hat{\mathbf{u}}_j \right)^2 \right]^{-1/2}, \qquad (4.24)$$

where ϵ_0 is a constant and χ is a measure of the shape anisotropy and is determined from the major and minor axes of the ellipsoid being used to describe the molecule

$$\chi = \frac{(\sigma_e/\sigma_s)^2 - 1}{(\sigma_e/\sigma_s)^2 + 1}, \qquad (4.25)$$

where σ_e and σ_s are the length and the diameter of the molecule, respectively. The

shape parameter is given by

$$\sigma(\hat{\mathbf{r}}_{ij}, \hat{\mathbf{u}}_i, \hat{\mathbf{u}}_j) = \sigma_0 \left[1 - \frac{\chi}{2} \left\{ \frac{(\hat{\mathbf{r}}_{ij}.\hat{\mathbf{u}}_i + \hat{\mathbf{r}}_{ij}.\hat{\mathbf{u}}_j)^2}{1 + \chi(\hat{\mathbf{u}}_i.\hat{\mathbf{u}}_j)} + \frac{(\hat{\mathbf{r}}_{ij}.\hat{\mathbf{u}}_i - \hat{\mathbf{r}}_{ij}.\hat{\mathbf{u}}_j)^2}{1 - \chi(\hat{\mathbf{u}}_i.\hat{\mathbf{u}}_j)} \right\} \right]^{-1/2}, \qquad (4.26)$$

where σ_0 is a constant. This model was studied by Kushick and Berne [56] using constant temperature molecular dynamics. They applied an electric field to the isotropic phase, which promoted orientational order, and then monitored the system with the electric field removed. It proved easy to generate an ordered system when the electric field was applied, but in its absence a stable ordered state was difficult to achieve, and any observed order was lost after sufficiently long simulations. Furthermore, the strength parameter ϵ does not depend on intermolecular vector $\hat{\mathbf{r}}_{ij}$ so that there is no difference between side-side and end-end interaction well-depths. Taking into account these unrealistic features of the Berne-Pechukas potential, Gay and Berne [6] proposed another anisotropic potential. The Gay-Berne potential is expressed as follows:

$$U^{GB}(\hat{\mathbf{r}}_{ij}, \hat{\mathbf{u}}_i, \hat{\mathbf{u}}_j) = 4\epsilon(\hat{\mathbf{r}}_{ij}, \hat{\mathbf{u}}_i, \hat{\mathbf{u}}_j) \left[\left(\frac{\sigma_0}{r_{ij} - \sigma(\hat{\mathbf{r}}_{ij}, \hat{\mathbf{u}}_i, \hat{\mathbf{u}}_j) + \sigma_0} \right)^{12} \right.$$
$$\left. - \left(\frac{\sigma_0}{r_{ij} - \sigma(\hat{\mathbf{r}}_{ij}, \hat{\mathbf{u}}_i, \hat{\mathbf{u}}_j) + \sigma_0} \right)^6 \right]. \qquad (4.27)$$

In this expression, the shape parameter, σ, has the same form as in the Berne-Pechukas model (4.26), while the energy parameter ϵ is given by

$$\epsilon(\hat{\mathbf{r}}_{ij}, \hat{\mathbf{u}}_i, \hat{\mathbf{u}}_j) = \epsilon_0 \left[\epsilon_1(\hat{\mathbf{u}}_i, \hat{\mathbf{u}}_j) \right]^{\nu} \left[\epsilon_2(\hat{\mathbf{r}}_{ij}, \hat{\mathbf{u}}_i, \hat{\mathbf{u}}_j) \right]^{\mu}, \qquad (4.28)$$

where ϵ_0 is a constant and $\epsilon_1(\hat{\mathbf{u}}_i, \hat{\mathbf{u}}_j)$ is the energy parameter used in the Berne-Pechukas potential. $\epsilon_2(\hat{\mathbf{r}}_{ij}, \hat{\mathbf{u}}_i, \hat{\mathbf{u}}_j)$ is a function analogous to that for σ,

$$\epsilon_2(\hat{\mathbf{r}}_{ij}, \hat{\mathbf{u}}_i, \hat{\mathbf{u}}_j) = 1 - \frac{\chi'}{2} \left\{ \frac{(\hat{\mathbf{r}}_{ij}.\hat{\mathbf{u}}_i + \hat{\mathbf{r}}_{ij}.\hat{\mathbf{u}}_j)^2}{1 + \chi'(\hat{\mathbf{u}}_i.\hat{\mathbf{u}}_j)} + \frac{(\hat{\mathbf{r}}_{ij}.\hat{\mathbf{u}}_i - \hat{\mathbf{r}}_{ij}.\hat{\mathbf{u}}_j)^2}{1 - \chi'(\hat{\mathbf{u}}_i.\hat{\mathbf{u}}_j)} \right\}, \qquad (4.29)$$

where

$$\chi' = \frac{(\epsilon_{ss}/\epsilon_{ee})^{1/\mu} - 1}{(\epsilon_{ss}/\epsilon_{ee})^{1/\mu} + 1}. \qquad (4.30)$$

The parameter ϵ_{ss} is the depth of the potential for a pair of parallel molecules arranged side-to-side and ϵ_{ee} is equivalent depth for two parallel molecules arranged end-to-end. The exponents μ and ν were originally adjusted to obtain a good fit to the linear four site Lennard-Jones potential. From the same comparison it was found that the elongation of the molecule σ_e/σ_s should be set to 3, and $\epsilon_{ss}/\epsilon_{ee}$ to 5. The anisotropic nature of Gay-Berne potential is depicted in Fig. 4.2, where the
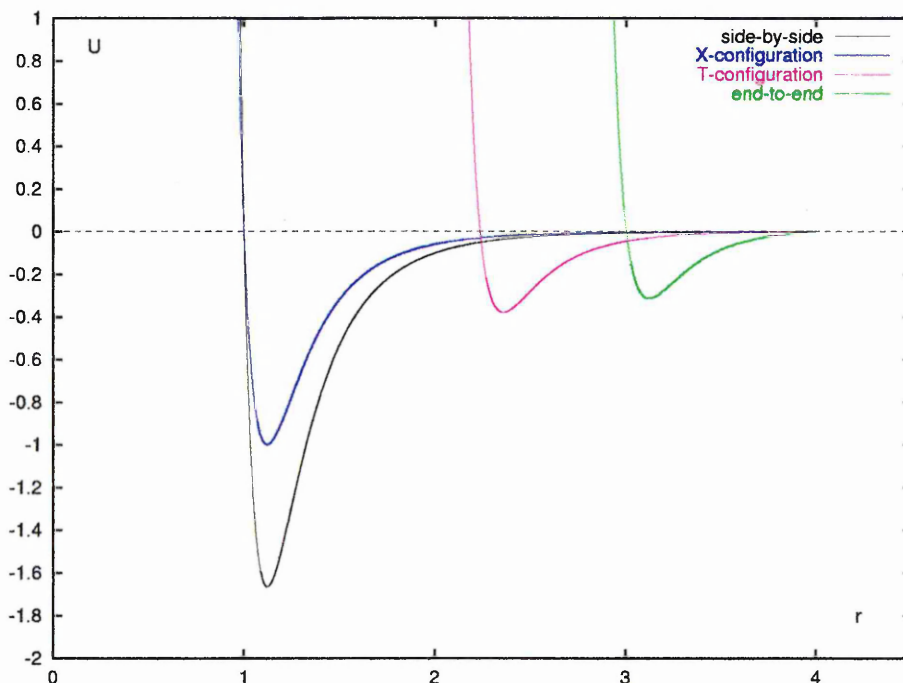
Figure 4.2: Energy profiles for different orientations of two Gay-Berne particles.

equipotential lines resulting from the interaction between a pair of parallel molecules are presented. The parameters of the Gay-Berne potential can be varied to yield a wide range of anisotropic potentials. If the anisotropy parameters, χ and χ', are set to zero, corresponding to a spherical molecule, the Gay-Berne potential reduces to the simple Lennard-Jones potential.

The original Gay-Berne parameterisation was studied by Adams *et al.*, de Miguel *et al.*, Emsley *et al.*, etc. Adams *et al.* [75] in their molecular dynamics simulations in the canonical ensemble showed that a spontaneous isotropic to nematic transition occurs at $\rho^* = 0.32$ between $T^* = 1.7$ and 1.8. De Miguel *et al.* studied liquid

vapour coexistence of a Gay-Berne fluid using the Gibbs Ensemble Monte Carlo method [76]. They obtained a saturation curve that appeared higher than that predicted by the density-functional approximation method. A complete phase diagram of the original Gay-Berne (Fig. 4.3) fluid was reported by de Miguel *et al.* in [77]. Using molecular dynamics simulations in the constant NVT ensemble, they iden-
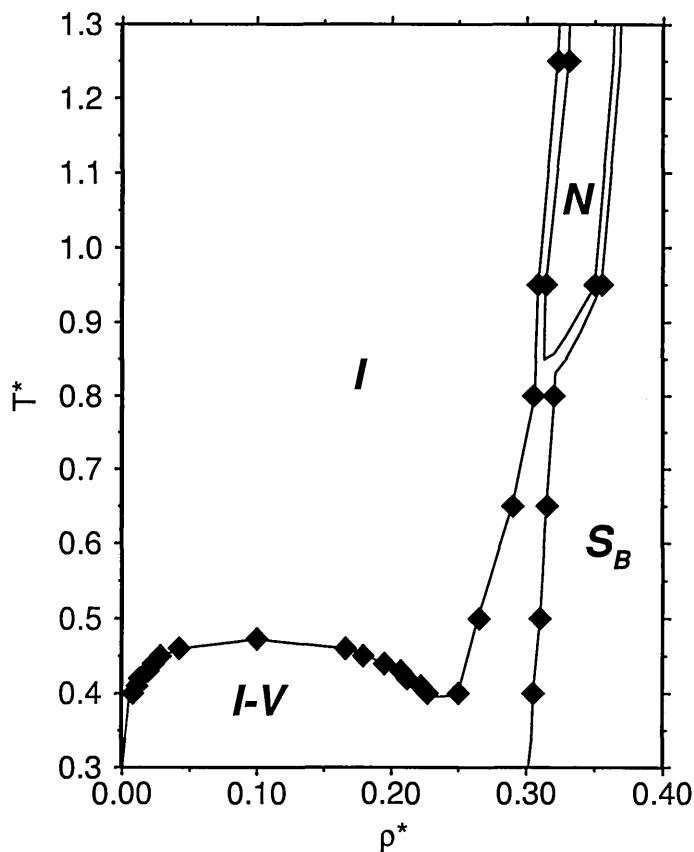
Figure 4.3: Gay-Berne phase diagram from [77]. The density and pressure are given in reduced units which are discussed later in Subsection 5.1.3.

tified isotropic fluid, nematic and smectic B phases. Emsley *et al.* [78] studied the temperature dependence of the nematic orientational order parameter $\langle P_2 \rangle$. They calculated the parameter $\Gamma = \frac{\Delta \ln T}{\Delta \ln V}_{\langle P_2 \rangle}$, the relative sensitivity of $\langle P_2 \rangle$ to temperature and density. It was found that Γ obtained for Gay-Berne model differed from experimental values. The authors showed that changing the Gay-Berne potential

by increasing the steepness of the repulsive term increased the calculated value of Γ, whilst changing the relative well depths for side-by-side compared to end-to-end arrangements of Gay-Berne particles left Γ virtually unchanged. These exploratory calculations suggested that Γ is a useful parameter for testing the parameterisations of model potentials.

The set of parameters $(\sigma_e/\sigma_s = 3; \epsilon_{ss}/\epsilon_{ee} = 5; \mu = 1; \nu = 2)$ was studied by Luckhurst *et al.* [79]. The existence of isotropic, nematic, smectic A, smectic B and crystalline phases was demonstrated. The phases were observed by monitoring appropriate correlation functions, order parameters, and also by graphical visualisation. Later, Luckhurst and Simmonds [80] estimated the parameters in the Gay-Berne potential by comparison with the multi-site potential constructed for p-terphenyl, which has a molecular structure typical of many mesogens. Two p-terphenyl molecules were constructed, each with 32 Lennard-Jones sites. As with the original Gay-Berne fitting, parameters were obtained from comparison of the Gay-Berne potential with the contours of a biaxially averaged set of multi-site interaction potentials. The resultant parameters were found to be $\mu = 0.8$, $\nu = 0.74$, $\sigma_{ee}/\sigma_{ss} = 4.4$ and $\epsilon_{ss}/\epsilon_{ee} = 39.6$. Thus, the repulsive core was more elongated in shape and the well depth anisotropy was considerable greater than that used in the previous examples.

Recently, more complete investigations of the phase diagram using parameterisations slightly different from original one have been conducted. De Miguel *et al.* [81] studied the effect of the anisotropic attractive interactions on the orientationally ordered phases by varying the ratio $\epsilon_{ss}/\epsilon_{ee}$ in the range $[1; 25]$ with fixed values of the other parameters. It was found that for this parameterisation smectic order is favoured at lower densities as $\epsilon_{ss}/\epsilon_{ee}$ is increased. When it is lowered, the smectic phase is preempted by the nematic phase. As a result, the nematic phase becomes increasingly stable at lower temperatures as $\epsilon_{ss}/\epsilon_{ee}$ is decreased. Also, evidence was found of a vapour-isotropic-nematic triple point for $\epsilon_{ss}/\epsilon_{ee} = 1$ and $\epsilon_{ss}/\epsilon_{ee} = 1.25$. For temperatures below this triple point, nematic-vapour coexistence was observed as, is found for many LCs in experiment.

The effects of elongation on the phase behaviour of the Gay-Berne fluid were studied by Brown *et al.* [82]. They explored a range of length-to-width ratios $3 \leq \sigma_e/\sigma_s \leq 4$, using a variety of molecular dynamics and Monte Carlo techniques, to determine the phase behaviour for each shape studied. Within the small range of elongation studied, the phase diagram showed significant changes. On increasing the ratio σ_e/σ_s, the liquid-vapour critical point moved to lower temperatures until it fell below the $I - S_B$ coexistence line, where liquid-vapour coexistence proved hard to establish. The liquid-vapour critical point seemed to be completely absent at $\sigma_e/\sigma_s = 4.0$. Also as elongation was increased, the $I - N$ transition was seen to move to lower density (and pressure) at given temperature. The lowest temperature at which the nematic phase was stable did not vary dramatically with σ_e/σ_s. On cooling, no S_B-crystal transition could be identified in the equation of state for any of these elongations, and it was suggested that, on the basis of simulation evidence, S_B and crystal are really the same phase for these models.

We have considered the use of the Gay-Berne potential in modelling of calamatic LCs, but it also can be used to model the interactions between disk-like molecules. Such simulations were performed by Bates and Luckhurst [83], and the system was found to exhibit isotropic, nematic discotic, and columnar phases. Generalisation of the Gay-Berne potential as well as its application to the simulation of mixtures will be considered in Subsection 4.2.5.

Quite recently a new Corner potential has been developed suitable for computer simulation studies of pure and mixed systems composed of rod-like, disk-like, and spherical molecules [84]. In this, the strength parameter ϵ and the range parameter σ are expanded in terms of a complete orthogonal basis set of functions, called S-functions, to obtain expansion coefficients typical of mesogenic molecules. The coefficients for the range parameter are determined by mapping the expansion onto prolate and oblate spherocylinders which are considered to be more realistic models for rod-like and disk-like molecules, respectively. Using this approach the expansion coefficients for the strength parameter were obtained by mapping onto those of two well-studied models: the original Gay-Berne model and the parameterisation with

exponents $\mu = 1, \nu = 2$.

4.2.4 Realistic Atom-Atom Potential Models

Despite the success achieved in simulating LCs with relatively simple models, in order to understand the stability of the various mesophases it can be necessary to incorporate detailed aspects of molecular structure into the model. The classical approach, involving assignment of Lennard-Jones potentials to each atom in the molecule, provides a complicated intermolecular potential [54]. Such a molecular potential can account for both changes in excluded volume and polarizabilty between different molecules, by the use of different nonbonded parameters for each atom type. For improved efficiency, some groups of atoms, like benzene or phenyl rings in the mesogen, can be treated as enlarged spherical extended atoms [85]. The combination of Gay-Berne and Lennard-Jones sites can provide even more realistic molecular models [86].

Applying the standard MD method to such a system is possible but requires a very small time step. So, the simulations are incredibly expensive and were actually impossible until the mid 90's. The quantum dynamics method is even more precise but much more expensive. In 1998 Clark, Adam and Crain determined accurate molecular structures, dipole moments and intermolecular potentials for mesogenic fragments and LC molecules from quantum mechanical computer simulations performed on 256 nodes of a Cray T3D [87]. They employed density functional theory (DFT) and used *ab. initio* pseudopotentials for the interaction between valence electrons and ions and the generalised gradient approximation to account for the many-body effects of exchange and correlation. The *ab initio* molecular dynamics method allows the simulation of motion of the individual atoms based on forces which are calculated quantum mechanically. It was initiated in 1985 [88] and combined DFT (an accurate and efficient scheme to treat the electronic structure) with classical mechanics (Newton's law for the nuclei) in a joint set of equations of motion.

4.2.5 Generalisation of the Gay-Berne Potential

The first attempt to simulate a bi-disperse Gay-Berne mixture was undertaken by Lukac and Vesely [89]. They studied a system of 256 Gay-Berne particles of two different length to breadth ratios using the standard MC method. The interaction between two unlike molecules was calculated by applying the Lorentz-Berthelot rule:

$$\sigma_{AB} = \frac{1}{2}[\sigma_{AA} + \sigma_{BB}], \qquad \epsilon_{AB} = \sqrt{\epsilon_{AA} \cdot \epsilon_{BB}}. \qquad (4.31)$$

This rule, applicable to spherical molecules, fails for anisotropic ones, because it does not distinguish between the two different T configurations (it incorrectly gives them both the same energy). Subsequently Cleaver *et al.* [90] proposed a generalisation of the Gay-Berne potential for the interaction between two unlike molecules which distinguished the two different T configurations. The shape parameter σ that describes the interaction between two molecules, i and j, with lengths (breadths) l_i and l_j (d_i and d_j) was found to be

$$\sigma(\hat{\mathbf{r}}_{ij}, \hat{\mathbf{u}}_i, \hat{\mathbf{u}}_j) = \sigma_0 \left[1 - \frac{\chi}{2} \left\{ \frac{(\alpha \hat{\mathbf{r}}_{ij}.\hat{\mathbf{u}}_i + \alpha^{-1}\hat{\mathbf{r}}_{ij}.\hat{\mathbf{u}}_j)^2}{1 + \chi(\hat{\mathbf{u}}_i.\hat{\mathbf{u}}_j)} + \frac{(\alpha \hat{\mathbf{r}}_{ij}.\hat{\mathbf{u}}_i - \alpha^{-1}\hat{\mathbf{r}}_{ij}.\hat{\mathbf{u}}_j)^2}{1 - \chi(\hat{\mathbf{u}}_i.\hat{\mathbf{u}}_j)} \right\} \right]^{-\frac{1}{2}}.$$

$$(4.32)$$

Here the parameters σ_0, χ and α are well defined functions of l_i, l_j, d_i and d_j. Since the work described in the following Chapters deals with the rod-sphere mixtures, let us consider the case of the rod-sphere interaction. If, for example, particle i is a sphere of diameter d, so $l_i = d_i = d$, both χ and α go to zero. The shape parameter, nevertheless, remains finite in this limit and tends to

$$\sigma(\hat{\mathbf{r}}_{ij}, \hat{\mathbf{u}}_j) = \sigma_0 \left[1 - \frac{l_j^2 - d_j^2}{l_j^2 + d^2} \cdot (\hat{\mathbf{r}}_{ij}.\hat{\mathbf{u}}_j)^2 \right]^{-1/2}. \qquad (4.33)$$

The energy parameter ϵ for the rod-sphere interaction is given by

$$\epsilon(\hat{\mathbf{r}}_{ij}, \hat{\mathbf{u}}_j) = \epsilon_0 \left[1 - \left(1 - \left(\frac{\epsilon_E}{\epsilon_S} \right)^{1/\mu} \right) (\hat{\mathbf{r}}_{ij}.\hat{\mathbf{u}}_j)^2 \right]^{\mu}, \qquad (4.34)$$

where the ratio $\frac{\epsilon_E}{\epsilon_S}$ controls the well-depth anisotropy of the interaction. Normally this would be set equal to the ratio $\frac{\epsilon_{ee}}{\epsilon_{ss}}$, but it could be varied as an independent

parameter. Using the generalised form of the Gay-Berne potential, mixtures of two species with different axial ratios have been studied. Bemrose *et al.* [91] performed constant *NVE* and *NPT* MD simulations of mixtures of rods with axial ratios of 3.5:1 and 3:1 at a range of concentrations. The order parameter of the longer molecules was found to be greater than that for the shorter molecules in both nematic and smectic phases. The transition temperature between ordered and disordered phases appeared to vary linearly with mole fraction. A 50/50 mixture of 1000 generalised Gay-Berne particles with axial ratios 2.0:1 and 2.5:1 was studied by Mills and Cleaver [92] using the Gibbs ensemble Monte Carlo method. This allowed nematic-isotropic coexistence and the processes of fractionation to be studied.

Chapter 5

Preliminary Simulations

This Chapter contains our first simulation results as well as some practical aspects of simulations and descriptions of the algorithms which were developed, computed, and validated for further utilisation. The practical aspects described here include the concepts of the periodic boundary conditions, the Neighbour List, and reduced units, which are used throughout in our simulations. The description of how we calculate the nematic order parameter, pressure and various distribution functions is given as well. The MD algorithm for elongated molecules is presented and then implemented to a system of original Gay-Berne particles. The simulations are performed under constant isochoric-isothermal conditions at a constant temperature and different densities (a compression series). Then a system of Hard Gaussian Overlap (HGO) particles of the same aspect ratio is simulated in both constant NVE and NPE ensembles using developed MC codes. Finally, the results of MC simulations of hard rod-sphere mixtures with different sphere concentration are presented, from which an approximate phase diagram of the system is built.

5.1 Practical Aspects

5.1.1 Periodic Boundary Conditions and Minimum Image Convention

A typical computer simulation system includes only 10^2 - 10^6 particles due to the computational overhead involved when considering large systems. In order to avoid surface effects in such a small system, periodic boundary conditions are applied. These involve effectively replicating the simulation box in all directions through space. If a particle leaves the system through one side, it then re-enters on the opposite side, thus keeping the number of particles constant. In such a system,
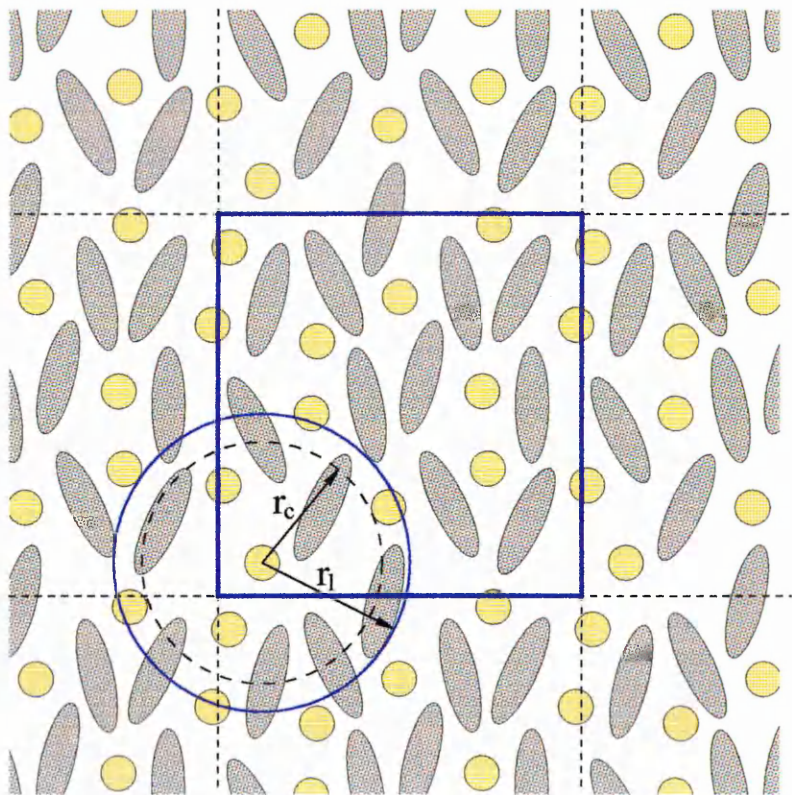
Figure 5.1: A two-dimensional periodic system.

the interaction between particles is computed according to the 'minimum image convention' - a particle interacts with its nearest neighbours (or 'images' from the neighbouring boxes). Implementation of a cutoff distance r_c (see Fig. 5.1), allows for short range potentials to neglect weak interactions on distances of a few molecular lengths. If L is a side of a cubic simulation box, the requirement $L > 2r_c$ has to be satisfied. This prevents direct interactions between any molecule and two or more periodic images of another molecule. Such interactions would impose an extra unphysical degree of symmetry upon the system. Since the simulation box has microscopic size it can not exhibit long wavelength fluctuations. For a cubic box of side L, the periodic boundary conditions suppress any density or orientational waves with a wavelength greater than L. Thus, care has to be taken in interpreting simulations of system behaviour in the vicinity of critical or transition points, where the range of fluctuations can become macroscopic, i.e. much greater than L.

Using a cutoff creates discontinuities in the potential energy and the force functions that can affect the results. The discontinuity in energy can be removed by imposing an appropriate shift on the potential so that it is zero at the cutoff distance. Both the energy and its first derivative can be made continuous at the cutoff point if a quadratic function is used [93]. In our simulations, we neglect discontinuity in forces and a simple energy shift is used (see App derivation for details).

5.1.2 Verlet Neighbour List

In computer simulations using a cutoff, we have to determine the nearest neighbours of each molecule at every time step. It is computationally expensive to check at each step the distances between each pair of molecules and compare it to r_c. Instead, the Verlet neighbour list can be used as an extremely useful tool for keeping track of the nearest neighbours of each molecule in the system. Here, a list of molecules within a distance r_l from each molecule is associated with that molecule (blue circle in Fig. 5.1). When calculating the forces and torques acting on that particle, the program does not therefore loop through all of the particles but only those appearing

in the list. From time to time it is necessary to renew the neighbour list, because molecules are moving and can either enter or leave the "neighbourhood" of the molecule. The value of r_l and the associated frequency of list rebuilding are set to ensure that the molecule always "knows" its neighbours within the distance r_c.

5.1.3 Reduced Units

Within computer simulations reduced units are used instead of dimension ones. If a system has some characteristic length, i.e. the length of the molecule, it is convenient to chose it to be a unit of length. The mass of the molecule can be chosen as a unit of mass which makes molecular momenta $\mathbf{p}_i$ and velocities $\mathbf{v}_i$ numerically identical, as well as the forces $\mathbf{F}_i$ and accelerations $\mathbf{a}_i$. In a mixture of two or more components, the assignment of masses of different species to some specific values does not affect its static properties as long as there are no mass-dependent interactions (i.e. a gravitational field) in the system. Since we do not concentrate on dynamic properties, we can therefore set all masses and moments of inertia to unity without losing generality.

There is a characteristic length, σ_0, and a characteristic energy, ϵ_0, in our model. Therefore, it is natural to measure all distances in units of σ_0 and energies in units of ϵ_0. As a consequence, the unit of temperature becomes ϵ_0/k_B, where k_B is Boltzmann's constant, the unit of time is equal to $\sqrt{m\sigma_0^2/\epsilon_0}$, and the unit of pressure is ϵ_0/σ_0^3. The following data from [4] is indicative of the correspondence between physical quantities and simulation parameters. For example, if for a Lennard-Jones model of liquid argon $\epsilon_0/k_B = 120K$ and $\sigma_0 = 0.34nm$, then the unit of time is $2 \times 10^{-12}s$. In our MD simulations, a typical time step is 0.0015 units of time which corresponds to $3 \times 10^{-15}s$ and the time available for the simulation as a whole is of the order of a few nanoseconds.

5.1.4 Observable Quantities

Such thermodynamic quantities as potential energy, temperature and pressure can be evaluated in a MD simulation every time step. The potential energy is given by the sum of all pairwise potentials in the system:

$$E_{pot} = \sum_{i=1}^{N} \sum_{j>i}^{N} U_{ij}. \tag{5.1}$$

The kinetic energy is essentially the sum of quadratic translational and rotational velocity terms. For example, for a system of N linear molecules the total kinetic energy is

$$E_{kin} = \sum_{i=1}^{N} \frac{m\mathbf{v_i}^2}{2} + \sum_{i=1}^{N} \frac{I\omega_i^2}{2}. \tag{5.2}$$

The value of the kinetic energy is directly connected to the temperature in the system. According to equipartition theory, on average an energy $\frac{1}{2}k_B\mathcal{T}$ is associated with each harmonic translational and rotational degree of freedom. This means that the kinetic temperature $\mathcal{T}$ of the mixture of N_{rod} rods and N_{sph} spheres can be found from the following equation:

$$\sum_{i=1}^{N_{sph}} \frac{m_{sph}\mathbf{v_i}^2}{2} + \sum_{i=1}^{N_{rod}} \frac{m_{rod}\mathbf{v_i}^2}{2} + \sum_{i=1}^{N_{rod}} \frac{I\omega_i^2}{2} = \left(\frac{5}{2}N_{rod} + \frac{3}{2}N_{sph}\right)k_B\mathcal{T} \tag{5.3}$$

A simple constraint method can be applied to simulate the system in the canonical or constant NVT ensemble. Here, translational and rotational velocities are re-scaled at each time step by a factor of $(T/\mathcal{T})^{1/2}$, where the instantaneous temperature $\mathcal{T}$ is defined by equation (5.3) and T is the constant thermodynamic temperature.

The pressure is calculated using the virial theorem,

$$P = \rho k_B T + \frac{1}{3V} \sum_{i=1}^{N} \sum_{j>i}^{N} \mathbf{r}_{ij} \cdot \mathbf{F}_{ij}. \tag{5.4}$$

As well as the thermodynamic quantities mentioned above we are also interested in structural properties which can be reflected by order parameters and distribution

functions. The orientational order parameter is measured as the largest eigenvalue of the Q-tensor:

$$Q_{\alpha\beta} = \frac{1}{N} \sum_{i=1}^{N} \left(\frac{3}{2} \cdot \hat{u}_{i\alpha} \hat{u}_{i\beta} - \frac{1}{2} \delta_{\alpha\beta} \right) \tag{5.5}$$

The radial and other pair distribution functions (see Section 2.3) are calculated by compiling histograms. The same technique is used to calculate the rod-rod, sphere-sphere, and rod-sphere pair radial distribution functions. The volume around a particle is divided into thin concentric spherical shells with radii ranging up to $L/2$. The thickness of shells defines the resolution of the method and is typically about $0.02\sigma_0$ in our simulations. The number of particles in each shell is counted and divided by the shell volume giving the local density. The radial density distributions are then averaged over all particles, and normalised with the overall number density to obtain the radial distribution function for this given configuration of the system. The same procedure is repeated several hundred times and averaged over a number of different configurations.

Similar methods are used to evaluate the parallel, $g_{\parallel}(r_{\parallel})$, and perpendicular, $g_{\perp}(r_{\perp})$, distribution functions. The director is defined first as the eigenvector of the Q-tensor (5.5) corresponding to the largest eigenvalue, and then the volume around a rod is divided into thin parallel layers perpendicular to the director to calculate $g_{\parallel}(r_{\parallel})$ or thin cylindrical shells to evaluate $g_{\perp}(r_{\perp})$. In the isotropic phase, the director changes its direction chaotically and both parallel and perpendicular distribution functions tend to unity at all distances after averaging. Nevertheless, some information about short range order can be obtained when choosing the direction of a given molecule as a guide to measuring those functions. The contribution of the nearest neighbours will be even more significant if we calculate $g_{\parallel}(r_{\parallel})$ within a thin tube and $g_{\perp}(r_{\perp})$ within a layer which is a few molecular lengths thick. These functions, called in the future $g_{tube}(r_{\parallel})$ and $g_{layer}(r_{\perp})$ respectively, depend on the choice of the radius of the tube and the semi-thickness of the layer.

It must be noted that any structural properties can be measured using the same approach in both MD and MC simulations. This is not true for the time dependent

thermodynamic quantities (the diffusion coefficient, for example).

5.2 MD simulations of the Pure Gay-Berne Fluid

5.2.1 The Algorithm

To compute the evolution of the system with time the so-called Velocity Verlet algorithm is used in this work. It has shown good long-term energy conservation properties and works relatively efficiently when compared with some other methods [94]. This algorithm stores the positional and rotational coordinates of each molecule at time t as well as their first derivatives with respect to time. Concerning the translation motion, velocities $\mathbf{v}_i(t)$ and current positions $\mathbf{r}_i(t)$ are updated every time step by the following rules:

$$
\begin{aligned}
\mathbf{v}_i(t + \frac{dt}{2}) &= \mathbf{v}_i(t) + \frac{dt}{2}\,\mathbf{a}_i(t) \\
\mathbf{r}_i(t + dt) &= \mathbf{r}_i(t) + dt\,\mathbf{v}_i(t + \frac{dt}{2})
\end{aligned}
$$

Then the forces in the system are evaluated, giving accelerations at time $t + dt$, and new velocities are calculated by:

$$
\mathbf{v}_i(t + dt) = \mathbf{v}_i(t + \frac{dt}{2}) + \frac{dt}{2}\mathbf{a}_i(t + dt).
$$

When computing rotational coordinates and angular velocities special measures have to be taken to maintain the orientational vector $\mathbf{u}_i$ at unit length, and to keep its first derivative, $\dot{\mathbf{u}}_i$, in a plane perpendicular to $\mathbf{u}_i$. The Lagrange multiplier method is an efficient tool for tackling this problem. According to this method, the orientational vector and its first derivative with respect to time are updated as follows:

$$
\begin{aligned}
\dot{\mathbf{u}}_i(t + \frac{dt}{2}) &= \dot{\mathbf{u}}_i(t) + \frac{dt}{2}\,\mathbf{g}_i^{\perp}(t) + \lambda\,\mathbf{u}_i(t) \\
\mathbf{u}_i(t + dt) &= \mathbf{u}_i(t) + dt\,\dot{\mathbf{u}}_i(t + \frac{dt}{2}),
\end{aligned}
$$

where $\mathbf{g}_i^{\perp}(t)$ is the perpendicular component of the force which causes rotation of particle i and λ is the Lagrange multiplier calculated as

$$\lambda = -\frac{1}{2}dt \left(\dot{\mathbf{u}}_i \cdot \dot{\mathbf{u}}_i + \frac{dt\mathbf{g}_i^{\perp}}{2}(2\mathbf{u}_i + \frac{dt}{2}\mathbf{g}_i^{\perp}) \right)$$

and further refined by two iterations of

$$\lambda_{new} = \lambda - \frac{(1 + \lambda\,dt)^2(\mathbf{u}_i \cdot \mathbf{u}_i) - 1 - 2\lambda\,dt}{2dt\,(1 + \lambda\,dt)}.$$

Finally, after calculating the new torques (this is done simultaneously with calculating the forces in the programme) the angular velocities at time $t + dt$ are evaluated:

$$\dot{\mathbf{u}}_i(t + dt) = \dot{\mathbf{u}}_i(t + \frac{dt}{2}) + \frac{dt}{2}\,\mathbf{g}_i^{\perp}(t + dt) + \left(\dot{\mathbf{u}}_i(t + \frac{dt}{2}) \cdot \mathbf{u}_i(t + dt) \right)\mathbf{u}_i(t + dt).$$

This completes the set $\{\mathbf{r_i}(t + \delta t); \mathbf{v_i}(t + \delta t); \mathbf{u}_i(t + dt); \dot{\mathbf{u}}_i(t + dt)\}$ required to to evolve the system on to the next time step.

Explicit expressions for the forces and torques acting on a Gay-Berne particle can be found in Appendix A.

5.2.2   Simulation Results

The following MD simulations were performed using a system of 380 Gay-Berne particles with the original parameterisation in the constant NVE and constant NVT ensembles. Periodic boundary conditions, minimum image convention and Verlet neighbour list were applied. The intermolecular potential was truncated and shifted at a distance $r_c = 4\sigma_0$. The Velocity Verlet algorithm was used with a time step $dt = 0.0015$. Firstly, the initial configuration was melted from a cubic lattice and equilibrated in the constant NVT ensemble at temperature $T = 0.7$. In order to check validity of the developed code a constant NVE ensemble simulation was conducted then to study deviations of the total energy in the system from its start value. It was found that for both short times (10 time steps) and long times (10^6 time steps) the total energy deviations were within $7 \cdot 10^{-5}$ units of energy per particle or 0.003% of the average. The average values of the order parameter and pressure

were found to be the same measured first at constant temperature at equilibrium and then under adiabatic conditions. The ratio of the transitional and rotational terms in the total kinetic energy was monitored during the constant NVE run. According
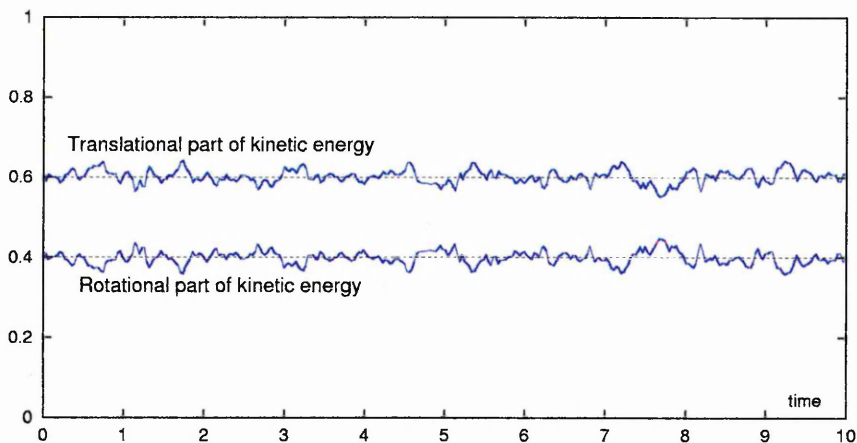
Figure 5.2: Distribution of kinetic energy between the translational and rotational terms.

to the theory for a system of linear molecules in equilibrium the translational and rotational kinetic energies have to be equal to $\frac{3}{5}$ and $\frac{2}{5}$ of total kinetic energy respectively. This is in perfect agreement with our simulation results shown in Fig. 5.2. The conservation of total linear momentum in the system was checked as well. It appeared that it had good short time conservative properties but at long times it went in a "random walk"-like fashion from zero. To keep the total momentum near zero it was decided to re-scale velocities every 10000 time steps.

The dependence of the order parameter and pressure on density was studied in the constant NVT ensemble. Starting from low density, the system was compressed at a constant temperature $T = 0.7$. Each run was started from the final configuration obtained at a neighbouring density and was equilibrated for 7×10^4 time steps. Quantities of interest were calculated and averaged over 5×10^4 additional time steps. The resulting values of the pressure and order parameter are shown in Fig. 5.3. These results were compared with analogous data obtained by de Miguel *et al.* [81], and found to be in excellent agreement. The isotropic-smectic transition was observed at the same pressure and density and pair distribution functions were
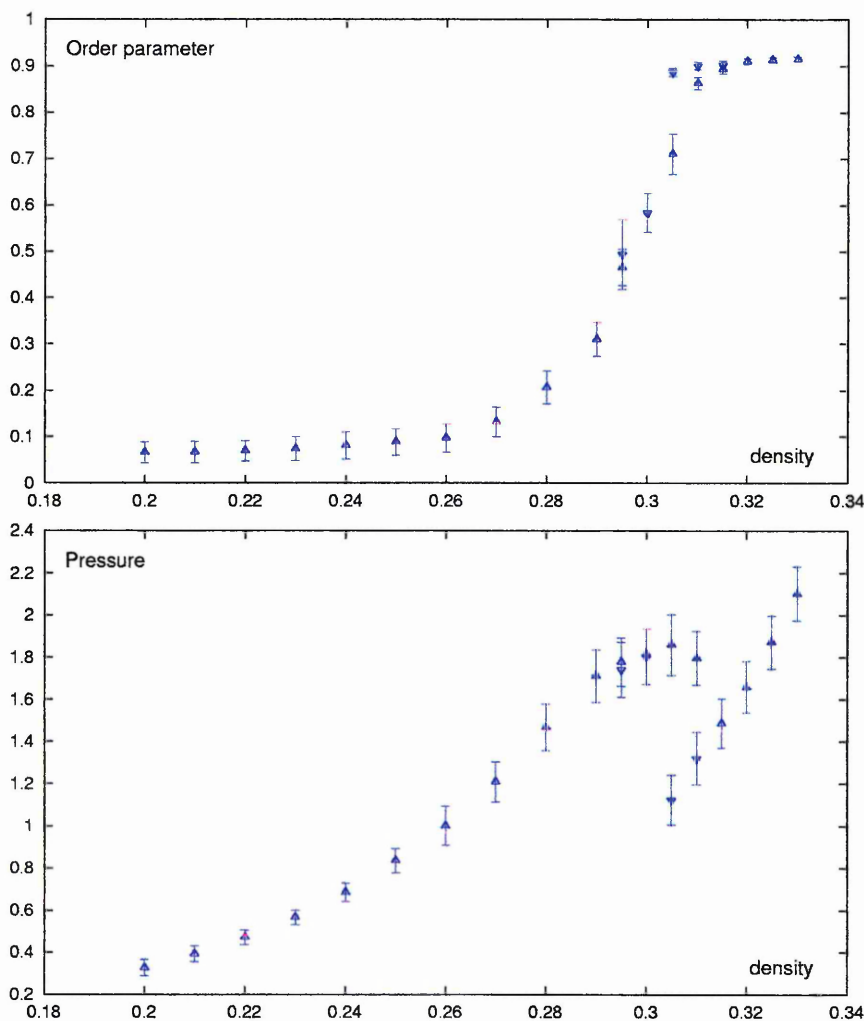
Figure 5.3: Order parameter and pressure versus density.

calculated to explore these phases. The radial, $g(r)$, parallel, $g(r_{\parallel})$, and perpendicular, $g(r_{\perp})$, distribution functions for both isotropic ($\rho = 0.20$) and smectic ($\rho = 0.31$) are presented in Fig. 5.4. In order to investigate the isotropic-smectic coexistence region several long runs were undertaken in the density range $0.29 \leq \rho \leq 0.32$. A subsequent series of decompression runs (up-side-down triangles in Fig. 5.3) revealed the existence of hysteresis as shown in the diagrams. For densities $\rho = 0.305$ and $\rho = 0.310$ two distinct states were found to be stable for long run times (10^6 time steps).
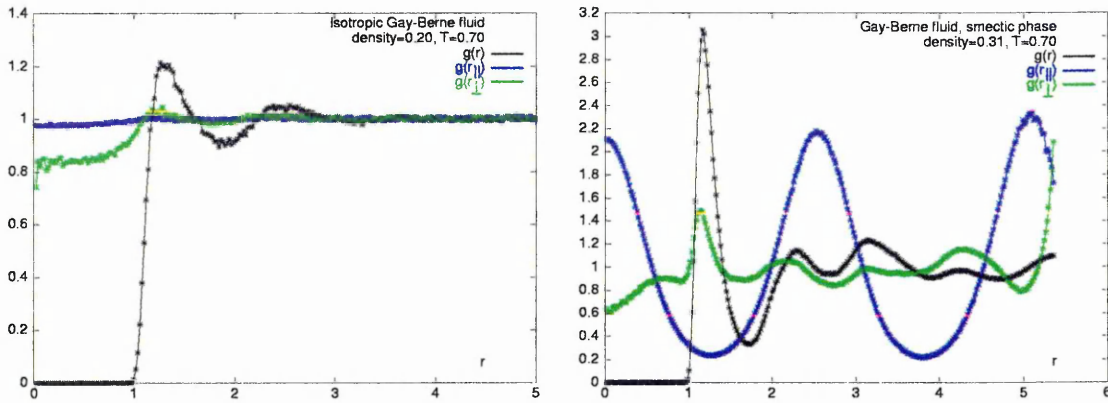
Figure 5.4: The pair distribution functions $g(r)$, $g(r_{\parallel})$ and $g(r_{\perp})$ for isotropic and smectic phases.

5.3 Hard Gaussian Overlap Particles

Since, in later Chapters, we will study the role of attractive interactions in mixtures it is reasonable to consider first a system without any attractions at all, i.e. a system of hard particles. The Gay-Berne potential possesses, at its core, the shape parameter of Hard Gaussian Overlap (HGO) model. This is why the results of simulations of HGO particles when compared with those obtained in the previous Section, can give us an idea of the role played by attractive interactions in the Gay-Berne fluid. This idea can be extended to mixtures of hard and soft particles of the same shape and will be revisited later in this thesis. Since in a system of hard particles, temperature becomes redundant as well as time, the methods described in the previous Section are not the most appropriate for use here. Instead, the Monte Carlo techniques will be used to study these hard particle systems.

5.3.1 The Method

Here the algorithms used for MC simulations of HGO particles in the constant NVE and NPE ensembles are presented. Note that the energy of the system of hard particles is always equal to zero and any simulation is always conducting under adiabatic conditions. If the system volume is constant, only two types of MC moves are considered:

61

- random displacement of a particle;

- random rotation of a particle.

The displacement is tackled using the standard MC algorithm described in Section 4.1.2. In order to turn a rod by a random angle ϕ the Barker-Watts method [95] has been employed. After generating an angle ϕ within $-\phi_{max} \leq \phi \leq \phi_{max}$ a random space-fixed axis is chosen and the rod is rotated around this axis by the angle ϕ. A new configuration is accepted if there are no overlaps with neighbouring rods. The rotational and displacement moves were combined together in our simulations after choosing appropriate values of ϕ_{max} and maximal displacement r_{max}. This meant that a single overlaps calculation was required for two moves that reduced the acceptance level by a factor less than 2. Typically, if the acceptance levels of the single moves were about 60%, then the acceptance of the combined move was of order 40%.

An extra MC move has to be employed to simulate the system under isobaric conditions. Here the volume of the system is changed by a random value ΔV ranging within $-\Delta V_{max} \leq \Delta V \leq \Delta V_{max}$. To do so, instead of re-scaling all particle positions, their sizes can be changed as

$$\sigma_{new} = \left(\frac{\Delta V}{V} + \frac{1}{\sigma_{old}^3} \right)^{-\frac{1}{3}}$$

Then, if the particles have become larger, the check of overlaps is conducted and, if none are found, the trial move is accepted with the probability

$$\chi = \min \left(1, \exp \left[-P\Delta V + 3N \ln \left(\frac{\sigma_{old}}{\sigma_{new}} \right) \right] \right).$$

If the particles have become smaller, no overlaps in the system can appear, and the acceptance criteria can be checked immediately. This method is applicable provided that the pressure tensor can be assumed to be isotropic and geometry of the simulation box is not expected to change during the run.

For hard particle systems, it is easier to conduct a series of simulations at constant pressure than constant volume in the sense that previous configuration can be used

to start a new run in the series. The system then changes its size automatically in response of the change in pressure. In the constant NVE simulations, compressing a system to higher density by simply re-scaling positional coordinates causes a number of overlaps which need to be removed. Two pragmatic ways of overcoming this problem are as follows. Firstly, to create a configuration of higher density the NPE algorithm can be used. Simply by setting the pressure to a high value this will compress the system up to the required density without creating overlaps. The other way around the problem requires use of MD code developed previously. If code written for the Gay-Berne fluid is modified by raising the steep repulsive interaction to the power of 24 instead of 12 and ϵ_0 is made 10 times greater, the forces and torques prove sufficient to remove existing overlaps in a matter of a few MD time steps. This method was employed because it required much less computer time at the studied range of densities.

5.3.2 Simulation Results

The system of 1000 HGO particles with aspect ratio 3 was studied in the constant NVE and NPE ensembles. The orientational order parameter and pair distribution functions were calculated at different densities. The constant volume simulations started from a configuration at $\rho = 0.25$ previously obtained using NPE algorithm from a low density simple cubic lattice configuration. The compression series was performed up to density $\rho = 0.33$ with a step of $\Delta rho = 0.01$. After equilibration at a given density for $5 \times 10^5 - 10^6$ MC cycles and calculation of the observable for further 5×10^5 MC cycles the system was compressed to a higher density using the MD algorithm described above. Here, one MC cycle involves N random MC displacement moves, where N is the number of particles in the system. Therefore, on average each particle experiences one trial move per cycle. The mean square displacement measurements were carried out to adjust appropriate values of maximum translational displacement Δr_{max} and rotation ϕ_{max}. It is a common practice to keep acceptance level about 50% although this does not always provide the best

convergence properties. The maximum mean square displacement was used as a criterion and the highest displacement was achieved at about 20% acceptance level. The displacement rate at both low and high densities was found to be about 2.5 times higher at 20% acceptance level than at 50%.

The constant volume simulation series revealed the isotropic-nematic transition to occur at a density of about 0.305. Then the system was studied further by the constant pressure simulations. It was found that the pressure of isotropic-nematic coexistence was between $4.95 < P_{IN} < 5.00$ and the densities of the coexisting phases were $\rho_I = 0.301$ and $\rho_N = 0.307$. In analogous simulations done by de Miguel and del Rio [96] using a smaller system of 500 HGO particles, these values were found to be $P_{IN} = 4.918$, $\rho_I = 0.2989$, and $\rho_N = 0.3046$. Normally due to the finite size effects the nematic-isotropic coexistence pressure and densities are expected to be slightly higher in a bigger system [97], therefore our results was found to be in a good agreement with the literature data.

The orientational order parameter measured in both ensembles in the range of densities $0.27 \leq \rho \leq 0.33$ is shown in Fig. 5.5. Here the results obtained from constant
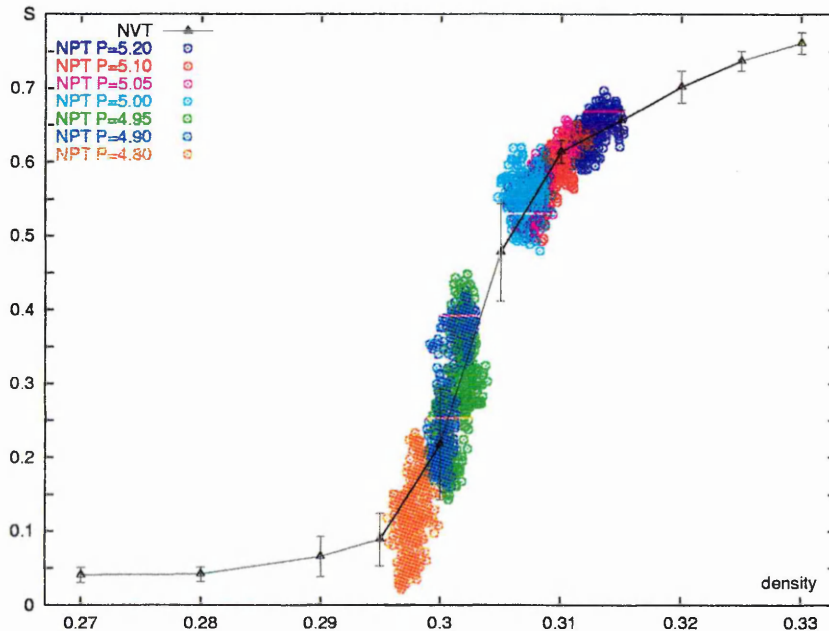

Figure 5.5: Isotropic-nematic transition in the system of HGO particles studied in both constant NVT (black line) and constant NPT (colour marked dots) ensembles.

pressure simulations are presented as sets of colour marked dots, whereas average values of the order parameter from the constant NVE simulations are shown along with their mean square deviations. Both methods gave essentially the same dependence of the order parameter on density, however, the simulations at constant pressure did not exhibit the metastable states seen at near transition densities in the constant volume runs. Comparing Fig. 5.5 to Fig. 5.3 we can see that ordering in the Gay-Berne fluid starts at lower densities. At the same time, HGO particles do not exhibit a smectic phase which is promoted by the relatively strong side-side attractions in the Gay-Berne fluid. The short range order in the isotropic phase is also different in the system of HGO and Gay-Berne particles. Figure 5.6 shows the set of pair distribution functions for both systems calculated at low density $\rho = 0.25$ (the temperature was set to $T = 0.7$ for the Gay-Bene system). The radius of the
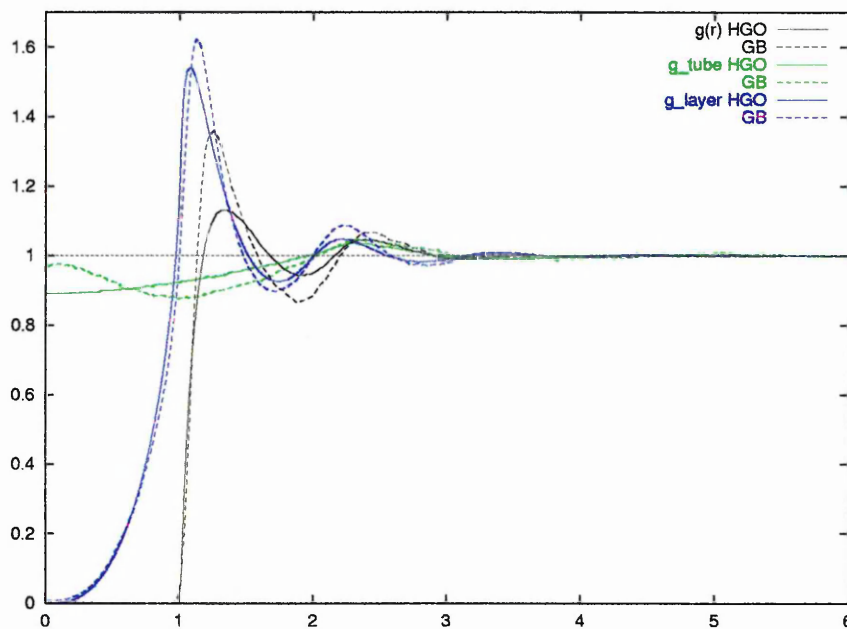
Figure 5.6: Pair distribution functions $g(r)$, $g_{tube}(r_{||})$ and $g_{layer}(r_{\perp})$, for HGO and Gay-Berne particles at the same density $\rho = 0.25$.

tube for $g_{tube}(r_{||})$ and the semi-thickness of the layer for $g_{layer}(r_{\perp})$ were chosen to be $\sqrt{5}$ which is the closest distance between two HGO particles in the T configuration. This provided that $g_{layer}(r_{\perp})$ approached zero at $r_{\perp} = 0$ in the system of hard particles. In the Gay-Berne fluid, separations less than 1 can be found and $g_{layer}(r_{\perp})$ approaches 0.0066 at $r_{\perp} = 0$. This is because of the "softness" of the

particles which allows them to form configurations prohibited for the hard core particles. The higher the temperature, the higher the number of such configurations. Thus, at high temperatures, the isotropic-nematic transition density will be shifted up for the "soft" particles because of the decrease in their effective volume. This is the main reason why the corresponding phase boundaries on the phase diagram shown in Fig. 4.3 have a slope.

The radial distribution functions in both systems (see Fig. 5.6) have two peaks corresponding to side-side and T configurations. Both peaks are higher for the Gay-Berne fluid because of the attractive regions near to the sides and ends of the particles. No signs of stable end-to-end configurations can be seen in either system and all distribution functions approach unity at a distance of about $4\sigma_0$.

5.4 Mixtures of Hard Rods and Spheres

Binary mixtures of HGO particles of length to breadth ratio 3:1 and small hard spheres with diameters equal to the breadth of rods are studied in this Section. Sphere concentrations of 5%, 10%, 15%, 20%, 30%, 40% and 50% are studied in the constant NVE ensemble using the MC technique. The total number of particles in the system was kept $N = 2048$ while the numbers of rods and spheres were adjusted to provide each desired concentration. A compression sequence was performed for each concentration, starting from a low isotropic density configuration and continuing until the nematic order parameter had reached a high value. The initial configuration for each run was obtained by taking an isotropic configuration with lower sphere concentration and substituting of some of its rods with spheres. The mean square particle displacement was monitored within these simulations to ensure that, within each run, the particles travelled distances comparable with the simulation box side; had the runs been significantly shorter than this, it would have been impossible to assess any possible demixing occurring in the system. Table 5.4 shows the number density range for which each mixture simulated. A step

Concentration	ρ_{START}	ρ_{FINISH}
5%	0.290	0.330
10%	0.295	0.350
15%	0.300	0.360
20%	0.320	0.410
30%	0.350	0.405
40%	0.410	0.445
50%	0.420	0.510

Table 5.1: Number density range of the performed compression series.

of $\Delta\rho = 0.005$ was used between neighbouring data points in each compression sequence and a modified version of an MD code (see Section 5.3.1) was employed to generate the initial configuration after each density increment. Figure 5.7 presents
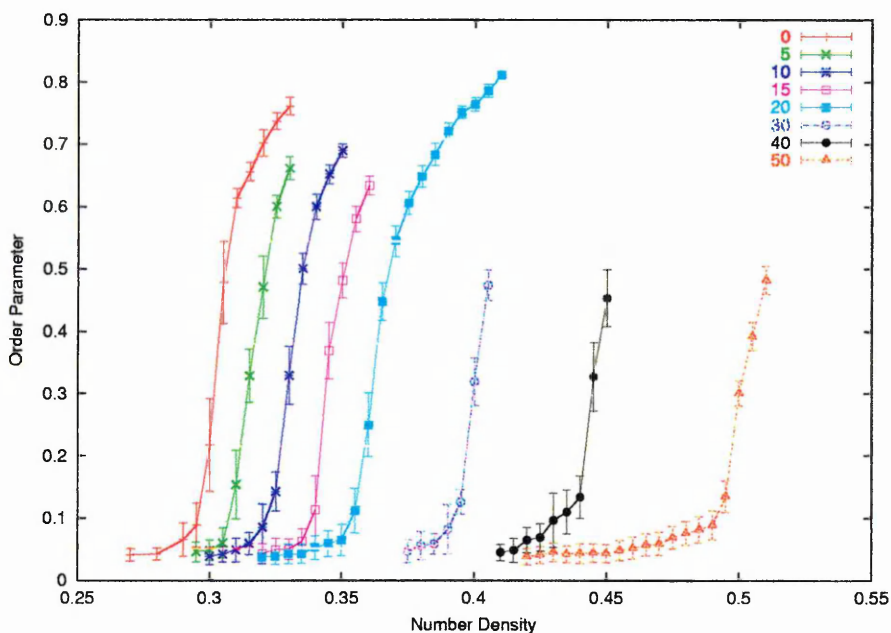
Figure 5.7: Order parameter dependence on number density for various mixtures.

the resultant density dependencies of the order parameter in all of the compression sequences performed. These indicate that an isotropic-nematic transition occurred during each sequence. However, the number density is not a convenient parameter with which to characterise systems with different concentrations. Since spheres are smaller than rods, a given number density corresponds to a different volume fraction

at different concentrations. If we take a rod as a linear assembly of three spheres, the total volume occupied by hard particles can be approximated by

$$V_{occupied} \approx N_{sph} \cdot V_{sph} + N_{rod} \cdot 3V_{sph} = V_{sph} \cdot (N_{sph} + 3N_{rod}) , \qquad (5.6)$$

where N_{sph} and N_{rod} are the numbers of spheres and rods and $V_{sph} = \pi/6$ is the volume of a sphere with unit diameter. The number density, ρ, is defined as the total number of particles divided by the volume. Therefore, the volume fraction can be written as

$$f_{occupied} = \frac{V_{occupied}}{V_{total}} \approx \frac{V_{sph} \cdot (N_{tot} + 2N_{rod})}{V_{total}} = \rho \cdot V_{sph} \cdot (3 - 2c_{sph}) , \qquad (5.7)$$

where c_{sph} is the sphere concentration ratio ranging from 0 to 1. Figure 5.8 shows
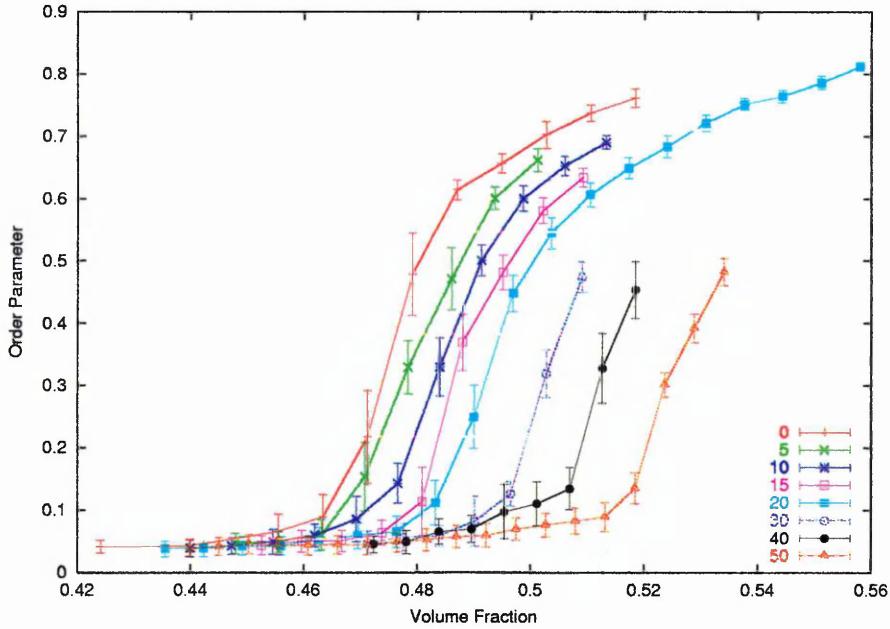
Figure 5.8: Order parameter dependence on volume fraction for various mixtures.

the nematic order parameter as a function of occupied volume fraction at various sphere concentrations. These show a clear tendency for the transition point to shift towards higher volume fractions as the concentration of spheres is increased. At the highest concentration of spheres studied, 50%, the density at which the isotropic-nematic transition occurred was such that the mobility of the particles was very low: 1.5×10^7 MC cycles were required to equilibrate the last configuration in this

compression sequence. Therefore, higher sphere concentrations were not studied because of the dramatic increase of the required computational time. Whether rod-sphere mixtures of even higher sphere concentrations exhibit a nematic phase depends mainly on their demixing properties. Clearly, there is no nematic phase in a system of pure hard spheres and addition of a small number of rods would not be able to induce orientational order unless these rods became segregated. This would require a relatively strong rod-rod attractive depletion interaction. The literature data show that a mixture of hard spheres with diameters σ and 10σ does not exhibit stable fluid-fluid coexistence [98]. However, although the components of our mixture have more moderate size difference, their shape difference may be sufficient to induce entropy driven demixing [36, 99].

The demixing properties of our 50% mixture were studied by monitoring the sphere-sphere radial distribution function. Figure 5.9(a) shows the corresponding $g_{ss}(r)$
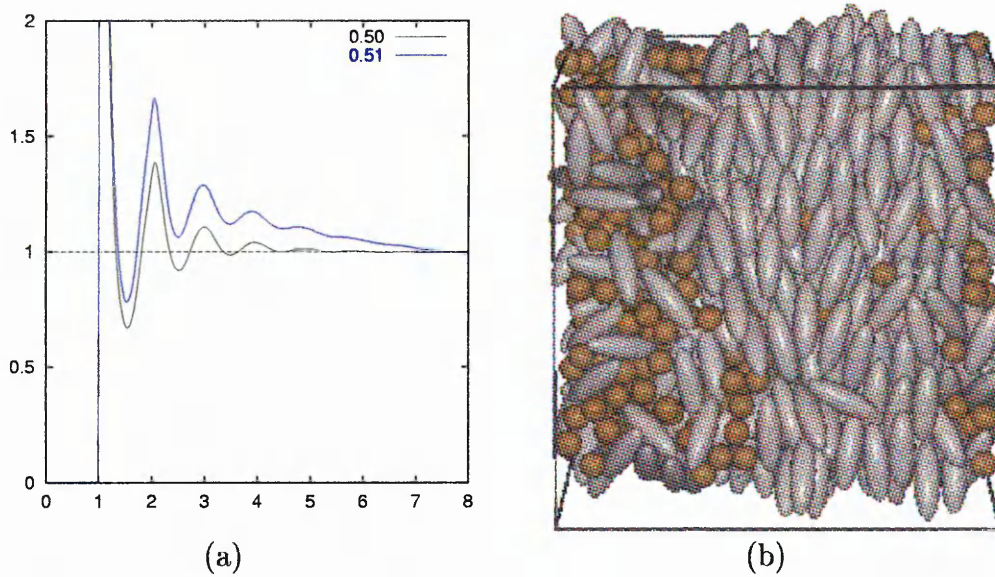
Figure 5.9: (a) Sphere-sphere radial distribution functions measured in 50% mixture at $\rho = 0.50$ and $\rho = 0.51$; (b) configuration snapshot taken at $\rho = 0.51$.

curves measured at $\rho = 0.500$, and $\rho = 0.510$. The latter clearly exhibits a monotonic decrease at large separations, typical behaviour for a macrophase separated system. At $\rho = 0.500$, however, no signs of demixing were apparent from $g_{ss}(r)$, although the observed nematic order parameter was 0.301 ± 0.020. A configuration snapshot taken

at $\rho = 0.51$ (Fig. 5.9(b)) confirms the demixing and shows a rod-rich phase, almost free of spheres, coexisting with a rod-sphere mixture with a high concentration of spheres. This suggests that the volume fraction of the mixing-demixing transition depends only weakly on sphere concentration especially at $0 \leq c_{sph} \leq 0.50$.

Subsequently, a 20% mixture was compressed to high densities to investigate its mixing-demixing behaviour. The sphere-sphere radial distribution function and cluster size distribution were calculated at each density to assess system homogeneity. Figure 5.10 shows these simulation results, averaged over at least 10^5 MC cycles.
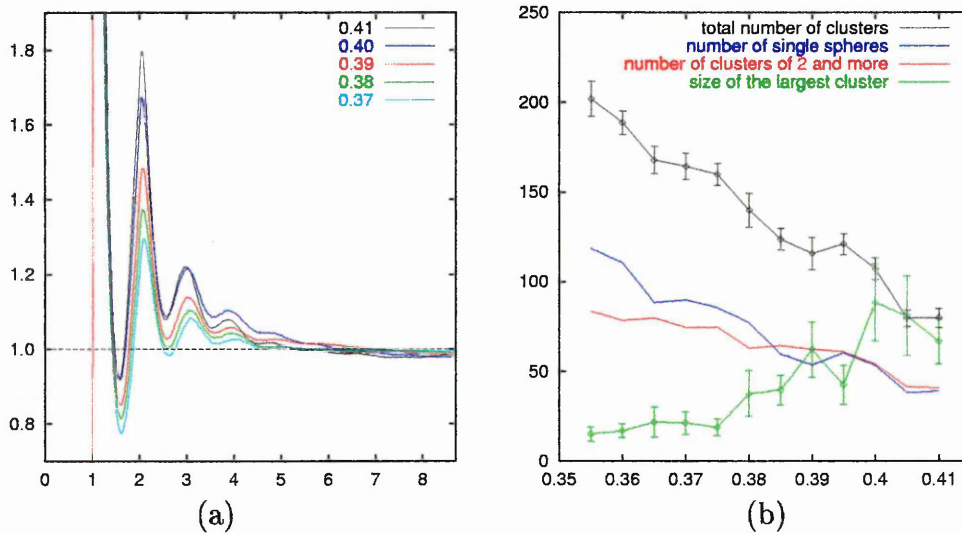
Figure 5.10: (a) Sphere-sphere radial distribution functions measured in 20% mixture at different densities; (b) average cluster size distribution at various densities.

The $g_{ss}(r)$ curves indicate weak but growing signs of demixing as the density is increased. Despite the increased probability of finding another sphere at short separations at high densities, $g_{ss}(r)$ approaches unity at larger r. This suggests a random distribution of small clusters of spheres. The data shown in Fig. 5.10(b) also suggest that this demixing was not macroscopic: about a hundred clusters of spheres (half of which were just single spheres) separated by distances greater than $1.5\sigma_0$ were found even at the highest density. However, the largest cluster contained about 20% of the total number of spheres at high densities. Since these runs were sufficiently long to allow an average sphere displacement to be greater than the simulation box side, these systems were certainly not glassy. Also, the clusters of spheres were

found to change dynamically during the runs. When compared to the 50/50 simulations, demixing would have been expected at about the same volume fraction, i.e. $f = 0.52$, which corresponds to a number density of $\rho \approx 0.38$. This is the density at which the size of the largest cluster started to increase significantly (Fig. 5.10(b)). This suggests that the 20% mixture had a weak tendency to demix, although, no macroscopic demixing was observed for this system size.

The simulations performed show that binary mixtures of hard spheres and HGO particles with aspect ratio 3 do not exhibit lamellar structures but only isotropic and nematic phases. The approximate phase diagram of the system is shown in Fig. 5.11, blue diamonds representing the simulation points. The solid red line
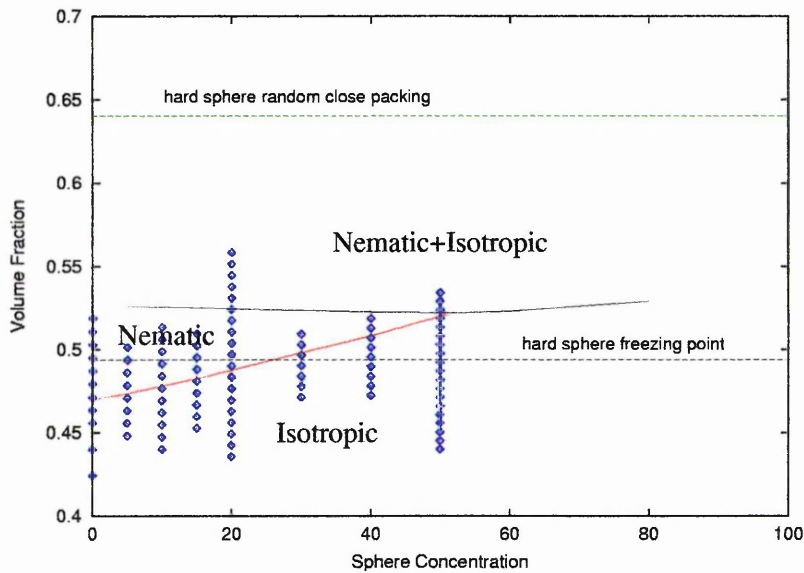
Figure 5.11: Approximate phase diagram of binary mixture of the hard particles.

connects points in which the increase of the nematic order parameter indicated a phase transition. It was impossible to evaluate the isotropic and nematic coexistence densities from our exploratory NVE simulations. However, we would expect these to be in close proximity to the red line in Fig. 5.11, due to the weakness of the transition.

Clearly, there is an upper limit on the occupied volume fraction in a system of hard particles. For a system of monodisperse hard particles, the random close packing

volume fraction is about 0.64 [100] (the dashed green line in Fig. 5.11). The freezing point in a hard sphere system, of approximately 0.494 is represented by the black dashed line. At this volume fraction, the entropy in a system of hard spheres can be maximised by the formation of crystal structure. We note that an analogous phenomenon takes place in rod-sphere mixtures. At zero and low sphere concentrations, an isotropic-nematic transition occurs at even lower volume fractions. At low concentrations of spheres we observed a nematic phase with randomly dispersed spheres in it, which supports the argument that mixing entropy is high. As the concentration of spheres was increased, the transition shifted towards higher volume fractions. For sphere concentrations of 50%, the onset of demixing occurred at a volume fraction of $f \approx 0.52$. The simulation method we used is not applicable to studying whether the system exhibits a crystalline phase at sufficiently high volume fractions or remains in a glassy configuration. It also fails at both low and high sphere concentrations, therefore, we cannot speculate about these parts of the phase diagram.

Incorporating attractive interactions into the model can reduce the relative influence of the mixing entropy and so give rise to macro or micro-phase separation. In the next Chapter, we will study various binary mixtures of Gay-Berne and Lennard-Jones particles in the bulk.

Chapter 6

Rod-Sphere Mixtures in bulk

In this Chapter, various mixtures of rods and spheres interacting via attractive-repulsive soft potentials are studied in the bulk. Maintaining the sizes of the particles as those there used in the previous Chapter, we concentrate on the role of attractive interactions in these systems.

Four mixtures, which differ only in their interactions between unlike particles, are studied at various concentrations using MD in the constant NVT ensemble. Some of the results are also validated in the constant NPT ensemble using MC techniques. First, we study the original parameterisation of the rod-sphere potential, characterised by a relatively strong side attraction. Then the behaviour of a system with a relatively strong end attraction is described in Section 6.3. A system with interaction strength independent of relative orientation of rod and rod-sphere vector is studied in Section 6.4. Finally, in Section 6.5, we consider a system which possesses a very strong end attraction, so combining the physical properties of both calamatic and lyotropic LCs.

6.1 The Model

The systems considered here are binary mixtures of Lennard-Jones particles and Gay-Berne particles with the original parameterisation (3,5,2,1) (see Section 4.2.3 for details). The parameters σ_0 and ϵ_0 are taken to be equal for both particle types. This means that the diameter of the spheres is equal to the breadth of the rods and the well depth of the sphere-sphere interaction is equal to that of two rods in the X-configuration. The interaction between unlike particles is described by the Generalised Gay-Berne potential considered in Section 4.2.5. Its parameters were originally derived in relation to the interaction between two Gay-Berne particles and, therefore, reflect their energetic properties. The relative strengths of the interactions in this system are given in Tab. 6.1. The energy parameter ϵ of the rod-sphere

Type of interaction	Well depth
Two spheres	1
Two rods (X-configuration)	1
Two rods (side-by-side)	1.666666
Two rods (end-to-end)	0.333333
Two rods (T-configuration)	0.381966
Rod and sphere (side)	1
Rod and sphere (end)	0.2

Table 6.1: Strengths of different types of interactions for system with original parameterisation.

potential, given by

$$\epsilon(\hat{\mathbf{r}}_{ij}, \hat{\mathbf{u}}_j) = \epsilon_{RS} \left[1 - \left(1 - \left(\frac{\epsilon_E}{\epsilon_S} \right)^{1/\mu} \right) (\hat{\mathbf{r}}_{ij}.\hat{\mathbf{u}}_j)^2 \right]^{\mu}, \qquad (6.1)$$

contains the ratio $\frac{\epsilon_S}{\epsilon_E}$ which controls the well-depth anisotropy of the interaction. In the original model, this ratio is set to $\kappa' = 5$ which means that spheres favour the sides of the rods rather than the ends. The potential energy contours corresponding to this case are shown in Fig. 6.1(a). By changing the ratio $\frac{\epsilon_S}{\epsilon_E}$ it is possible to create systems in which the spheres either favour the ends of the rods ($\frac{\epsilon_S}{\epsilon_E} > 1$, see Fig. 6.1(b)) or make no distinction between the rods' ends and sides ($\frac{\epsilon_S}{\epsilon_E} = 1$, see Fig. 6.1(c)). To assess the significance of this interaction, in this Chapter we are

74

(a)
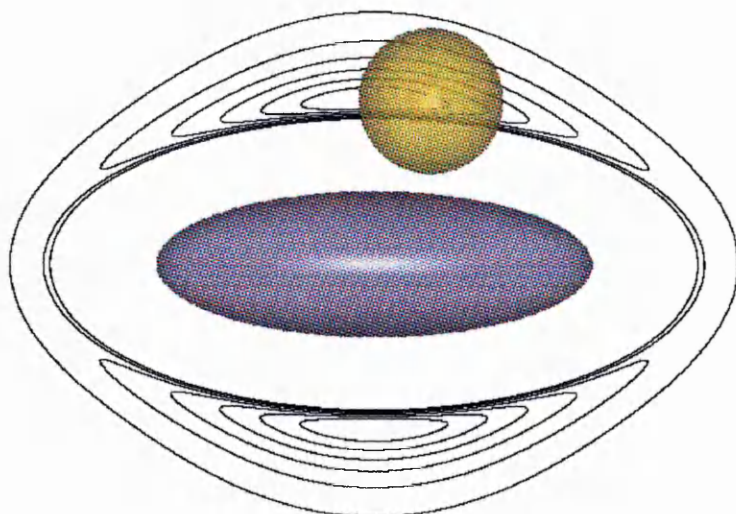
(b)
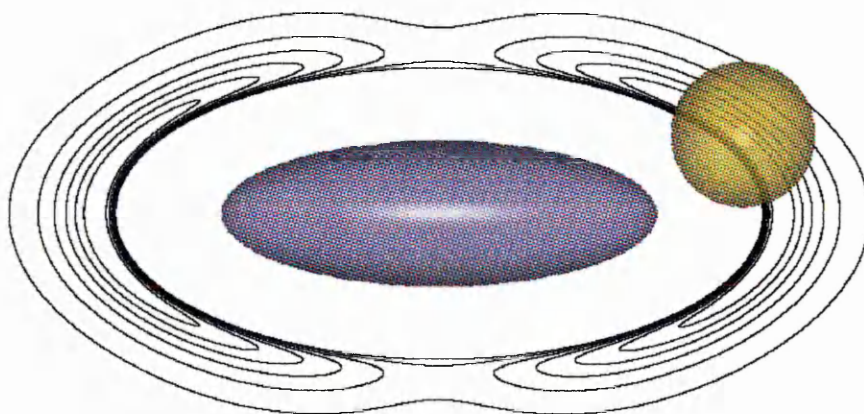
(c)
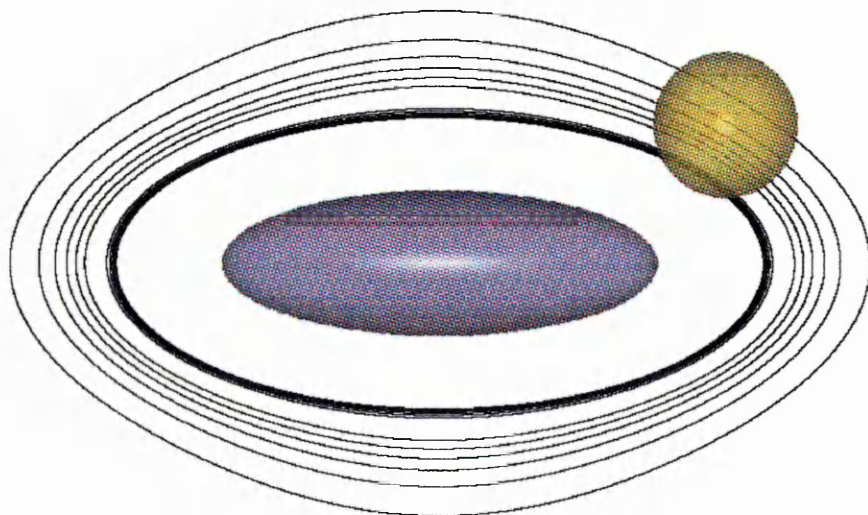
Figure 6.1: Rod-sphere potential energy contours for different values of the ratio $\frac{\epsilon_S}{\epsilon_E}$:
(a) $\frac{\epsilon_S}{\epsilon_E} = 5$, (b) $\frac{\epsilon_S}{\epsilon_E} = 0.2$, (c) $\frac{\epsilon_S}{\epsilon_E} = 1$.

going to look at four systems which differ only in their parameterisation of the rod-sphere potential. Table 6.2 contains the values of the parameters of equation (6.1) and the corresponding side, ϵ_S, and end, ϵ_E, well depths which define the rod-sphere interaction anisotropy in each system. System (i) has the original parameterisation,

System	ϵ_{RS}	ϵ_S/ϵ_E	ϵ_S	ϵ_E
(i)	1	5	1	0.2
(ii)	0.2	0.2	0.2	1
(iii)	1	1	1	1
(iv)	1	0.2	1	5

Table 6.2: Rod-sphere energy parameters of four mixtures.

in systems (ii) and (iv) the spheres favour ends of the rods, and system (iii) has the interaction shown in Fig. 6.1(c). Systems (ii) and (iv) both have the potential energy contour map shown in Fig. 6.1(b), the difference being that all rod-sphere interactions in the latter are five times stronger then those in the former. In the following sections, we present MD and MC simulations performed on these systems, with a view to constructing their approximate phase diagrams.

6.2 System (i)

This Section presents the results of MD simulations performed on mixtures with the original interaction parameters of the rod-sphere potential given in the previous Section. Several series of compression and cooling runs were performed to build up an approximate phase diagram of the mixture, first, at a 50/50 rod-sphere concentration ratio, and then at lower concentrations of spheres.

6.2.1 50/50 Mixture

The behaviour of system (i) was investigated by surveying the temperature and density dependence of a 50/50 mixture of Lennard-Jones and Gay-Berne particles. The

system, which contained 512 rods and 512 spheres, was simulated using the MD algorithm described in Section 5.2.1 and the expressions for the forces and torques given in Appendix A. Analogous to the simple GB fluid study presented in Section 5.2, firstly, the developed code was validated in the constant NVE ensemble. After it had passed the conservation and stability tests, a compression series was performed over the range of densities $0.22 \leq \rho \leq 0.50$ at a constant temperature of $T = 0.7$. At each density, the nematic order parameter, potential energy per particle and pressure were measured for 2×10^5 time steps preceded by at least 5×10^5 time steps of equilibration. Table 6.3 presents the average values of these quantities

Number density	Potential energy	Order Parameter	Pressure
0.40	-3.972 ± 0.030	0.074 ± 0.027	1.03 ± 0.08
0.41	-4.064 ± 0.031	0.084 ± 0.037	1.17 ± 0.08
0.42	-4.145 ± 0.028	0.101 ± 0.044	1.37 ± 0.09
0.43	-4.207 ± 0.029	0.142 ± 0.061	1.58 ± 0.08
0.44	-4.281 ± 0.033	0.181 ± 0.088	1.82 ± 0.10
0.45	-4.402 ± 0.041	0.495 ± 0.049	1.93 ± 0.12
0.46	-4.536 ± 0.055	0.658 ± 0.063	2.07 ± 0.10
0.47	-4.910 ± 0.033	0.856 ± 0.016	1.85 ± 0.10
0.48	-5.050 ± 0.032	0.891 ± 0.011	2.04 ± 0.10
0.49	-5.149 ± 0.032	0.912 ± 0.008	2.32 ± 0.11
0.50	-5.241 ± 0.032	0.926 ± 0.006	2.67 ± 0.11

Table 6.3: Potential energy per particle, the nematic order parameter and pressure calculated on $0.40 \leq \rho \leq 0.50$ at $T = 0.7$.

together with their mean square deviations. The nematic order parameter indicates a phase transition at a density of about $\rho = 0.45$. The high values of the order parameter at densities greater than $\rho = 0.46$ suggest a smectic phase. The parallel distribution function, $g_\|(r_\|)$, measured in the vicinity of the transition and shown in Fig. 6.2(a), confirms the presence of a smectic phase with an interlayer separation of about $2.62\sigma_0$. Since the rod length is $3\sigma_0$ this suggests overlapping of neighboring layers. The rod-rod and sphere-sphere radial distribution functions calculated at $\rho = 0.42$ and $\rho = 0.47$ and shown in Fig. 6.2(b) indicate that the structure of the sphere-rich phase remained almost unchanged in this density range, implying that density changes were accommodated by the rearrangement of the rod-like par-
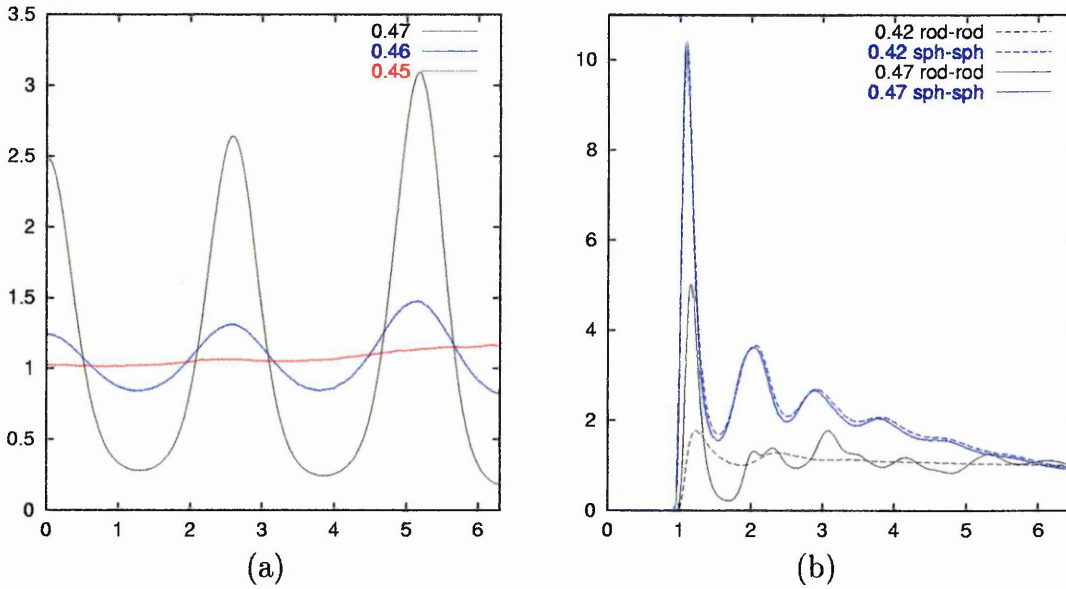
Figure 6.2: (a) Parallel distribution function, $g_\parallel(r_\parallel)$, at $T = 0.7$ and different densities; (b) radial distribution functions for like particles measured at $\rho = 0.42$ and $\rho = 0.47$.

ticles. The peak distribution of the rod-rod radial distribution function measured at $\rho = 0.47$ also suggests a hexagonal arrangement within the smectic layers, typical for the S_B phase. The high values of the sphere-sphere radial distribution functions at short separations indicate that some demixing occurred in this system. Indeed, if the spheres group together then the probability of finding one sphere close to another is higher than in the case a homogenous mixture. Two configuration snapshots taken below and above the transition point are shown in Fig. 6.3. These indicate coexistence between rod-rich and sphere-rich phases at both densities considered, as well as the isotropic-smectic transition exhibited by this system. The spheres formed a cylinder at ($\rho = 0.42$) and ($\rho = 0.47$), whereas snapshots taken at lower densities (not shown here) showed the spheres forming a spherical droplet suspended in the rod-rich phase. There are two principal mechanisms that could induce the observed drop-shape change. The first is that due to the periodic boundary conditions and, therefore relevant at all densities. The second mechanism driving the droplet elongation is the ordering transition of the rod-rich phase. Simulations were performed for a system containing a half of the particles of each type in order to explore the periodic boundary condition effect. To describe the droplet elongation

(a)   (b)
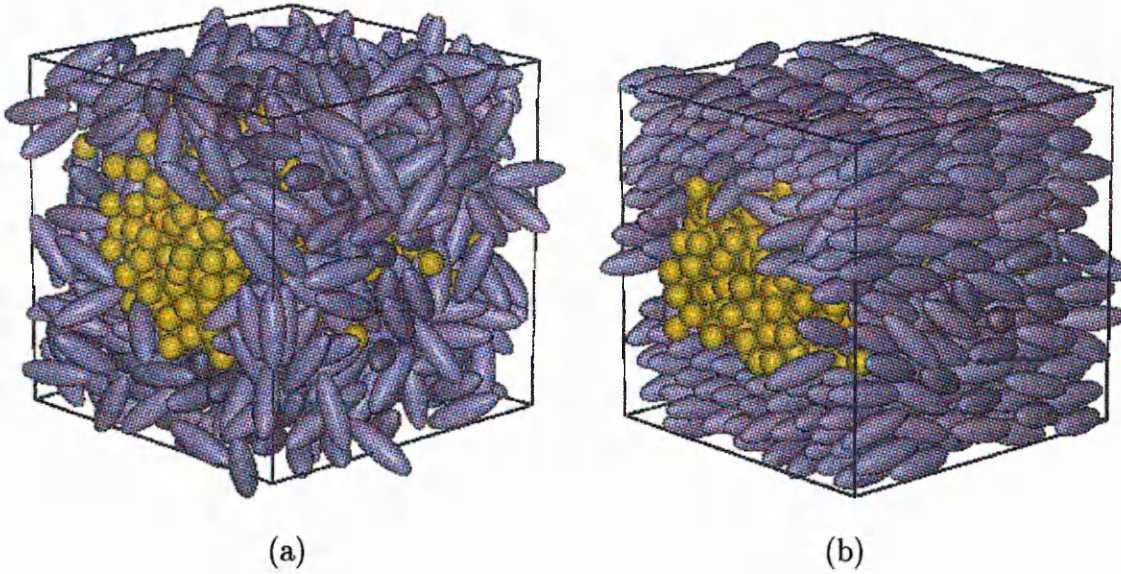
Figure 6.3: (a) Isotropic ($\rho = 0.42$) and (b) LC phase ($\rho = 0.47$) at T=0.7.

quantitatively, its tensor of inertia was calculated at every density for runs of 10^5 time steps. For this purpose an algorithm was developed to determine the location of the centre of mass of the droplet taking into account the periodic boundary conditions. First, sphere j from which the sum of squared distances to the other spheres was minimal was found and all particles were translated by vector $-\mathbf{r_j}$. This was to place the centre of mass of the droplet close to the origin of the reference frame which coincided with the center of the simulation box. Then, further translation by the vector

$$\mathbf{r_{shift}} = \frac{1}{N_{sph}} \sum_{i=1}^{N} \mathbf{r_i} \qquad (6.2)$$

was performed to provide the center mass of the droplet to be exactly in the centre of the simulation box. Finally, the inertia tensor was calculated as follows

$$I_{\alpha\beta} = \sum_{i=1}^{N} \mathbf{r_{i_\alpha}} \mathbf{r_{i_\beta}}, \qquad (6.3)$$

and diagonalised using a standard numerical method [101]. The elongation of the droplet was calculated as a run average of the ratio of the greatest eigenvalue of tensor (6.3) to the semi-sum of the other two. Figure 6.4(a) shows the density dependence of both the order parameter and the elongation of the droplet of spheres for
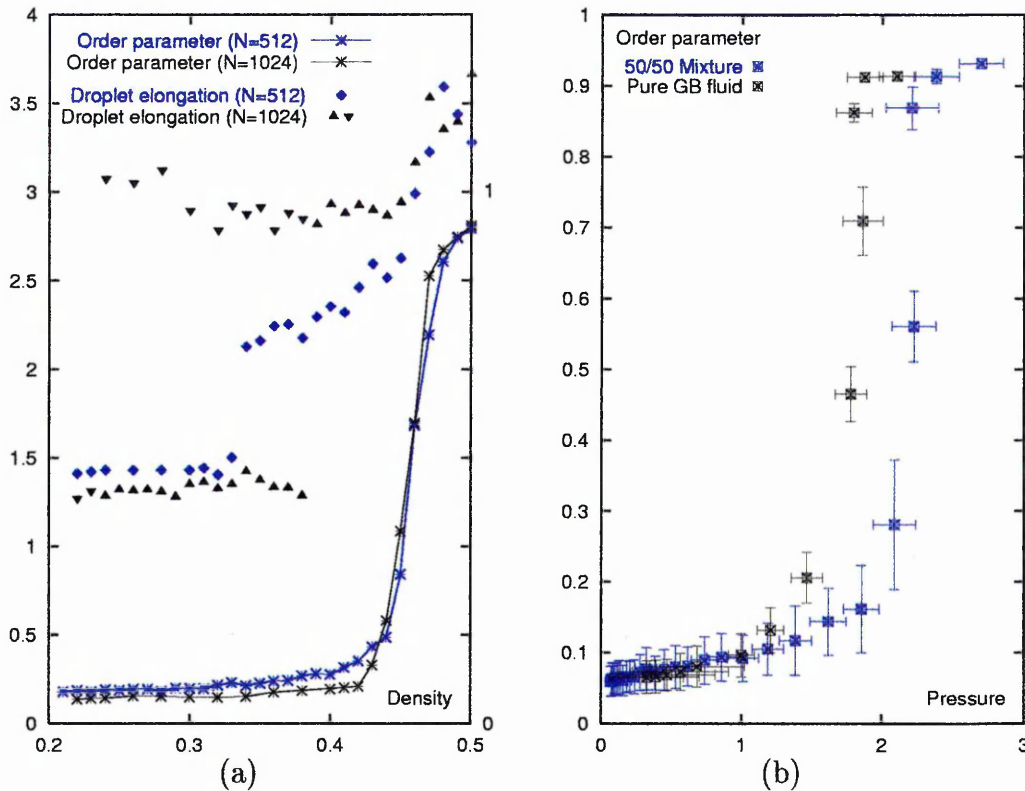
Figure 6.4: (a) The elongation of the droplet and the order parameter measured in the systems containing 1024 and 512 particles in total. (b) The order parameter versus pressure for the 50/50 mixture and pure Gay-Berne fluid.

both systems. In the system of 512 particles in total, the droplet started to elongate at a lower density while the isotropic-smectic transition occurred at approximately the same point as in the larger system. In both systems the droplet changed from spherical to prolate well below the isotropic-smectic transition density, at $\rho \approx 0.345$ in the smaller system (see blue diamonds in Fig. 6.4(a)) and at $\rho \approx 0.385$ in the larger system (blue triangles in Fig. 6.4(a)). The droplet then underwent further elongation at the density of the rods' orientational transition ($\rho \approx 0.46$) in both systems. When expansion runs were performed for the larger system staring from the configuration at $\rho = 0.39$ (blue up-side-down triangles in Fig. 6.4(a)), the droplet remained cylindrical until $\rho = 0.24$. No such hysteresis was observed for the smaller system, however. These simulations show that the system of 1024 particles was still too small for the effect of the periodic boundary conditions to be neglected. Another point to note is that the system configuration at a particular density and tempera-

ture was found to be dependent on the initial configuration (the observed hysteresis). Therefore, the time available for simulation was not sufficient for the system to distinguish between the metastable state induced by the periodic boundary conditions and the thermodynamically stable state.

As well as causing an obvious increase in the transition density, the presence of small spheres also led to a shift in the transition pressure. Fig. 6.4(b) shows that a higher pressure was needed in this 50/50 rod-sphere mixture to obtain the order parameter values seen in the pure Gay-Berne fluid.

The presence of the cylinder formed by spheres broke the orientational and translational symmetry of the simulation box as well as inducing some alignment of the rods. In order to explore the role of the rod-sphere interactions and distinguish it from the excluded volume effect a series of auxiliary runs was performed with hard particles. For this, system configurations were taken at various densities and simulated as mixtures of HGO particles and hard spheres after all overlaps had been removed. The coordinates of the spheres were kept fixed allowing the rods, driven by pure steric repulsion, to find their preferred arrangement near the cylinder. The distribution of cosines of the angles ϕ_i between the cylinder axis and the rods' orientation vectors, $\hat{\mathbf{u}}_i$, was evaluated and averaged over a number of configurations. Equivalent distributions were calculated for the angles θ_i between the radial direction of the cylinder and the vectors $\hat{\mathbf{u}}_i$. The results for densities $\rho = 0.42$ and $\rho = 0.47$, calculated for the systems of soft and hard particles, are shown in Fig. 6.5. It can be seen that in the isotropic phase the rods' alignment with the cylinder axis is similar in both systems (the red and black lines in Fig. 6.5(a) practically coincide). However, the radial distributions are slightly different; due to the relatively strong rod-sphere side attraction, more rods were found "laying" on the surface of the cylinder in the soft particle system. At higher density, the soft particles formed a more ordered phase (smectic not nematic) characterised by a higher order parameter value and narrower and higher peaks of the corresponding probability distributions. Thus, we can conclude that the preferred orientation of the rods near the cylindrical surface is parallel to the cylinder axis. It does not change as rods undergo a phase transition
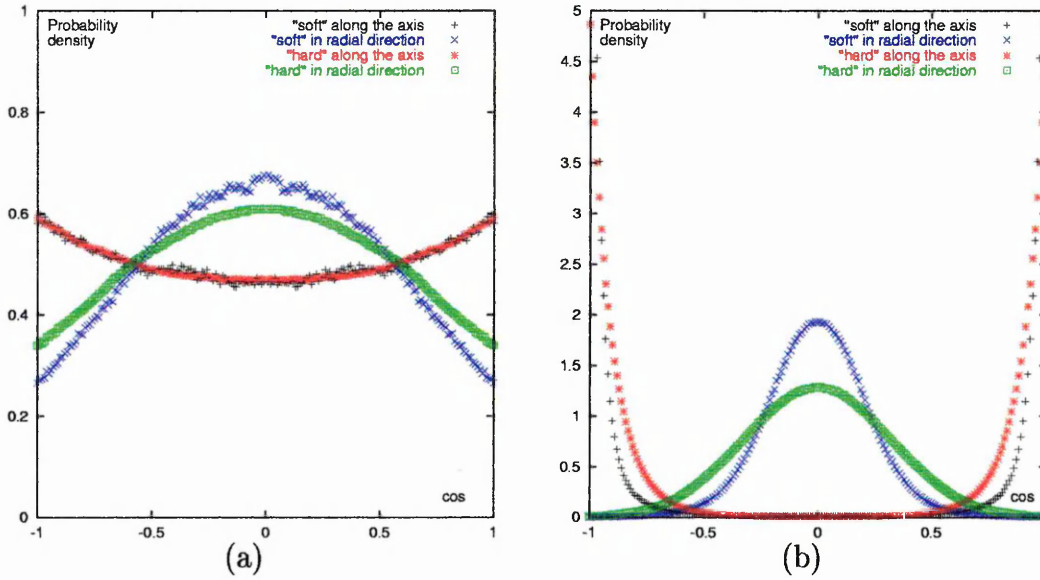
Figure 6.5: Probability distribution of the orientation of the rods along the axis of the cylinder and along the radial direction in the systems of soft and hard particles at (a) $\rho = 0.42$ and (b) $\rho = 0.47$.

from an isotropic to an LC phase, and it is the same for both systems studied.

More simulations were performed at low temperatures and low densities to explore the effect of attractive interactions. The mixture was also studied over a wide density range at high temperatures to define a mixing-demixing line. The rest of this Section relates to a switching effect found at low temperatures and is followed by a discussion of the composed phase diagram.

An interesting switching effect was found at low temperatures when cooling the system from the configurations obtained during the compression run at $T = 0.7$ described above. If the system was cooled down at density $\rho = 0.45$ or $\rho = 0.44$, then at a temperature of above $T = 0.6$ it developed smectic order analogous to that shown in Fig. 6.3 with the director parallel to the axis of the cylinder. If the cooling run was started from the configuration at $\rho = 0.43$ and $T = 0.7$, the system remained isotropic at $T = 0.6$, and a smectic phase formed at $T = 0.5$ with the director perpendicular to the axis of the cylinder (Fig. 6.6(a)). The cooling run at lower density $\rho = 0.42$ did not reveal the smectic phase at $T = 0.5$. The nematic order parameter was $S = 0.18 \pm 0.05$ which was too high for an isotropic

(a)   (b)
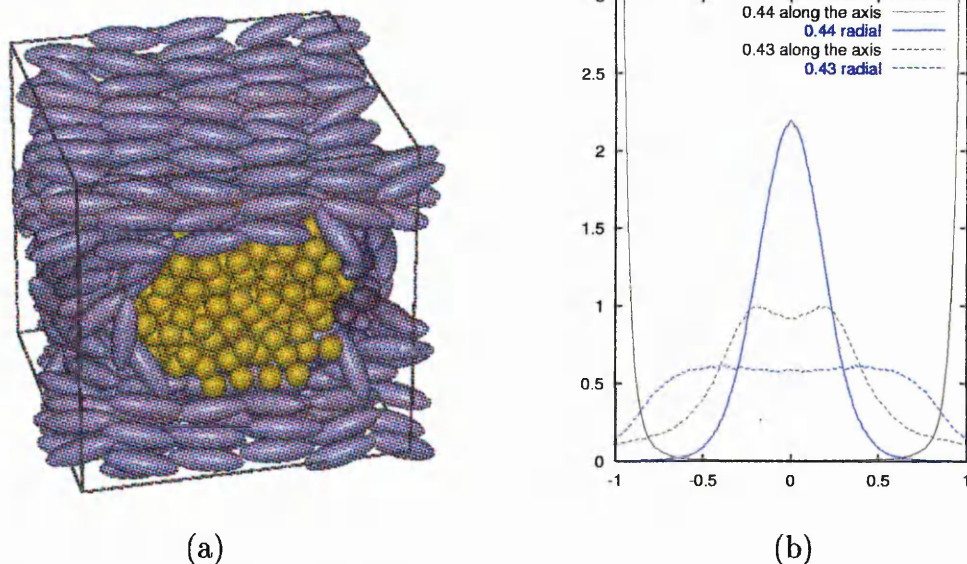
Figure 6.6: (a) Snapshot taken at $\rho = 0.43$ and $T = 0.5$; (b) probability distribution of the rods' orientation along the axis of the cylinder and along the radial direction for configurations with perpendicular ($\rho = 0.43$) and parallel ($\rho = 0.44$) alignments at $T = 0.5$.

phase but the director did not have preferable orientation and changed during the simulation. The probability distribution analysis indicated rods' orientation similar to that calculated at higher temperature $T = 0.7$ and the same density. This suggests that the order parameter increase was due to pre-transitional behaviour rather than the influence of the cylinder.

The type of the alignment was found to be stable in respect to compression or expansion at constant temperature. If we started the simulation from the higher density configuration at $\rho = 0.44$ and expanded the simulation box to $\rho = 0.43$ and then $\rho = 0.42$, the system did not switch to the configuration with perpendicular alignment. Instead, the director remained parallel to the cylinder axis as it had been oriented before the expansion. The opposite was also true: the director remained perpendicular to the axis of the cylinder if the configuration shown in Fig. 6.6(a) was compressed to a higher density. Typical probability distributions of the rods' orientations with respect to the cylinder axis are shown for both types of alignment in Fig. 6.6(b). These quantitatively describe the preference of the rods to be per-

pendicular at $\rho = 0.43$ and parallel at $\rho = 0.44$ to the cylinder axis. Table 6.4

Alignment	$\rho = 0.42$	$\rho = 0.43$	$\rho = 0.44$
parallel	-4903 ± 37	-5066 ± 27	-5167 ± 27
perpendicular	-4701 ± 24	-4996 ± 26	-5104 ± 28

Table 6.4: Potential energies of configurations with different types of alignment at $T = 0.5$.

shows the total potential energies of the configurations obtained from both cooling and compression/expansion runs. The system's favouring of the higher energy perpendicular configuration at $\rho = 0.42$ and $\rho = 0.43$ when cooled down must be a high entropy of this arrangement. The entropy of the isotropic state seen at $\rho = 0.42$ is certainly much higher than that of the smectic phase. Similarly, at $\rho = 0.43$, the two line defects formed parallel to the cylinder (6.6(a)) possess higher entropy than uniform smectic layers. The free volume appears to be sufficient to allow these defects to form at $\rho = 0.43$ and but this is not the case at $\rho = 0.44$ where the configuration with parallel alignment appears thermodynamically favorable. The configuration with perpendicular alignment at $\rho = 0.43$ and $T = 0.5$ was observed if the final configuration of the cooling run at $\rho = 0.42$ and $T = 0.5$ was compressed up to $\rho = 0.43$.

Two more runs with the sphere positions frozen were performed for hard particle systems at $\rho = 0.43$ and $\rho = 0.44$ after all overlaps had been removed. These were started from the final configurations of the cooling runs at $T = 0.5$ which were considered to be the low free energy configurations. It was found that at $\rho = 0.43$ the rods did not form a nematic phase whereas at $\rho = 0.44$ the nematic order parameter was $S = 0.38 \pm 0.07$, certainly was too high for an isotropic phase. In both cases the preferred alignment of the rods was along the cylinder axis, as would be expected from the previous results (Fig. 6.5). This implies that in the absence of side rod-sphere attractions to impose planar alignment upon the rods near the cylinder surface, the preference of the rods is to be parallel to the cylinder axis, this being an excluded volume effect. At density $\rho = 0.43$ HGO particles do not develop nematic order, whereas the Gay-Berne particles form a smectic at this point at $T = 0.5$

due to their strong side-side interactions. As the smectic phase develops under isochoric conditions from less dense isotropic phase, some extra volume becomes available in the simulation box. This would normally be compensated by stretching the interlayer spacing to avoid developing of empty space in the box. This suggests, therefore, that the configuration observed at $\rho = 0.43$ and $T = 0.5$ develops due to this particularity of the constant NVT ensemble. Several MC runs in constant NPT ensemble were carried out to clarify this point. The simulations were started from an MD configuration equilibrated at $\rho = 0.42$ and $T = 0.7$. The temperature was set to $T = 0.5$ and pressure to $P = 0.5$ which was slightly less than the pressure calculated in MD runs at $\rho = 0.42$ and $T = 0.5$. The resulting data for this and the following run are shown in Tab. 6.5 They indicate that the isotropic-smectic

Pressure	0.5	0.6
Density	0.414 ± 0.003	0.481 ± 0.002
Order Parameter	0.123 ± 0.042	0.927 ± 0.006

Table 6.5: The equilibrium densities and order parameters evaluated in constant NPT MC runs.

coexistence pressure at $T = 0.5$ is between 0.5 and 0.6 pressure units. They also suggest that the isotropic and smectic coexistence densities are close to $\rho_I = 0.414$ and $\rho_S = 0.481$ respectively. This summaries that all MD configurations observed in the density range $0.42 \leq \rho < 0.48$ were metastable.

Several runs at various concentrations and temperatures were undertaken to build up an approximate phase diagram of the 50/50 mixture. Figure 6.7, the resulting diagram, shows isotropic, nematic, and smectic phases separated by coexistence regions. The dashed line separates a homogenous isotropic mixture from a mixture with some signs of demixing. Figure 6.7 shows that with increasing temperature the density of the order-disorder transition is shifted to higher values and eventually disappears. The fact that the analogous mixture of hard particles is homogeneous at these densities supports the existence of an upper limit temperature above which neither LC ordering nor demixing can be observed in the system of soft particles. At temperatures below $T = 0.85$, the pure Gay-Berne fluid does not have a ne-
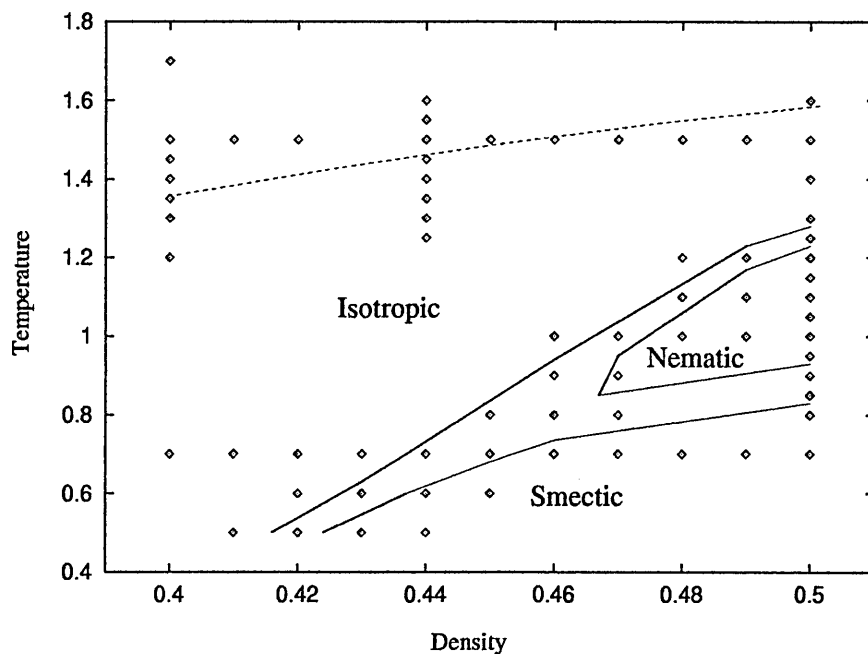
Figure 6.7: Phase diagram of the 50/50 mixture. Diamonds indicate state points at which simulations were conducted; dashed line is the demixing line.

matic phase; therefore, states with a nematic-like order parameter observed at low temperatures are likely to be metastable. Apart from the metastability typical for the constant NVT ensemble near a phase transition the presence of the cylinder formed by spheres imposes some degree of order upon the rods. This creates a paranematic-like state with a director parallel to the cylinder axis. In contrast with the pretransitional behaviour of pure Gay-Berne particles, the order parameter does not fluctuate significantly if the cylinder is present in the simulation box. This supports the idea of the low temperature paranematic phase which can be observed due to a relatively small simulation box size. In a bigger system, however, once macroscopic demixing had occurred the phase behaviour of the rod-rich phase would be similar to that of the pure Gay-Berne fluid.

At all densities, demixing occurs at a higher temperature than that at which LC phases can be observed, and the LC phase always forms in the presence of a cylinder formed by the spheres. This breaks the symmetry of the simulation box and, in the NVT ensemble, conflicts with the formation of smectic layers, because only a

whole number of layers can be accommodated in the box. In order to satisfy this condition the smectic layers tilt and the director makes an angle with the cylinder axis. This tilt, which can be clearly observed, for example, at $T = 0.7$ and $\rho = 0.50$ (Fig. 6.8(a)) is an artifact of the ensemble used here. Due to it the smectic phase

(a)

(b)
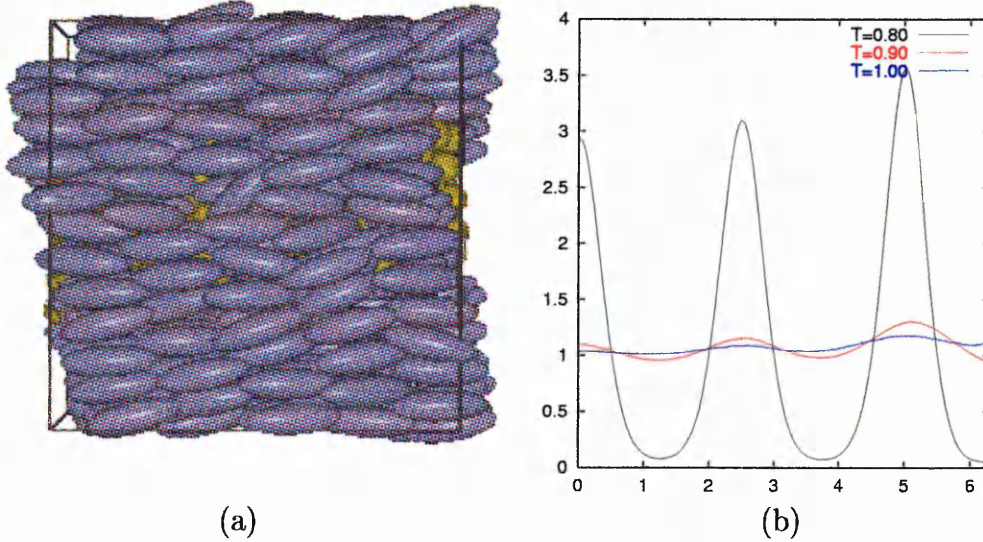
Figure 6.8: (a) System configuration at $T = 0.7$ and $\rho = 0.50$; (b) parallel distribution functions, $g_{\parallel}(r_{\parallel})$, measured at density $\rho = 0.50$ and different temperatures.

might have formed at lower temperatures if the simulation box geometry had allowed. Figure 6.8(b) shows parallel distribution functions calculated during the cooling run at $\rho = 0.50$.

To locate the demixing curve we cooled the system down at constant density observing the sphere-sphere radial distribution functions. When the spheres started to form a droplet, the probability of finding one sphere close to another increased, whereas the probability of finding two spheres far apart decreased. Figure 6.9 shows how the sphere-sphere radial distribution functions changed with decreasing temperature at densities $\rho = 0.40$ and $\rho = 0.44$. The points at which demixing started, according to increase of $g_{ss}(r)$ at short separations, are taken to be $T = 1.35$ for both densities. When cooling the system at density $\rho = 0.40$, some signs of demixing were seen at $T = 1.50$, but the system mixed again at lower temperatures. This effect was reversible and was also seen in a system twice the size of that considered in Fig. 6.9. Therefore, it is not associated with a metastable state or the size of
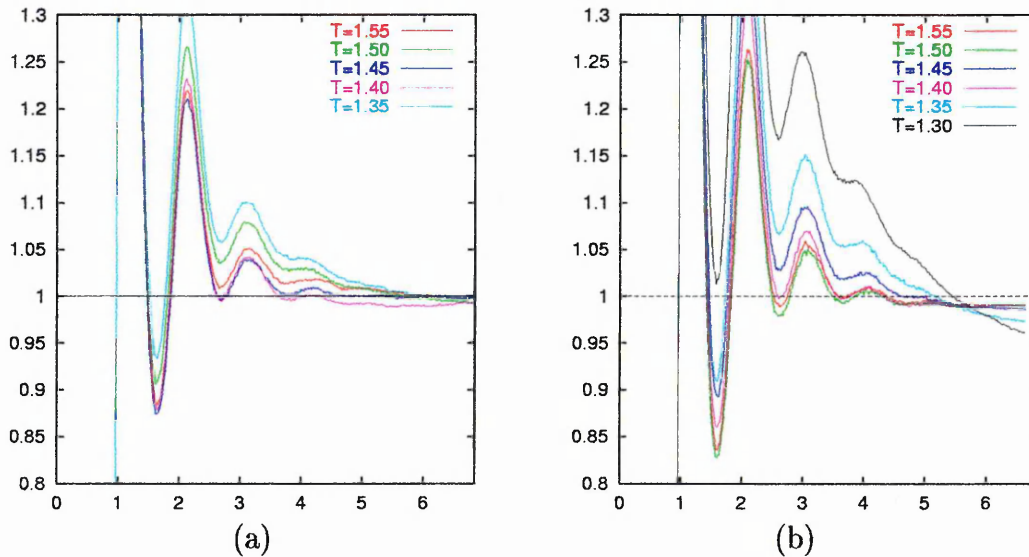
Figure 6.9: Sphere-sphere radial distribution functions calulated at (a) $\rho = 0.40$ and (b) $\rho = 0.44$ at different temperatures.

the simulation box. At $\rho = 0.44$, this effect was not so significant but was, nevertheless, observed at temperature $T = 1.55$. In Section 6.2.3 we will look at the mixing-demixing transition in more details using Gibbs ensemble MC method.

6.2.2   Low Concentrations of Spheres

Two systems containing $N = 2048$ particles in total are considered in this Section. One is an 80/20 mixture of 1638 rods and 410 spheres and the other contains 1844 rods and 204 spheres, i.e. a 90/10 concentration ratio. Both systems were simulated in the constant NVT ensemble using MD methods and their approximate phase diagrams were constructed.

The 80/20 simulations were started from a hard particle configuration previously equilibrated at density $\rho = 0.30$, the initial temperature being set to $T = 1.0$. After equilibration, the system was compressed at constant temperature up to a density of $\rho = 0.42$ with a step of $\rho = 0.01$. Typically, each equilibration run consisted of 5×10^5 time steps. The potential energy per particle, the nematic order parameter, and pressure were monitored and then averaged for additional 2×10^5 time steps

when the system was believed to be in equilibrium. The resulting average values
of these quantities and their mean square deviations are presented in Tab. 6.6.
The variation of the nematic order parameter indicates a phase transition at a

Density	Energy	Order Parameter	Pressure
0.30	-2.550 ± 0.021	0.034 ± 0.012	1.79 ± 0.05
0.31	-2.625 ± 0.022	0.036 ± 0.013	2.07 ± 0.06
0.32	-2.687 ± 0.023	0.035 ± 0.012	2.39 ± 0.06
0.33	-2.743 ± 0.024	0.037 ± 0.014	2.76 ± 0.07
0.34	-2.792 ± 0.025	0.045 ± 0.016	3.19 ± 0.07
0.35	-2.835 ± 0.025	0.050 ± 0.018	3.66 ± 0.08
0.36	-2.860 ± 0.027	0.083 ± 0.044	4.20 ± 0.08
0.37	-3.265 ± 0.039	0.533 ± 0.024	4.30 ± 0.09
0.38	-3.374 ± 0.030	0.652 ± 0.016	4.72 ± 0.09
0.39	-3.480 ± 0.036	0.729 ± 0.013	5.22 ± 0.10
0.40	-3.510 ± 0.038	0.769 ± 0.011	5.90 ± 0.10
0.41	-3.568 ± 0.043	0.810 ± 0.010	6.63 ± 0.11
0.42	-4.355 ± 0.032	0.917 ± 0.004	6.64 ± 0.11

Table 6.6: Potential energy per particle, nematic order parameter (S), and pressure
at T=1.0 and different densities.

density of about $\rho = 0.37$. The run at this density required 2×10^6 time steps
for equilibration which suggested that some slow process occurred at this phase
point. The sphere-sphere radial distribution functions calculated at $\rho = 0.36$ and
$\rho = 0.37$ (Fig. 6.10(a)) confirm this to be macrophase separation. According to
system snapshots, this involved the spheres forming a droplet suspended in the
rod-rich phase. On further compression at $T = 1.0$, smectic order developed at a
density of about $\rho = 0.415$ as the parallel distribution functions measured at different
densities indicate (Fig. 6.10(b)).

Configurations of the system at nematic ($\rho = 0.39$) and smectic ($\rho = 0.42$) states
are presented in Fig. 6.11. In the nematic, two point defects, boojums, can be seen
near the poles of the droplet which interacted with each other due to the periodic
boundary conditions. This resembles the case of two colloidal particles in close
proximity suspended in a nematic. If rods favour planar alignment on the colloid's
surface, two boojums form making an angle of $30 - 45^o$ with the colloid separation
vector [46]. At higher densities, where the smectic phase was formed, the droplet
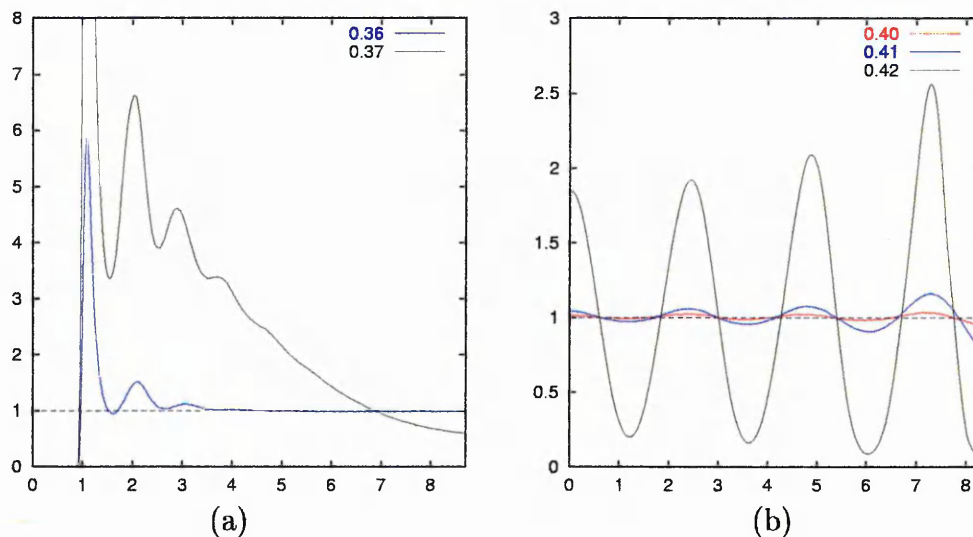
Figure 6.10: (a) Sphere-sphere radial distribution functions, $g_{ss}(r)$, and (b) parallel distribution functions, $g_{\parallel}(r_{\parallel})$, measured at $T = 1.0$ and various densities.

(a)   (b)
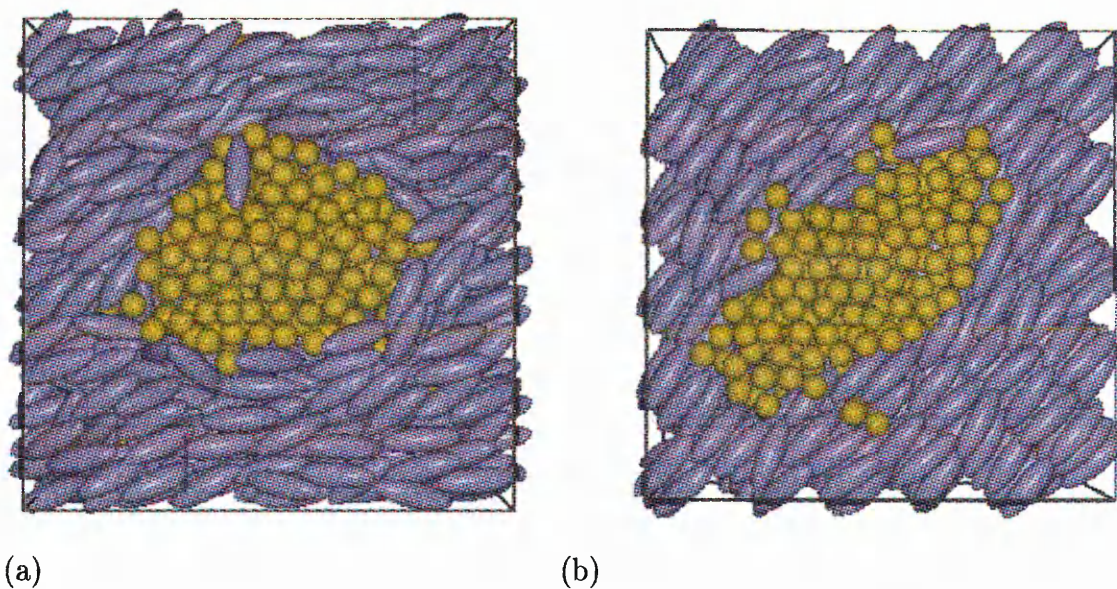
Figure 6.11: Droplet of spheres suspended (a) in a nematic ($\rho = 0.39$) and (b) smectic ($\rho = 0.42$) phase at $T = 1.0$.

of spheres was encapsulated within several smectic layers and no distortion of the director field was observed.

The density dependence of the droplet's shape was studied by calculating its tensor of inertia. The elongation was measured as the ratio of the highest component of the tensor and the semi-sum of the two others. The resulting values of the

elongation, averaged over 10^5 time steps, are presented in Tab. 6.7. These data

Density	0.38	0.39	0.40	0.41	0.42
Elongation	1.28 ± 0.18	1.32 ± 0.12	1.41 ± 0.13	1.65 ± 0.15	1.94 ± 0.14

Table 6.7: Density dependence of the droplet elongation.

indicate higher elongation of the droplet at higher densities, suggesting both that the droplet was elongated along the director and that the rod-rich phase induced higher elongation as its elastic constant increased with density. In order to check whether the droplet was elongated along the director the angle between the director and the eigenvector corresponding to the highest eigenvalue of the inertia tensor was measured at different densities. The resulting data confirm that most of the time the droplet is elongated along the director although there were some configurations in which it is not. At densities $\rho = 0.41$ and $\rho = 0.42$, the droplet was found always to be elongated along the director.

A cooling run was undertaken at constant density $\rho = 0.37$. Starting from the configuration at $\rho = 0.37$ and $T = 1.0$, the temperature was decreased down to $T = 0.7$ with a step of $\Delta T = 0.1$. The radial and parallel distribution functions shown in Fig. 6.12 indicate a nematic-smectic transition occurring at a temperature of about $T = 0.85$. The positions of the peaks of the radial distribution function resembles that of the pure Gay-Berne fluid in its S_B phase (Section 5.2). The parallel radial distribution function gives an interlayer distance of about $2.44\sigma_0$, which indicates that neighbouring smectic layers interdigitated significantly, as suggested by Fig. 6.11.

A similar cooling run was conducted at a lower density, $\rho = 0.30$, in order to study the mixing-demixing behaviour of the system in its isotropic phase. It was found that at a temperature of about $T = 0.9$ the first signs of demixing appeared and at $T = 0.8$ a single droplet of spheres was observed. The corresponding radial rod-sphere and sphere-sphere distribution functions are shown in Fig. 6.13 Several further runs were performed at other temperatures and densities in order to map out the system's phase diagram more completely. The resulting phase diagram (Fig. 6.14)
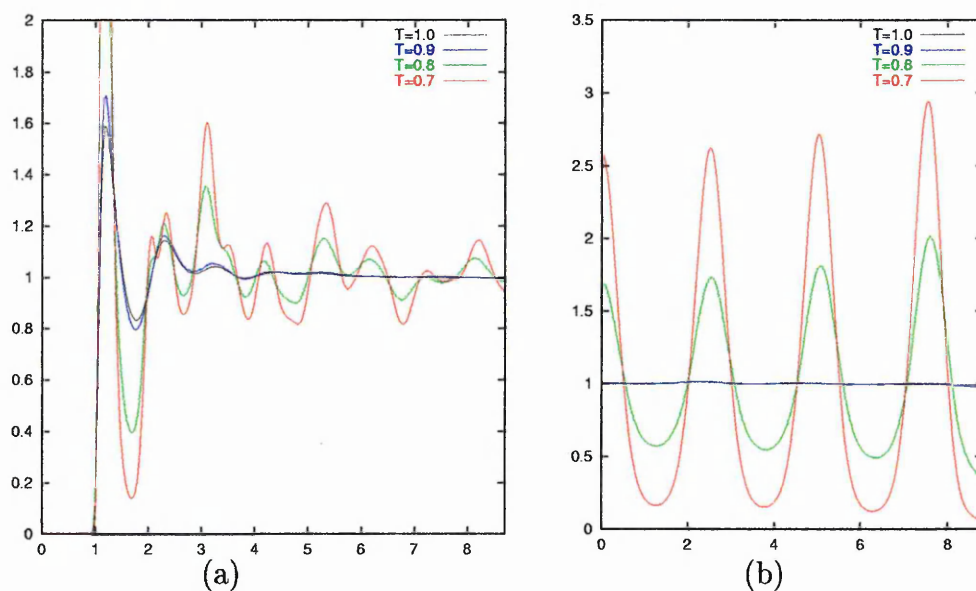
Figure 6.12: (a) Radial, $g(r)$, and (b) parallel, $g_{\parallel}(r_{\parallel})$, distribution functions calculated at density $\rho = 0.37$ and different temperatures.
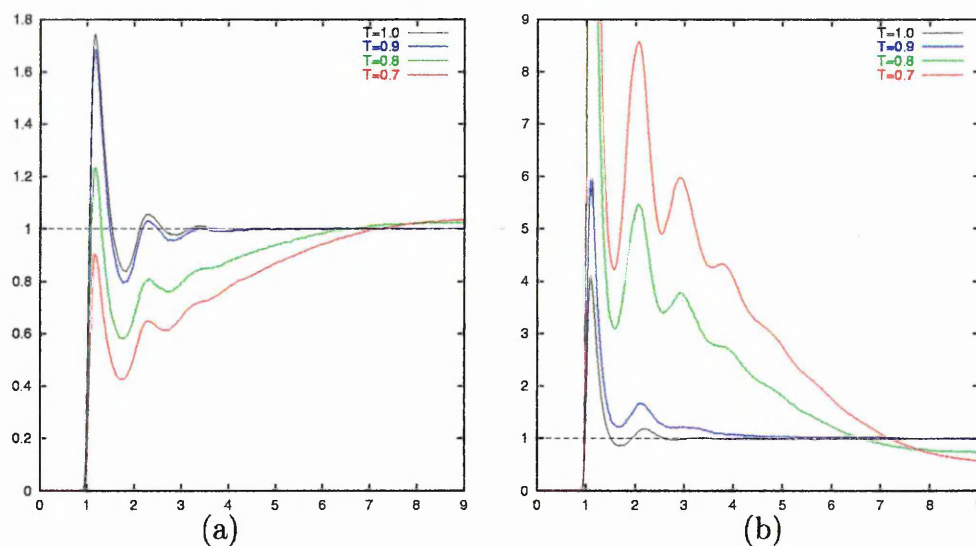
Figure 6.13: (a) Radial rod-sphere, $g_{rs}(r)$, and (b) sphere-sphere, $g_{ss}(r)$, distribution functions at density $\rho = 0.30$ and different temperatures.

shows that the simulated 80/20 rod-sphere mixture exhibits the same phases as the pure Gay-Berne fluid, i.e. Isotropic, Nematic and Smectic B. The presence of the spheres, therefore, does not change the phase behaviour of the rods dramatically; it only adds an extra mixing-demixing transition to the system behaviour. Unlike the 50/50 mixture studied in the previous Section, the demixing line now crosses
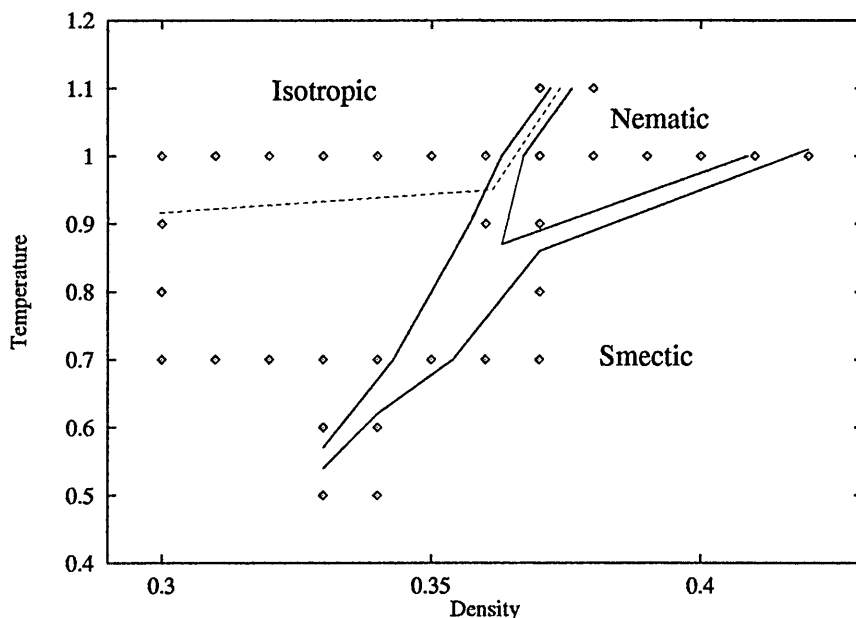
Figure 6.14: Phase diagram of a 80/20 mixture. Diamonds indicate state points at which simulations were conducted; dashed line is the demixing line.

the phase boundary and we were able to observe the formation of a nematic when compressing a well mixed isotropic mixture at $T = 1.0$ and $\rho = 0.36$. The dynamics of this transition involves two processes: formation of the sphere-rich phase and the isotropic-nematic transition of the rod-rich phase. The gradually decreasing potential energy and monotonic growth of the nematic order parameter during the $\rho = 0.37$ run indicate that those two processes take place cooperatively. At densities below $\rho = 0.36$, the phase transitions and demixing are driven mainly by energy, since the system of hard particles is isotropic and homogenous at those densities. If the system is cooled down at constant low density $0.33 \leq \rho \leq 0.36$, it first demixes into two coexisting phases and then, at a lower temperature, the rod-rich phase develops smectic order. At higher densities, the nematic order develops at temperatures $T \geq 0.9$ and the spheres demix to form a single droplet at the same temperatures. The nematic with randomly dispersed spheres was not observed. Instead, on heating at $\rho = 0.37$, the system remixed and lost its orientational order at $T = 1.1$. At $\rho = 0.38$ and $T = 1.1$ the system remained demixed and kept its nematic order. Demixing at high densities was not studied properly because of the

increasing computer time required to allow it to occur fully.

Analogous simulations were performed for a 90/10 mixture containing 1844 rods and 204 spheres. The initial configuration was produced by changing the identity of some of the rods in an 80/20 configuration at $\rho = 0.26$ corresponding to an isotropic well mixed state. The system was equilibrated at $T = 0.7$ for 7×10^5 times steps and then compressed from this point at constant temperature. The nematic order parameter and radial distribution functions indicated that the mixture remained uniform and homogeneous up to a density of about $\rho = 0.32$ at which both an isotropic-smectic transition and demixing occurred. A heating run was conducted at constant density $\rho = 0.34$ in the range of temperatures $0.7 \leq T \leq 1.2$. The measured values of the nematic order parameter and their mean square deviations are shown in Tab. 6.8 These data suggest that as the temperature was increased the

T	0.7	0.8	0.9	1.0	1.1
S	0.90 ± 0.01	0.65 ± 0.02	0.58 ± 0.02	0.41 ± 0.05	0.16 ± 0.03

Table 6.8: Temperature dependence of the nematic order parameter, S, at $\rho = 0.34$.

system underwent a smectic-nematic transition at a temperature of about T=0.8. On further heating, the nematic order parameter decreased further and dropped down to the values typical for the isotropic phase around T=1.2. Figure 6.15 shows how the parallel distribution function changed with temperature. It indicates some weak long-range positional correlations at $T = 0.8$, where the order parameter suggests a nematic phase. However, neither the pure Gay-Berne fluid nor the 80/20 mixture studied above (Fig. 6.14) exhibited nematic order at such a low temperature. This suggests that this is a metastable configuration which might be retaining a memory of the smectic layering of the initial configuration even after equilibration for 1.4×10^6 MD time steps. The complete schematic phase diagram of a 90/10 mixture is presented in Fig. 6.16. It recovers all of the phases observed for the pure Gay-Berne fluid and shows that the mixing-demixing transition in this mixture always occurs cooperatively with the phase transition. Once the droplet of spheres forms in the system, the rod-rich phase behaves like the equivalent pure Gay-Berne fluid.
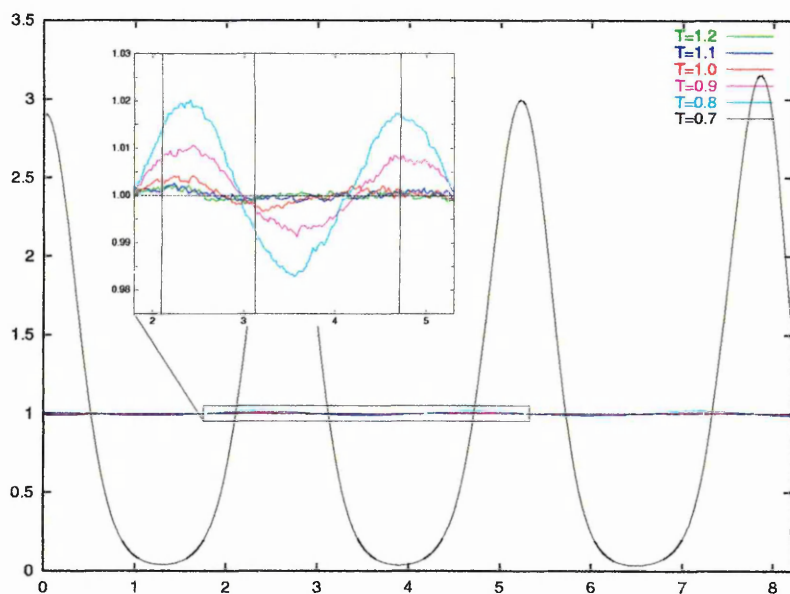
Figure 6.15: Parallel distribution functions, $g(r_\parallel)$, at $\rho = 0.34$ and different temperatures.
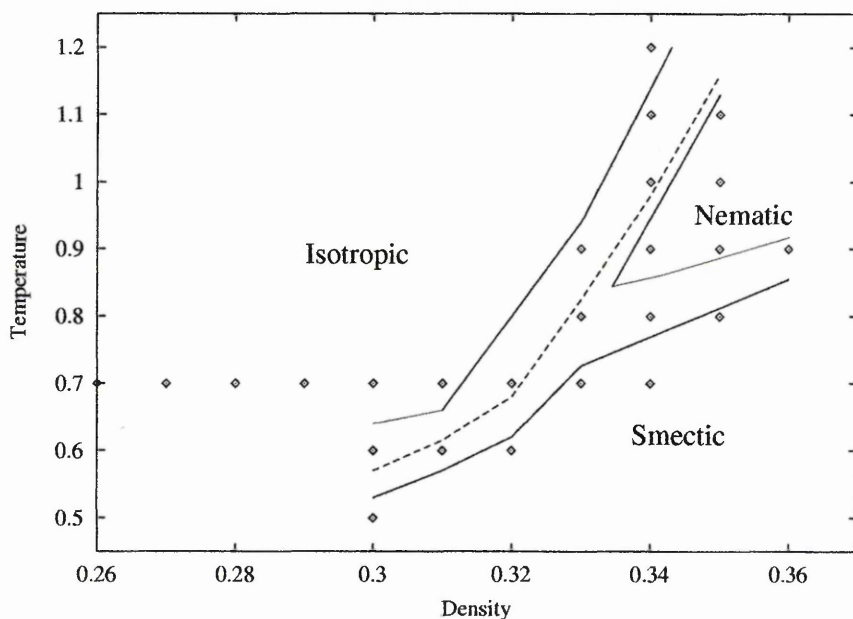

Figure 6.16: Phase diagram of a 90/10 mixture.

6.2.3 Demixing Transition

It is difficult to study the demixing transition accurately simply by analysing the sphere-sphere radial distribution functions obtained in constant NVT simulations.

95

Firstly, the smaller the system the higher the energy barrier between mixed and demixed phases because of the contribution of surface energy terms. This also shifts the temperature of demixing from its macroscopic value and makes it simulation box size dependent. Secondly, if macroscopic demixing has taken place, the simulation box does not represent adequately the bulk state. Instead, we have a microscopic droplet suspended in a rod-rich phase. Thirdly, if the size of the droplet is comparable with the simulation box and the phase boundary is extended, it is difficult to say whether or not demixing has taken place. So far, the criterion used to characterise demixing in our simulations has been the observation of a steep change in the radial sphere-sphere distribution function.

A good tool for the direct study of two phase equilibria is the Gibbs Ensemble Monte Carlo (GEMC) method developed by Panagiotopoulos [102]. In the original formulation of this approach, the system simulated comprises two separate boxes that represent two coexisting phases. Each of these boxes is surrounded by periodic images of itself and there are no real interfaces between the phases. The total number of molecules in the system $N^I + N^{II} = N$ and total volume $V^I + V^{II} = V$ are kept constant as well as the thermodynamic temperature T. Three kinds of trial moves are used to generate new configurations of the system: particle displacement, particle exchange and volume rearrangement. The algorithm ensures that the coexisting boxes have the same pressures and chemical potentials, i.e. they are in thermodynamic equilibrium. In our implementation of this algorithm, every MC cycle consisted of N single particle displacement moves, $3N$ exchange moves and one volume rearrangement move. The displacement move was implemented using the standard Metropolis algorithm described in Subsection 4.1.2. For the exchange move, a particle was chosen at random and, if it was a sphere, an attempt was made to insert it in the other box at a random position. If a rod was selected, an attempt was made to swap it with a random sphere from the other box, so as to increase the probability of achieving a successful move. This move was accepted with probability

given by

$$\chi = \min\left(1, \frac{N_{rod}^I N_{sph}^{II}}{(N_{rod}^{II}+1)(N_{sph}^I+1)} \times \exp\left(\frac{-\Delta U}{k_B T}\right)\right)$$ (6.4)

if a rod was selected in box I, and by

$$\chi = \min\left(1, \frac{V^{II} N^I}{V^I(N^{II}+1)} \times \exp\left(\frac{-\Delta U}{k_B T}\right)\right).$$ (6.5)

if it was a sphere. The volume rearrangement move consisted of a correlated change of the simulation boxes' volumes. In this we made a uniform random change in the volume of one of the boxes, for example, compressing it and respectively expanding the other box by simply scaling the particle coordinates. If we attempted to change volume of box I, V^I, by ΔV the move was accepted with probability given by

$$\chi = \min\left(1, \exp\left(-\frac{\Delta U}{k_B T} + N^I \ln(1 + \frac{\Delta V}{V^I}) + N^{II} \ln(1 - \frac{\Delta V}{V^{II}})\right)\right).$$ (6.6)

A GEMC code was developed to study the coexistence of sphere-rich and rod-rich phases at 50% sphere concentration. The simulated system consisted of $N = 2048$ particles in total and two identical replicas of an MD box were used as an initial configuration. The level of acceptance of insertion moves appeared to be too low at near transition densities. Even at low density $\rho = 0.35$ only about 6 out of 1000 sphere insertions were successful. This lead to the conclusion that the system was too dense for successful application of the GEMC method at near transition densities. Nevertheless, a cooling run was undertaken at $\rho = 0.35$ to see how the system would demix at low density. In parallel with this, a cooling series of MD runs was conducted for comparison.

Starting from high temperature $T = 1.4$ the isotropic uniform configuration was cooled down to $T = 0.8$ with a step of $\delta T = 0.1$. Typically each run consisted of at least 2×10^5 MC cycles, but runs up to 4 times longer than this were required to equilibrate the system at low temperatures. When cooled, the two simulation boxes were found to contain equivalent 50/50 isotropic rod-sphere mixture at temperatures down to $T = 1.1$. The evolution of the box energies during the simulation at $T = 1.1$ are shown in Fig. 6.17(a). As the temperature was decreased further, the potential
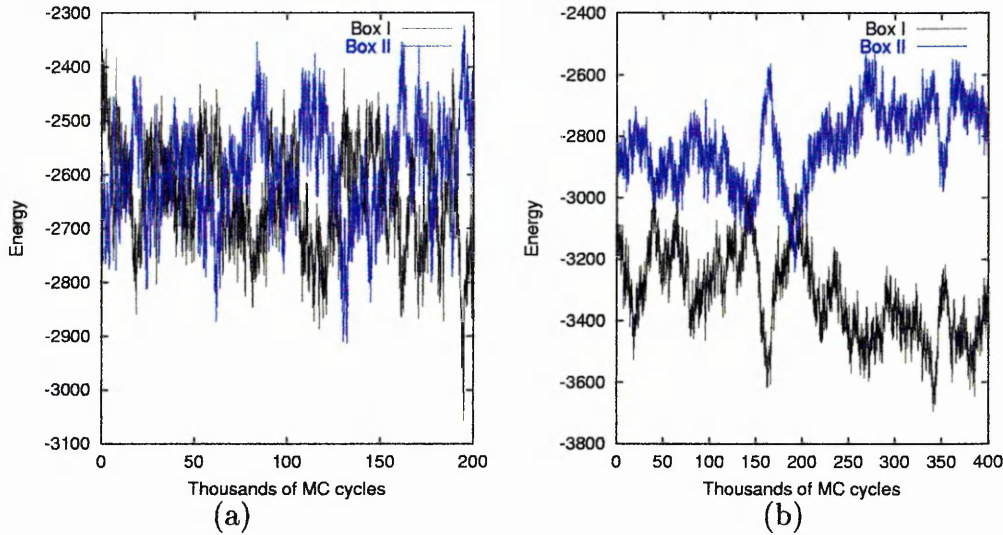
Figure 6.17: Energies of the two coexisting boxes at (a) $T = 1.1$ and (b) $T = 0.9$.

energy fluctuations increased (Fig. 6.17(b)), although both boxes contained similar mixtures. At temperature $T = 0.9$, the coexistence between rod-rich (on average containing 57% of rods) and sphere-rich (containing about 43% of rods) phases was observed. At temperature $T = 0.8$, phase separation occurred and one of the boxes contained mainly spheres, while the other one contained almost all of rods and some spheres at a concentration of about 12%. There were, however, some successful insertions of rods into the sphere-rich phase, the average number of rods being 1.66 which corresponded to the a concentration of less than 0.2%.

On heating this system did not exhibit the same behaviour at $T = 0.9$ as it had on cooling. Instead, it remained in a demixed state, with the average number of rods in the sphere-rich phase stabilising at about 7.5. On further heating, the system followed the same path as on cooling. Figure 6.18 shows the evolution of the potential energy for each simulation box during the cooling run and then during the reverse heating runs. The total potential energy is the same in both cases which suggests that the state observed on cooling was not metastable and the simulation length was sufficient to achieve equilibrium at this temperature. Therefore, the temperature of mixing-demixing transition was determined to be about $T \approx 0.9$.
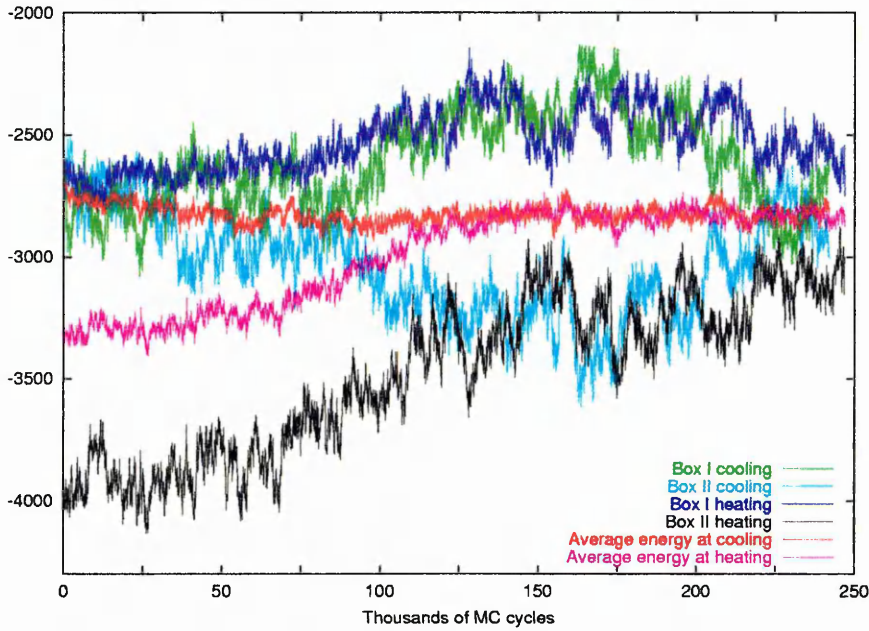
Figure 6.18: Energies of the two coexisting boxes at $T = 1.0$ at cooling and heating.

MD simulations were performed at the same state points to assess the behaviour of these mixtures at different temperatures. Figure 6.19 shows sphere-sphere radial dis-
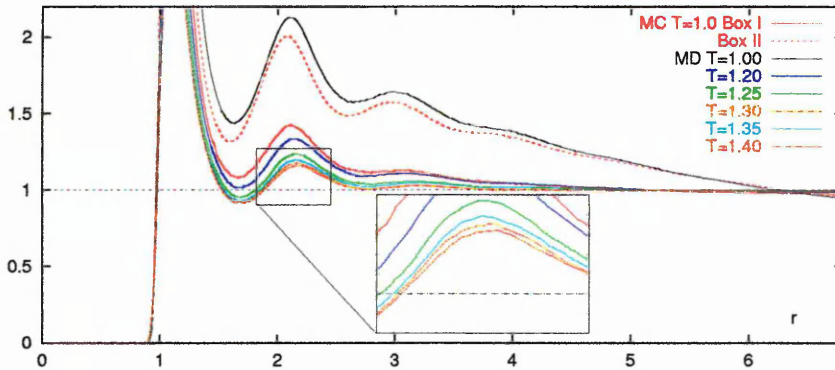
Figure 6.19: Sphere-sphere radial distribution functions at $\rho = 0.35$ and different temperatures.

tribution functions evaluated from our both MC and MD simulations. The functions calculated in the MD runs indicate that demixing took place at noticeably higher temperature than $T = 0.9$, namely it started at a temperature of about $T = 1.2$. The two coexisting phases in our MC simulations at temperature $T = 1.0$ had distribution functions typical for demixed states. This suggests that first changes in

99

$g_{ss}(r)$ observed in our MD simulations were associated with earlier stage of demixing when small domains of spheres were rapidly formed and destroyed, whereas no macroscopic demixing occurred in the system.

6.3   System (ii)

In the original parameterisation of the rod-sphere potential studied in the previous Section, the spheres were attracted to the sides of the rods five times more strongly than to their ends. In this Section we will study a rod-sphere mixture which has the opposite tendency, i.e. the end attraction is five times stronger than the side. However, all other interaction and shape parameters remain unchanged in this and the following Sections. Figure 6.20 shows the rod-sphere potential profiles
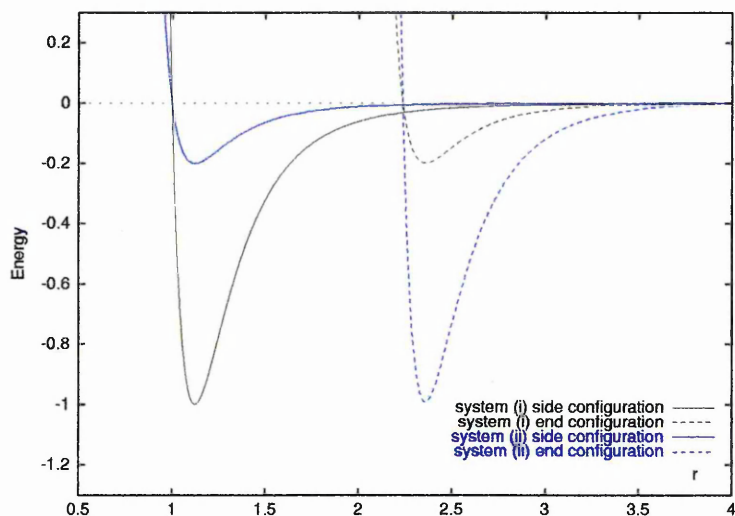
Figure 6.20: Rod-sphere potentials for systems (i) and (ii).

for different configurations in systems (i) and (ii). The corresponding parameters of equation (6.1), which provide the strong end rod-sphere interaction, are $\epsilon_{RS} = 0.2$ and $\epsilon_S/\epsilon_E = 0.2$. The next Subsection presents results of MD and MC simulations of a 50/50 mixture. This is followed by a Subsection containing the results obtained for lower concentrations of spheres and a brief discussion.

6.3.1   50/50 Mixture

A system of 512 rods and 512 spheres interacting via the potentials described above was simulated in the constant *NVT* ensemble using the same MD method as was

used to study system (i). Simulations were started at high temperature $T = 1.5$ and the mixture was compressed from density $\rho = 0.40$ up to $\rho = 0.50$. The nematic order parameter measured during this compression sequence indicated that the system remained isotropic over the whole range of densities. The sphere-sphere radial distribution functions, shown in Fig. 6.21, suggest however that the compres-
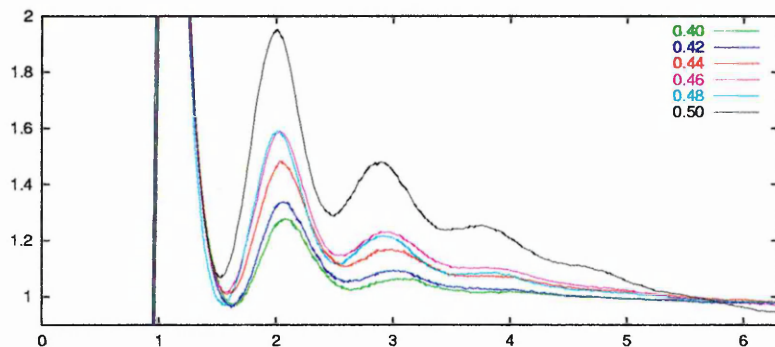
Figure 6.21: Sphere-sphere radial distribution functions at $T = 1.5$ and different densities.

sion was performed close to the demixing line and it was crossed at $\rho \approx 0.49$. In order to define the demixing line more precisely, two cooling runs were undertaken at densities $\rho = 0.42$ and $\rho = 0.50$. A steep change in the sphere-sphere radial distribution function was observed at a temperature between $1.40 < T < 1.50$ at the lower density (Fig. 6.22(a)) and between $1.50 < T < 1.60$ at $\rho = 0.50$. This indicates that the demixing line has a slight positive slope and it is consistent with our conclusion that it was crossed during the compression run at a density of about $\rho = 0.49$. Comparing this behaviour to system (i)'s demixing behaviour (Fig. 6.7) we note that system (ii) does not exhibit reverse mixing on cooling, i.e. its demixing properties vary monotonously with temperature at constant density. Also, the demixing shown by system (ii) occurred at slightly higher temperatures, i.e. its tendency to demix was stronger than that of system (i).

Figure 6.22(b) shows a system configuration at the end of the cooling sequence performed at $\rho = 0.42$. Here, the sphere-rich phase forms a cylindrical droplet surrounded by the rods aligned by the droplet's surface. This configuration shows significant distortion resulting from the periodic boundary conditions and clearly

does not represent a macroscopic bulk system. To study the system's behaviour at higher densities, we chose to use a non-cubic simulation box instead of compressing this unphysically formed configuration. A box with dimensions $9.261 \times 9.261 \times 25.403$, which correspond to the density of $\rho = 0.47$, was simulated at different temperatures. The initial configuration was obtained by applying a nonsymmetric constant volume MC move to an initially cubic box at high temperature $T = 1.7$. To monitor demixing in the system the probability distributions of rods and spheres along the long simulation box side were calculated over 5×10^5 time steps preceded by 10^6 time steps of equilibration. The resulting distributions shown in Fig. 6.23 indicate that the concentrations of the spheres and rods were not uniform along the simulation box, and suggest coexistence between sphere-rich and rod-rich regions. A snapshot of the last configuration of this run is shown in Fig. 6.24(a). This system was cooled down to $T = 0.7$ starting from this configuration with a step of $\Delta T = 0.05$. The constant pressure and constant volume MC methods both failed when applied to this system because the shortest simulation box side half length became too close to the radius of the Verlet neighbour list, $R_L = 4.5\sigma_0$. Therefore, the geometry of the box was kept unchanged and standard MD methods were applied in the constant NVT ensemble. The nematic order parameter and profiles of the particle probability distribution were measured during this cooling sequence. The resultant
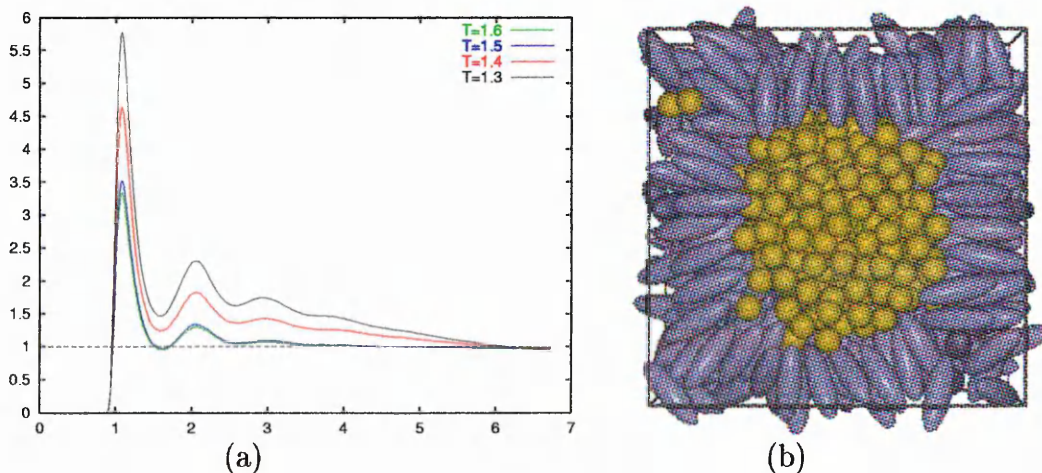

Figure 6.22: (a) Radial sphere-sphere functions at $\rho = 0.42$ and different temperatures; (b) configuration snapshot taken at $\rho = 0.42$ and $T = 0.7$.
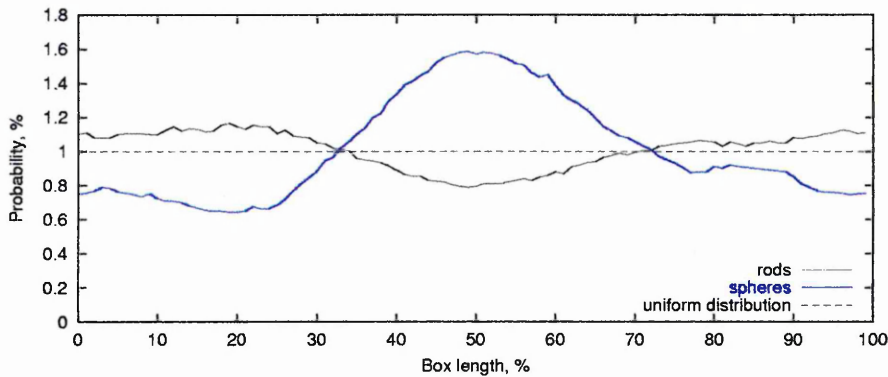
Figure 6.23: Distribution of rods and spheres along the simulation box at $T = 1.70$.

concentration profiles indicated that with decreasing temperature the sphere-rich phase became free of rods, whereas the rod-rich phase still contained some spheres. Figure 6.24 shows the configuration snapshots, taken at various temperatures, to illustrate this process. The nematic order parameter indicated an orientational phase transition at a temperature of about $T = 1.20$. It was classified as an isotropic-nematic transition according to the parallel distribution functions measured at sub-transition temperatures. Some spheres could be still found in the rod-rich phase at this point. The director was found to be parallel to the longest side of the simulation box, which can be explained by the influence of the phase interface present in the system. Those rods close to the interface between the rod-rich and the sphere-rich phases were aligned perpendicular to it, thus inducing the orientation of the other rods. The development of smectic order at lower temperatures was affected by the periodic boundary conditions. The long simulation box side proved unable to accommodate a whole number of layers and the director, therefore, was forced to tilt slightly in order to establish an acceptable commensurability (Fig. 6.24(d)). A constant pressure MC run was then performed at constant temperature $T = 0.70$ and pressure $P = 2.0$. This time the box side fluctuations remained within the allowed limits, i.e. all sides were always longer than $2R_L$. The equilibrium simulation box size was found to be 9.357 ± 0.047 by 9.163 ± 0.040 by 24.898 ± 0.120, which corresponds to a density of $\rho \approx 0.48$. This run revealed that, under isobaric conditions, the stable configuration was one in which the smectic layers were parallel to the interface and the director was parallel to the longest simulation box side.

(a) T=1.70
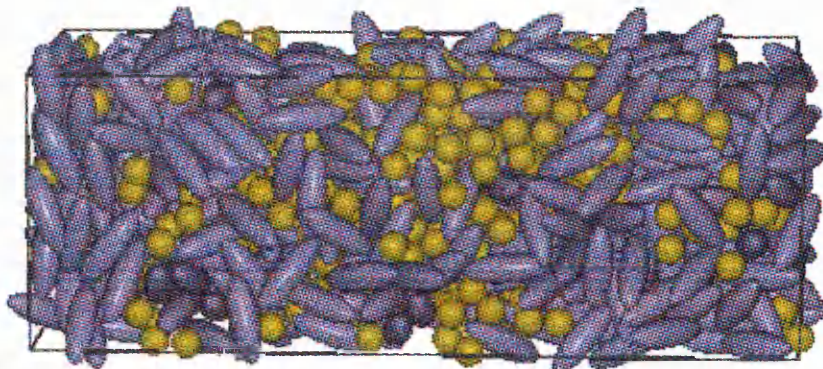
(b) T=1.35
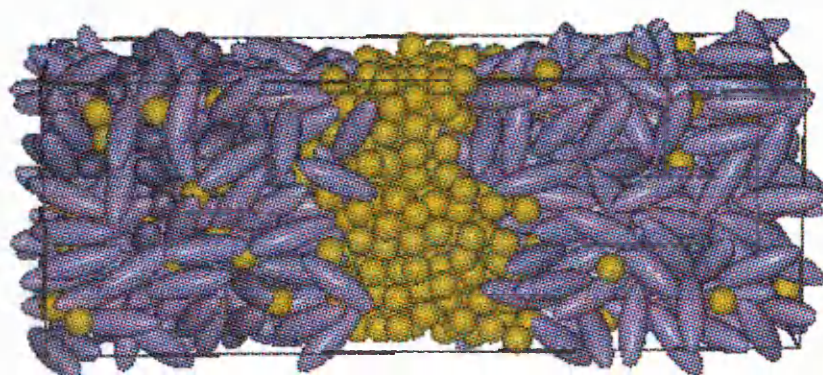
(c) T=1.10
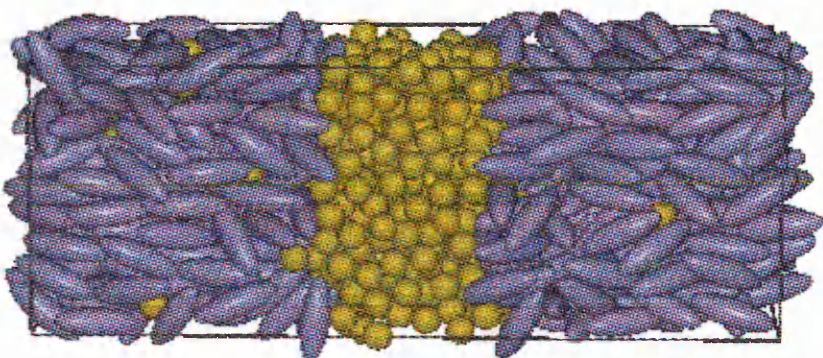
(d) T=0.70
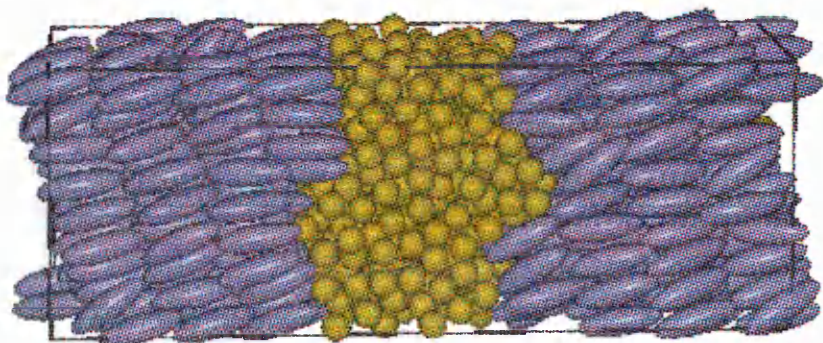
Figure 6.24: Snapshots of a noncubic simulation box at $\rho = 0.47$ and different temperatures.

6.3.2   Low Concentration of Spheres

In this Subsection two mixtures containing 20% and 10% of spheres are studied. Both systems were simulated in the constant NVT ensemble using MD methods and their behaviour was compared to that of the analogous mixtures with strong side rod-sphere interaction described in Section 6.2.2.

The simulations of an 80/20 mixture were started from a hard particle configuration of 1638 rods and 410 spheres at density $\rho = 0.30$. The temperature was set to $T = 1.0$ and the system was equilibrated for 1.4×10^6 time steps. High values of the calculated sphere-sphere distribution function at short distances suggested some local clustering of the spheres, although it also approached unity at large separations, indicating random distribution of these clusters (Fig 6.25(a)). There

(a)   (b)
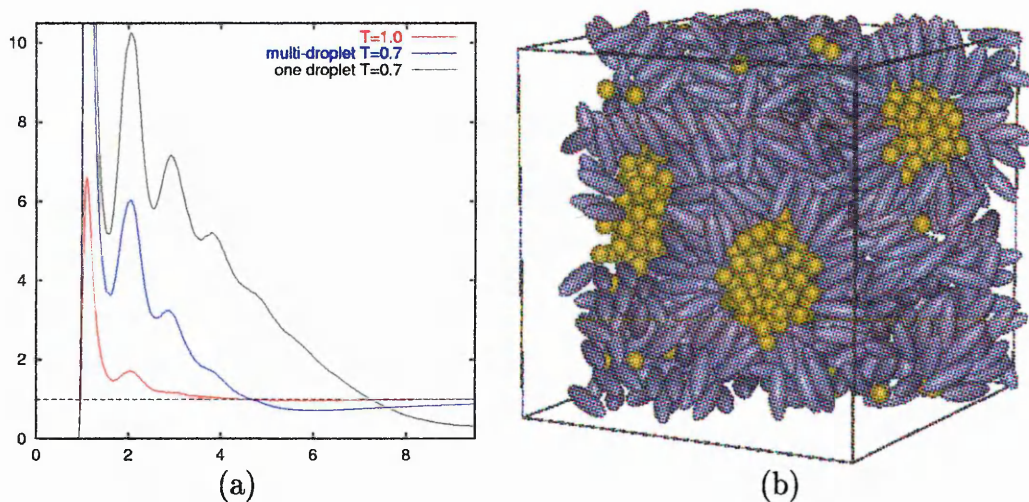
Figure 6.25: (a) Radial sphere-sphere functions, $g_{ss}(r)$, at $\rho = 0.30$ and $T = 1.0$ and at $T = 0.7$ for one and multi-droplet configurations; (b) A multi-droplet configuration at $\rho = 0.30$ and $T = 0.7$.

were found 153 ± 17 clusters separated by distances greater than $1.5\sigma_0$ at $\rho = 0.30$ and $T = 1.0$. By comparison, an analogous mixture of hard particles at the same density contained 248 ± 12 randomly formed clusters. The cluster size distribution was found to be quite different as well. 7 clusters of 20 or more spheres (the largest of them was of 38 ± 13) were found in the soft particle system whereas the largest cluster in the system of hard particles contained only 10 ± 3 spheres. Analogous

analysis of the 80/20 mixture of type (i) at $\rho = 0.30$ and $T = 1.0$ revealed 182 ± 11 clusters the largest of which contained 20 ± 4 spheres. These data show that at low sphere concentration system (ii) has a higher tendency to demix when compared to system (i) which, in turn, has more signs of segregation than the hard particle system.

If the system's temperature was quenched down to $T = 0.70$, coalescence of some of the clusters was observed reducing their total number down to 53 ± 4. Most of the clusters were single or paired spheres but 4 of them, with on average about 85 particles each, contained most of the particles (Fig. 6.25(b)). The time available for simulation was not sufficient for all of these droplets to coalesce and, having developed this arrangement, the system structure remained relatively unchanged after 3×10^6 time steps.

In contrast, a configuration with a single droplet was obtained if a cooling sequence with a moderate temperature decrement of $\Delta T = 0.05$ was performed starting from the configuration previously equilibrated $\rho = 0.30$ and $T = 1.0$ At $T = 0.70$, the single droplet configuration was found to have lower potential energy than the multi-droplet one (-3.413 ± 0.023 against -3.359 ± 0.027 per particle). It also had higher orientational entropy because fewer rods were aligned by the surface. Thus, despite its slightly lower mixing entropy, the configuration with a single droplet is the thermodynamically favourable arrangement. The fact that on rapid cooling we observed the multi-droplet configuration shown in Fig. 6.25(b) was due to the initial formation of several droplets each surrounded by a layer of rods. These layers kept the droplets apart at a distance of order of $6\sigma_0$ and made it impossible for them to coalesce.

It would be pointless to study cluster size distribution or their arrangement at low temperatures in a simulation box containing 4-5 large clusters. Therefore, the single-droplet configuration was chosen for our further simulations in order to explore the shape of the droplet of spheres suspended in the rod-rich phase. A compression series at constant temperature $T = 0.7$ was performed in the density range $0.30 \leq \rho \leq 0.35$ with a step of $\Delta\rho = 0.01$. Significant influence of the periodic boundary conditions

upon the system's structure was found. Due to the strong homeotropic anchoring, the droplet of spheres was surrounded by a layer of rods and the resultant sub-particle was of size comparable to the simulation box side. The periodic boundary conditions caused some unrealistic effects, i.e. with increasing density the droplet's shape started to resemble the geometry of the box. Due to this failure of the method at low temperatures, only the high temperature system behaviour was studied.

The configuration obtained at $\rho = 0.30$ and $T = 1.0$ was compressed at constant temperature up to density $\rho = 0.42$ with a step of $\Delta\rho = 0.1$. The nematic order parameter, potential energy, pressure and distribution functions were measured during this sequence and averaged over 2×10^5 MD time steps after at least 7×10^5 time steps of equilibration. Then, cluster analysis was undertaken to investigate the demixing property of the system. Table 6.3.2 shows how the nematic order parame-

Density	Order parameter	Number of clusters	Largest cluster size
0.30	0.031 ± 0.012	153 ± 17	38 ± 13
0.31	0.036 ± 0.013	136 ± 11	131 ± 14
0.32	0.040 ± 0.014	137 ± 9	126 ± 8
0.33	0.049 ± 0.016	129 ± 7	148 ± 8
0.34	0.046 ± 0.013	117 ± 7	197 ± 7
0.35	0.052 ± 0.017	111 ± 6	236 ± 5
0.36	0.103 ± 0.041	93 ± 6	273 ± 6
0.37	0.480 ± 0.031	60 ± 6	330 ± 8
0.38	0.564 ± 0.018	43 ± 3	359 ± 2
0.39	0.707 ± 0.013	36 ± 3	366 ± 3
0.40	0.778 ± 0.011	29 ± 3	377 ± 3
0.41	0.811 ± 0.009	21 ± 2	387 ± 2
0.42	0.932 ± 0.003	11 ± 1	398 ± 1

Table 6.9: The order parameter and cluster distribution at $T = 1.0$.

ter and the cluster distribution changed with increasing density. The sphere-sphere radial distribution functions shown in Fig. 6.26(a) indicate a macroscopic phase separation at density $\rho \approx 0.31$. At $\rho = 0.35$ more than a half of the spheres formed a single droplet while the others were dispersed in the rod-rich phase which was still isotropic (Fig. 6.26(b)). With increasing density, even a greater number of spheres became segregated from the rod-rich phase reducing the total number of clusters
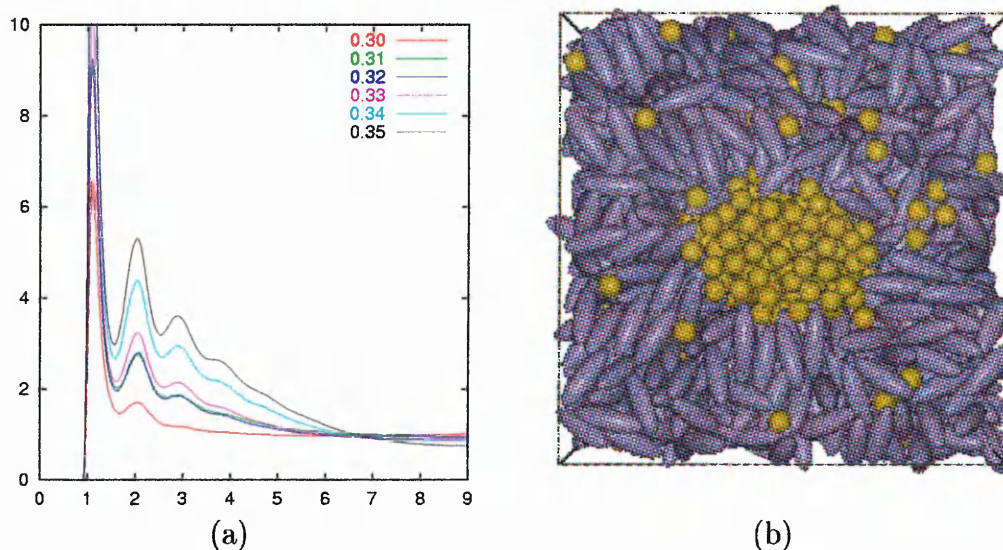
Figure 6.26: (a) Radial sphere-sphere distribution functions, $g_{ss}(r)$, measured at $T = 1.0$ and different densities; (b) configuration snapshot taken at $\rho = 0.35$ and $T = 1.0$.

in the system. An isotropic-nematic transition was observed at a density of about $\rho = 0.365$ analogous to 80/20 mixture of type (i). However, here the demixing occurred before the phase transition, not cooperatively. An analogous scenario was seen for the 80/20 mixture of system (i) at lower temperatures, which again indicates a higher tendency of system (ii) to demix.

Once a single droplet of spheres had formed, the homeotropic anchoring on its surface imposed radial alignment upon the rods (Fig. 6.26(b)). When, at higher densities, the nematic phase developed, conflict arose between this orientation and the nematic bulk alignment. This could affect both the shape of the droplet and give rise to a defect of the director field. The tensor of inertia of the largest cluster was calculated during the simulations to quantify the shape anisotropy of the droplet. The ratio of the semi-sum of two largest components of the inertia tensor to the smallest one was then used as a characteristic parameter of how oblate the droplet was. Table 6.10 presents the data averaged over at least 3×10^5 time steps. There is no clear correlation between the droplet's shape and the density. At the density range $0.37 \leq \rho \leq 0.39$ the droplet became more oblate as the density increased while at higher densities this trend reversed. The mean square deviations of this

Density	0.37	0.38	0.39	0.40	0.41
Shape parameter	1.62 ± 0.23	1.90 ± 0.19	2.22 ± 0.36	1.76 ± 0.23	1.73 ± 0.21

Table 6.10: Density dependence of the shape parameter of the droplet suspended in a nematic.

shape parameter were relatively large, therefore, indicating significant droplet shape fluctuations. Figure 6.27(a) shows how the droplet shape parameter changed with
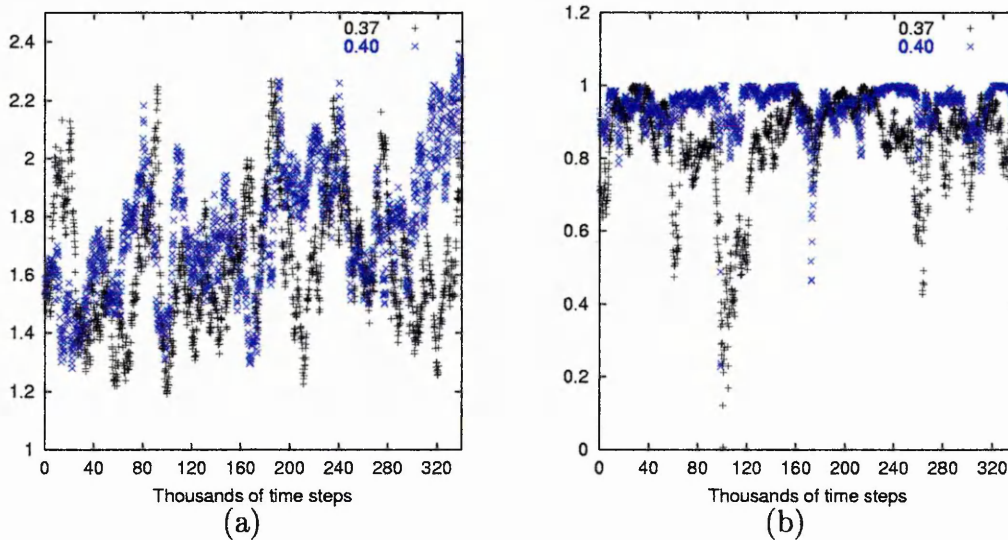
Figure 6.27: (a) Shape parameters and (b) directional cosines corresponding to the smallest component of the inertia tensor at $\rho = 0.37$ and $\rho = 0.40$.

time in the runs at $\rho = 0.37$ and $\rho = 0.40$. These data indicate that the droplet shape was subject to rapid changes due to the dynamic process of its composition. Indeed, the sphere-rich phase can be considered as a dense core surrounded by an outer cloud of spheres. Due to Brownian motion, every time the cluster analysis was performed, different spheres from the "cloud" were counted as being united with the "core" to form the main cluster. This lead to the significant fluctuations of the droplet shape and orientation shown in Fig. 6.27. Another aspect explored here is the correlation between the droplet shape and the director of the rod-rich phase. The direction cosines of the director were calculated in the reference frame of the inertia tensor eigenvectors. It was found that the eigenvector corresponding to the smallest eigenvalue was aligned along the director most of the time. In

other words, the droplet of spheres was found to be flattened along the director. Figure 6.27(b) demonstrates that this correlation was enhanced at higher density: $\langle \cos \theta_I \rangle = 0.83 \pm 0.17$ at $\rho = 0.37$ and $\langle \cos \theta_I \rangle = 0.94 \pm 0.06$ at $\rho = 0.40$. At a density of about $\rho = 0.42$ a smectic phase developed. At this point almost all of the spheres belonged to the largest cluster and its shape was found to be more stable than those formed at lower densities. The shape parameter was equal to 2.34 ± 0.12 and the average directional cosine was $\langle \cos \theta_I \rangle = 0.986 \pm 0.009$. Figure 6.28 shows system

(a)   (b)
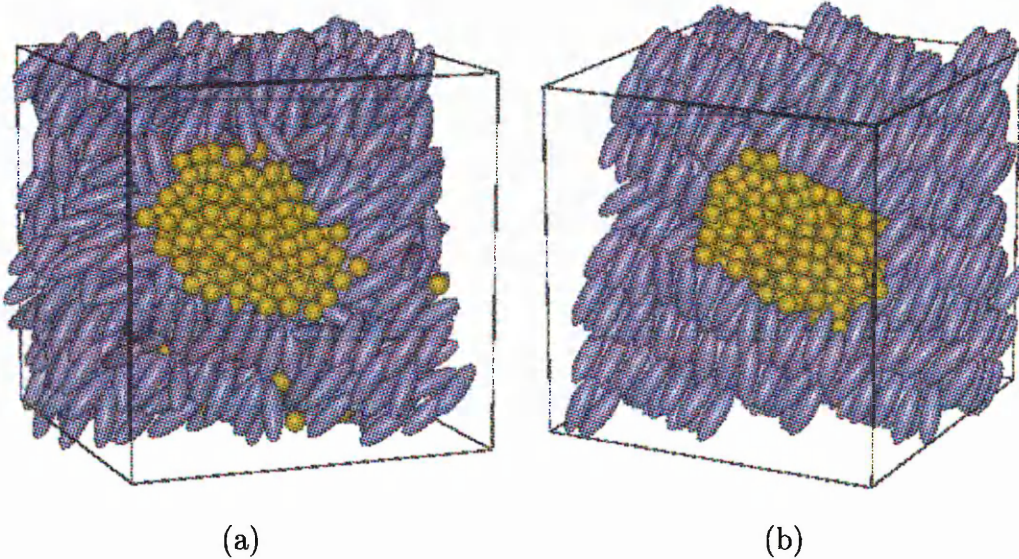
Figure 6.28: (a) Nematic phase at $\rho = 0.38$ and $T = 1.0$; (b) smectic phase at $\rho = 0.42$ and $T = 1.0$.

configurations at nematic and smectic phases at $\rho = 0.38$ and $\rho = 0.42$ respectively. The Saturn ring defect would be expected in the equatorial plane of the spherical droplet suspended in a nematic with strong homeotropic anchoring [27]. Taking into account the large fluctuations of the droplet's shape and the relatively small simulation scale it would be difficult to locate this line defect. In the smectic phase, by contrast, the droplet adjusted a cylindrical shape about 3 smectic layers thick and no defect was observed (Fig. 6.28(b)).

A 90/10 mixture was studied at temperature $T = 1.0$ in the density range $0.30 \leq \rho \leq 0.36$. A hard particle configuration at $\rho = 0.30$ was used to start this compression series. The system was equilibrated for 7×10^5 time steps, after which it

111

remained homogenous and isotropic. It was then compressed to higher densities with a step of $\Delta\rho = 0.1$. The nematic order parameter and radial distribution functions were monitored as before to determine the system's structure. Cluster analysis was performed as well since it proved to be an informative tool for studying demixing at low sphere concentrations. Table 6.11 presents the resultant data. These indicate

Density	Order parameter	Number of clusters	Largest cluster size
0.31	0.054 ± 0.019	130 ± 8	9 ± 3
0.32	0.049 ± 0.014	124 ± 6	10 ± 2
0.33	0.072 ± 0.021	129 ± 7	9 ± 2
0.34	0.392 ± 0.036	117 ± 8	11 ± 4
0.35	0.617 ± 0.021	106 ± 7	16 ± 4
0.36	0.714 ± 0.011	73 ± 6	102 ± 3
0.35^{exp}	0.630 ± 0.020	84 ± 6	84 ± 4

Table 6.11: The order parameter and cluster distribution at $T = 1.0$.

that the mixture remained mixed in the interval of densities $0.30 \leq \rho \leq 0.35$ even after the isotropic-nematic transition had taken place at $\rho \approx 0.34$. The corresponding sphere-sphere radial distribution functions and a configuration snapshot taken at $\rho = 0.35$ and $T = 1.0$ are shown in Fig. 6.29. The homogenous nematic phase at

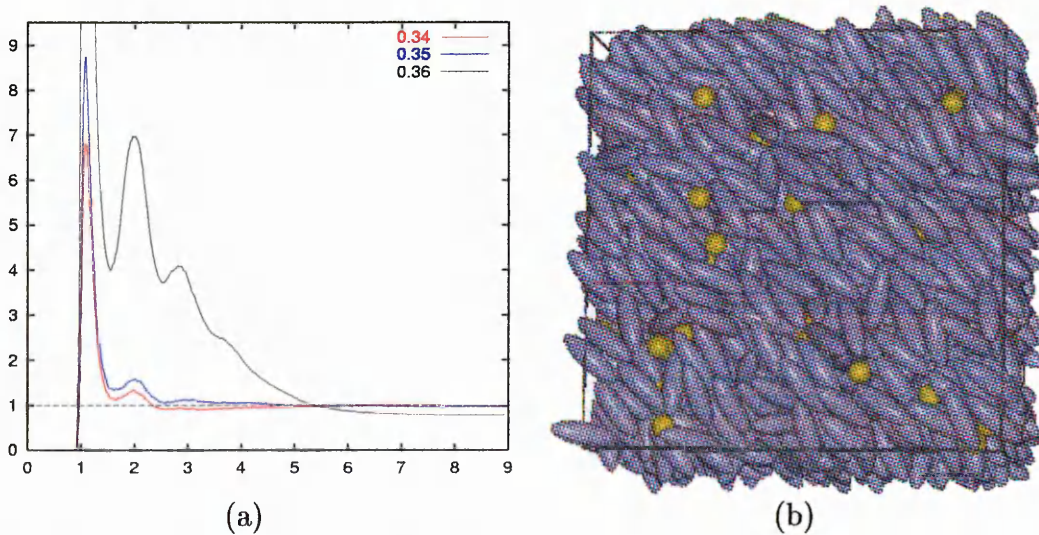(a)   (b)

Figure 6.29: (a) Sphere-sphere radial distribution functions, $g_{ss}(r)$, at $T = 1.0$ and different densities; (b) homogenous nematic phase at $\rho = 0.35$ and $T = 1.0$.

$\rho = 0.35$ was equilibrated for 10^6 time steps. During this run, stable values of the

potential energy and the nematic order parameter were observed. At the higher density $\rho = 0.36$, the system started to demix forming a single droplet. In a subsequent run, when the system was expanded back to $\rho = 0.35$, the single droplet reduced in size slightly, but remained stable at the simulation time scale. Thus, the nematic phase at $\rho = 0.35$ and $T = 1.0$ was observed to be homogenous or heterogenous depending on the initial configuration the simulation was started from. Table 6.12 shows that the heterogenous configuration has lower potential energy. However, its

Configuration	Energy	Order Parameter	Pressure
homogenous	-3.073 ± 0.033	0.630 ± 0.020	4.54 ± 0.09
heterogenous	-3.228 ± 0.032	0.642 ± 0.024	4.43 ± 0.09

Table 6.12: Parameters of two stable configurations at $\rho = 0.35$ and $T = 1.0$.

mixing entropy is much lower making it unclear which configuration has lower free energy. The observation of hysteresis at such a transition is not, however, surprising.

6.3.3 Discussion

According to the simulation results, system (ii) is found to have stronger demixing than system (i). Indeed, at the same concentration and density it starts to demix at slightly higher temperatures. Interestingly, a 20/80 mixture under compression at $T = 1.0$ demixes before the isotropic-nematic transition, whereas a 10/90 mixture does not demix until post-transitional densities. At the same temperature system (i) cooperatively undergoes isotropic-nematic transition and demixing for both concentrations.

Under rapid cooling from an isotropic mixed configuration at 20% sphere concentration, system (ii) exhibits a micellar structure. The core of each micelle, formed by spheres, is nearly spherical in shape and is covered by a layer of rods. On the contrary, a thermodynamically more favourable single large droplet configuration develops at low cooling rate. This configuration has lower potential energy and higher orientational entropy, because there are more rods in the isotropic phase not

aligned by the surface. The only entropy term which benefits from a multi-droplet configuration is the mixing entropy. However, this is expected to be small because spheres have already been demixed. At 50% concentration of spheres, only a single droplet configuration was observed. This suggests that spheres would demix in a macroscopic system at this concentration rather than form small separate droplets. On the other hand, at low concentrations of spheres, there is a possibility of a macroscopically stable micellar phase. In experimental systems, micelles form in a solution above the critical micellar concentration and are known to be dynamic aggregates, making and breaking on time scales of 10^{-6} to 10^{-3} s [103]. To draw an analogy with typical surfactant systems we can consider a rod with a sphere attached to its end as an amphiphilic entity and all single rods as solvent. The sphere concentration, therefore, represents the concentration of surfactant in the system. The fact that the mixing behaviour is so different at 10% and 20% concentration of spheres may be due to the onset of micelle formation concentration in the isotropic phase of the 20% system. Time scales of order of 10^{-6}s are well beyond those available to our method, however, making investigation of micellar processes inaccessible for current computational hardware.

The shape of a single droplet suspended in a rod-rich phase is found to depend on the parameterisation of the rod-sphere potential. It was nearly spherical in both systems (i) and (ii) at low temperatures and low densities when the rod-rich phase is isotropic. In a nematic phase, the shape of the droplet was defined by the competition between the anchoring energy, nematic elasticity and surface tension. It was also strongly affected by the periodic boundary conditions due to the relatively large size of the droplets formed. In system (i) there was some evidence of elongation of the droplet, whereas a droplet suspended in a nematic in system (ii) was rather oblate. This tendency was not fully consistent and proved somewhat difficult to observe, especially in system (ii). Once smectic order developed, in each system, however, the droplets were encapsulated between the smectic layers and adopted shape anisotropies which were stable and of the expected type.

According to the continuum theory the order of nematic phase leads to the conflict

between the alignment of the rods on the droplet surface and the bulk director. This can give rise to defect formation a pair of boojums if the anchoring is planar (like in system (i)) and the Saturn ring or the Satellite defect if the anchoring is homeotropic (like in system (ii)) (see Section 2.5 for details). If $\hat{k}$ is a unit vector normal to the surface, the anisotropic part of the surface free energy density is expressed [104] as following:

$$f_S = \beta_{11}\hat{k} \cdot \mathbf{Q} \cdot \hat{k} + \beta_{20}\mathbf{Q} : \mathbf{Q} + \beta_{21}\hat{k} \cdot \mathbf{Q} \cdot \mathbf{Q} \cdot \hat{k} + \beta_{22}(\hat{k} \cdot \mathbf{Q} \cdot \hat{k})^2, \qquad (6.7)$$

where $\mathbf{Q}$ is the tensor order parameter and β_{ij} are elasticity constants. If K is the curvature of the surface at a given point then this area is subject to the force which normal component can be written as:

$$F_\perp = -Kf_S\hat{k} + \hat{k}\left(K\hat{k} - \nabla_S\right)\frac{\partial f_S}{\partial \hat{k}} \qquad (6.8)$$

Consider the case of a droplet suspended in a liquid crystal with a strong homeotropic anchoring. If the Saturn ring defect forms, the director field near the surface will not be radial but have a splay in the equatorial plane of the droplet (Fig 6.30(a)). The

Bulk director

Bulk director

(a)   (b)
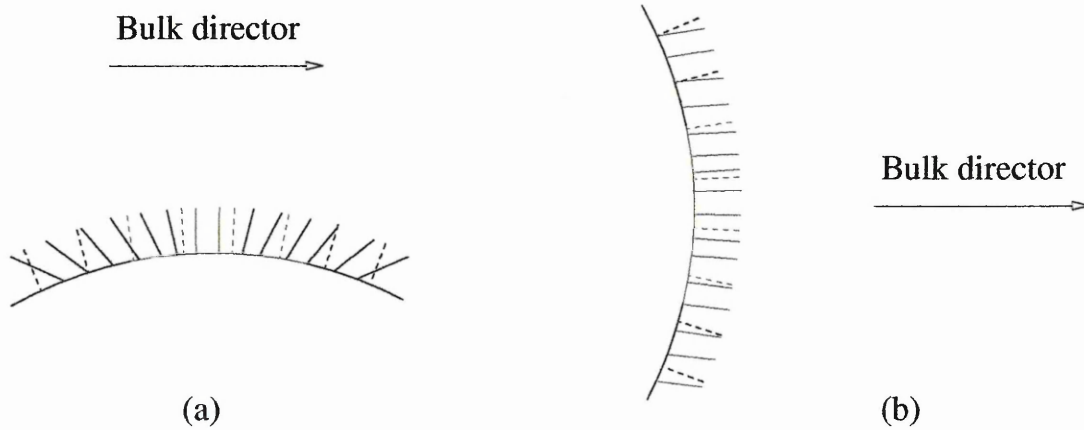
Figure 6.30: Director field (a) in the equatorial plane of the droplet and (b) near the pole. Dashed lines shows the radial direction.

divergence of the director field is much higher near the defect than on the droplet's poles where there are no singularities of the director field (Fig 6.30(b)). This means that the derivative $\frac{\partial f_S}{\partial \hat{k}}$ is much greater in the equatorial plane, and higher surface forces are required to compensate the second term in equation (6.8) in order to

achieve the equilibrium condition, $F_\perp = 0$, on the surface. This causes the droplet to become oblate along the director in the case of homeotropic anchoring. Note that in any case the surface of the droplet has higher curvature near the defect.

6.4 System (iii)

The mixture studied in this Section is of type (iii) as described in Section 6.1. The strength of the rod-sphere interaction here has no orientational dependence and is characterised by a constant well depth ϵ_0. Analogous to the previous two systems, the results of simulations are presented for different concentrations of spheres. A 50/50 mixture is studied first followed by simulations of mixtures with lower concentrations of spheres.

6.4.1 50/50 Mixture

A system containing 512 rods and 512 spheres interacting via potential of type (iii) was simulated in the constant NVT ensemble using previously validated MD code. Starting from a hard particle configuration at $\rho = 0.40$ the system was equilibrated at temperature $T = 1.2$ for 7×10^5 time steps during which it remained isotropic and uniform. Then it was compressed at constant temperature up to density $\rho = 0.50$. The nematic order parameter remained low over this whole range of densities and no isotropic-nematic transition was observed. Figure 6.31(a) presents the sphere-sphere radial distribution functions calculated at different densities which indicate no demixing in the system. To study the effect of attractive interactions we then cooled the system down to $T = 0.7$ with a step of $\Delta T = 0.1$ at low density $\rho = 0.40$ and then compressed it up to $\rho = 0.50$ with a step of $\Delta \rho = 0.01$. During these cooling and compression series the nematic order parameter was always low indicating no long-range orientational ordering in the system. The sphere-sphere radial distribution functions shown in Fig. 6.31(b) did not reveal any significant changes in the system's structure for the compression sequence at $T = 0.7$. Analogous to the compression
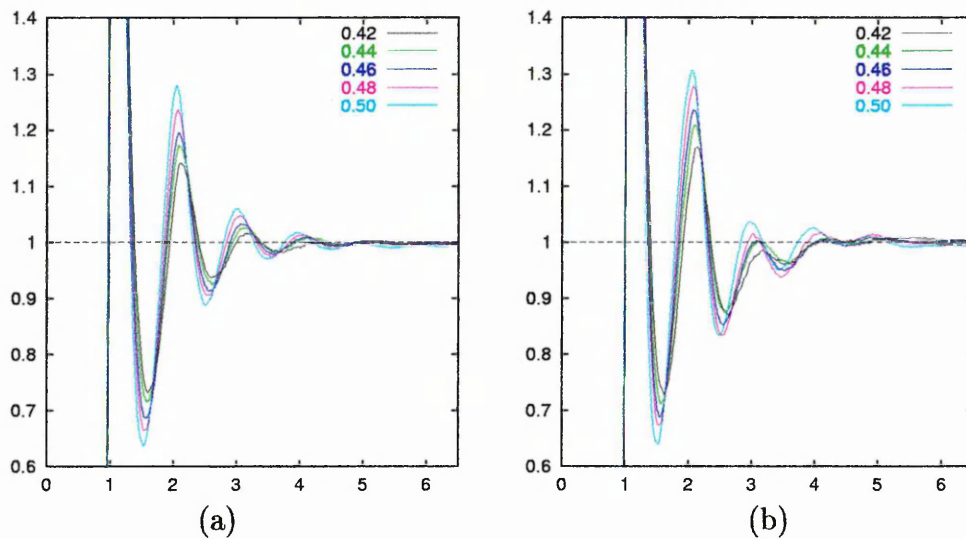
Figure 6.31: Sphere-sphere radial distribution functions, $g_{ss}(r)$, at temperature (a) $T = 1.2$ and (b) $T = 0.7$.

run at higher temperature, the system's behaviour was found to be similar to that of the hard particle system, i.e. neither demixing nor orientational ordering was observed at this concentration. Figure 6.32(a) shows a set of radial distribution
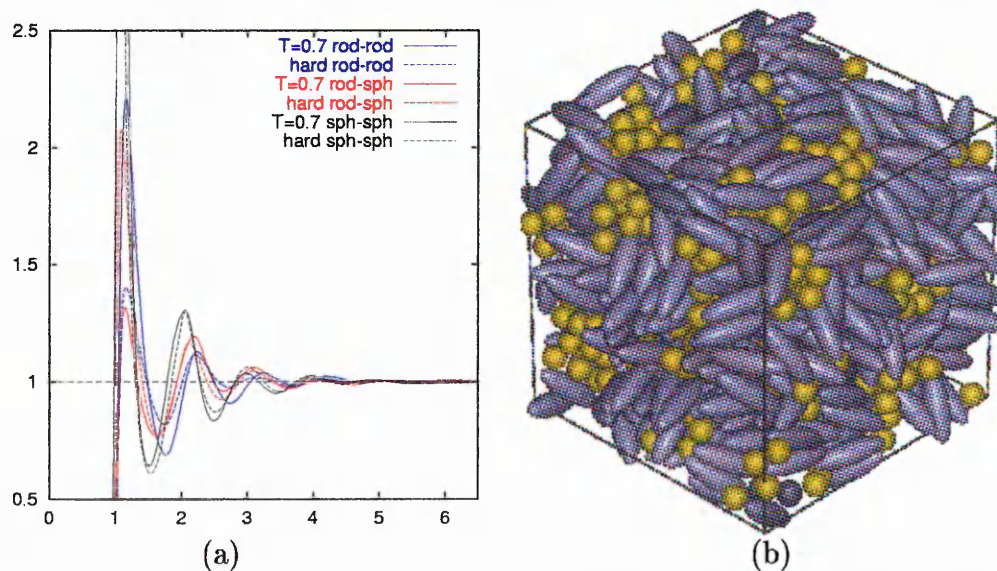
Figure 6.32: (a) Radial distribution functions, $g_{rr}(r)$, $g_{rs}(r)$, $g_{ss}(r)$, calculated at $\rho = 0.50$ and $T = 0.7$ compared to those of the hard particle system; (b) A snapshot of configuration at $\rho = 0.50$ and $T = 0.7$.

functions calculated at the same density $\rho = 0.50$ in the studied mixture at $T = 0.7$

and in the system of hard particles. They indicate that the system of soft particles has a greater number of the rod side-by-side configurations. The relatively strong rod-rod attractions affect the short-range order, leading to a small increase the nematic order parameter. For comparison, the nematic order parameter measured in the hard particle system at $\rho = 0.50$ was 0.089 ± 0.020, whereas system (iii) yields values 0.142 ± 0.053 and 0.188 ± 0.061 at $T = 1.2$ and $T = 0.7$ respectively. However, as the radial distribution functions indicate, qualitatively system (iii) forms the same structure as was seen in a hard particle system. This suggests that a temperature of $T = 0.7$ is still quite high for this type of mixture and that a lower temperature is required for the effect of the attractive interactions to become more significant.

Two short series of cooling runs were performed, therefore, at low, $\rho = 0.42$, and high, $\rho = 0.48$, densities. Starting from the configurations equilibrated before at $T = 0.7$, the system was cooled down to $T = 0.6$ and then further to $T = 0.5$. The order parameter remained low at both densities, although system snapshots indicated some local structuring: fragments of smectic layers and sphere-rich layers were observed. The sphere-sphere radial distribution functions calculated at $\rho = 0.42$ and $\rho = 0.48$ and different temperatures are shown in Fig. 6.33. They suggest the
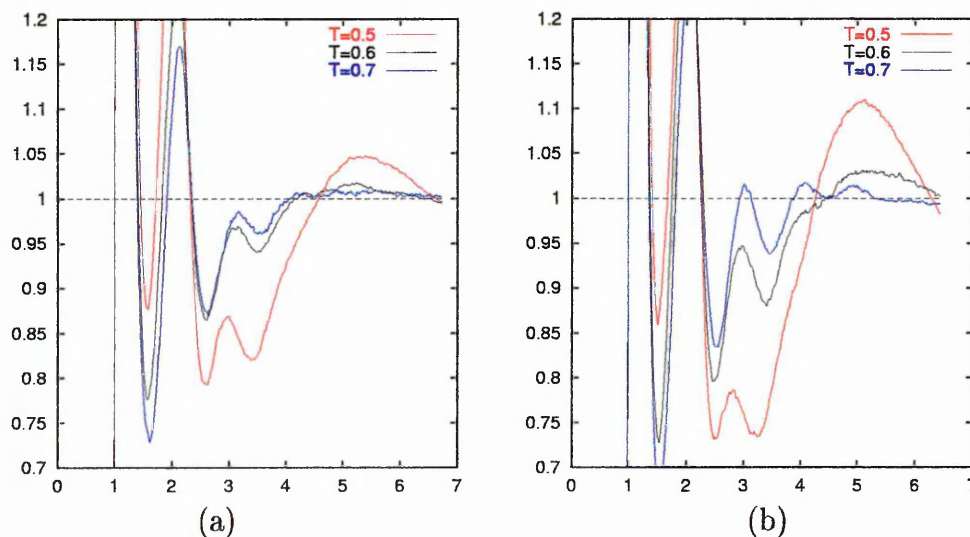

Figure 6.33: Sphere-sphere radial distribution functions, $g_{ss}(r)$, at density (a) $\rho = 0.42$ and (b) $\rho = 0.48$.

presence of structural regularities at low temperatures with periodicity of about

$5\sigma_0$. Cluster analysis indicated a bicontinuous interconnected network, i.e. there was no separate clusters of spheres. The observed structure was formed due to a combination of the relatively strong rod-rod attraction and the weak demixing properties. This effect were not observed in systems (i) and (ii) because of the strong demixing which occurred at much higher temperatures.

Since the periodicity of the low temperature structure was of order of a half of the system box side, a larger system was required to study this structure properly. There was a possibility of a lamellar phase in which layers of rods were separated by layers of spheres. The structure observed in the small simulation box might, therefore, have been affected by too rapid cooling or/and the influence of the periodic boundary conditions. A system of 8192 rods and 8192 spheres was simulated on 64 nodes of parallel supercomputers (SG Origin 3000 and Cray T3E-1200E) at CSAR in Manchester. The parallel code used for these simulations was a version of GBMOLDD [105] which had been modified by Richard Webster so as to include the specific rod-sphere interaction used in this system. Richard Webster also assisted in the submission and running of these CSAR-based simulations. The initial configuration was obtained by replicating eight images of a simulation box of 2048 hard particles, so giving a system of 16384 particles in total. In order to prevent simulation of eight identical configurations in parallel, the initial translational velocities were randomised according to the Maxwell-Boltzmann distribution [4]. Thus, for each velocity component required

- two random numbers ψ_1 and ψ_2 were generated on (0,1);

- a velocity component $v_i^\alpha = \cos 2\pi\psi_1 \sqrt{-2T ln \psi_2}$ was calculated.

This configuration was equilibrated at $T = 0.6$ for 3.5×10^5 time steps. Here such parameters as the time step, cutoff radius, neighbour list radius etc., were set to the same values as were used in our previous MD simulations. Series of large system runs were then performed, a complete list of which, in the order in which they were performed is given in Tab. 6.13. These runs consisted of two cooling series at $\rho = 0.40$

Density	Temperature	Time steps	Potential energy
0.40	0.60	350,000	-4.6216 ± 0.0084
0.40	0.58	300,000	-4.6910 ± 0.0089
0.40	0.57	150,000	-4.7275 ± 0.0086
0.40	0.56	300,000	-4.7720 ± 0.0083
0.40	0.55	300,000	-4.8121 ± 0.0096
0.41	0.55	250,000	-4.9529 ± 0.0092
0.42	0.55	580,000	-5.0963 ± 0.0087
0.42	0.54	580,000	-5.1467 ± 0.0078
0.42	0.53	580,000	-5.1963 ± 0.0096
0.42	0.52	500,000	-5.2592 ± 0.0076
0.42	0.51	250,000	-5.3145 ± 0.0096
0.43	0.51	480,000	-5.4694 ± 0.0090
0.44	0.51	440,000	-5.6305 ± 0.0092
0.45	0.51	900,000	-5.7993 ± 0.0087

Table 6.13: Parameters of the CSAR-based runs performed for a system of 16384. Each run was started from the final configuration of the previous one.

and $\rho = 0.42$ and two compression series at $T = 0.55$ and $T = 0.51$. The first cooling series was started at $\rho = 0.40$ and carried on with a step of $\Delta T = 0.01$ while the pressure was positive. According to the results of linear extrapolation, the pressure would have gone negative at $T = 0.54$, therefore, the system was compressed to higher densities to maintain positive pressure. The temperature dependence of the potential energy was almost linear in both cooling runs. It also showed nearly linear density dependence during the compression run. Thus, no discontinuities were observed in the potential energy or its first derivatives while the system transformed from the uniform isotropic configuration to that shown in Fig. 6.34. Cluster analysis was performed and radial distribution functions calculated to map out the structural changes in the system. Table 6.14 shows that with decreasing temperature and increasing density the size of the largest cluster increased and that this was accompanied by a corresponding decrease of the total number of clusters. Since at $T = 0.51$ almost every sphere in the system had a neighbouring sphere at separation less than 1.5σ, they formed a single cluster that contained all but a few spheres. Together with the absence of macroscopic phase separation, this indicates that the formed structure remained bicontinuous. Figure 6.35 presents sphere-sphere radial
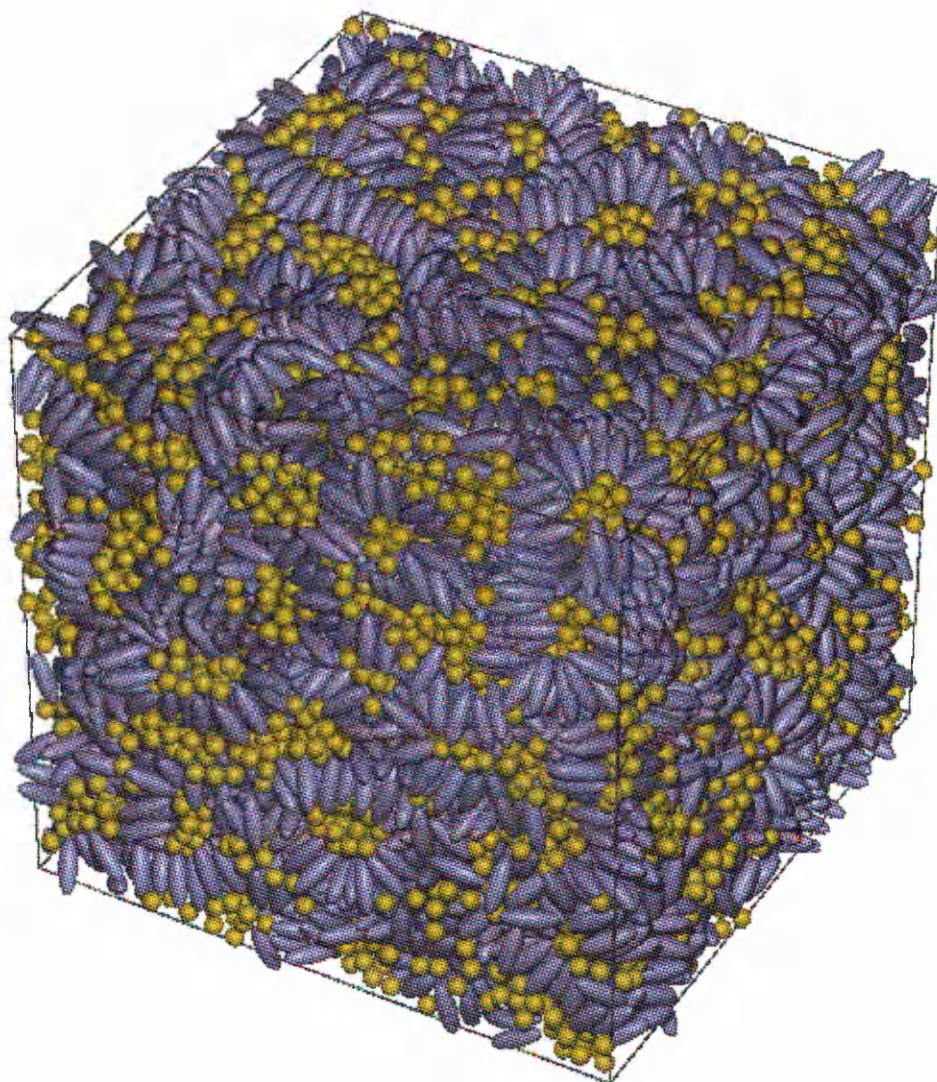
Figure 6.34: Snapshot of a system of 16384 particles at $\rho = 0.45$ and $T = 0.51$. The simulation box side is $33.144\sigma_0$.

Density	Temperature	Number of clusters	Largest cluster's size
0.40	0.60	235 ± 15	7802 ± 47
0.40	0.58	225 ± 12	7840 ± 39
0.40	0.56	210 ± 14	7869 ± 42
0.43	0.51	90 ± 9	8074 ± 26
0.44	0.51	71 ± 9	8110 ± 13
0.45	0.51	49 ± 7	8139 ± 9

Table 6.14: The cluster size distributions for the cooling run at $\rho = 0.40$ and compression run at $T = 0.51$.
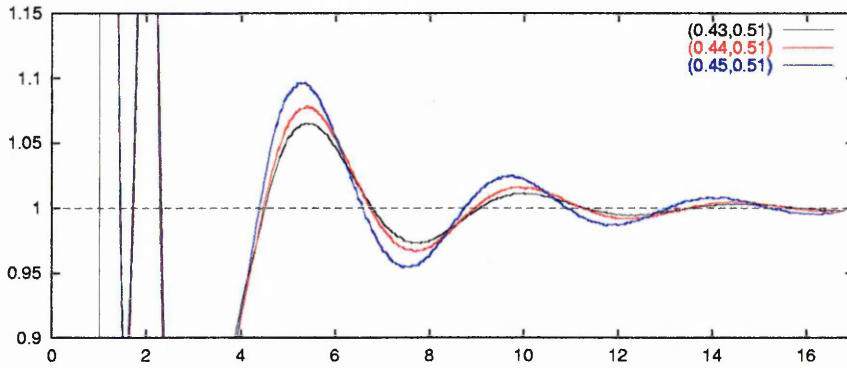
Figure 6.35: Sphere-sphere radial distribution functions, $g_{ss}(r)$, at temperature $T = 0.51$ and different densities.

distribution functions measured during the compression run at $T = 0.51$. They indicate the same periodicity as was observed in the system of 1024 particles (Fig. 6.33). However, these functions approach unity at separations greater than $10\sigma_0$ which suggests that, despite some local ordering developed in the system, there are no long range transitional correlations in the observed microphase-separated structure.

The temperatures at which microphase separation occurred in this system were relatively low, and there was a possibility that the system's state was rather glassy. To check whether the observed state was fluid or the networks of rods and spheres were frozen, the particle displacement was calculated. Figure 6.36 demonstrates how rod and sphere displacement probability densities changed with time at $\rho = 0.45$ and $T = 0.51$. These indicate that all particles in the system were moving around and that none of them became immobilized at a fixed location. Figure 6.37 shows how the mean square displacement changed with time. In the case of Brownian or random walk motion, the mean square displacement is known to be a linear function of time:

$$< (\mathbf{r}(t) - \mathbf{r}(0))^2 >= 6Dt, \qquad (6.9)$$

where D is the diffusion coefficient. However, this dependence is not linear in the case of some complex systems such as polymers, for example, for which the mean square displacement is proportional to t^ν, where $\nu < 1$ [106]. The double logarithmic scale used in Fig. 6.37 reveals how the exponent ν changed in the time range $0.3 \le t \le 450$.
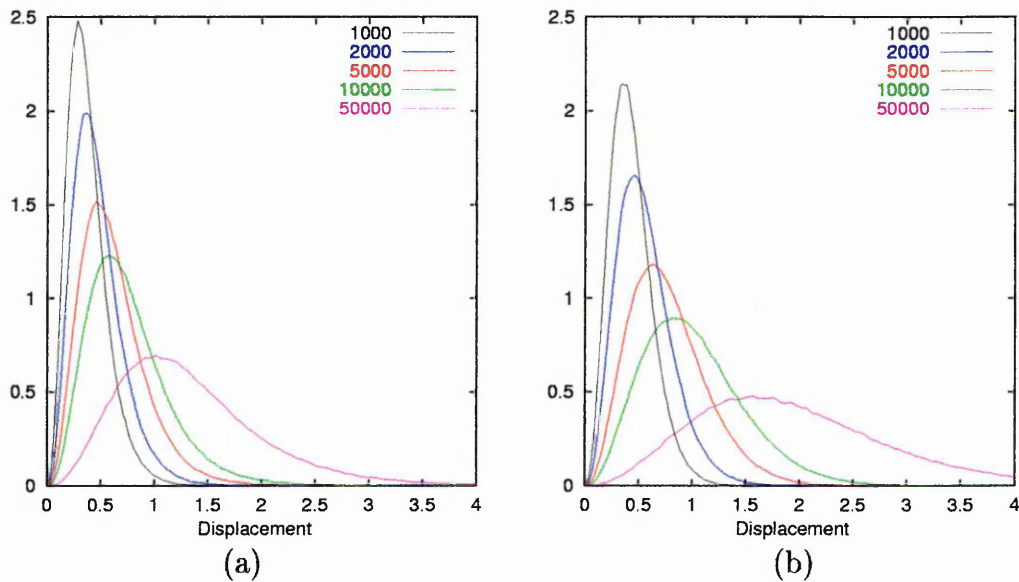
Figure 6.36: (a) Rod and (b) sphere displacement probability densities at $\rho = 0.45$ and $T = 0.51$ calculated after a given number of time steps.
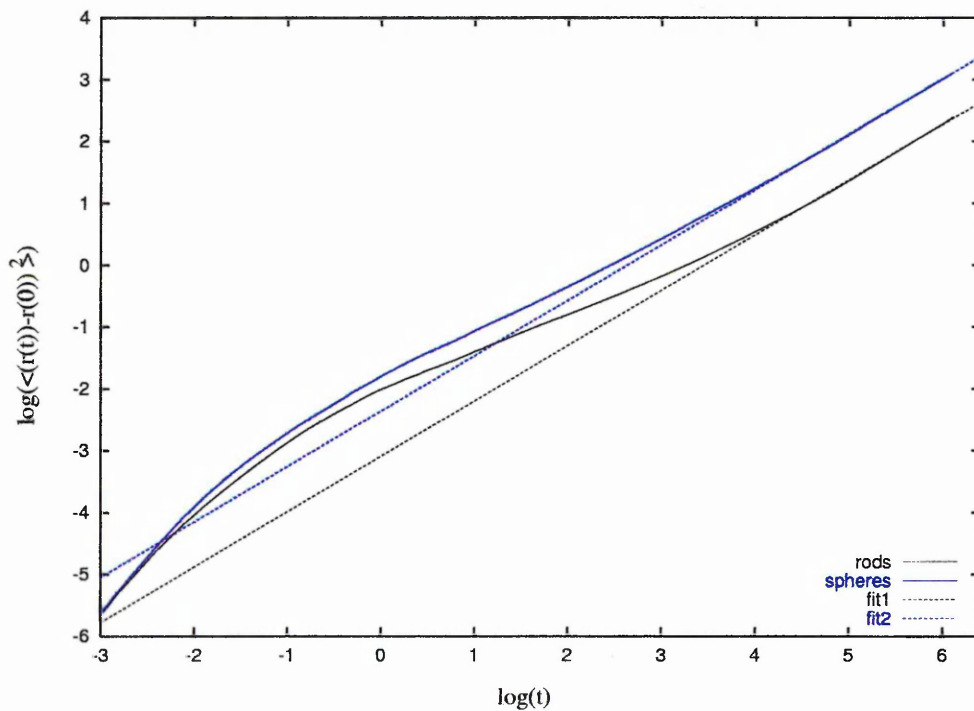

Figure 6.37: Time dependance of the mean square displacement at $\rho = 0.45$ and $T = 0.51$ plotted in the double logarithmic scale.

At small times of several thousands time steps, the diffusion of both rods and spheres was not macroscopic due to the strong short time correlations in particle positions.

Only after about 30,000 time steps, when each rod, on average, had moved from its initial position by about $1.3\sigma_0$ ($1.8\sigma_0$ for spheres) did both dependencies became linear. The slopes of the tangents shown in Fig. 6.37 are almost equal for both curves at $\nu = 0.91 \pm 0.02$. The average rods' displacement for the whole simulation time at $\rho = 0.45$ and $T = 0.51$ (9×10^5 time steps) was estimated as $5.8\sigma_0$. The equivalent figure for the spheres was $8.3\sigma_0$. This indicates that the system was in a liquid state and suggests that the particles were moving in an approximately Brownian manner when in structures such as that shown in Fig. 6.34.

6.4.2   Low Concentration of Spheres

In this Section we study mixture (iii) at sphere concentrations of 20% and 30% for the systems containing 2048 particles in total. Since a 50/50 mixture, studied in the previous Section, remained isotropic and uniform over a wide range of temperatures, we will concentrate here mainly on the low temperature behaviour.

Constant NVT MD simulations were started from a hard particle configuration at 20% sphere concentration at density $\rho = 0.32$ and equilibrated at temperature $T = 0.7$ for 10^6 time steps. Then the system was compressed at constant temperature up to density $\rho = 0.38$ with a step of $\Delta\rho = 0.01$, allowing 7×10^5 time steps for equilibration followed by 7×10^5 steps for each production run. The potential energy per particle and nematic order parameter calculated during these simulations are presented in Fig. 6.38. The potential energy changed almost linearly with increasing density; this indicated the weakness of the phase transition which occurred at a density of about $\rho = 0.36$. The parallel distribution functions measured in the vicinity of the transition indicated development of smectic layers at a density of about $\rho = 0.37$ (Fig. 6.38(b)). There were weak signs of demixing at high densities but neither macroscopic demixing nor long-range periodicity of the sphere distribution were observed. The compression run at lower temperature $T = 0.6$ revealed a stable smectic phase at densities higher than $\rho = 0.37$ with an order parameter of more than 0.85. Figure 6.39(a) shows that the distribution of spheres in this system
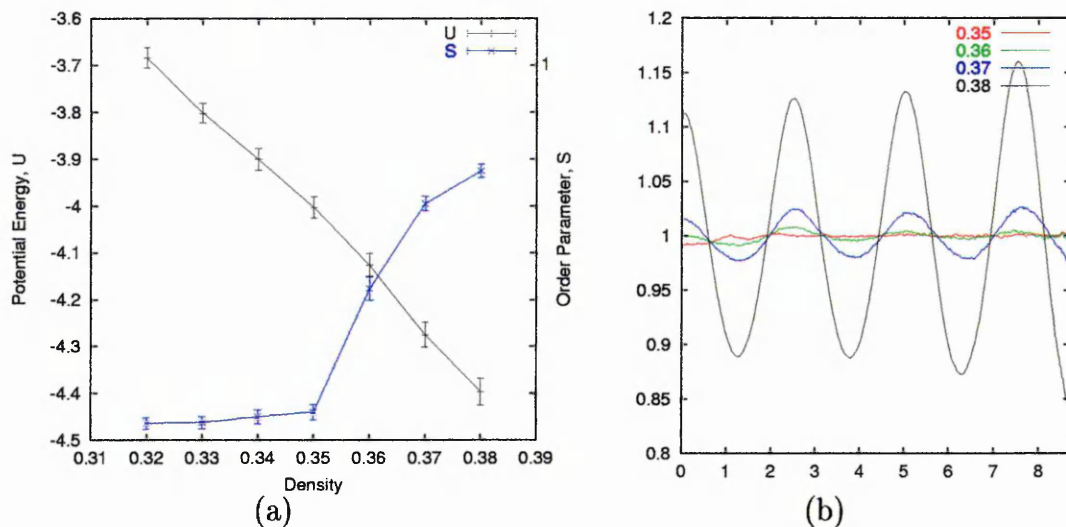
Figure 6.38: (a) Potential energy per particle and nematic order parameter measured during the compression run at $T = 0.7$; (b) parallel distribution function, $g_{\parallel}(r_{\parallel})$, calculated at temperature $T = 0.7$ and different densities.
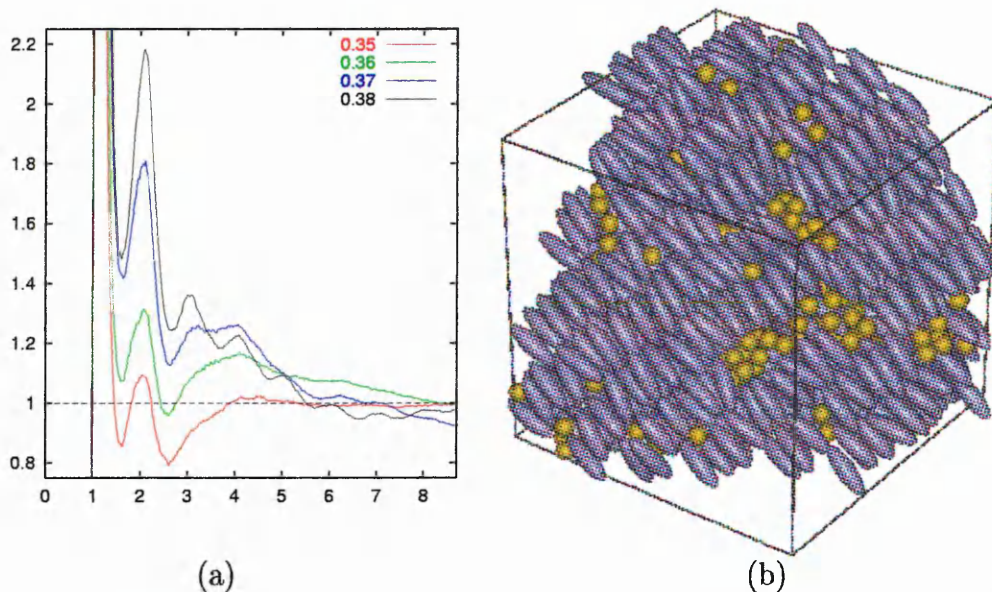
Figure 6.39: (a) Sphere-sphere radial distribution function, $g_{ss}(r)$, calculated at $T = 0.6$ and different densities; (b) configurational snapshot at $\rho = 0.38$ and $T = 0.6$.

was not homogeneous, i.e. they tended to form groups. Since these sphere-sphere radial distribution functions approach unity at large separations, these groups must have been distributed randomly throughout the system. The corresponding structure of such a system, taken at $\rho = 0.38$ and $T = 0.6$, is pictured in Fig. 6.39(b).

The cluster analysis of this configuration confirmed local clustering in the system. The sizes and numbers of the clusters separated by distances greater than 1.5σ are shown in Tab. 6.15. A third compression series, at $T = 0.5$, did not reveal any

Size	1	2	3	4	5	7	8	9	12	62	83	129
Number	13	21	1	4	2	2	1	2	1	1	1	1

Table 6.15: Cluster size distribution at $\rho = 0.38$ and $T = 0.6$.

qualitative changes in the system behaviour. It remained isotropic and mixed in the range of densities $0.30 \le \rho \le 0.34$ and then, at $\rho = 35$, a structure similar to that shown in Fig. 6.39(b) was observed.

A compression run at temperature $T = 1.0$ was performed in the range of densities $0.36 \le \rho \le 0.40$. The main motive for running this series was to find a stable homogeneous nematic phase. So far, only the system of hard particles had exhibited a nematic phase in which the spheres were uniformly distributed over the simulation box. Systems (i) and (ii) showed very strong demixing and spheres tended to separate macroscopically from the rod-rich phase. During the performed compression sequence, the behaviour of the nematic order parameter indicated a phase transition at $\rho \approx 0.38$. On further compression, the system remained in a nematic phase as indicated by the parallel distribution function $g_{\parallel}(r_{\parallel})$. The sphere-sphere radial distribution functions were measured and the cluster analysis was performed to study the demixing property of these configurations. Figure 6.40(a) illustrates no macroscopic phase separation at densities $0.38 \le \rho \le 0.41$. However, the decrease of the total numbers of clusters with increasing density suggests some local clustering. Figure 6.40(b) shows how the total number of clusters changed with simulation time at $\rho = 0.38$ and $\rho = 0.40$ and Tab. 6.16 summarises the simulation results for all densities. These closely resemble analogous data obtained for hard particles, so indicating that the effect of attractive interactions in this mixture was weak at $T = 1.0$, leading to the formation of a homogeneous nematic phase.

If the sphere concentration was reduced to, for example 10%, the demixing tendency
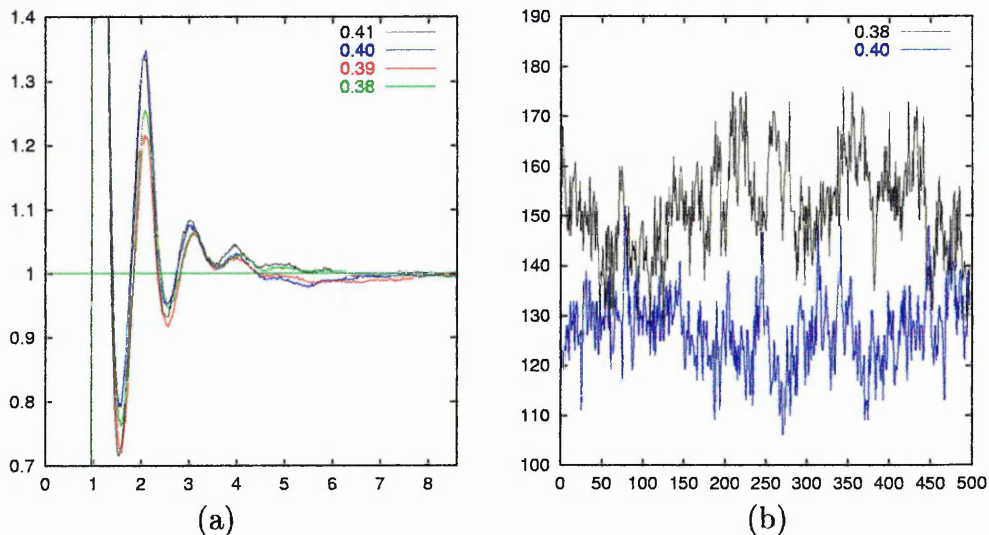
Figure 6.40: (a) Radial sphere-sphere distribution functions, $g_{ss}(r)$, measured at $T = 1.0$ and different densities; (b) cluster number during the runs at $\rho = 0.38$ and $\rho = 0.40$.

Density	Order parameter	Number of clusters	Largest cluster size
0.36	0.069 ± 0.021	182 ± 11	17 ± 5
0.37	0.087 ± 0.034	180 ± 10	19 ± 6
0.38	0.522 ± 0.028	151 ± 10	28 ± 9
0.39	0.650 ± 0.021	139 ± 8	29 ± 9
0.40	0.718 ± 0.015	124 ± 9	38 ± 11
0.41	0.768 ± 0.013	114 ± 8	44 ± 15

Table 6.16: The order parameter and cluster distribution at $T = 1.0$.

would be enhanced and the structures formed would be similar to those seen at 20% but containing fewer spheres. However, at higher sphere concentrations, there is a possibility of locating a lamellar phase in which spheres are present in a number sufficient to fill in the spaces between the smectic layers. A 70/30 rod-sphere mixture was, therefore, simulated at low temperatures and a range of densities to explore the possible existence of such a phase. Two compression series were performed at temperatures $T = 0.6$ and $T = 0.5$. Starting from density $\rho = 0.36$, the compressions were carried on until the nematic order parameter indicated a phase transition. This occurred at a density of about $\rho = 0.40$ at $T = 0.6$, and at $\rho \approx 0.39$ at $T = 0.5$. Very long runs (5×10^6) time steps were required to equilibrate the sys-

tem at these data points. The sphere-sphere radial distribution function calculated at pre-transitional densities did not indicate macrophase separation (see the red graph in Fig. 6.41 for example). However, the cluster distribution was quite differ-
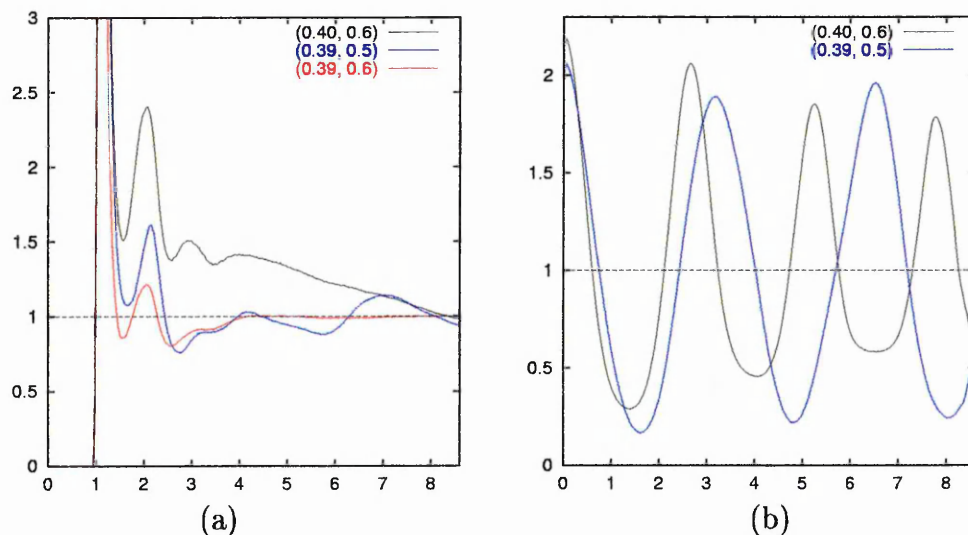
Figure 6.41: (a) $g_{ss}(r)$ and (b) $g_{\parallel}(r_{\parallel})$ distribution functions calculated at ($\rho = 0.40$, $T = 0.6$) and ($\rho = 0.39$, $T = 0.5$).

ent from that typical for a uniform mixture, e.g. 10 clusters of size ranging between 20 and 60 were observed at $\rho = 0.36$, $T = 0.6$. This distribution did not change significantly with increasing density up to the transition point, were the sphere-rich phase became continuous. Analogous compression at temperature $T = 0.5$ revealed somewhat different system behaviour. Here, two large clusters were observed once smectic order had developed at $\rho = 0.39$. Figure 6.41(a) shows that the sphere distributions were different in the structures formed on cooling at $T = 0.6$ and $T = 0.5$. The former had signs of macroscopic phase separation, whereas the latter suggested some microscopic structure with a periodicity of about $7\sigma_0$. The parallel distribution functions calculated for both structures are shown in Fig. 6.41(b). There is a clear difference in the interlayer spacing which suggests that layers of spheres may have been sandwiched between the smectic layers in the lower temperature configuration. Figure 6.42 shows configuration snapshots of both, microphase separated and periodic, structures. The higher temperature configuration presents the coexistence of two phases: the bicontinuous phase similar to that formed by the 50/50 mixture and
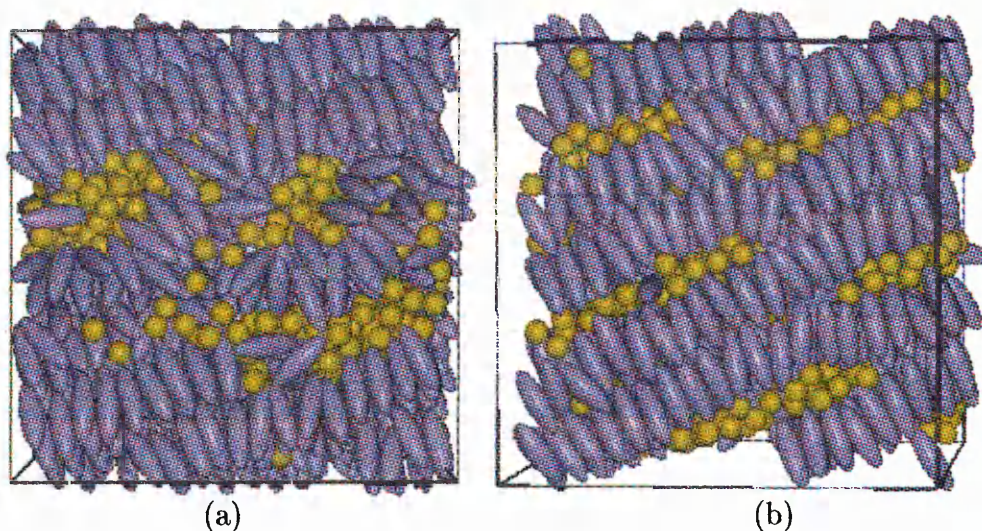
Figure 6.42: (a) Configuration snapshot taken at $\rho = 0.40$ and $T = 0.6$; (b) configuration snapshot taken at $\rho = 0.39$ and $T = 0.5$.

the rod-rich smectic phase. The low temperature configuration is a lamellar phase in which spheres do not fill completely the space between the layers of rods but do form a periodic supramolecular structure. The peak of the sphere-sphere radial distribution function observed at separations about $7\sigma_0$ corresponds to the separation of two layers of spheres having two smectic layers between them. A weak peak at separations of about 4σ corresponds to the spheres situated at a single rod's ends. There are no distinct peaks in $g_\|(r_\|)$ corresponding to the neighbouring smectic layers, however its peaks are broader than those of the defect-free Gay-Berne smectic. This suggests that neighbouring layers of rods and layers separated by a layer of spheres contribute to a single peak in $g_\|(r_\|)$.

To check whether the periodic structure observed at $\rho = 0.39$ and $T = 0.5$ was thermodynamically stable, auxiliary MC runs in the constant NPT ensemble were performed. A configuration previously equilibrated at $\rho = 0.38$ and $T = 0.5$ was used to start the first MC run, the pressure being set to $P = 1.4$. Each MC cycle comprised 2048 particle displacement moves and one volume change move. The initial run, comprising 3×10^5 MC cycles yielded equilibrium density of 0.388 ± 0.001, at which the nematic order parameter indicated no LC phase. A much longer run of 2×10^6 was required to equilibrated the system at $P = 1.5$. At this pressure, a

smectic phase developed at a density of $\rho = 0.406 \pm 0.001$. Further equilibration was performed using an unsymmetrical MC volume move to reduce the effects of periodic boundary conditions. After 10^6 MC cycles, the system still was not fully equilibrated, i.e. the potential energy was still slowly decreasing. The system did not macrophase separate at this point, but a lamellar-like structure was seen. Figure 6.43(a) shows
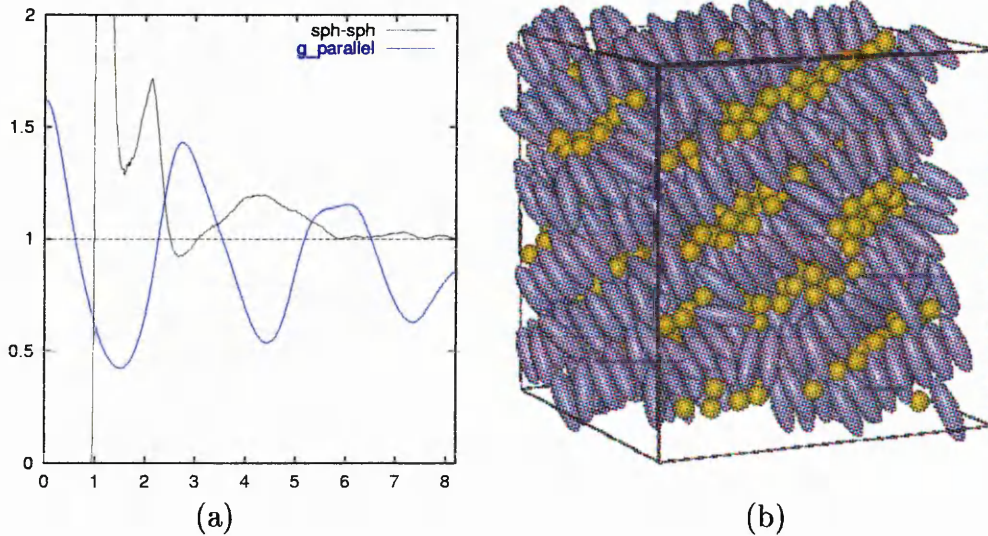
Figure 6.43: (a)Distribution functions $g_{ss}(r)$ and $g_{\parallel}(r_{\parallel})$ calculated at $P = 1.5$ and $T = 0.5$; (b) configurational snapshot taken at $P = 1.5$ and $T = 0.5$.

distribution functions $g_{ss}(r)$ and $g_{\parallel}(r_{\parallel})$ calculated at $P = 1.5$ and $T = 0.5$. The $g_{ss}(r)$ indicates some periodicity of the same order observed in our MD simulations at $\rho = 0.39$ and $T = 0.5$. It can be seen (Fig. 6.43(a)) that $g_{\parallel}(r_{\parallel})$ peaks have contributions from both neighbouring smectic layers and smectic layers separated by spheres. Figure 6.43(b) illustrates the configurational snapshot taken at this data point. This suggests that the slow equilibration of this state point was associated with rearrangements of the smectic layers.

6.4.3 Discussion

System (iii) exhibits very weak demixing when compared to systems (i) and (ii). Here, the rod-sphere potential has a well-depth function which is independent of the relative orientation of the particles. The same energy of the rod-sphere interaction is

realised in the side configuration of system (i) and in the end configuration of system (ii). However, the demixing appears to be more favourable for these systems rather than staying in the homogeneous high energy configurations. Since, in system (iii), the potential energy would not change much with demixing, the entropic consideration ensure that the system remains mixed over the wide range of densities and temperatures. At low temperatures, however, the side-by-side configurations of the rods make a significant contribution to reducing the potential energy and dominate the entropic effect. This results in the formation of microphase-separated structures in which the spheres are expelled from the layers of rods but do not demix fully, because of the associated entropy penalty. The single particle dynamics for these structures was found to be approximately diffusive, which may explain the absence of long-range correlations in the system. The 50/50 rod-sphere concentration ratio appeared to be too sphere-rich to allow development of lamellar phases and it was difficult to observe it at lower concentrations too. The reducing of the sphere-sphere interaction would decrease the surface tension of the sphere-rich phase and make it energetically cheaper to form layers of spheres.

6.5   System (iv)

In this Section, the results of simulations performed on the system of type (iv) are reported together with appropriate analysis. Here, the rod-sphere interaction is characterised by a very strong end attraction. It is five times as strong as the sphere-sphere interaction or the rod-rod interaction in the X configuration. The motivation for this parameterisation comes from the idea of combining the calamatic and lyotropic LC properties, thereby, introducing possibilities of novel phase formation. As before, the model behaviour is first studied starting for a 50/50 mixture, before lower sphere concentrations are considered.

6.5.1 50/50 Mixture

In this Section, a 50/50 mixture of rods and spheres interacting via the potentials of type (iv)(see Section 6.1 for details) is studied using our standard constant NVT MD method. A system of 1024 particles in total was equilibrated at density $\rho = 0.40$ and temperature $T = 1.5$ for 3×10^6 time steps. Due to the very strong interactions present in the system, this temperature, quite high for the systems studied above, appeared to be relatively low, i.e. the calculated pressure was close to zero in this simulation. The nematic order parameter indicated no orientational ordering at this point, whereas the sphere-sphere distribution function suggested some periodicity of order of about $5\sigma_0$. Cluster analysis indicated a bicontinuous structure and a configurational snapshot was similar to that of the mixture (iii) at low temperatures (Fig. 6.34). The system was heated to $T = 2.9$ with a step of $\Delta T = 0.2$. The radial distribution functions measured during this series are shown in Fig. 6.44(a). These
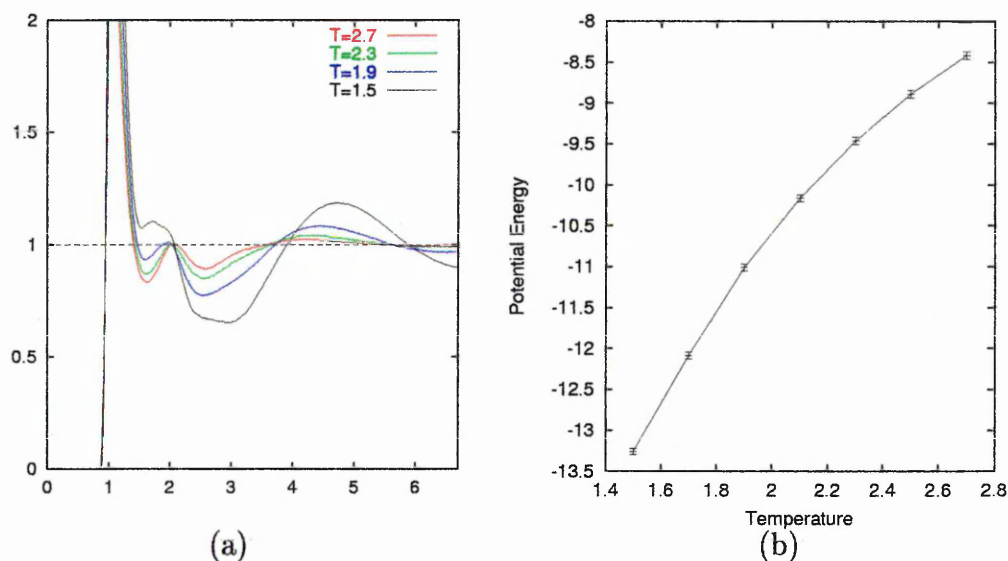

Figure 6.44: (a) Sphere-sphere radial distribution functions and (b) potential energy per particle calculated at $\rho = 0.40$ and different temperatures.

indicate that the periodicity observed at low temperatures disappeared on heating and that the mixture became uniform. This process was not accompanied by any measurable discontinuities of the potential energy (Fig. 6.44(b)) or pressure.

In order to determine the density dependence of the formed structure, two compression series were undertaken at high, $T = 2.9$, and low, $T = 1.5$, temperatures. Figure 6.45 shows the rod-sphere radial distribution functions measured at densities
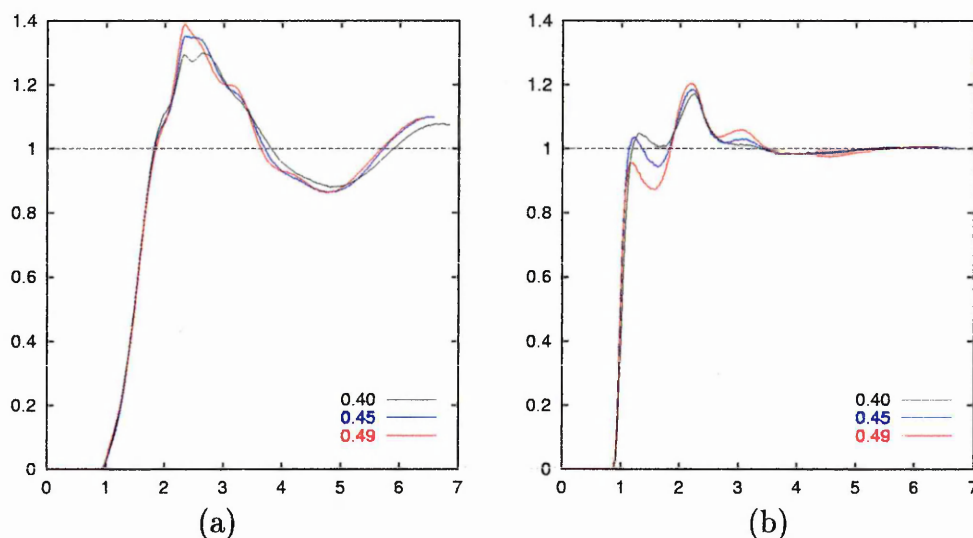
Figure 6.45: Rod-sphere radial distribution functions calculated at different densities at (a) $T = 1.5$ and (b) $T = 2.9$.

$\rho = 0.40$, $\rho = 0.45$, and $\rho = 0.49$. These do not indicate any significant density dependency of the system's structure at both low and high temperatures.

To explore the long-range order further, a larger system of 8192 particles in total was simulated. The initial configuration was obtained by replicating 8 configurations of a system of 1024 particles at $\rho = 0.40$ and $T = 2.7$. The initial velocities were set according to the random Maxwell-Bolzmann distribution scheme described at page 119. The system was cooled from $T = 2.7$ with a step of $\Delta T = 0.2$ allowing at least 4×10^5 time steps of equilibration after each decrement. Runs two and three times longer than this were required at temperatures 1.7 and 1.5 respectively. The structures formed in large and small simulation boxes were characterised by essentially the same distribution functions. Nevertheless, it actually became possible to visualise the long range correlations when using the larger box. Figure 6.46 shows a set of radial pair distribution functions calculated at $\rho = 0.40$ and $T = 1.5$. The positions of the peaks of the rod-rod and sphere-sphere distribution functions almost coincide at large separations while the radial distribution of pairs of unlike particles
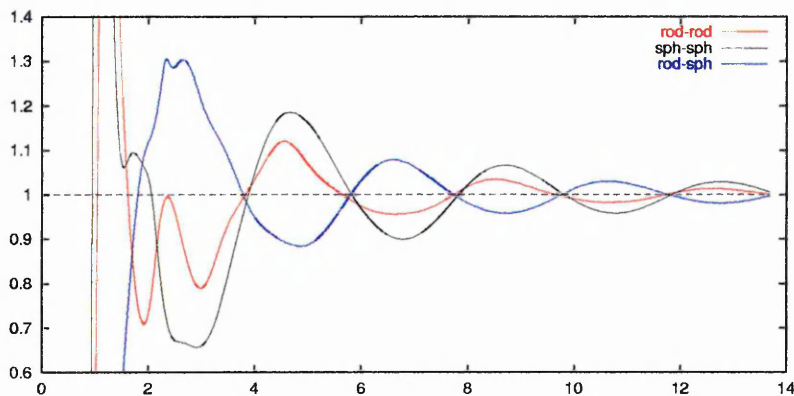
Figure 6.46: Radial distribution functions $g_{rr}(r)$, $g_{ss}(r)$, and $g_{rs}(r)$ measured at $\rho = 0.40$ and $T = 1.5$.

has minima at these same points. This suggests that rods and spheres formed two similar and interpenetrating structures. Two configuration snapshots taken at $\rho = 0.40$ and $T = 1.5$ are shown in Fig 6.47. Here, the rods are represented by
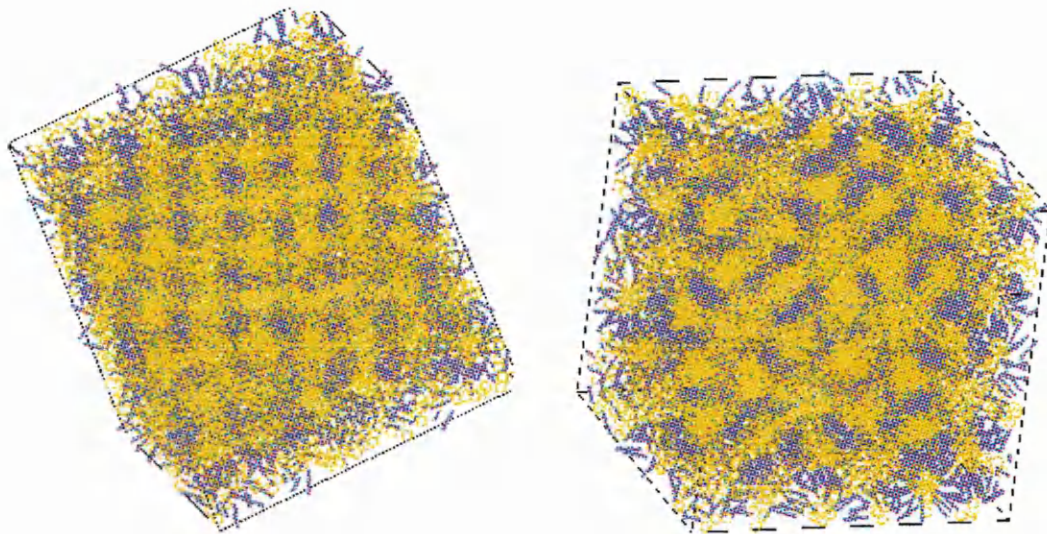
Figure 6.47: Two semitransparent snapshots of the same configuration at $\rho = 0.40$ and $T = 1.5$ taken from different points of view.

thin blue lines and the spheres are empty yellow circles, this simple graphics make it possible to see significant depth into the simulation box. There is a clear cubic pattern in the first snapshot, whereas the yellow spots form a hexagonal pattern in the second. These suggest that the formed structure has the symmetry of a cubic phase.

Particle mean square displacement measurements were carried out to explore the dynamic properties of this structure. It appeared that both rods and spheres experienced quite significant diffusion and did not have fixed positions. The average displacement of rods over 3×10^5 time steps was found to be more than $6\sigma_0$, and about $8\sigma_0$ for the spheres. The time dependencies of these are shown in Fig. 6.48. These indicate that both rods and spheres diffused similarly at long times, i.e. the
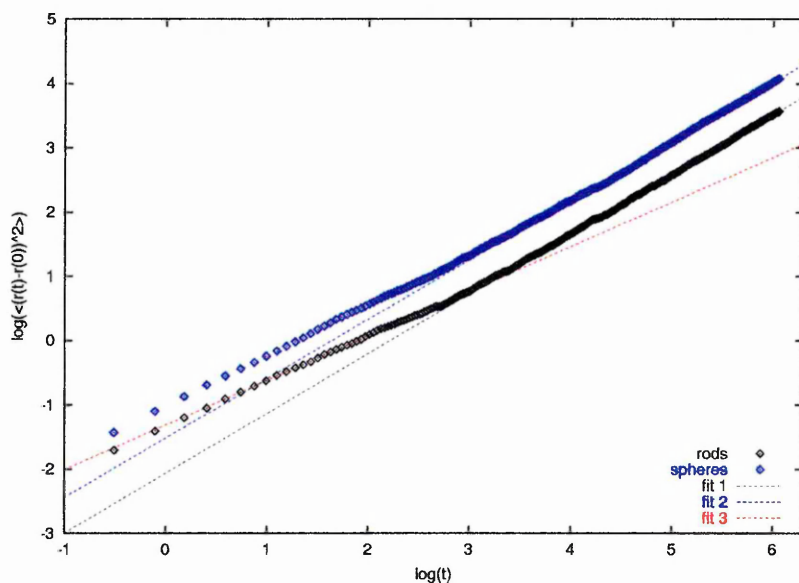
Figure 6.48: Time dependance of the mean square displacement at $\rho = 0.40$ and $T = 1.5$ plotted in the double logarithmic scale.

slopes of both curves in double logarithmic scale are the same and equal to 0.93 ± 0.01. The short time behaviour (for times less then 30,000 time steps and displacements less than $2\sigma_0$) was different and did not match that for long times.

6.5.2 Low Concentration of Spheres

In this Section several mixtures containing 10%, 20%, 30%, and 40% of spheres are studied. The systems were simulated in the constant NVT ensemble using MD method. Some of the results were validated in the constant NPT using MC techniques.

The simulations of a 90/10 mixture were started from a hard particle configuration

of 1844 rods and 204 spheres at density $\rho = 0.30$. The temperature was set to $T = 2.0$ and the system was equilibrated for 7×10^6 time steps. According to the nematic order parameter it remained in an isotropic phase, and the cluster analysis did not reveal a macroscopic phase separation, i.e. about a hundred clusters with the largest one composed of 7 particles were observed. A cooling series with a step of $\Delta T = 0.1$ was performed at a constant density starting from this point. The size distribution of the clusters did not change much with decreasing temperature. At temperatures below $T \approx 1.1$ the spheres formed stable clusters and their distribution did not change with time. Table 6.17 shows the cluster size distribution which was

Size	1	2	3	4	5	6
Number	19	32	13	11	4	3

Table 6.17: Cluster size distribution at $\rho = 0.30$ and $T \leq 1.0$.

established at $T = 1.0$ and remained unchanged at lower temperatures. This static distribution suggests that these clusters of spheres were localised in the rod-rich phase. The sphere-sphere and rod-sphere radial distribution functions calculated at different temperatures are shown in Fig. 6.49. They indicate supramolecular
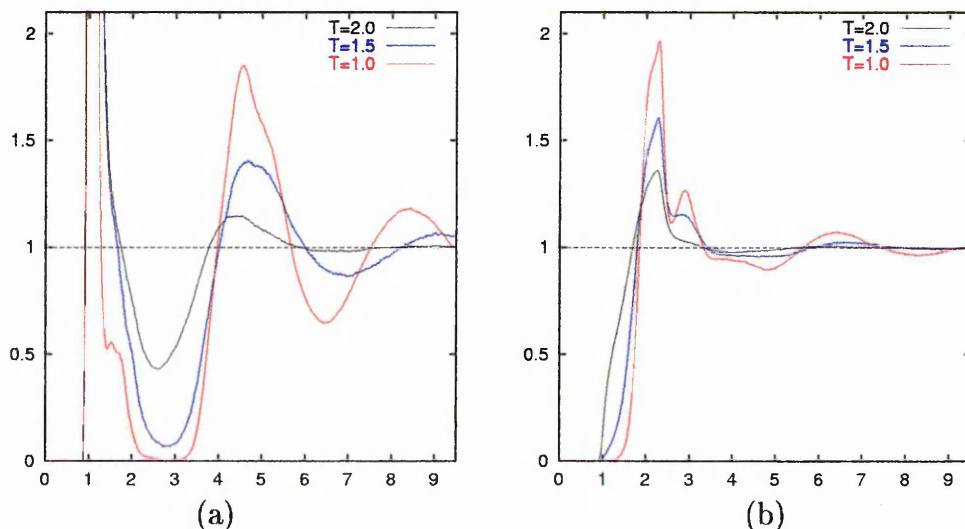
Figure 6.49: (a) Sphere-sphere, $g_{ss}(r)$, and (b) rod-sphere, $g_{rs}(r)$, radial distribution functions measured at $\rho = 0.30$ and different temperatures.

periodicity developed at low temperatures. The fact that there are some prohibited

sphere-sphere separations at around $3\sigma_0$ is consistent with the hypothesis of clusters of spheres forming a stable pattern. The rod-sphere distribution function indicates that the probability of finding a sphere near the rod's side decreases with decreasing temperature, whereas it becomes more likely to find a sphere near the rod's end at low temperatures. Figure 6.50(a) shows a configurational snapshot taken at

(a)   (b)
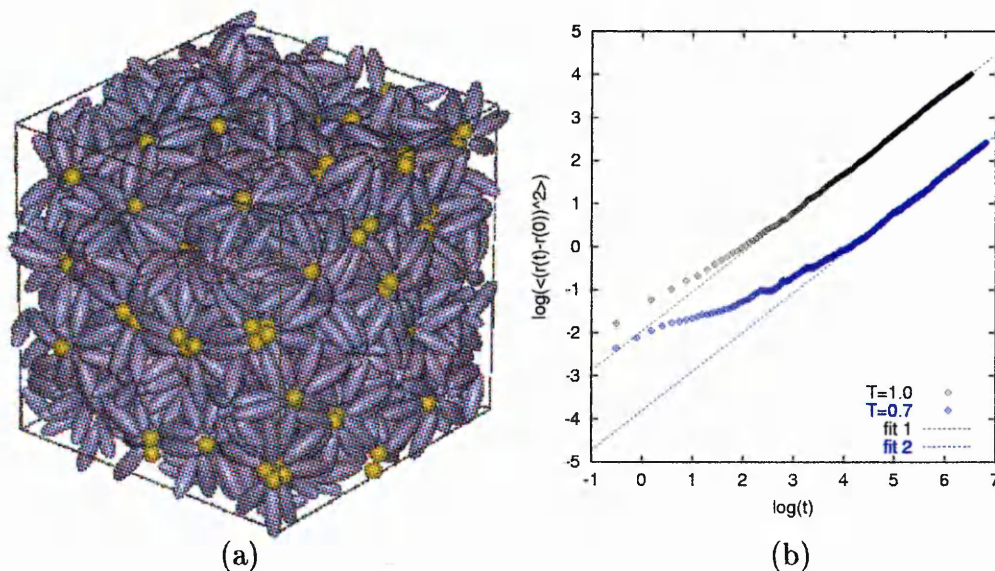
Figure 6.50: (a) Configuration snapshot taken at $\rho = 0.30$ and $T = 0.7$; (b) time dependance of the mean square displacement of rods at $T = 0.7$ and $T = 1.0$.

$\rho = 0.30$ and $T = 0.7$. This shows a periodic structure which resembles the symmetry of the hexagonal close packed (HCP) lattice. The dynamic characteristics of this structure were studied by measuring the mean square displacement of the particles. Figure 6.50(b) shows the rods' displacements measured at temperatures $T = 0.7$ and $T = 1.0$. In the double logarithmic scale, both have tangents with an identical slope of $\nu = 0.93 \pm 0.02$ which coincides with that measured for the 50/50 mixture. The diffusion coefficients at these temperatures were quite different; although at the lower temperature the rods were still clearly diffusing (after 7×10^5 time steps the average displacement was about $3.5\sigma_0$). The sphere displacement was difficult to analyse due to the relatively small number of spheres in the system and very low displacement rate. For example, at $T = 0.7$, the average sphere displacement after 7×10^5 time steps was less than σ_0 and the data were too noisy for a fit to be attempted. Since the cluster distribution did not change with time, however,

this observed sphere displacement was restricted to being within clusters of spheres, whereas rods were able to move around from cluster to cluster.

The system density dependence was studied at constant low, $T = 1.0$, and high, $T = 2.0$, temperatures. Both compression series were performed in the interval of densities $0.30 \leq \rho \leq 0.40$ with a step of $\Delta\rho = 0.01$. Quantities of interest were averaged over 2×10^5 time steps after the system had equilibrated for at least 5×10^5 time steps. The averaged values of the nematic order parameter along with their mean square deviations are shown in Fig. 6.51(a) for both compression sequences. The micellar structure formed at low temperatures proved to be very stable. The
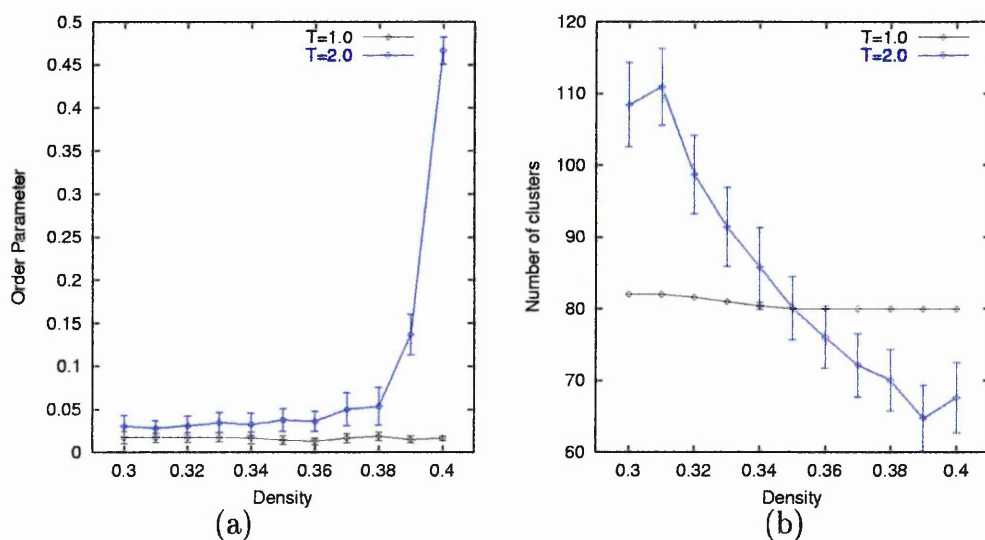
Figure 6.51: (a) Density dependence of the nematic order parameter measured at $T = 1.0$ and $T = 2.0$; (b) cluster distribution during compression series at $T = 1.0$ and $T = 2.0$.

order parameter was always low and the cluster distribution remained unchanged as well (Fig. 6.51(b)). At higher temperature, the excluded volume effect overcame attractive interactions at high densities and the increase in order parameter indicated an isotropic-nematic transition. We did not compress the system further because it was already at a very high density, and particle diffusion was already slow.

So far, we have seen system (iv) exhibiting a cubic-like structure at 50/50 rod-sphere concentration ratio and a micellar crystal phase in a 90/10 mixture. These phases

are typical for amphiphilic systems in which solute molecules have a hydrophilic and hydrophobic ends [103]. The system we study here is quite different from this, however, since the interaction is symmetrical and the spheres cannot be considered as a solvent. Nevertheless, amphiphilic systems are known to form a hexagonal structure in a concentration range between micellar and cubic phase concentrations. In this phase, cylinders of radially aligned prolate molecules form a supramolecular hexagonal periodic structure. To this end, several series of cooling runs were performed at 20%, 30%, and 40% sphere concentrations in search of a similar self-assembling structure. Since both 10% and 50% systems had shown a little density dependence, the cooling series were performed at low densities where particle mobility was higher.

A system of 1638 rods and 410 spheres (20% of spheres) was cooled down at a constant density $\rho = 0.30$. Starting from $T = 2.4$ the temperature was reduced to $T = 1.0$ with a step of $\Delta T = 0.1$. Cluster analysis was carried out and distribution functions were calculated to study the system's structure. It was found that at low temperatures, about $T = 1.0$, a number of relatively stable clusters of spheres formed. Table 6.18 shows the size distribution of these clusters observed at $T = 1.0$.

Size	3	4	5	6	7	8	9	10
Number	5	11	21	21	11	3	1	1

Table 6.18: Cluster size distribution at $\rho = 0.30$ and $T = 1.0$ for an 80/20 mixture.

There were about 74 clusters separated by distances greater than $1.5\sigma_0$, most of them containing 5 or 6 spheres. The sphere-sphere and rod-sphere radial distribution functions, shown in Fig. 6.52, indicate a structure similar to that observed for the 90/10 mixture at low temperatures. It has the same periodicity but this time the cluster size is bigger and the distribution functions capture slightly different sphere distribution within the clusters.

A 70/30 mixture was simulated in the constant NPT ensemble using MC techniques. To study a low temperature and low density configuration, the temperature was set to $T = 1.2$ and pressure to $P = 0.5$. The system was equilibrated for $5 \times$
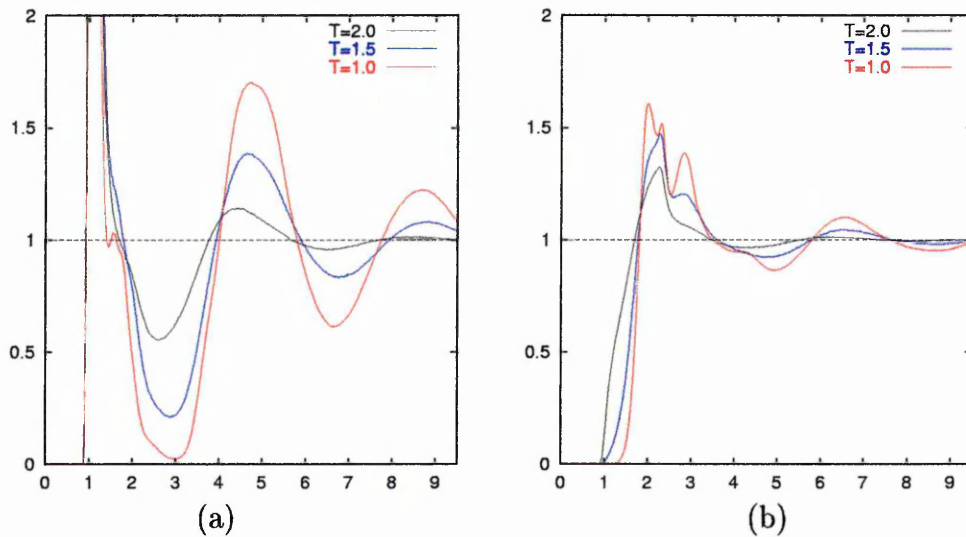
Figure 6.52: (a) Sphere-sphere, $g_{ss}(r)$, and (b) rod-sphere, $g_{rs}(r)$, radial distribution functions measured at $\rho = 0.30$ and different temperatures.

10^5 MC cycles which resulted in an equilibrium number density of $\rho = 0.342 \pm 0.002$. The measured radial distribution functions, shown in Fig. 6.53(a), indicate
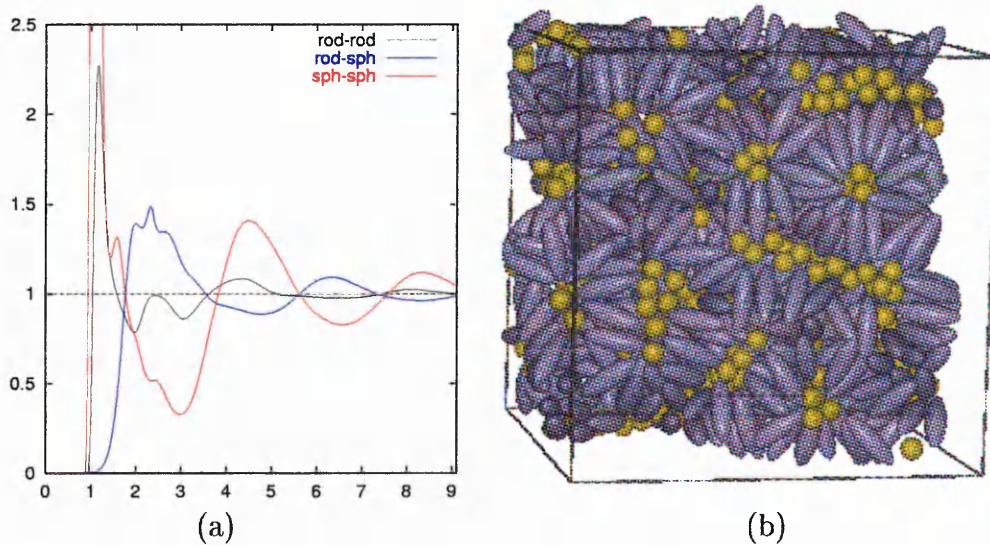
Figure 6.53: (a) Radial distribution functions $g_{rr}(r)$, $g_{rs}(r)$, and $g_{ss}(r)$ measured at $P = 0.5$ and $T = 1.2$; (b) configurational snapshot taken at $P = 0.5$ and $T = 1.2$.

periodicities similar to those seen for 10% and 20% mixtures. Cluster analysis, however, indicated much larger clusters. There were about 15 clusters containing more than 20 spheres. Figure 6.53(b) shows a configurational snapshot taken at

this data point. It illustrates that here the concentration of spheres was too high to accommodate the micellar structure seen at lower sphere concentrations. When 30% of spheres are present in the system, it appears that some of the micelles merge to form large prolate assemblies. These elongated structures appeared to be randomly oriented, however, rather than adopting the high degree of alignment needed for a conventional hexagonal supramolecular structure.

An *NPT* MC simulation of a 60/40 mixture at $T = 1.2$ and $P = 1.0$ did not reveal any hexagonal phase either. The radial distribution functions again indicated some periodicity of order of $5\sigma_0$ but cluster analysis showed that more than 90% of the spheres were members of the same cluster, indicating the structure to be bicontinuous.

6.5.3 Discussion

The end rod-sphere interactions are the dominant interactions in system (iv). The addition of some spheres to the pure Gay-Berne fluid here, therefore, dramatically changes its properties. At temperatures about $T = 1.0$, relatively high for the pure Gay-Berne fluid, mixtures develop highly ordered structures. The isotropic and uniform configuration is now only found at much higher temperatures of order of $T = 3.0$. One consequence of this effective temperature shift is that weak attractive interactions become insignificant. Therefore, all of the novel phases formed mainly due to the strong end rod-sphere attractions. Following this idea, we went on to explore a simpler model which possessed this property. A hard particle mixture with added square well attractive regions was simulated. In this model, a rod had two spherical attractive regions situated near its ends at distance L from its centre (Fig. 6.54). The diameters of the attractive regions were set to σ_0 to ensure that only one sphere could "stick" to each rod's end. The distance L which controlled the size of the active area accessible to the spheres, could be adjusted within the range $\sqrt{5} - 0.5 \leq L \leq \sqrt{5}$. If the centre of a sphere was found within the attractive region then the energy of such a rod-sphere configuration was ϵ_{rs} and zero otherwise.
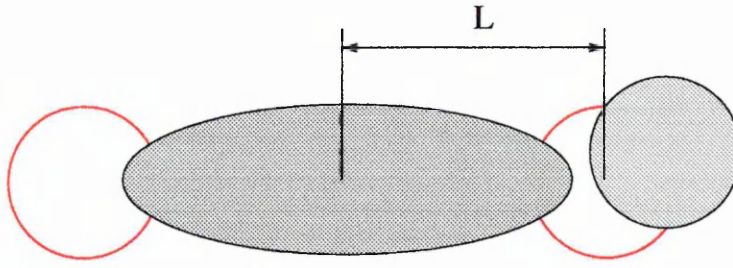
Figure 6.54: Model of hard particles with embedded attractive regions (shown as red circles).

50/50 and 80/20 rod-sphere mixtures interacting via this potential were studied at two values of L, $L_1 = \sqrt{5} - 0.3$ and $L_2 = \sqrt{5}$. The temperature was set to $0.2\epsilon_{rs}$ and remained unchanged for all simulations. Two 50/50 mixtures with different values of L were equilibrated in the constant NVT ensemble at $\rho = 0.40$ for 2×10^6 MC cycles. The equilibrium values of the potential energy were $(-1836 \pm 11)\epsilon_{rs}$ for L_1 and $(-1942 \pm 10)\epsilon_{rs}$ for L_2. These corresponded to the number of rod-sphere configurations, i.e. there were 1024 rods in the system, therefore, the lowest energy possible was $-2048\epsilon_{rs}$. The nematic order parameter measured during both runs was typical for an isotropic phase. Figure 6.55(a) shows the sphere-sphere and rod-
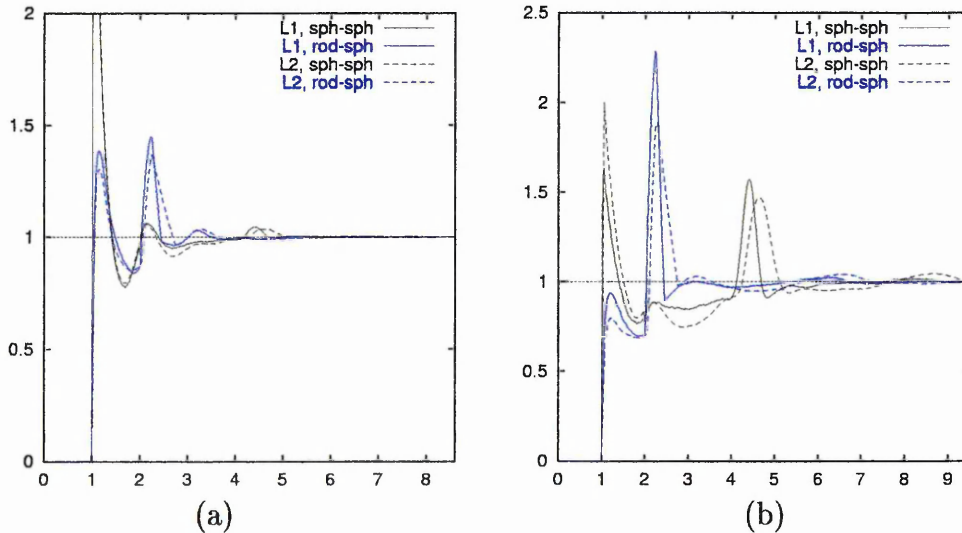
Figure 6.55: (a) Radial distribution functions $g_{rr}(r)$, $g_{rs}(r)$, and $g_{ss}(r)$ measured at $P = 0.5$ and $T = 1.2$; (b) configurational snapshot taken at $P = 0.5$ and $T = 1.2$.

sphere radial distribution functions calculated for both systems. These indicate

neither demixing nor supramolecular periodicity. A weak peak of $g_{ss}(r)$ observed at separations about $4.5\sigma_0$ corresponds to two spheres attached to the ends of the same rod.

Analogous simulations were performed for two 80/20 mixtures with the same values of the parameter L ($L_1 = \sqrt{5} - 0.3$ and $L_2 = \sqrt{5}$). These systems were simulated at $\rho = 0.30$ for 10^6 MC cycles and the nematic order parameter indicated an isotropic phase in both cases. Figure 6.55(b) shows the resultant set of the radial distribution functions. No long range correlations were observed for L_1, whereas a small peak at sphere-sphere separations of about $8.7\sigma_0$ was observed for L_2. This suggests that increasing of the attractive regions is in favour of micellar phase formation. However, the systems simulated failed to exhibit stable pariodic structures. The compression of these systems did not reveal any qualitative structural changes either.

The reason why this simple model did not reproduces the phase behaviour observed for system (iv) might be the saturation of the rod-sphere bonds. In mixtures of type (iv), the number of spheres attracted to the rod's end was limited only by steric repulsions, whereas a single sphere screens the rod's end attraction in the model studied above. When comparing areas under the peaks of the rod-sphere distribution functions (for example, Fig 6.52 and Fig. 6.55(b)) we can conclude that, on average, about two spheres can be found near each rod's end in mixture (iv) and less than one sphere in the model considered above. This indicates that the structures observed in the previous Section were formed due to strong end rod-sphere attractions which had coordination numbers of more than one. The structural periodicity slightly changed with the sphere concentration (and system density as well) and was of order of 4.7σ in the micellar, cubic and all intermediate phases.

Chapter 7

Rod-Sphere Mixtures Subjected to a Field

This Chapter presents our simulation results on bulk rod-sphere mixtures subjected to an external field. Here, as well as the pairwise interactions with its neighbours each rod-like particle will be subject to an additional energy which depends only on its orientation in the global reference frame. The spheres, however, will not be affected by this field. Without loss of generality we will present and discuss our results in terms of an applied magnetic field.

The response of liquid crystal molecules to an external field is the major characteristic utilised in device applications. If a magnetic field is applied, the molecules experience an aligning torque: if the molecules have positive magnetic susceptibility, they tend to align parallel to the field forming an ordered phase under sufficiently strong field; in the case of a negative magnetic susceptibility, the molecules tend to lie in the plane perpendicular to the field and are free to rotate in that plane. Thus, the magnetic field breaks the orientational symmetry of the system by introducing either a preferred direction to align with or a plane to align in. The sense of this response depends only upon the intrinsic properties of the molecules.

An applied field can cause significant changes in the microscopic structure of a liq-

uid crystalline system. The following Sections describe how the structure of the rod-sphere mixtures studied in Chapter 6 can be influenced by such a field. Mixtures of spheres and rods with positive magnetic susceptibility are considered in the next Section. This is followed by an equivalent set of results for negative magnetic susceptibility Section and, finally, a discussion.

7.1   Positive Magnetic Susceptibility

The behaviour of a liquid crystal in an applied magnetic field is determined by the sign of the magnetic susceptibility

$$\chi = \chi_\| - \chi_\perp,$$

where $\chi_\|$ and $\chi_\perp$ are molecular susceptibilities along and normal to the molecular axis. The majority of LCs have positive χ and this scenario is the most often studied. In the presence of static magnetic field $\mathbf{H}$, a molecule gains an extra energy

$$U_H = -\frac{1}{2}\chi H^2 \cos^2 \theta, \tag{7.1}$$

where θ is the angle between $\mathbf{H}$ and the orientational unit vector $\hat{\mathbf{u}}_i$. More negative energy values correspond to larger $\cos\theta$ which are achieved at small angles θ. Therefore, molecules with positive χ tend to align parallel to the field to minimise their energy.

Overall, the forces exerted on a molecule by a magnetic field may influence only its rotation without affecting directly its translational motion. Substituting expression (7.1) into formula (A.6) from Appendix A we obtain the torque acting upon rod i:

$$\tau_H = -\frac{\partial U_H}{\partial(\hat{\mathbf{u}}_i \cdot \mathbf{H})}[\hat{\mathbf{u}}_i \times \mathbf{H}] = \chi H \cos\theta[\hat{\mathbf{u}}_i \times \mathbf{H}]. \tag{7.2}$$

To update orientational coordinates in the computer code we need expressions for $\mathbf{g}_\perp$, which act perpendicular to the molecular axis. If the field is applied in the

145

z-direction, i.e. $\mathbf{H} = (0, 0, H)$, the components of $\mathbf{g}\perp$ are:

$$g_\perp^x = -\chi H^2 u_z^2 u_x$$
$$g_\perp^y = -\chi H^2 u_z^2 u_y$$
$$g_\perp^z = \chi H^2 u_z (1 - u_z^2).$$

The response of nematic LCs to external fields is of great interest for LC applications and also provides information about fundamental dynamic processes [107]. Whether the system has orientational order or not, application of an external field increases the degree of order. For example, field-induced demixing and phase transitions are known to occur [8]. If a magnetic field is applied to an ordered phase it can both change the orientation of the director and increase the degree of order in the system. In the case of a nematic phase, this process involves rotation of the molecules such that they align with the field. In contrast, the magnetic field-induced alignment in smectic phases is qualitatively different. This complex process involves the flow of molecules and is strongly influenced by the nature of the containing surface for the smectic A phase [108]. Within this work, we do not address the dynamics associated with switching the field: only the final equilibrium configuration and its structural properties are of the immediate interest. The following Subsections investigate the effect of a static magnetic field on the rod-sphere mixtures of types (i)-(iv) studied previously in Chapter 6.

7.1.1 System (i)

The first simulations performed using a field were based on a 50/50 mixture of system (i) described in Section 6.2. Without loss of generality, the magnetic susceptibility, χ, was set to 2, making H^2 numerically to be the maximum energy of a rod under an applied field H. The system's response to fields of different strengths was studied for a system of 1024 particles in total at low density, $\rho = 0.40$, and high temperature, $T = 1.7$. At this data point, this system is known to exhibited an isotropic uniform configuration under zero field (Subsection 6.2.1). Fields in the range $0 \leq H \leq 4$ with a step of $\Delta H = 0.5$ were applied and the nematic order

parameter, S, was measured and averaged over 10^5 time steps after the system had equilibrated at each field strength. Figure 7.1(a) shows the resultant dependence
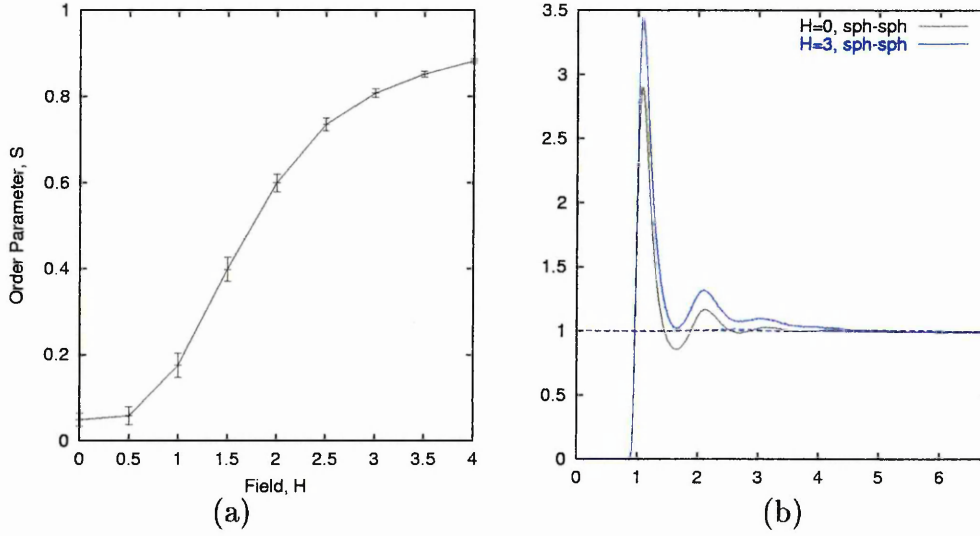
Figure 7.1: (a) Order parameter versus magnetic field at $\rho = 0.40$ and $T = 1.7$; (b) distribution function $g_{ss}(r)$ measured at $\rho = 0.40$ and $T = 1.7$ without and under field ($H = 3.0$).

$S(H)$. The stronger the field the less disorientating effect of the particles' thermal fluctuations and, therefore, the higher the measured order parameter. Note that the average kinetic energy associated with each rod is equal to $\frac{5}{2}T$, whereas each rod's maximum energy in the field is H^2. If these two energies are of the same order, the magnetic field will impose significant alignment upon the rods. In out simulations, this corresponds to fields of about $H = \sqrt{2.5 \times 1.7} \approx 2$ which is in a reasonable agreement with the results shown in Fig. 7.1(a). Unlike the isotropic-nematic transition, the field-induced ordering is continuous and the mean square deviations of S at given H are small when compared to the order parameter fluctuations near the transition point (see Fig. 5.3 for example). Figure 7.1(b) shows the sphere-sphere radial distribution function calculated both without a field and under relatively strong field $H = 3.0$. These indicate some very weak signs of demixing under the applied field. Despite the high order parameter observed in this run, the parallel distribution function did not indicate any smectic layering, i.e. only orientational long range order is present in the system.

Rather, a field $H = 2.0$ was applied to a 50/50 mixture previously equilibrated at high density $\rho = 0.50$ and high temperature $T = 1.7$. Without the field, the system was isotropic and uniform at this data point, whereas at lower temperatures it demixed and phase separated forming a cylinder of spheres embedded in a smectic phase (Subsection 6.2.1). Applying the field resulted in the formation of a similar structure, i.e. the spheres formed a cylinder while the rods ordered into an LC phase with a high value of the order parameter $S = 0.798 \pm 0.010$. Figure 7.2(a) shows
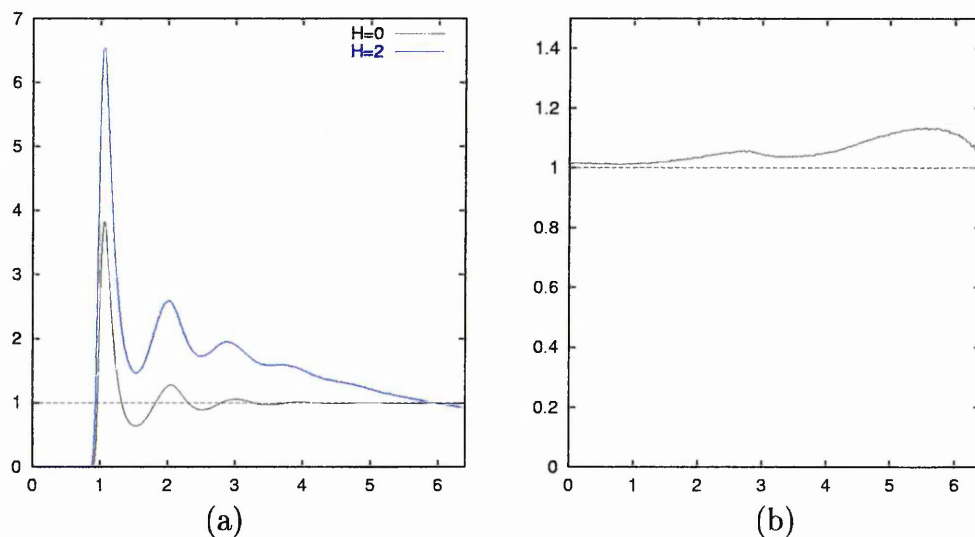
Figure 7.2: (a) Sphere-sphere radial distribution functions, $g_{ss}(r)$, calculated at $\rho = 0.50$ and $T = 1.7$ without magnetic field and under $H = 2$; (b) $g_{\parallel}(r_{\parallel})$ at this data point under field $H = 2.0$.

the sphere-sphere radial distribution functions illustrating that demixing occurred in the system under an applied field. $g_{\parallel}(r_{\parallel})$, shown in Fig. 7.2(b), does not indicate smectic layers, however. This leads to the conclusion that the temperature of $T = 1.7$ would appear to have been too high for the Gay-Berne particles to develop a smectic phase at this density. The low temperature behaviour of this 50/50 mixture was not studied because, once demixed, the system had already attained axial symmetry. Even in the isotropic phase, a cylinder of spheres was found which imposed this type of symmetry. Applying a field would only increase the degree of order along this cylinder axis.

A field was applied to a 90/10 mixture at $\rho = 0.31$ and $T = 0.7$. Without the field,

at this data point, the mixture was isotropic and homogeneous (Subsection 6.2.2). Since the temperature was relatively low, a moderate field of $H = 1.0$ was set. After equilibration for 1.5×10^6 MD time steps the order parameter was found to be $S = 0.86 \pm 0.01$ and the parallel distribution function, shown in Fig. 7.3(a), indicated

(a)   (b)
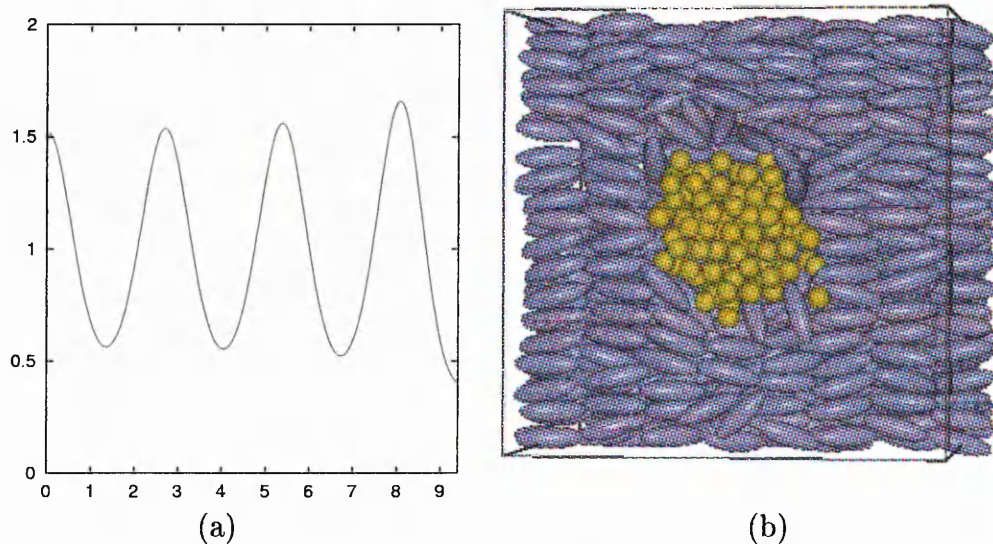
Figure 7.3: (a) Parallel distribution function, $g_{\parallel}(r_{\parallel})$, measured at $\rho = 0.31$, $T = 0.7$ under field $H = 1.0$; (b) configuration snapshot taken at this data point.

smectic layers. The calculated sphere-sphere radial distribution function was typical for macrophase separated systems. Therefore, applying the field in this data point caused both isotropic-smectic and demixing transitions. Figure 7.3(b) illustrates the final configuration of this run. The direction of applied field, in this figure and all the following figures in this Section, is horizontal.

7.1.2 System (ii)

In this Subsection, assuming positive magnetic susceptibility of the Gay-Berne particles, we study mixtures of type (ii), previously described in Section 6.3, under a magnetic field. Here we concentrate on the high temperature system behaviour. Low temperature behaviour is studied only at low sphere concentration because of the strong influence of the periodic boundary conditions observed for demixed configurations of 50/50 mixtures (see Section 6.3).

A 50/50 mixture was studied in the constant NVT ensemble under applied field $H = 2.0$ at high temperature $T = 1.7$ using MD. Two runs were performed starting from isotropic uniform configurations at $\rho = 0.40$ and $\rho = 0.50$. After equilibration for 7×10^5 MD time steps, the sets of distribution functions were computed. The lower density configuration exhibited behaviour very similar to that observed in system (i) under the same conditions, i.e. very weak signs of demixing were seen. Similarly rods were aligned by the magnetic field although no smectic layering was observed. The resulting $g_{ss}(r)$ and $g_{\parallel}(r_{\parallel})$ distribution functions for the higher density run at $\rho = 0.50$ are shown in Fig. 7.4(a). These indicate macroscopic phase separation

(a)   (b)

Figure 7.4: (a) Sphere-sphere, $g_{ss}(r)$, and parallel, $g_{\parallel}(r_{\parallel})$, distribution functions measured at $\rho = 0.50$, $T = 1.7$ under field $H = 2.0$; (b) configuration snapshot taken at this data point.

and no smectic layers in the system. This behaviour is similar to that observed in system (i) under the same external conditions. However, the snapshot shown in Fig. 7.4(b) illustrates that the cylindrical droplet of spheres formed perpendicular to the director. The tensor of inertia of this droplet was measured and the eigenvector corresponding to its largest eigenvalue was found to be nearly perpendicular to the director at all times. Clearly the formation of the cylinder was due to the periodic boundary effect. In a macroscopic system corresponding to 50/50 mixture of type (i) or (ii), macroscopic phase separation would occur and the rod-sphere potential

would affect the rods' anchoring on the phase interface. The field-induced change in the orientation of the cylinders of sphere is not, therefore, a significant observation.

Subsequently, a 90/10 mixture was simulated at $\rho = 0.31$ and $T = 1.0$ under fields $H = 1.0$ and $H = 2.0$. After an equilibration run of 7×10^5 MD time steps at $H = 1.0$, the nematic order parameter was found to be of 0.638 ± 0.018. The sphere-sphere radial distribution function, shown in Fig. 7.5(a), indicates uniform
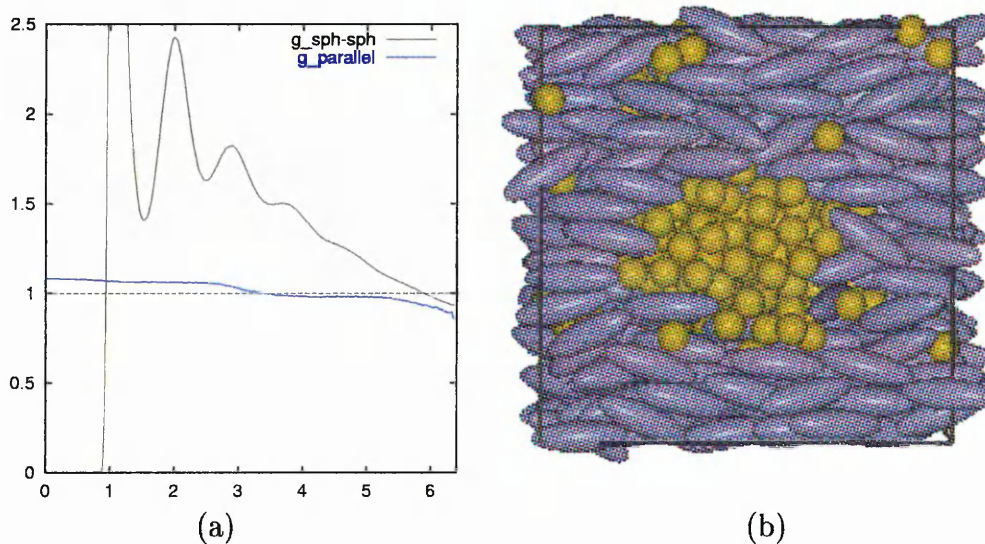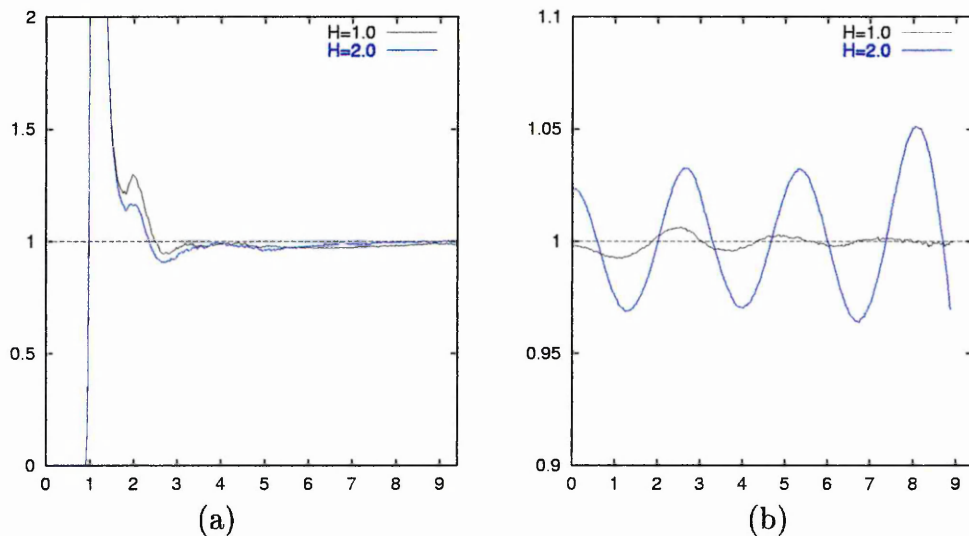

Figure 7.5: (a) Sphere-sphere, $g_{ss}(r)$, and (b) parallel, $g_{\parallel}(r_{\parallel})$, distribution functions measured at $\rho = 0.31$, $T = 1.0$ under fields $H = 1.0$ and $H = 2.0$.

distribution of the spheres in the system. In a subsequent run, at $H = 2.0$, the resultant order parameter was 0.840 ± 0.007, and the distribution functions continued to indicate a homogeneous sphere distribution. Figure 7.5(b) shows that, under the higher field, some weak (note the scale along the y-axis) positional correlations of the rods' arrangement were observed. Unlike for a 90/10 mixture of type (i) at $T = 0.7$, temperature $T = 1.0$ appeared to be too high to allow development of a stable smectic phase at this density.

A droplet of spheres suspended in the rod-rich phase was studied, therefore, at low temperatures below the demixing point. A 90/10 mixture was subjected to a constant magnetic field of $H = 2.0$ under isochoric-isothermal conditions at temperature $T = 0.7$ and pressure $P = 1.0$. After equilibration for 2×10^5 MC cycles, the system

was found to be in a smectic phase. The order parameter was 0.938 ± 0.007 and the director was parallel to the field. Configuration snapshots indicated that a disk-like droplet of spheres was encapsulated within one smectic layer. The measurements of the inertia tensor gave the following values of its components: $I_1 = 1240$, $I_2 = 700$, and $I_3 = 96$ in units of $m\sigma_0^2$. The eigenvector corresponding to I_3 was parallel to the applied field.

7.1.3 System (iii)

The mixture described in Section 6.4 exhibits very weak demixing properties over a wide range of densities and temperatures. Only at relatively high sphere concentrations was the development of smectic layers affected by the spheres, resulting in microphase separated bicontinuous structures. Applying a field to a 50/50 mixture of type (iii) might be expected to both change this low temperature structure and lead to some order if it is applied at higher temperatures and densities. In this Subsection, the effect of a field on a 50/50 mixture is studied using both MD and MC techniques.

A system of 1024 particles in total at 50/50 rod-sphere concentration ratio was simulated in the constant NVT ensemble at densities $\rho = 0.40$ and $\rho = 0.50$ at a relatively high temperature of $T = 1.2$. The system's behaviour was studied at fields $H = 1.0$ and $H = 2.0$. After equilibration for 7×10^5 MD times steps, the configurations were further equilibrated under isobaric-isothermal conditions for 2×10^5 MC cycles. Each cycle included 1024 random displacement moves and one asymmetrical volume rearrangement. All three dimensions of the simulation box were allowed to fluctuate independently so as to reduce the effect of the periodic boundary conditions. The constant pressure chosen for the lower density runs was $P = 2.43$, $P = 7.40$ being used for the higher density ones. These were the pressures calculated at $T = 1.2$ in the constant NVT ensemble for zero field at densities $\rho = 0.40$ and $\rho = 0.50$ respectively. There was a small field dependence on the pressure in the constant NVT ensemble and, consequently, the equilibrium density

varied slightly with field strength in the constant NPT ensemble. Table 7.1 shows

Pressure	Field	Density	Order parameter
2.43	1.0	0.401 ± 0.010	0.292 ± 0.035
2.43	2.0	0.408 ± 0.012	0.720 ± 0.014
7.40	1.0	0.498 ± 0.008	0.559 ± 0.021
7.40	2.0	0.507 ± 0.008	0.827 ± 0.008

Table 7.1: The equilibrium density and nematic order parameter in various constant NPT runs at $T = 1.2$.

average values of the equilibrium densities and nematic order parameters in the performed MC runs. These indicate that the same field induces higher order at higher densities. The distribution functions, however, do not indicate any significant changes in the systems' structure. Figure 7.6 shows $g_{ss}(r)$ and $g_{\parallel}(r_{\parallel})$ distribution

Figure 7.6: (a) Sphere-sphere, $g_{ss}(r)$, and (b) parallel, $g_{\parallel}(r_{\parallel})$, distribution functions measured at $P = 7.40$, $T = 1.2$ under fields $H = 1.0$ and $H = 2.0$.

functions calculated at the higher densities under fields $H = 1.0$ and $H = 2.0$. These indicate that the spheres were uniformly distributed in the simulation boxes and that the rods did not form a convincing smectic. The effect of the applied field was even weaker at lower densities.

The low temperature behaviour of this 50/50 mixture under an applied field was studied at temperatures $T = 0.7$ and $T = 0.6$. A field of $H = 1.0$ was applied to the

configuration previously equilibrated at $\rho = 0.40$ and $T = 0.7$ in the constant NVT ensemble. After 7×10^5 MD steps, the system was further equilibrated for 6×10^5 MC cycles under constant pressure $P = 0.6$. The nematic order parameter was found to be 0.567 ± 0.018, although the pair distribution functions did not indicate any significant changes in the system's structure. In a subsequent MC run at $H = 2.0$, the nematic order parameter rose to 0.867 ± 0.007 and the structural properties of the mixture changed. Figure 7.7 shows the $g_{ss}(r)$ and $g_{\parallel}(r_{\parallel})$ distribution functions for
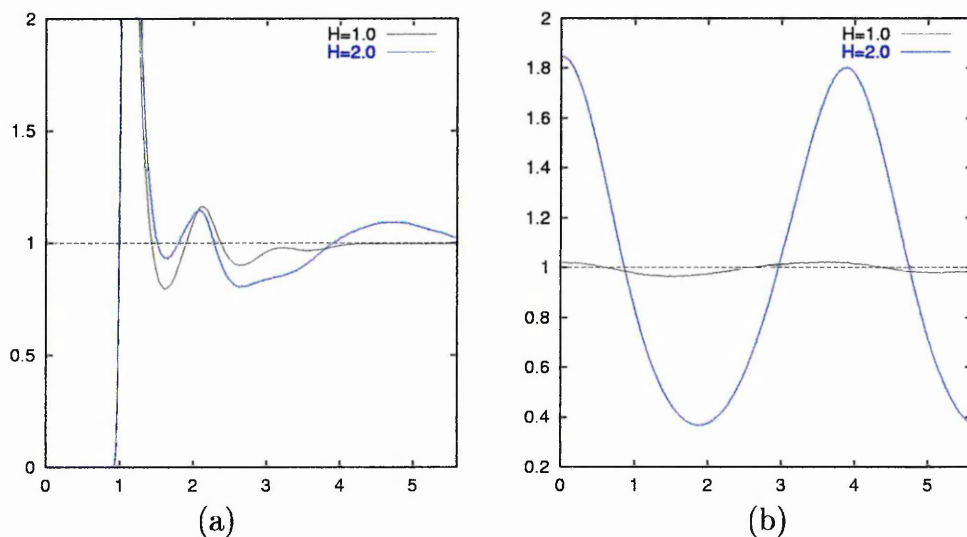
Figure 7.7: (a) Sphere-sphere, $g_{ss}(r)$, and (b) parallel, $g_{\parallel}(r_{\parallel})$, distribution functions measured at $P = 0.60$, $T = 0.7$ under fields $H = 1.0$ and $H = 2.0$.

both the $H = 1.0$ and $H = 2.0$ runs. They indicate that a stable lamellar structure developed under the stronger field, whereas the more moderate field influenced only the rods' orientations leaving their translational correlations unaffected. Similar results were obtained for this same mixture at the lower temperature of $T = 0.6$. Here, the mixture was simulated using constant NPT MC method at $P = 0.6$ and $T = 0.6$ under a field of $H = 1.0$. This time the $H = 1.0$ field proved sufficiently strong to cause development of a lamellar structure. Figure 7.8 shows the corresponding set of distribution functions and the final configuration from this MC run.

Equivalent behaviour was then found in a high density, low temperature system. A 50/50 mixture at $\rho = 0.50$ and $T = 0.7$ was simulated under a field of $H = 1.0$ for 7×10^5 MD time steps. Then it was equilibrated further at a constant pressure of
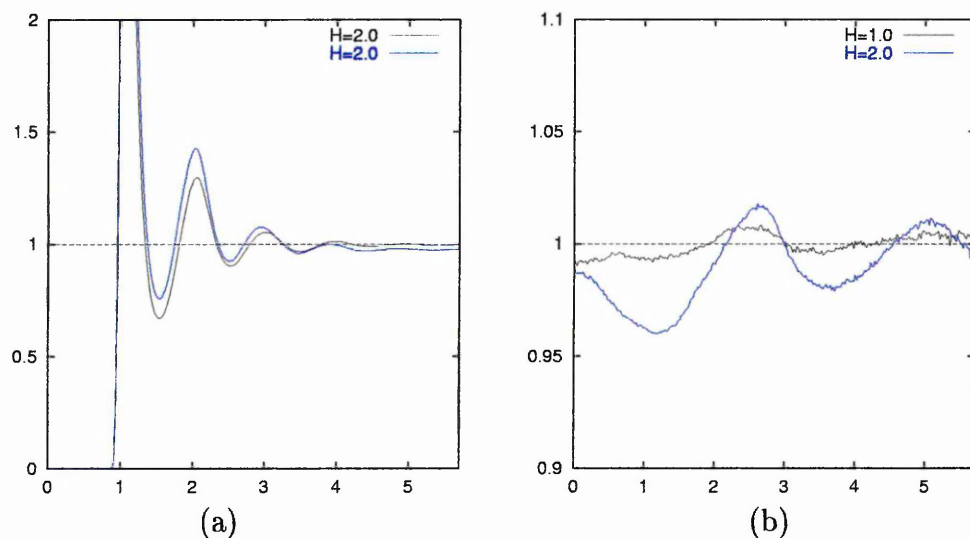
Figure 7.8: (a) Sphere-sphere, $g_{ss}(r)$, and parallel, $g_{\|}(r_{\|})$, distribution functions measured at $P = 0.6$, $T = 0.6$ under $H = 1.0$. (b) configuration snapshot taken at this data point.

$P = 4.00$ for 10^6 MC cycles. Eventually a lamellar structure, similar to that seen at lower densities, developed.

The response of system (ii) to an applied magnetic field may be summarised as follows. With or without an applied field, a 50/50 mixture of type (iii) exhibits very little density dependence. If a field is applied at high temperatures, the rod's orientation changes and a paranematic phase is formed with spheres homogeneously distributed within it. As the temperature is decreased, the rod-rod side interactions promote stable layers provided the rods are aligned by a sufficiently strong field. Thus, a lamellar phase forms in which layers of rods are separated by layers of spheres. At even lower temperatures, the system develops a bicontinuous structure at zero field. If a strong field is applied, this structure orders into a lamellar configuration.

7.1.4 System (iv)

This Subsection presents simulation results obtained when system (iv) was subjected to a constant magnetic field. It was shown in Section 6.5 that this type of mixture exhibits long range positional ordering at low temperatures. A cubic phase was observed at a 50/50 rod-sphere concentration ratio (Subsection 6.5.1) and a micellar crystal phase with hexagonal symmetry developed at lower sphere concentrations. 50/50 and 80/20 mixtures are studied in this Subsection using the constant NPT MC method.

A 50/50 mixture of type (iv) under an applied field of $H = 2.0$ was simulated in the constant NPT ensemble at $T = 1.5$ for 3×10^5 MC cycles. The pressure was chosen to be $P = 0.3$ to yield a low density simulations with high particle mobility. Under these conditions, the system formed a lamellar structure similar to that shown in Fig. 7.8. Figure 7.9(a) shows a set of distribution functions indicating microphase
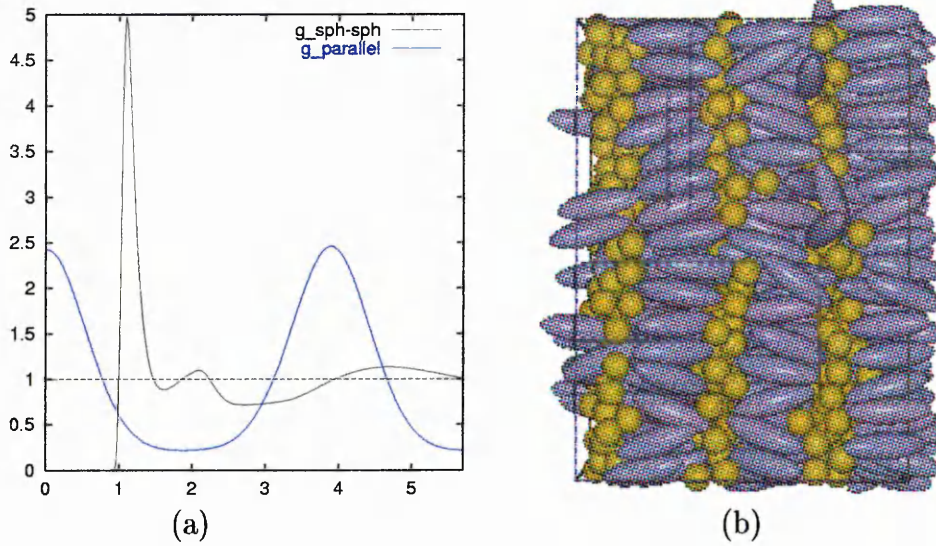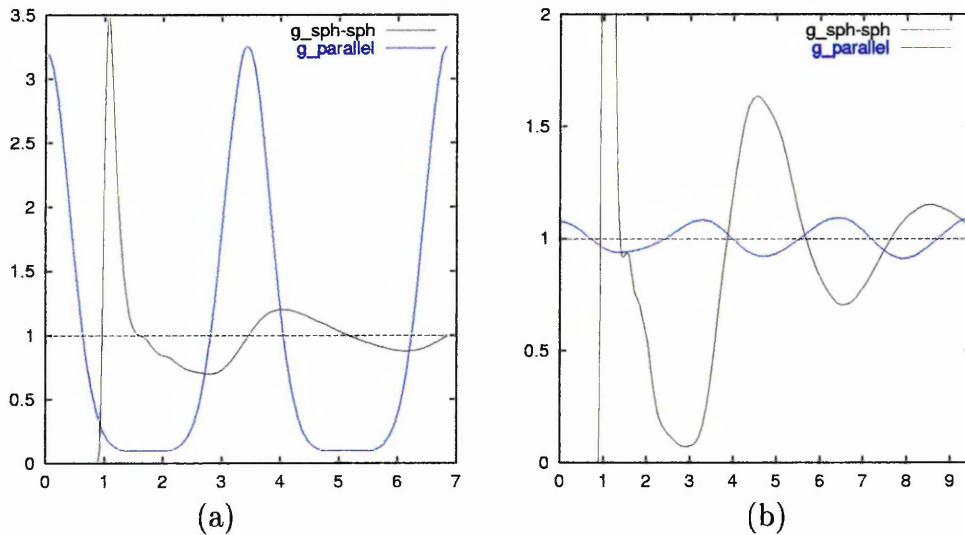

Figure 7.9: Sphere-sphere, $g_{ss}(r)$, and parallel, $g_{\parallel}(r_{\parallel})$, distribution functions measured under field $H = 2.0$ at $P = 0.3$: (a) 50/50 mixture at $T = 1.5$ (b) 80/20 mixture at $T = 1.0$.

separation in the system. Here the layers of rods are separated by a distance of about $3.44\sigma_0$ and the interlayer space is filled with spheres.

An 80/20 mixture was simulated at $T = 1.0$ and $P = 0.3$ under a field of $H = 2.0$.

Its distribution functions, measured after 3×10^5 MC cycles of equilibration run, are shown in Fig. 7.9(b). The periodicity of the hexagonal close packing observed without the field (see Fig. 6.52) is preserved at $H = 2.0$ according to $g_{ss}(r)$. The $g_{\|}(r_{\|})$ curve indicates a weak correlation in the rods' arrangement, due to the positional correlation of rods in the HCP-structure which are now aligned by the field. Cluster analysis was performed and its results are presented in Tab. 7.2. They show

Size	3	4	5	6	7	8	9	11	12
Number	6	15	21	17	8	2	2	1	2

Table 7.2: Cluster size distribution at $P = 0.30$ and $T = 1.0$ under $H = 2.0$.

that the cluster size distribution was very similar to that observed at zero field in Subsection 6.5.2. This indicates that a field of $H = 2.0$ was too weak to change the topology of the system's structure. Therefore, a stronger field of $H = 3.0$ was applied to the 80/20 mixture under the same conditions ($T = 1.0$, $P = 0.3$). Starting from the final configuration of the previous run, 10^6 MC cycles were performed. Figure 7.10(a) shows the resulting distribution functions $g_{ss}(r)$ and $g_{\|}(r_{\|})$. They indicate a novel structure which has not been observed in our simulations this far. According to $g_{\|}(r_{\|})$, the rods formed layers separated by a distance of about $3.15\sigma_0$. The distinctive shape of the peaks in $g_{\|}(r_{\|})$ suggests that these layers also had some internal structure. $g_{ss}(r)$ indicates that the system was still microphase separated but that it was no longer in the HCP-structure observed at zero field. Figure 7.10(a) shows a configuration snapshot taken in the end of the MC run. It illustrates that, under this strong field, spheres formed threads perpendicular to the field which, in turn, were arranged in a hexagonal array. Cluster analysis indicated 14 large clusters ranging from 17 to 48 spheres. This cluster size distribution was completely different from that observed under the weaker field (Tab. 7.2). Therefore, under sufficiently strong field, it appears that rearrangement of the rods caused the clusters of spheres to unite and form narrow channels which were aligned perpendicular to the field in a distorted hexagonal array.
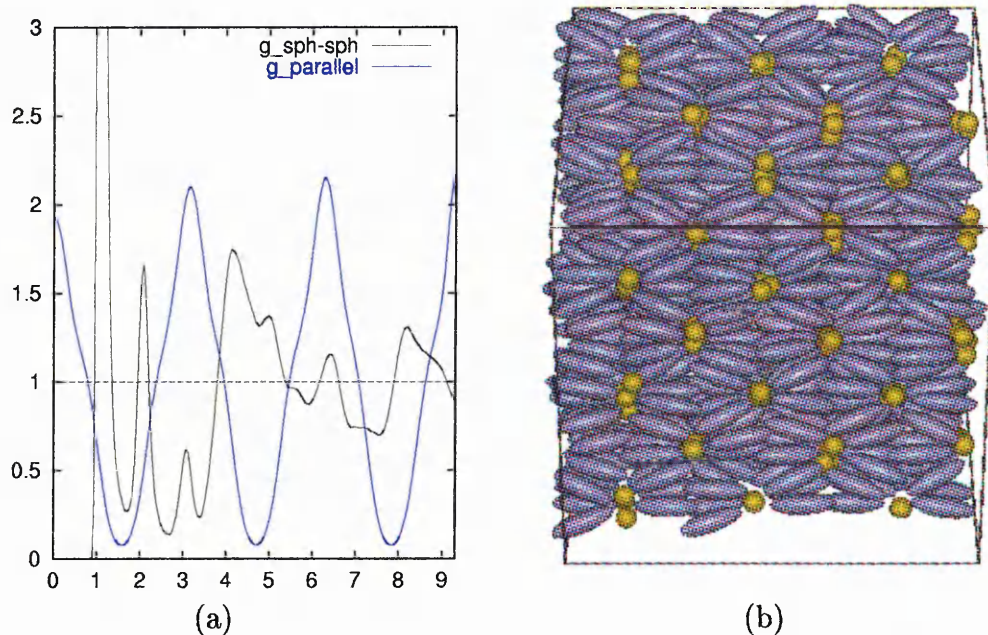
Figure 7.10: (a) Sphere-sphere, $g_{ss}(r)$, and parallel, $g_{\|}(r_{\|})$, distribution functions measured at $T = 1.0$ and $P = 0.3$ under field $H = 3.0$; (b) configuration snapshot taken at this data point.

7.2 Negative Magnetic Susceptibility

In this Section, mixtures (i)-(iv) are studied under a static magnetic field for the case of negative magnetic susceptibility of the Gay-Berne particles. As was mentioned in the beginning of this Chapter, LCs with negative magnetic susceptibility tend to align perpendicular to the applied field. Rotation within the plane of preferred alignment is not affected by the field, however, so that the reduction in the rods' rotational entropy is not so great as it was in the case of positive susceptibility. As a result, field-induced effects are generally weaker.

7.2.1 System (i)

In this Subsection, mixtures of type (i) are studied in the presence of a field but now the magnetic susceptibility of the Gay-Berne particles is treated to be negative ($\chi = -2.0$). As in Subsection 7.1.1, a 50/50 mixture was studied first at high tem-

perature $T = 1.7$ and at both low, $\rho = 0.40$, and high, $\rho = 0.50$, densities. For the former, an isotropic and homogeneous configuration, previously equilibrated at zero field at $\rho = 0.40$ and $T = 1.7$, was subjected to fields ranging between $0 \leq H \leq 4.0$ with a step of $\Delta H = 0.5$. The average values of the potential energy per particle and the nematic order parameter obtained for the even runs of this sequence are shown in Tab. 7.3. Unlike the case of the positive magnetic susceptibility material, the poten-

Field	Energy	Order parameter
0.0	-2.343 ± 0.051	0.051 ± 0.018
1.0	-2.220 ± 0.051	0.091 ± 0.021
2.0	-2.101 ± 0.050	0.193 ± 0.025
3.0	-2.069 ± 0.052	0.247 ± 0.025
4.0	-2.059 ± 0.055	0.280 ± 0.034

Table 7.3: Potential energy per particle and nematic order parameter measured at $\rho = 0.40$ and $T = 1.7$ under various fields.

tial energy did not change significantly when the field was applied. Here, a positive energy penalty was associated with rods which were not aligned perpendicular to the field. As a result, the potential energy increased with increasing field. The nematic order parameter did not describe the structure adequately because there was no preferred axis for the rods to align along. The radial distribution functions measured under various fields did not indicate any signs of demixing. Figure 7.11(a) shows $g_{ss}(r)$ measured under both a relatively strong field $H = 3.0$ and zero field.

For 50/50 mixture of system (i) the effect of the applied field at high density, $\rho = 0.50$, was more significant. Here, the system was subjected to a magnetic field of $H = 2.0$ at $\rho = 0.50$ and $T = 1.7$ and was equilibrated for 1.4×10^6 MD time steps. The run-time energy evolution indicated that the system underwent some changes during this run. Figure 7.11(b) shows sphere-sphere radial distribution functions which indicate that demixing took place in the system. Configuration snapshots taken at this data point showed a cylindrical droplet of spheres with indistinct boundaries which was surrounded by rods aligned perpendicular to the field ($S = 0.58 \pm 0.03$). This was confirmed by the anisotropy of the droplet's inertia tensor (the anisotropy parameter (Subsection 6.2.1) was found to be of 2.05 ± 0.08).
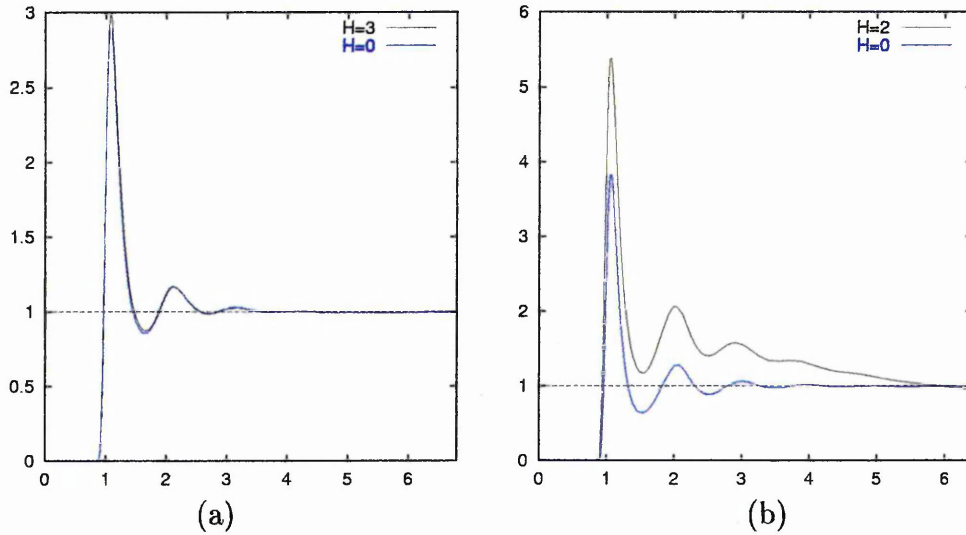
Figure 7.11: Sphere-sphere radial distribution function, $g_{ss}(r)$, calculated at $T = 1.7$ at (a) $\rho = 0.40$ and (b) $\rho = 0.50$ with and without applied field.

The eigenvector corresponding to its largest eigenvalue was found to be aligned along the x-direction, i.e. was perpendicular to the field. Cluster analysis was performed to confirm that most of the spheres (more than 90%) were members of the largest cluster.

Subsequently, a field $H = 2.0$ was applied to a 90/10 mixture of type (i) at $T = 0.7$ to study its low temperature behaviour. An isotropic homogeneous configuration, previously equilibrated at $\rho = 0.31$ using MD, was used to start a constant NPT MC run. The pressure was set to $P = 1.8$, which was the equilibrium pressure measured in the MD run with zero applied field. After 2×10^6 MC cycles, the system equilibrated at a density of about 0.34 and a high value of the order parameter, $S = 0.65 \pm 0.03$, indicating an LC phase. The distribution functions, shown in Fig. 7.12(a), indicated both demixing and layering in the system. These are typical for the case of a droplet of spheres embedded in a smectic phase. This is confirmed by Fig. 7.12(b), a configuration snapshot taken at the end of the MC run, which shows several droplets of spheres encapsulated in a smectic phase.
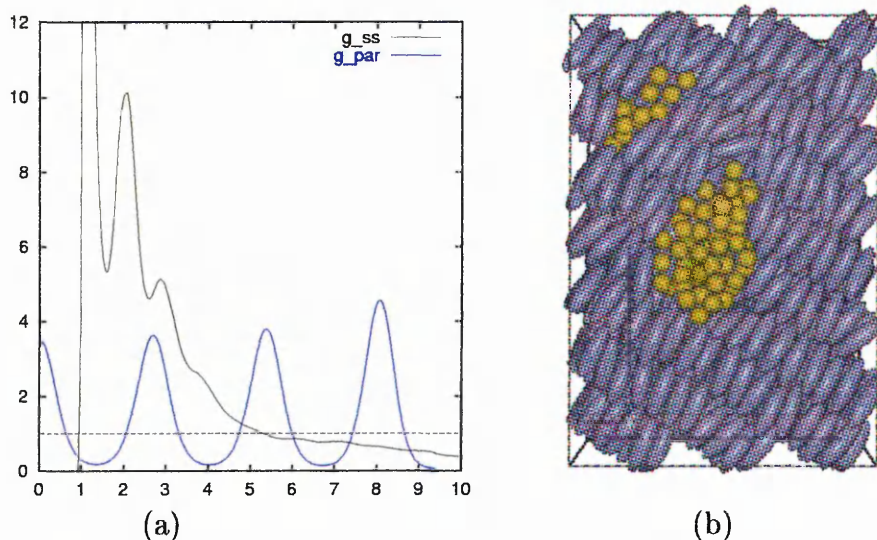
Figure 7.12: (a) Sphere-sphere, $g_{ss}(r)$, and parallel, $g_{\parallel}(r_{\parallel})$, distribution functions measured for 90/10 mixture of system (i) at $T = 0.7$ and $P = 1.8$ under field $H = 2.0$; (b) configuration snapshot taken at this data point, field into the page.

7.2.2 System (ii)

According to the results of the previous Subsection, the application of a magnetic field to system (i) did not reveal any qualitatively new behaviour when compared to the analogous results of Section 7.1. From our previous study (Section 6.3), system (ii) is known to have stronger tendency to demix than system (i) under equivalent conditions. This means that it can be found in a uniform mixed state only at high temperatures. However, at such high temperatures the difference between mixtures (i) and (ii) becomes irrelevant . This suggests, that applying a field to an isotropic homogeneous mixture of type (ii) is unlikely to cause any changes at low densities but may cause macroscopic demixing at high densities. Therefore, for this system only a phase separated 90/10 mixture was simulated at low temperature to investigate the effect of applied field on the shape of the droplet of spheres. Analogous to Subsection 7.1.2, the system was studied in the constant NPT ensemble at $T = 0.7$ and $P = 1.0$ under a field $H = 2.0$. After 3×10^5 MC sweeps, the nematic order parameter was found to be 0.663 ± 0.018. The parallel distribution function was calculated to investigate the presence of layers in the system. Figure 7.13(a) illustrates that while stable smectic layers were not present, $g_{\parallel}(r_{\parallel})$ showed some
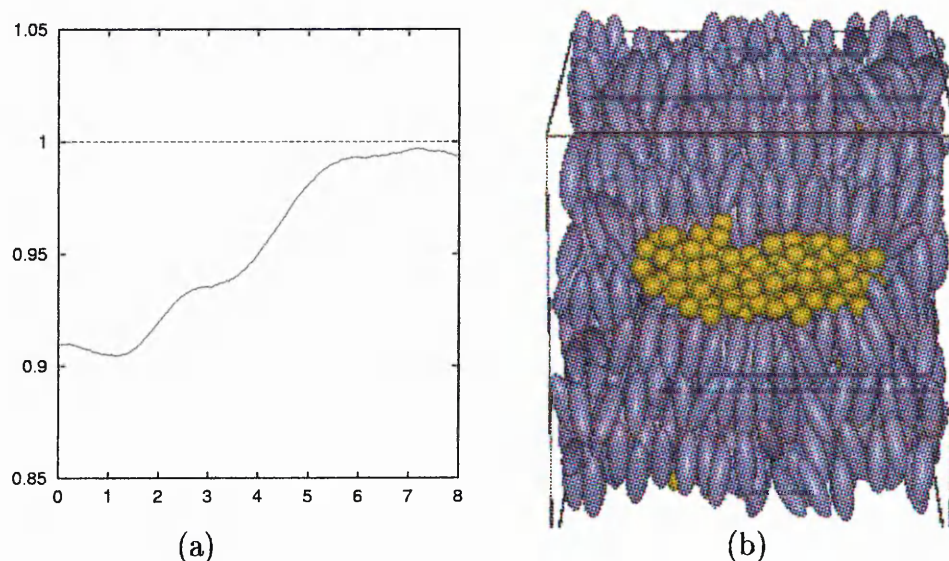
Figure 7.13: (a) The parallel distribution function, $g_{\parallel}(r_{\parallel})$, distribution functions measured at $T = 0.7$ and $P = 1.8$ under field $H = 2.0$; (b) configuration snapshot taken at this data point, field is horizontal.

correlations not typical for a nematic phase. Figure 7.13(b) shows a configuration snapshot taken at the end of this MC run. It illustrates a droplet of spheres, almost cylindrical in shape, elongated along the field. The tensor of inertia of this droplet was measured and a time average of the ratio of the largest of its component to the semi-sum of the other two was found to be of 6.46 ± 0.17.

The responses to an applied field on the 90/10 mixtures studied in this Subsection and in Subsection 7.1.2 were found to be quite different under the same external conditions. In both cases the shape of the droplet suspended in the isotropic rod-rich phase changed when the field $H = 2.0$ was applied. If the rods had positive magnetic susceptibility a filed-induced isotropic-smectic transition was observed and the droplet of spheres became flattened along the field. In case of the negative magnetic susceptibility, the droplet became highly elongated along the field direction, but no smectic phase was observed.

162

7.2.3 System (iii)

This Subsection presents simulation results for system (iii) subjected to a constant magnetic field. Only low temperature low density behaviour was studied here for two reasons. Firstly, mixtures of this type demonstrate weak density dependence, but low densities are more attractive for simulation purposes as equilibration is established quicker. Secondly, no unusual behaviour was shown by this this system at high temperatures (Subsection 7.1.3). Therefore, there is no expectation that any novel phase formation will be seen in the case of a negative magnetic susceptibility.

A 50/50 mixture of type (iii) was simulated under constant NPT conditions at $T = 0.6$ and $P = 0.6$ under a field of $H = 2.0$. As usual, the asymmetrical volume rearrangement move was employed to reduce the influence of the periodic boundary conditions. After equilibration for 10^6 MC cycles, the system developed a microphase separated structure similar to that observed in Subsection 6.4.1. Figure 7.14(a) shows the calculated $g_{rr}(r)$ and $g_{ss}(r)$ distribution functions. $g_{ss}(r)$ increases at
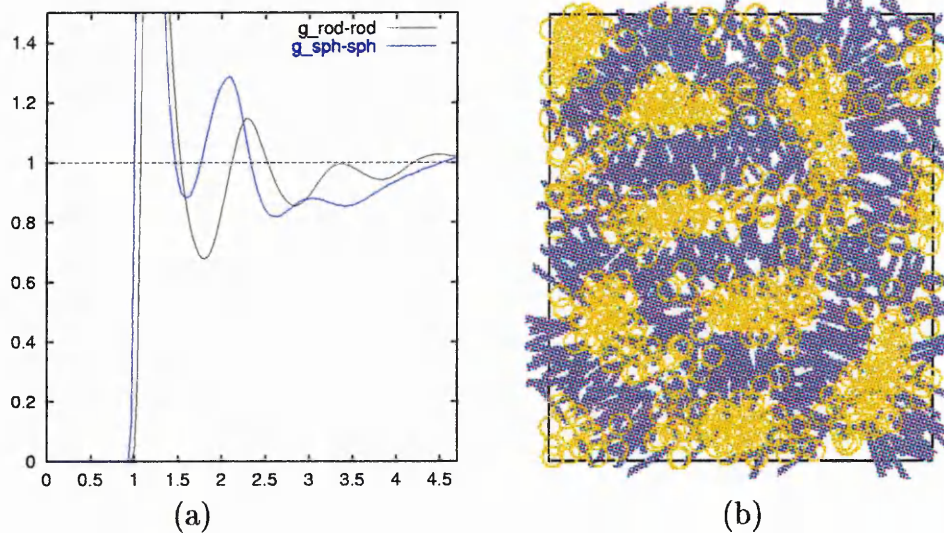

Figure 7.14: (a) Rod-rod, $g_{rr}(r)$, and sphere-sphere, $g_{ss}(r)$, radial distribution functions calculated at $T = 0.6$ and $P = 0.6$ under field $H = 2.0$; (b) configuration snapshot taken at this data point.

separations greater than $4\sigma_0$, which suggests that some periodicity is present in the system. Unfortunately, the standard method of calculating the distribution functions

fails at separations larger than half of the shortest simulation box side, which, in this run, was found to be 9.52 ± 0.23. Nevertheless, the analysis of configurational snapshots indicated that several cylinders of spheres were formed, aligned along the field axis (Fig. 7.14(b)). Here, the rods are represented by thin blue lines and spheres are empty yellow circles, so that it is possible to see a significant depth into the sample. The direction of the applied field in this Figure is out of the page. The simulation box appeared to be too small to distinguish whether these cylinders formed a regular structure or a random arrangement. Cluster analysis failed to resolve individual cylinders, however, a single cluster of spheres being found instead.

7.2.4   System (iv)

Two mixtures of type (iv) are studied in this Subsection. Analogous to Subsection 7.1.4, a cubic phase structure at 50/50 rod-sphere concentration ratio and a hexagonal micellar phase at 80/20 are subjected to a constant magnetic field.

A field $H = 2.0$ was applied to a 50/50 mixture of type (iv) at $T = 1.5$ and $P = 0.3$. Starting from a configuration previously equilibrated in the NVT ensemble, a constant NPT MC run was performed with the field on for 4×10^5 MC cycles. Figure 7.15(a) shows the calculated distribution functions which are typical of those obtained for microphase separated systems. A snapshot, shown in Fig. 7.15(b), illustrates a hexagonal array of cylinders of spheres aligned parallel to the field. Cluster analysis was performed to explore whether these cylinders were isolated one from another. Most of the time when the separation distance was set at $1.5\sigma_0$ this returned one large cluster, but sometimes 1-3 clusters of 50-65 spheres each were found separated from the rest. When separation distance was reduced to $1.2\sigma_0$, however, all 9 large clusters, seen in Fig. 7.15(b), could be distinguished. Despite the dynamics of the process and constant changing of the cluster size distribution, at some point, the snapshot distribution shown in Tab. 7.4 is instructive. This distribution suggests that there were indeed 9 large clusters of spheres, although some single spheres could be still found in the regions between them.
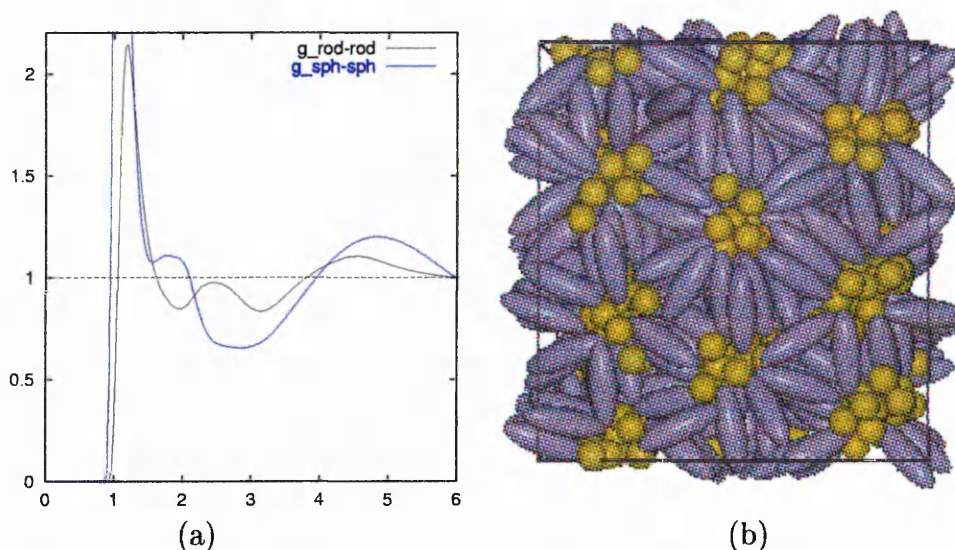
Figure 7.15: (a) Sphere-sphere, $g_{ss}(r)$, and parallel, $g_{\parallel}(r_{\parallel})$, distribution functions measured at $T = 1.5$ and $P = 0.3$ under field $H = 2.0$; (b) configuration snapshot taken at this data point.

Size	1	2	44	49	51	52	53	56	63
Number	34	1	1	1	1	2	1	2	1

Table 7.4: Snapshot distribution of clusters separated by a distance more than $1.2\sigma_0$.

An 80/20 mixture was simulated under conditions analogous to those used in Subsection 7.1.4. Fields $H = 2.0$ and $H = 3.0$ were applied to the HCP micellar structure at $P = 0.3$ and $T = 1.0$. The simulation results of these two runs of 2×10^5 MC cycles each are summarised in Tab. 7.5. The cluster size distribution at $H = 2.0$ was

Applied Field	2.0	3.0
Order Parameter	0.156 ± 0.006	0.234 ± 0.007
Number of clusters	68	27
Largest cluster	17	27

Table 7.5: Simulation results of two constant NPT MC runs performed at $P = 0.3$ and $T = 1.0$ under fields $H = 2.0$ and $H = 3.0$.

similar to that observed at zero field, i.e. about 70 clusters were found most of which contained 5 or 6 spheres were found. In contrast, most of the clusters observed at $H = 3.0$ consisted of 10-25 spheres. Figure 7.16(a) shows the sphere-sphere radial distribution functions measured at both $H = 2.0$ and $H = 3.0$. Whereas the former
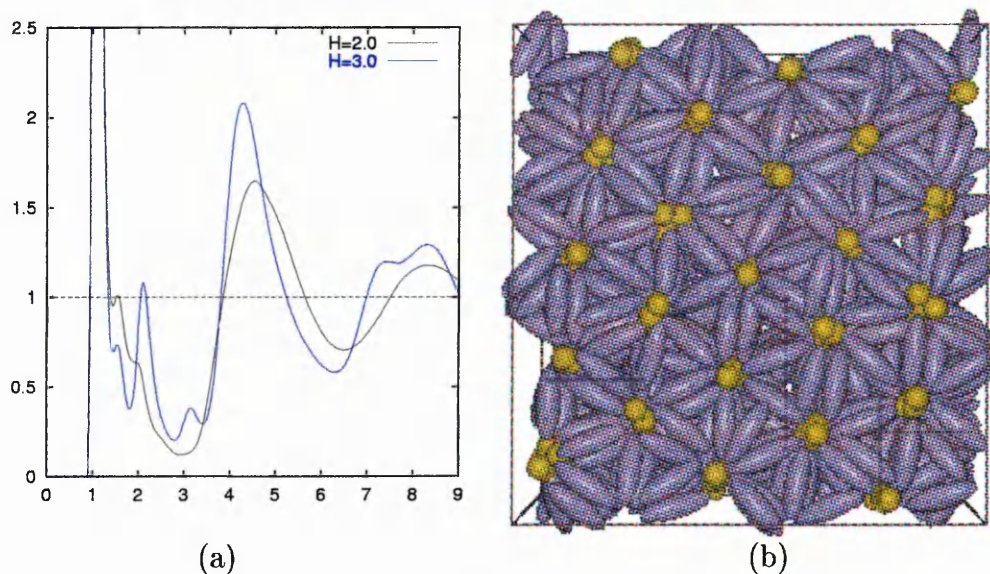
Figure 7.16: (a) Sphere-sphere radial distribution functions measured at $P = 0.3$ and $T = 1.0$ under fields $H = 2.0$ and $H = 3.0$; (b) configuration snapshot taken at $H = 3.0$, field into the page.

resembles sphere distribution observed under zero field, the latter resembles $g_{ss}(r)$ seen in Subsection 7.1.4 for a hexagonal array of channels of spheres. The period of this structure is about $d_h = 4.26\sigma_0$, and peaks typical for a hexagonal arrangement at $\sqrt{3}d_h$ and $2d_h$ can be seen. Figure 7.16(b) illustrates that these well defined channels of spheres are aligned parallel to the field.

7.3 Discussion

When a magnetic field is applied to an LC system, whether characterised by positive or negative magnetic susceptibility, it imposes some degree of order upon it, therefore, reducing its entropy. In terms of the free energy, $F = U - TS$, a similar effect may be caused by decreasing the temperature which reduces the entropy contribution too. In other words, both the decrease of temperature and the application of a field may provoke similar system responses. The difference is that while T acts isotropically, an applied field affects different modes in different directions.

Several examples of field-induced demixing and phase transitions were found in our

simulations. The resultant structures were often of the same type and symmetry as would have formed at a lower temperature. Nevertheless, in some cases a novel phase was developed when a sufficiently strong field was applied to the rod-sphere mixture. In all cases, these were systems with a tendency to develop microphase separated structures. A low temperature bicontinuous structure formed by system (iii) at 50% sphere concentration (Fig. 6.34) transformed, under a magnetic field, into a lamellar phase (Fig. 7.8). A completely different configuration was developed by the same system under the same external conditions if the rods had negative magnetic susceptibility. In this case, the system tended to form cylinders of spheres coated by layers of rods (Fig. 7.14). Structures of the same kind but with hexagonal periodicity were formed by system (iv) at both 20% and 50% sphere concentrations. Interestingly, with positive magnetic susceptibility, these two mixtures developed structures of different symmetry. A 50/50 mixture exhibited a lamellar phase, whereas an 80/20 mixture developed a novel structure with spheres forming a hexagonal array of channels perpendicular to the applied field (Fig. 7.9)

The property of formation of a hexagonal array of channels under an applied field has the potential to be utilised in switching devices or in field controlled drug delivery systems. For example, an 80/20 mixture of type (iv) at low temperatures develops an HCP micellar structure in which the spheres are isolated in small clusters. If a field is applied, these clusters transform in a hexagonal array of channels, therefore, dramatically changing system's transport properties. This process is time reversible, i.e. the isolated clusters of spheres re-form after the field has been switched off. This relaxation was simulated in the constant NPT ensemble and an MC run of 6×10^5 cycles was found to be sufficient to equilibrate the system. This run took about four times as long as the switching under applied field which suggests that, in an experimental system, both processes would be achieved on similar time scales. At higher temperatures, the relaxation time would decrease, and the conductive properties of the sample would increase at the same time. Provided a temperature window exists in which the system has low conductivity under zero field and short switching and relaxation times, the possibility of creating a field controlled device

arises. The properties of the mixture to allow the self-assembly of the conductive channels under the applied field are expected to be as following:

- the mixture does not have a tendency to macroscopic demixing;

- the end rod-sphere interactions are the dominant interactions in the system (the results obtained in Section. 6.5.2 suggest this interaction may also have to be not saturating);

- the rod-rod side-by-side interactions are significant;

- the rods tend to align perpendicular to the applied field.

To our knowledge, there are no evidence of such experimental systems exists.

Chapter 8

Rod-Sphere Mixture near a Curved Surface

In this Chapter, a rod-sphere mixture is studied in two cases involving spherical geometry: near convex and concave surfaces. The motivation for this work comes from a number of experimental, theoretical and simulation works on LC-colloid and Polymer Dispersed LC (PDLC) systems. The following Section introduces a new potential developed to describe the interaction between the mixture components and a large spherical colloidal particle. A rod-sphere mixture with the original Gay-Berne parameterisation is then used to explore the capabilities of this model. The second Section of this Chapter addresses the alternative scenario of a rod-sphere mixture confined in a spherical pore. Again, a novel model description and exploratory simulation results are given. The method employed in both Sections is the constant NVT MD.

8.1 LC-Colloid system

With a wide variety of practical applications and numerous opportunities for investigating basic chemistry and physics, colloidal systems such as suspensions of

solid particles and emulsified dispersions of surfactant-coated liquid droplets, are of great interest to a variety of researchers. In Section 2.5, a theoretical background to colloid-LC systems was given. Here, some literature simulation results are briefly considered first as a basis of our research. A description of our model is given then, followed by simulation results and their analysis.

Since the size of colloidal particles is normally much greater than the size of a single LC molecule, molecular scale simulations are limited to the study of single colloidal particles suspended in an LC. Even in this limit, these simulations suffer significantly from periodic boundary effects [109]. Nevertheless, different kinds of computer simulation methods are capable of studying defects of the director field near a colloidal particle, as was described in Section 2.5. The aggregation of several colloids due to director-field mediated interactions have been successfully demonstrated for two dimensional systems using numerical simulations [110] and Lattice Boltzmann technique [111]. Interesting results have also been obtained for relatively small $3D$ systems with a single colloidal particle. For example, a Saturn ring defect was observed by Billeter and Pelcovits [112] in a system of 2048 Gay-Berne particles with the original parameterisation and one spherical particle with a diameter of $3\sigma_0$. A system similar to this, although containing up to a million rods and a colloid up to $30\sigma_0$ in diameter, was studied by Andrienko and Allen [109]. Here, it was found that for homeotropic anchoring, only the Saturn ring defect was stable at small colloid sizes and that only with a colloid $30\sigma_0$ in diameter a satellite defect remain stable over simulation time scales. According to the density and order parameter maps measured in this study [109], the position of the core region of the ring defect in these simulations was found to be a linear function of the colloid radius R. For a relatively small colloid with radius $3.0\sigma_0$, the estimated radius of the defect was $R_d = 3.162\sigma_0$, meaning that it was located very close to the colloid surface. The order parameter profiles from [109] also indicate no irregularities at distances larger than $4\sigma_0$ from the colloid surface. This implies that a relatively small simulation box can be used to simulate colloid-LC systems even in the case of homeotropic anchoring. In this Section, a rod-sphere mixture containing a colloidal particle of

radius $3\sigma_0$ is studied in the constant NVT ensemble using MD. The main aim is to study the effect of spherical additives on defect formation. A 90/10 rod-sphere mixture of type (i) is used throughout these studies.

8.1.1 The Model

To introduce a spherical colloidal particle in our simulations the colloid-rod and colloid-sphere interactions have to be defined. The forms of the colloid-rod potential used in both [112] and [109] were not found satisfactory. The potential used in [109] was a shifted Lennard-Jones potential with both energy and shape parameters independent of the rod's orientation. The potential used in [112] consisted of two terms, one purely repulsive and the other controlling surface anchoring, :

$$U(\hat{\mathbf{u}}_i, \mathbf{r}_i) = 4\epsilon_0 \left(\frac{\sigma_0}{r - \sigma(\hat{\mathbf{u}}_i, \hat{\mathbf{r}}_i) + \sigma_0} \right)^{18} - W \frac{(\hat{\mathbf{u}}_i \cdot \hat{\mathbf{r}}_i)^6}{r^6} \tag{8.1}$$

Here the shape parameter $\sigma(\hat{\mathbf{u}}_i, \hat{\mathbf{r}}_i)$ is defined according to the Generalised Gay-Berne mixing rules (4.33) and the parameter W is a phenomenological anchoring coefficient. The exponent 18 instead of 12 was chosen here to reduce the active interaction region and make the repulsion "harder". Therefore, equation (8.1) was based on an assumption of a particular orientation dependence of the anchoring energy (which is the only attractive interaction in this model) and contains artificially adjusted parameters.

A new form for the potential describing the interaction between a small spherical or prolate particle and a large spherical colloid was therefore developed. To be consistent with our previous model, the large colloidal particle was considered as a number of smaller spherical particles taken to interact with a given external particle via one of the 6-12-power potentials previously studied. Direct evaluation of such a multi-site interaction would be quite expensive and alternative effective colloid-small-particle potentials are proposed here. This approach assumes a uniform distribution for the particles forming the colloid and a pair-wise potential interaction approximation.

The colloid-sphere potential was defined as the Lennard-Jones potential integrated

over the colloid volume. To determine this, we first evaluate the potential created by a spherical shell of radius a at a distance r from its centre. For the sake of simplicity,
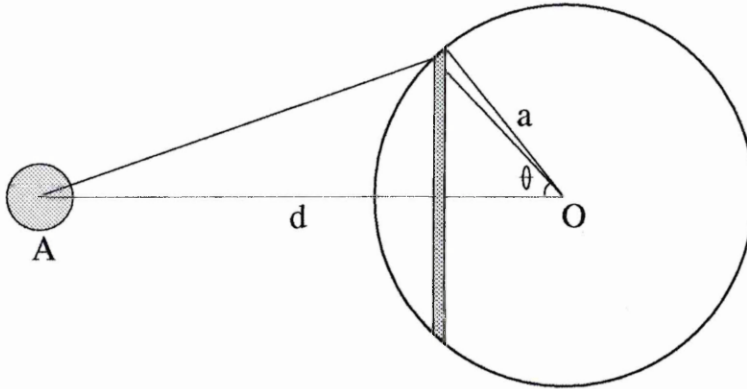
Figure 8.1: Spherical particle near colloid

The interaction between two point particles is considered here to be proportional to $\frac{1}{r^n}$. A ring on the sphere given by constant θ and $0 \le U < 2\pi$ has its points equally separated from the point A (Fig. 8.1). If da is the thickness of the spherical shell and $a\,d\theta$ is the width of the ring, the potential created by this ring in the point A is:

$$dU(r, a, \theta) = \int\limits_0^{2\pi} \frac{a\,d\theta\,da\rho a \sin\theta\,dU}{(r^2 + a^2 - 2ar\cos\theta)^{n/2}} = 2\pi a^2 da\rho \frac{\sin\theta\,d\theta}{(r^2 + a^2 - 2ar\cos\theta)^{n/2}},$$

where the constant $\rho = \frac{N_{total}}{4\pi a^2 da}$ is the number density of the microscopic particles being assumed to make up the colloid. Integration over the whole sphere surface gives:

$$U(r, a) = 2\pi a^2 da\rho \int\limits_0^{\pi} \frac{\sin\theta\,d\theta}{(r^2 + a^2 - 2ar\cos\theta)^{n/2}} = |x = \cos\theta| =$$

$$\frac{N_{total}}{2} \int\limits_{-1}^{1} \frac{dx}{(r^2 + a^2 - 2arx)^{n/2}} = \frac{M_{total}}{2ar(n-2)}\left[\frac{1}{(r-a)^{n-2}} - \frac{1}{(r+a)^{n-2}}\right], \quad n \ne 2.$$

The total potential created at the point A by a colloid is a sum of potentials of concentric spherical shells. In order to calculate it we have to integrate $U(r, a)$ over

172

all radii $0 \leq a \leq R$,

$$U_{colloid}(r) = \int_0^R \frac{4\pi a^2 \rho \, da}{2ar(n-2)} \left[\frac{1}{(r-a)^{n-2}} - \frac{1}{(r+a)^{n-2}} \right] =$$

$$\frac{2\pi\rho}{r(n-2)} \int_0^R a \left[\frac{1}{(r-a)^{n-2}} - \frac{1}{(r+a)^{n-2}} \right] da =$$

$$\frac{2\pi\rho}{r(n-2)} \left[\frac{r}{n-3} \left(\frac{1}{(r-R)^{n-3}} - \frac{1}{(r+R)^{n-3}} \right) - \frac{1}{n-4} \left(\frac{1}{(r-R)^{n-4}} - \frac{1}{(r+R)^{n-4}} \right) \right].$$

In the vicinity of the colloid's surface $(r-R) \ll (r+R)$ and terms containing $(r+R)$ in their denominator can be neglected at sufficiently large n. For exponents $n = 6$ and $n = 12$, this approximation is reasonable, and the resultant expression for the colloid-sphere potential is:

$$U_{CS}(r) = \epsilon_{CS} \left[\frac{1}{45(r-R)^9} - \frac{1}{6(r-R)^3} - \frac{1}{40r(r-R)^8} + \frac{1}{4r(r-R)^2} \right], \qquad (8.2)$$

where ϵ_{CS} is an adjustable parameter that depends on the packing of particles forming the colloid and on the strength of their interaction with an external particle. Figure 8.2 shows the colloid sphere potential for $R = 3\sigma_0$ and $\epsilon_{CS} = 4\epsilon_0$ as an example. The blue line in this Figure corresponds to a 3-9 potential obtained for a
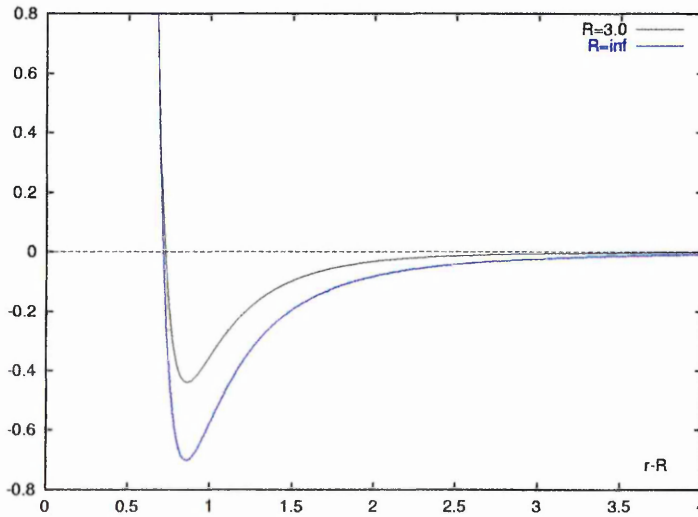

Figure 8.2: The colloid-sphere potential for $R = 3\sigma_0$ and and $R = \infty$ at $\epsilon_{CS} = 4\epsilon_0$.

plane surface, which is the limit of expression (8.2) at $R = \infty$.

Formula (8.2) can be generalised to describe the interaction between the colloid and an elongated particle. An analogous approach was made for the Gay-Berne potential which took the Lennard-Jones form with orientation dependent parameters. Thus the colloid-rod interaction in our model will be described by:

$$U_{CR}(\mathbf{r}, \hat{\mathbf{u}}) = \epsilon_{CR} \left[\frac{1}{45(r - R - \sigma_{CR} + 1)^9} - \frac{1}{6(r - R - \sigma_{CR} + 1)^3} - \frac{1}{40r(r - R - \sigma_{CR} + 1)^8} + \frac{1}{4r(r - R - \sigma_{CR} + 1)^2} \right], \qquad (8.3)$$

where

$$\epsilon_{CR}(\mathbf{r}, \hat{\mathbf{u}}) = \epsilon_0^* \left(\frac{1 - \chi''}{1 - \chi'' \sin^2 \theta} \right)^\mu, \qquad (8.4)$$

$$\sigma_{CR}(\mathbf{r}, \hat{\mathbf{u}}) = \sigma_0 \sqrt{\frac{1 - \chi \sin^2 \theta}{1 - \chi}}. \qquad (8.5)$$

Here, θ is the angle between the vectors $\mathbf{r}$ and $\hat{\mathbf{u}}$ and the parameters χ and χ'' are the same as those defined for the rod-sphere interaction (see Subsection 4.2.5). The expressions (8.4) and (8.5) were originally determined for a rod-plane system and can be adopted for the colloid-rod interaction for two reasons:

- The size of the colloid is large in comparison to the size of the rod and the curvature of the colloid's surface can be neglected in the first approximation.

- We are most interested in strong anchoring when the rods tend to have radial alignment, an arrangement in which the σ parameter has the same values for both convex and planar surfaces.

Due to the orientational dependence of the potential (8.3) its shift at a spherical cut-off distance, r_c, has to be orientation dependent as well in order to provide a zero potential at the cut-off. The shifted colloid-rod interaction potential is, then, expressed as

$$U_{CR}^{total}(\mathbf{r}, \hat{\mathbf{u}}) = U_{CR}(\mathbf{r}, \hat{\mathbf{u}}) - U_{CR}^c(\mathbf{r}, \hat{\mathbf{u}}), \qquad (8.6)$$

174

where

$$
\begin{aligned}
U_{CR}^c(\mathbf{r}, \hat{\mathbf{u}}) \;=\; & \epsilon_{CR}\left[\frac{1}{45(r_c - R - \sigma_{CR} + 1)^9} - \frac{1}{6(r_c - R - \sigma_{CR} + 1)^3}\right. \\
& \left. - \frac{1}{40 r_c(r_c - R - \sigma_{CR} + 1)^8} + \frac{1}{4 r_c(r_c - R - \sigma_{CR} + 1)^2}\right]. \quad (8.7)
\end{aligned}
$$

The explicit forms of the forces and torques exerted by a colloidal particle are calculated in App. A.

8.1.2 Simulation Results

This Subsection presents simulation results of a 90/10 rod-sphere mixture of type (i) (2048 particles in total) in the presence of a spherical colloid of radius $3\sigma_0$. The new model described above introduces three new independent energy parameters: the strength and anisotropy of the colloid-rod interaction and the strength of the colloid-sphere interaction. Following the concept of the colloid being composed of smaller spheres, we will consider two cases of the colloid-rod interaction anisotropy: $k'_{CR}=5.0$ and $k'_{CR}=0.2$. These correspond, respectively, to radial and planar anchoring. However, the resultant anisotropy of the interaction, when calculated according to formula (8.3), $\epsilon_{CR}^{end}/\epsilon_{CR}^{side} \neq k'_{CR}$, is a function of the colloid's radius. The values of $\epsilon_{CR}^{end}/\epsilon_{CR}^{side}$ for $R = 3\sigma_0$ were found to be 5.599 and 0.224 respectively. The strength of the colloid-sphere interaction was set to $\epsilon_{CS} = 4 * 2.285871\epsilon_0$ to provide a unit well depth (compare to Fig. 8.2). The planar anchoring interaction was scaled as well so $\epsilon_{CR}^{side} = K_A$ and $\epsilon_{CR}^{end} = 0.224 K_A$, where the parameter K_A controlled the strength of the anchoring. In a similar way, the radial anchoring interaction was set to provide $\epsilon_{CR}^{side} = 0.200 K_A$ and $\epsilon_{CR}^{end} = 1.120 K_A$. This normalised the side colloid-rod interaction to have well depth $K_A\epsilon_0$ for planar anchoring and $0.200 K_A\epsilon_0$ for radial anchoring.

In our model, whether a radial anchoring is strong or not is determined by the well depth of the end colloid-rod interaction, ϵ_{CR}^{end}. However, if it is too deep (the case $\epsilon_{CR}^{end} = 5$ was tested), the rods will simply form a radially aligned shell around the colloid, effectively forming an enlarged colloid of diameter $12\sigma_0$. To avoid this,

we set $K_A = 2$ which gives a colloid-rod interaction depth $2.24\epsilon_0$ for rod aligned along the radial direction. Note that this energy is of the same order as the average kinetic energy, $E_{kin} = \frac{5}{2}k_BT$, of a single rod at $T \approx 1.0$. The same anchoring strength $K_A = 2$ was used for the simulation with planar anchoring. In this case, the maximum side colloid-rod interaction well depth was $2\epsilon_0$.

One compression sequence and one cooling sequence were performed for a system with radial anchoring of strength $K_A = 2.0$. The initial configuration was artificially created from a bulk configuration of 2048 particles by placing a colloidal particle of zero size in the simulation box and gradually growing it up to $R = 3\sigma_0$. This configuration was then equilibrated in the constant NVT ensemble for 7×10^6 MD time steps at $\rho = 0.30$ and $T = 1.0$. The system remained isotropic and homogeneous and no signs of surface alignment could be seen on configurational snapshots. The system was then compressed at a constant temperature of $T = 1.0$ up to density $\rho = 0.35$ with a step of $\Delta\rho = 0.01$. The potential energy per particle and nematic order parameter measured during this sequence are presented in Tab. 8.1. These data

Density	Energy	Order Parameter
0.30	-2.756 ± 0.022	0.044 ± 0.014
0.31	-2.792 ± 0.024	0.058 ± 0.016
0.32	-2.845 ± 0.029	0.063 ± 0.018
0.33	-2.938 ± 0.029	0.183 ± 0.024
0.34	-3.037 ± 0.029	0.590 ± 0.022
0.35	-3.098 ± 0.031	0.688 ± 0.017

Table 8.1: Potential energy per particle and nematic order parameter measured at $T = 1.0$ and different densities.

indicate an isotropic-nematic transition at $\rho \approx 0.33$. Figure 8.3(a) shows the rod-rod and sphere-sphere distribution functions measured at $\rho = 0.35$ and $T = 1.0$. These are typical for a homogeneous mixture and Fig. 8.3(b) illustrates a configuration snapshot which confirms this.

According to our simulation results, it was not clear whether the colloid caused any stable defect of the director field. The results also suggest that, at $T = 1.0$, the anchoring of strength $K_A = 2$ was not sufficiently strong to induce radial alignment of
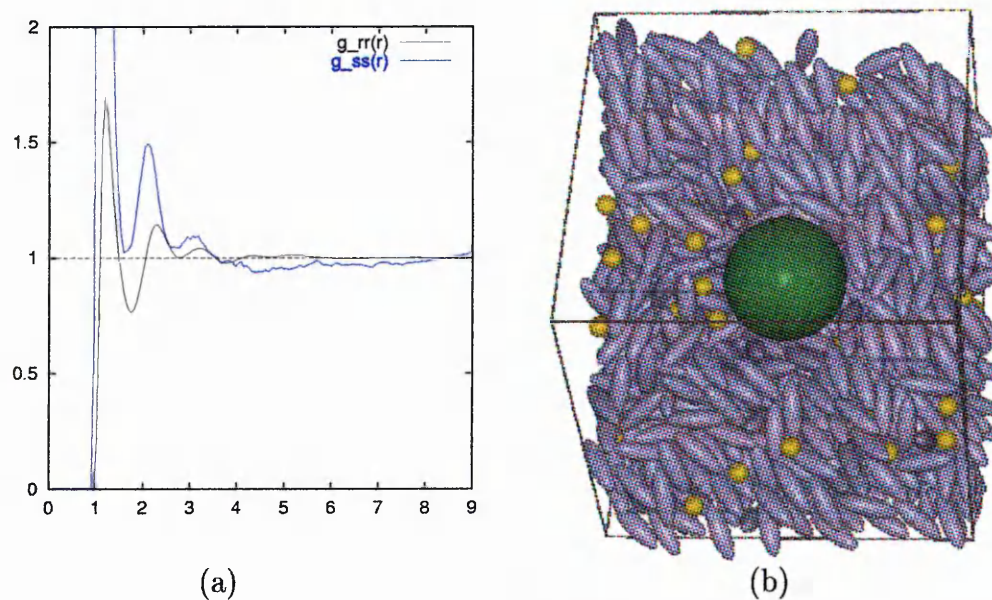
Figure 8.3: (a) Radial distribution functions $g_{rr}(r)$, and $g_{ss}(r)$ measured at $\rho = 0.35$ and $T = 1.0$; (b) configurational snapshot taken at this data point.

the rods. Therefore, lower temperature behaviour was studied to effectively increase the effect of attractive interactions.

A cooling sequence was performed at a constant density of $\rho = 0.34$. The temperature was reduced with a decrement of $\Delta T = 0.05$ down to $T = 0.85$. Table 8.2 summarises the results of this run. The nematic order parameter increases with de-

Temperature	Energy	Order Parameter
1.00	-3.037 ± 0.029	0.590 ± 0.021
0.95	-3.263 ± 0.028	0.626 ± 0.014
0.90	-3.582 ± 0.029	0.653 ± 0.002
0.85	-3.869 ± 0.033	0.692 ± 0.002

Table 8.2: Potential energy per particle and nematic order parameter measured at $\rho = 0.34$ and different temperatures.

creasing temperature while the potential energy decreases. The radial distribution functions indicated the onset of macroscopic phase separation at $T = 0.90$. Interestingly, according to configurational snapshots, the droplet of spheres was formed in the equatorial plane of the colloidal particle. To this end, the sphere probability distribution in the simulation box along the director was studied at $T = 0.85$.

Here the number of spheres was calculated in slices perpendicular to the director and normalised by their volume and the total number of spheres counted (similar to calculating $g_{\parallel}(r_{\parallel})$). Figure 8.4(a) shows the simulation results averaged over 2×10^5

Figure 8.4: (a) Sphere probability distribution along the director at $\rho = 0.34$ and $T = 0.85$; (b) configurational snapshot taken at this data point.

time steps. This indicates that the spheres indeed were allocated in the equatorial plane. Moreover, distributions similar to that shown in Fig. 8.4(a) but averaged over shorter times were not symmetrical around zero (the equatorial plane), even though they resulted in a symmetrical distribution after averaging. This suggests that the droplet of spheres oscillated around its equilibrium. Since it did not couple directly with a colloid, the force which kept it in the equatorial plane was associated rather with the nematic elasticity than with the attraction by the colloid. It must be noted that a droplet of spheres can be considered as a sub-particle with planar surface anchoring. Therefore, our simulation results suggest that two spherical particles with different types of the surface anchoring will experience an attraction when suspended in a nematic. To our knowledge, experiments involving such mixtures of colloidal particles have not been performed yet. However, this effect may introduce new possibilities of establishing novel self-assembling structures at mesoscopic length scales.

178

When compared to the bulk simulations, the studied 90/10 mixture demonstrates different mixing properties. The presence of the colloid in the simulation box reduces the free volume available for rods and spheres, i.e. it occupies approximately 3.5% of the box. Therefore, under compression at a constant temperature $T = 1.0$, the mixture was expected to demix at $\rho = 0.34$. However, it remained homogeneous even at $\rho = 0.35$ in the presence of the colloid. This suggests that the distorted director field associated with a colloid stabilises the homogeneous nematic phase. When the temperature was reduced, the nematic phase was not stable any longer and the spheres segregated to minimise the system's free energy.

A 90/10 mixture of type (i) was also simulated near a colloidal particle with planar anchoring of strength $2K_A$. Analogous to the simulations discussed above, the system was compressed at a constant temperature of $T = 1.0$ in the range of densities $0.30 \leq \rho \leq 0.35$. The potential energy per particle and nematic order parameter measured during this sequence are shown in Tab. 8.3. These data indicate an

Density	Energy	Order Parameter
0.30	-2.761 ± 0.024	0.044 ± 0.016
0.31	-2.834 ± 0.026	0.068 ± 0.018
0.32	-2.901 ± 0.027	0.125 ± 0.031
0.33	-2.982 ± 0.029	0.455 ± 0.017
0.34	-3.061 ± 0.029	0.581 ± 0.018
0.35	-3.129 ± 0.034	0.678 ± 0.019

Table 8.3: Potential energy per particle and nematic order parameter measured at $T = 1.0$ and different densities.

isotropic-nematic transition, however, no demixing was found according to the calculated distribution functions. Subsequently, a cooling run was performed starting from the final configuration at $\rho = 0.35$ and $T = 1.0$. The system was cooled to $T = 0.85$ with a step of $\Delta T = 0.05$. According to the sphere-sphere radial distribution function, at $T = 0.90$ a mixing-demixing transition occurred. The sphere probability distribution was also measured at this point, as was done in the case of homeotropic anchoring considered above. Figure 8.5 shows that this time the spheres were located near to the poles of the colloid. A configuration snapshot
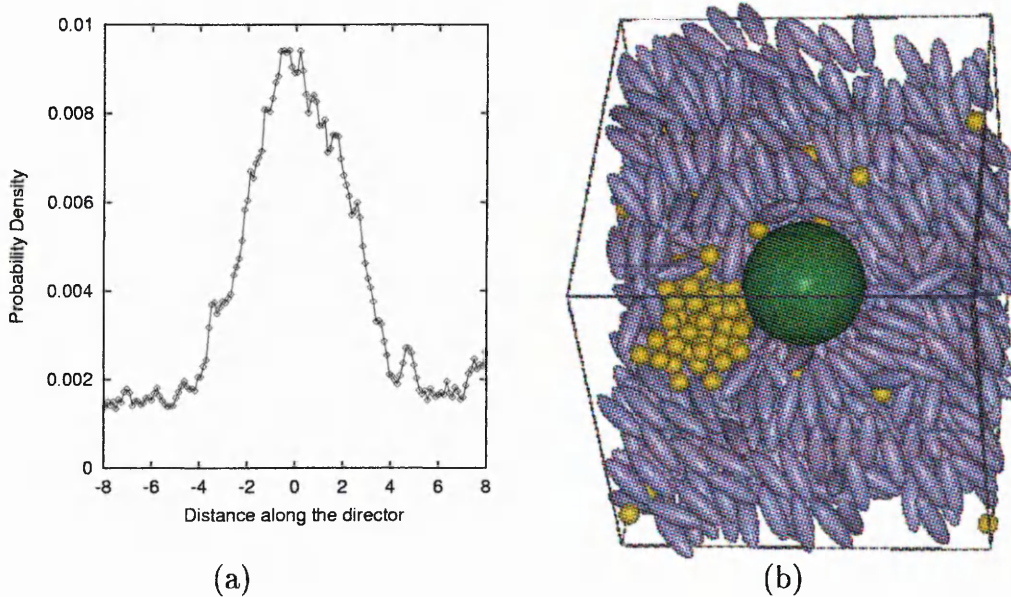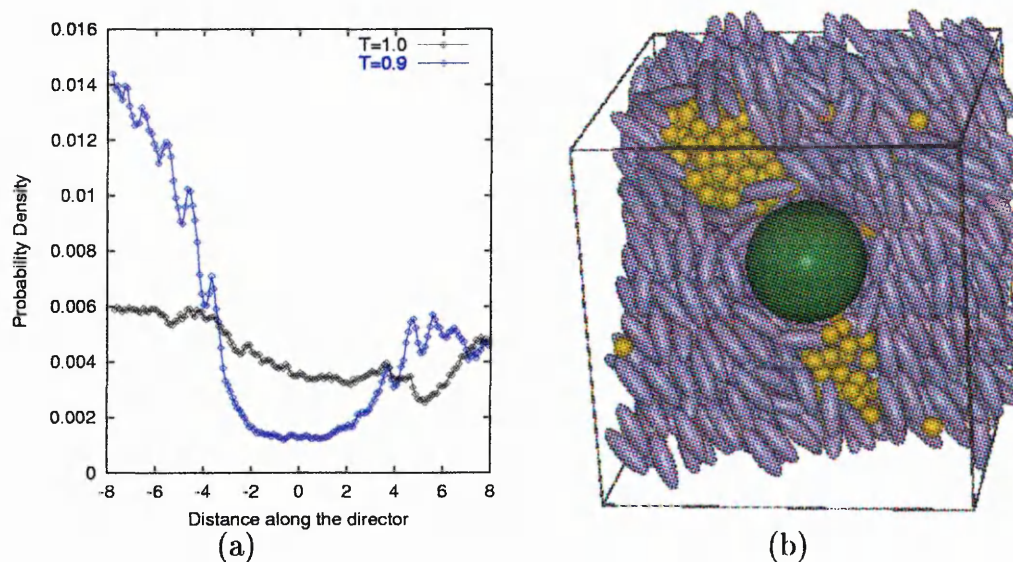
Figure 8.5: (a) Sphere probability distribution along the director at $\rho = 0.35$ and $T = 0.9$; (b) configurational snapshot taken at this data point.

taken at $\rho = 0.35$ and $T = 0.9$ illustrates two droplets of spheres of different size located near the colloid's poles.

In this case, the simulation results indicate that the spheres segregate in the region of defects: a colloid with planar anchoring is known to form a pair of boojums at its poles [47].

8.2   PDLC system

Polymer Dispersed LC (PDLC) systems are currently attracting considerable attention because of their large area of optical applications including flat panel displays and light shutters. Here, the nematic LC is confined to sub-micrometer size cavities of the polymer matrix. The size, shape, and distribution of these cavities as well as their surface interactions can be adjusted by a suitable choice of a polymer and the process of the sample preparation [113]. PDLC systems are of particular interest for computer simulation because the LC droplets contain a sufficiently small number of molecules, i.e. a few thousand, to be close to the number of particles

normally used in simulations. The very first simulations of PDLC systems were performed [114] using the Lebwohl-Lasher lattice model [57]. Many features, typical for PDLC systems, were observed for this model subject to various boundary conditions and external field. Figure 8.6 shows director configurations for both homeotropic
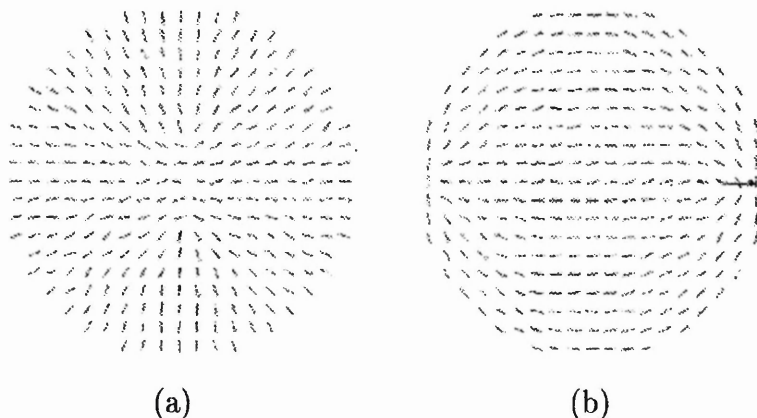

(a)   (b)

Figure 8.6: Director configuration within a spherical domain for strong (a) homeotropic and (b) planar anchoring conditions (from [115]).

and planar anchoring conditions. The director is horizontal in both cases and pair point defects of the director field can be clearly seen on each snapshot. A general case study of the director field within an ellipsoidal domain [115] reveals that homeotropic surface anchoring leads to very different director configurations in non-spherical ellipsoidal domains, whereas planar anchoring gives similar bipolar configurations in all cases. Despite the success of the mesoscopic approach, lattice models cannot provide information about density distribution, for example. The Gay-Berne model was employed by Emerson and Zannoni [116] to simulate a PDLC system. The case of the homeotropic surface anchoring was studied and the development of concentric shells of radially aligned particles was observed. However, this order did not propagate towards the centre of the domain, unless it was either relatively large or an alternative to the original parameterisation of Gay-Berne potential with exponents $\mu = 1$ and $\nu = 3$ was used.

In all examples above the anchoring was controlled by setting both the positions and orientations of the rods on the domain surface and keeping them unchanged during the simulation. In this Section, a new surface potential is developed to describe the

interaction between particles and spherical walls more naturally. This is followed by exploratory simulation results and discussion.

8.2.1   Model Description

Analogous to the way the case of a concave surface was studied in Section 8.1, the sphere and rod interactions with a convex surface are evaluated here. Due to its different topology, potential (8.2) cannot be used to describe interaction with a convex surface just by substituting positive curvature radius R with $-R$. However, both potentials have to approach the same limit of the flat-wall potential as R approaches infinity.

Consider a Lennard-Jones particle inside a spherical cavity of radius R at distance h from its surface (Fig. 8.7). The space outside the cavity is occupied by a polymer
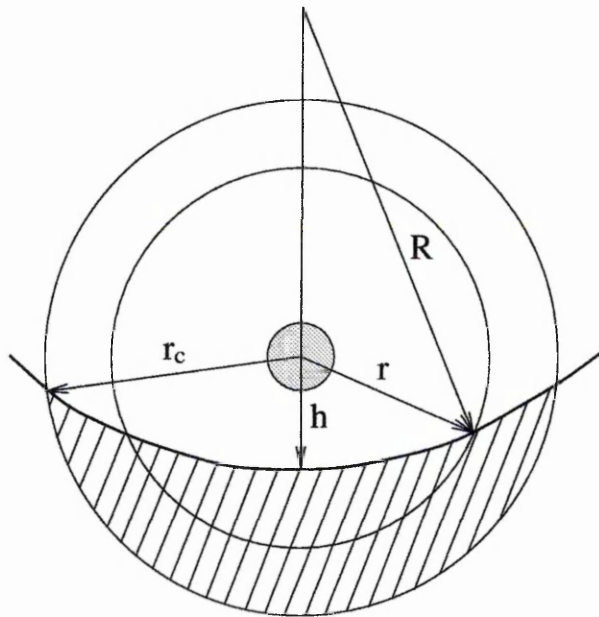

Figure 8.7: Spherical particle near a convex surface

which interacts with this particle within the cut-off distance r_c. Therefore, to calculate the total potential, the interaction has to be integrated over the volume shaded in Fig. 8.7. This volume can be presented as a number of spherical shells with radii

r ranged $h \leq r \leq R$. The contribution to the total potential of each such a shell is proportional to

$$\frac{S(r)dr}{r^n},$$

where

$$S(r) = 2\pi r^2 (1 - \cos\theta)$$

is the surface of the shell and θ is the angle between vectors $\mathbf{h}$ and $\mathbf{r}$. Substituting

$$\cos\theta = \frac{2hR - h^2 - r^2}{2(R-h)r}$$

into expression for $S(r)$ and integrating over the whole range of r we obtain the total potential:

$$
\begin{aligned}
U(h) &= k \int_h^{r_c} \frac{dr}{r^n} 2\pi r^2 \left(1 - \frac{2hR - h^2 - r^2}{2(R-h)r} \right) \\
&= \frac{k\pi}{R-h} \left[\int_h^{r_c} r^{-n+3} dr + 2(R-h) \int_h^{r_c} r^{-n+2} dr - h(2R-h) \int_h^{r_c} r^{-n+1} dr \right] \\
&= \frac{k\pi}{R-h} \left[\frac{1}{n-4} \left(\frac{1}{h^{n-4}} - \frac{1}{r_c^{n-4}} \right) + \frac{2(R-h)}{n-3} \left(\frac{1}{h^{n-3}} - \frac{1}{r_c^{n-3}} \right) \right. \\
&\qquad \left. - \frac{h(2R-h)}{n-2} \left(\frac{1}{h^{n-2}} - \frac{1}{r_c^{n-2}} \right) \right]
\end{aligned}
$$

For the exponents $n = 6$ and $n = 12$ this gives the potential we will use in our simulations:

$$
\begin{aligned}
U^{sph}(h) &= \frac{\epsilon_{PS}}{R-h} \left[\frac{1}{8} \left(\frac{1}{h^8} - \frac{1}{r_c^8} \right) + \frac{2(R-h)}{9} \left(\frac{1}{h^9} - \frac{1}{r_c^9} \right) - \frac{h(2R-h)}{10} \left(\frac{1}{h^{10}} - \frac{1}{r_c^{10}} \right) \right. \\
&\qquad \left. + \frac{1}{2} \left(\frac{1}{h^2} - \frac{1}{r_c^2} \right) + \frac{2(R-h)}{3} \left(\frac{1}{h^3} - \frac{1}{r_c^3} \right) - \frac{h(2R-h)}{4} \left(\frac{1}{h^4} - \frac{1}{r_c^4} \right) \right] \quad (8.8)
\end{aligned}
$$

Potential (8.8) can be employed to describe interaction between the spherical wall and prolate particle i by introducing orientation dependent parameters

$$H = h - \sigma(\mathbf{r}_i, \hat{\mathbf{u}}_i) + 1, \quad R_c = r_c - \sigma(\mathbf{r}_i, \hat{\mathbf{u}}_i) + 1.$$

This gives

$$
\begin{aligned}
U^{rod}(H) = & \frac{\epsilon_{PR}}{R-H}\left[\frac{1}{8}\left(\frac{1}{H^8}-\frac{1}{R_c^8}\right)+\frac{2(R-H)}{9}\left(\frac{1}{H^9}-\frac{1}{R_c^9}\right)- \right. \\
& \frac{h(2R-H)}{10}\left(\frac{1}{H^{10}}-\frac{1}{R_c^{10}}\right)\frac{1}{2}\left(\frac{1}{H^2}-\frac{1}{R_c^2}\right)+ \\
& \left.\frac{2(R-H)}{3}\left(\frac{1}{H^3}-\frac{1}{R_c^3}\right)-\frac{h(2R-H)}{4}\left(\frac{1}{H^4}-\frac{1}{R_c^4}\right)\right],
\end{aligned} \qquad (8.9)
$$

where the parameters ϵ_{PR} and $\sigma(\mathbf{r}_i,\hat{\mathbf{u}}_i)$ are used in the forms (8.4) and (8.5) respectively. The angle θ is defined now as the angle between the positional vector of the particle $\mathbf{r}_i$ and its orientational vector $\hat{\mathbf{u}}_i$, and $\cos\theta$ is expressed via their scalar product:

$$
\cos\theta = \frac{\mathbf{r}_i\cdot\hat{\mathbf{u}}_i}{R-h} = \frac{a}{R-h}.
$$

Analogous to the interaction with a colloid, potentials (8.8) and (8.9) introduce three new independent energy parameters. These are the strength and anisotropy of the surface-rod interaction and the strength of the surface-sphere interaction. These potentials also depend on R, therefore, the interactions depend on the domain size and change with density. The black solid lines in Fig. 8.8 show both planar and
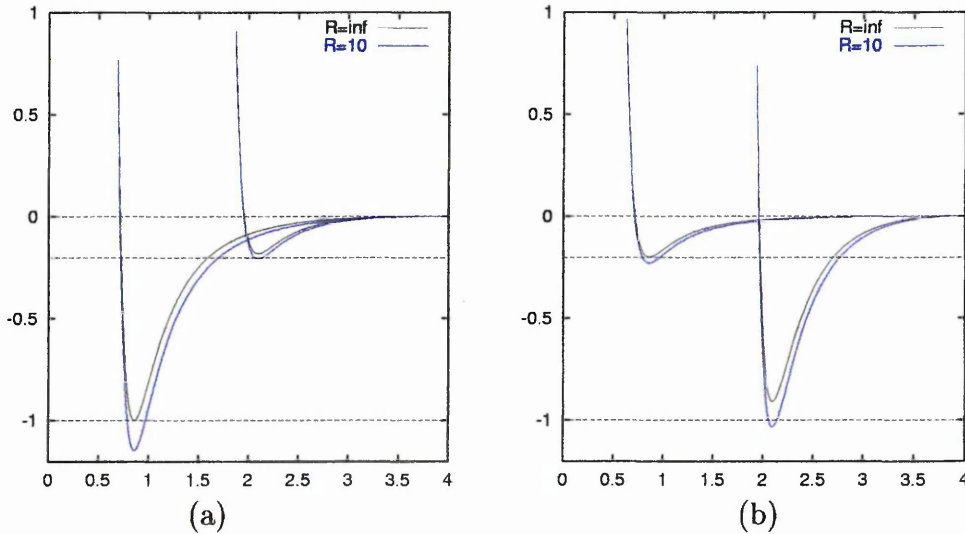

Figure 8.8: Potential profiles for (a) planar and (b) homeotropic anchoring as a function of separation from the surface. The black lines are for a flat surface and blue lines are for a curved surface of radius $R = 10\sigma_0$.

homeotropic types of potential (8.9) normalised to provide respectively ϵ_0 and $0.2\epsilon_0$

well depths for planar and homeotropic arrangements of rods near a flat surface. The blue lines here are the potential profiles for a curved surface of radius $R = 10\sigma_0$. These illustrate that the contribution of the surface curvature to the potential is rather smaller than was this case for the colloid-rod potential.

8.2.2 Simulation Results

A 90/10 rod-sphere mixture of type (i) confined in a spherical domain was simulated for both planar and homeotropic anchoring conditions.

First, a PDLC system with planar anchoring was simulated in the constant NVT ensemble using MD. The anchoring strength was set to $K_A = 1$ which means that the interactions were as shown in Fig. 8.8 in blue. The system did not have periodic boundary conditions and only direct interactions were calculated. The coordinates of 2048 particles in a cubic simulation box of side $L = 18.97$ were used as the initial configuration for a spherical simulation box with initial radius $R = \frac{1}{2}\sqrt{3}L$. Then, the radius was gradually reduced to provide a number density of $\rho = 0.29$. Here, under a number density we understand a number of particles per unit volume, taking the total volume to be the volume of the spherical cavity, i.e. $V = \frac{4}{3}\pi R^3$. However, the actual volume available for the particles is less than this, due to the interaction with the spherical wall. This point must be taken into account when a comparison is made to a bulk mixture.

After equilibration for 1.4×10^6 time steps at $\rho = 0.29$ and $T = 1.0$, a compression sequence was performed up to $\rho = 0.335$ at a constant temperature with a density step of $\Delta\rho = 0.005$. The average values of the potential energy per particle and the nematic order parameter obtained for the even runs of this compression sequence are shown in Tab. 8.4. These data indicate an isotropic-nematic transition at a density of $\rho \approx 0.31$. The transition density, as was expected, appeared to be lower than the bulk transition density at the same temperature. The system homogeneity was difficult to assess because the standard procedure of calculating the pair radial

Density	Energy	Order parameter
0.29	-2.694 ± 0.026	0.063 ± 0.026
0.30	-2.728 ± 0.026	0.072 ± 0.026
0.31	-2.765 ± 0.027	0.173 ± 0.027
0.32	-2.827 ± 0.030	0.292 ± 0.022
0.33	-2.857 ± 0.031	0.425 ± 0.023

Table 8.4: Potential energy per particle and nematic order parameter measured at $T = 1.0$ during the compression sequence.

distribution functions was not applicable due to the geometrical confinements. Instead, the radial density particle distribution was calculated to assess the system's structural properties. Figure 8.9 shows the probability density distributions for rods
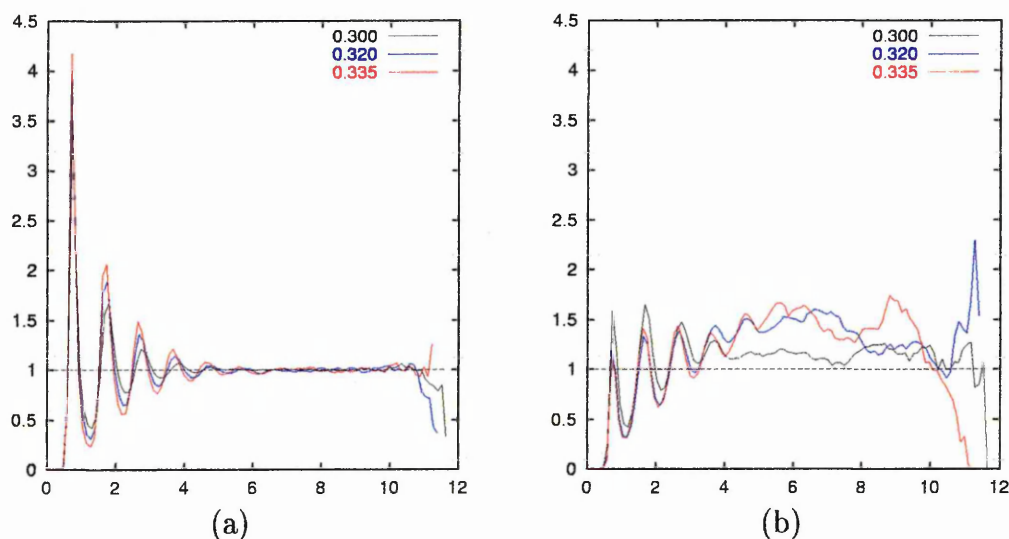
Figure 8.9: Probability density distribution of (a) rods and (b) spheres as a function of the distance to the spherical wall at $T = 1.0$ and different densities.

and spheres averaged over 2×10^5 MD time steps at different data points of the compression sequence. To make these data more comprehensible they are presented not as radial dependencies but as functions of the distance to the spherical wall. Both rod and sphere distributions exhibit short range order at short separations from the wall. This suggests that rods formed concentric layers, some spheres also residing within these layers. The interlayer distance was of order $0.95\sigma_0$ and slightly decreased as the density was increased.

The radial probability density distribution does not allow clear distinction between mixed and demixed configurations, however, and cluster analysis was performed to assess the homogeneity of the system. It was found that the total numbers of clusters separated by distances greater than $1.5\sigma_0$ were practically the same for all runs performed. There were about 100-120 clusters in the system, most of which were single spheres. The number cluster distribution slightly changed with increasing density showing enlargement of bigger clusters. However, the largest cluster contained only about 25 spheres even at the highest density $\rho = 0.335$. This suggests that no macroscopic demixing occurred during this compression, although, a weak tendency to demixing was observed at high densities.

Therefore, a cooling sequence was performed at a constant density of $\rho = 0.32$. The temperature was reduced with a decrement of $\Delta T = 0.1$ from $T = 1.0$ to $T = 0.7$. Table 8.5 summarises the results of this sequence. The nematic order parameter

Temperature	Energy	Order parameter
1.0	-2.827 ± 0.030	0.292 ± 0.022
0.9	-3.043 ± 0.030	0.427 ± 0.034
0.8	-3.350 ± 0.028	0.529 ± 0.015
0.7	-4.149 ± 0.029	0.741 ± 0.008

Table 8.5: Potential energy per particle and nematic order parameter measured at $\rho = 0.32$ during the cooling series.

increased as the temperature was decreased, whereas the potential energy decreased markedly indicating a possible isotropic-smectic transition at $T = 0.7$. Configuration snapshots taken at the beginning and the end of this compression series are shown in Fig 8.10. The low temperature configuration is typical for a smectic phase and also exhibits demixing in the system. Cluster analysis revealed that the system indeed had separated microscopically under cooling. Table 8.6 summarises these simulation results averaged over 10^4 time steps. These data indicate that the clusters started to enlarge significantly at $T = 0.8$, and two clusters of almost identical size contained almost 90% of the total number of spheres at $T = 0.7$. Therefore, the macroscopic demixing, cooperatively with the nematic-smectic transition, took place under cooling and spheres segregated near the defect points as shown in Fig 8.10(b).
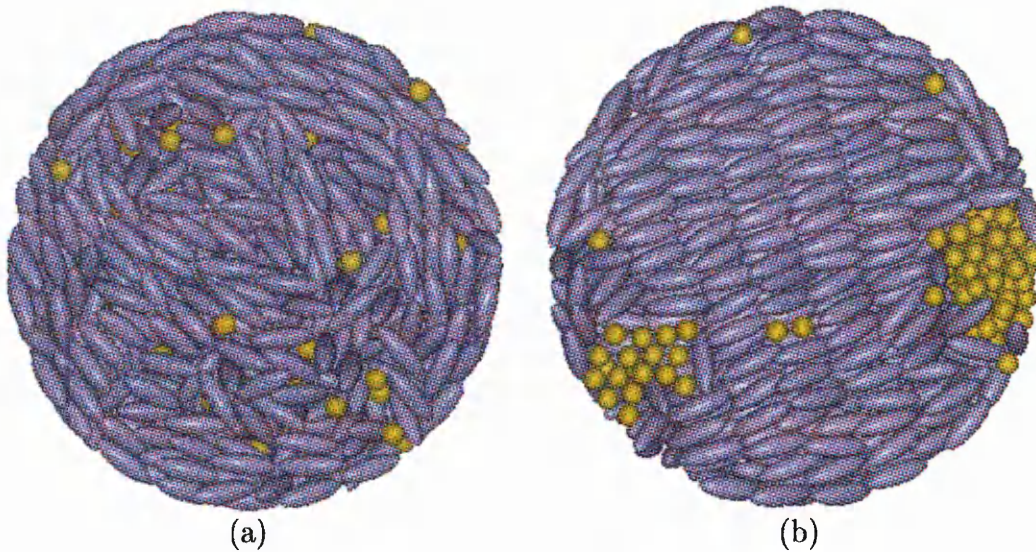
(a)   (b)

Figure 8.10: Configuration snapshots taken at $\rho = 0.320$ at temperatures (a) $T = 1.0$ and (b) $T = 0.7$.

Temperature	1.0	0.9	0.8	0.7
Number of clusters	112	106	62	21
Single spheres	77	72	47	15
Largest cluster	15	23	68	94
Next to the largest	10	13	53	87

Table 8.6: Cluster size distribution at $\rho = 0.32$ and different temperatures.

To study the case of homeotropic anchoring conditions, the anchoring strength was set initially to $K_A = 2$. This meant that the interactions were twice as strong as those shown in Fig. 8.8(b) in blue. The same 90/10 mixture as considered above was equilibrated for 1.4×10^6 MD time steps at $\rho = 0.32$ and $T = 1.0$. This resulted in a configuration which did not exhibit a radial alignment of the rods near the spherical wall, i.e. the anchoring was not sufficiently strong. Figure 8.11(a) shows the probability rod density distributions as functions of rod-wall separation calculated for this configuration and for a configuration at $K_A = 3$ which was simulated subsequently. The peak distribution is qualitatively different for these two curves and indicates that rods were aligned in a more radial direction at $K_A = 3$. Figure 8.11(b) shows a configuration snapshot taken at this data point which confirms a degree of radial alignment.
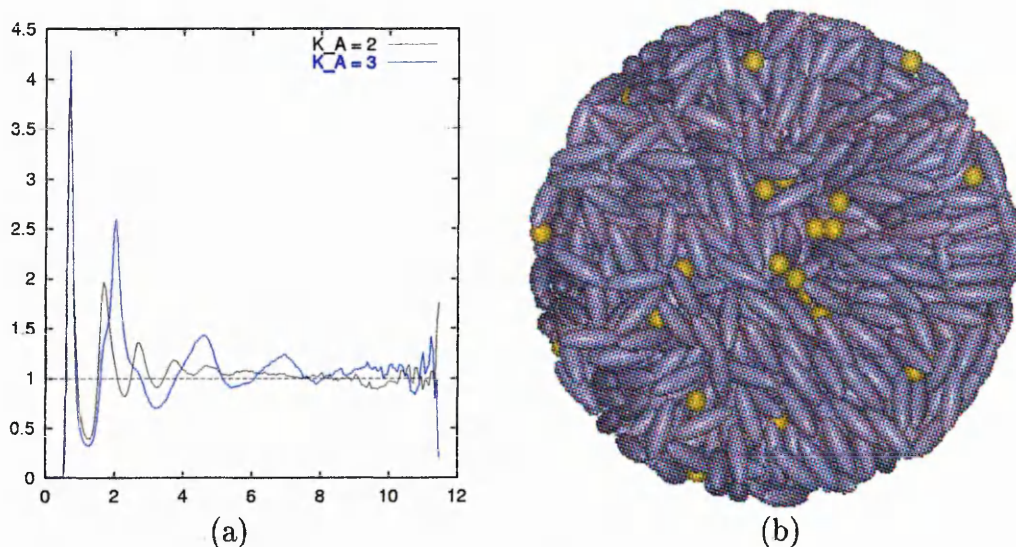
(a)   (b)

Figure 8.11: (a) rod probability density distributions calculated at $\rho = 0.32$ and anchoring $K_A = 2$ and $K_A = 3$ at $T = 1.0$; (b) configuration snapshot taken at $\rho = 0.32$ and $T = 1.0$ for anchoring $K_A = 3$.

A cooling series was performed for anchoring $K_A = 3$ at a constant density $\rho = 0.32$ over range of temperatures $0.70 \leq T \leq 1.00$ with a decrement of $\Delta T = 0.05$. The average values of the potential energy per particle and the nematic order parameter obtained for the even runs of this cooling sequence are shown in Tab. 8.7. These data

Temperature	Energy	Order parameter
1.00	-2.977 ± 0.050	0.123 ± 0.026
0.90	-3.526 ± 0.044	0.057 ± 0.026
0.80	-4.081 ± 0.037	0.077 ± 0.034
0.70	-4.636 ± 0.027	0.113 ± 0.015

Table 8.7: Potential energy per particle and nematic order parameter measured at $T = 1.0$ during the cooling sequence at $\rho = 0.32$.

do not indicate any phase transition, i.e. the potential energy is an almost linear function of the temperature and the nematic order parameter is low in each run. In comparison, an equilibrium bulk system forms a stable nematic phase at $T = 1.0$ and a stable smectic phase at $T = 0.7$ (Subsection 6.2.2). However, the confined mixture was found to exhibit different behaviour due to the strong interactions with the spherical wall. The probability density distributions were calculated to assess the system structure. Figure 8.12(a) demonstrates that the correlations in rod positions
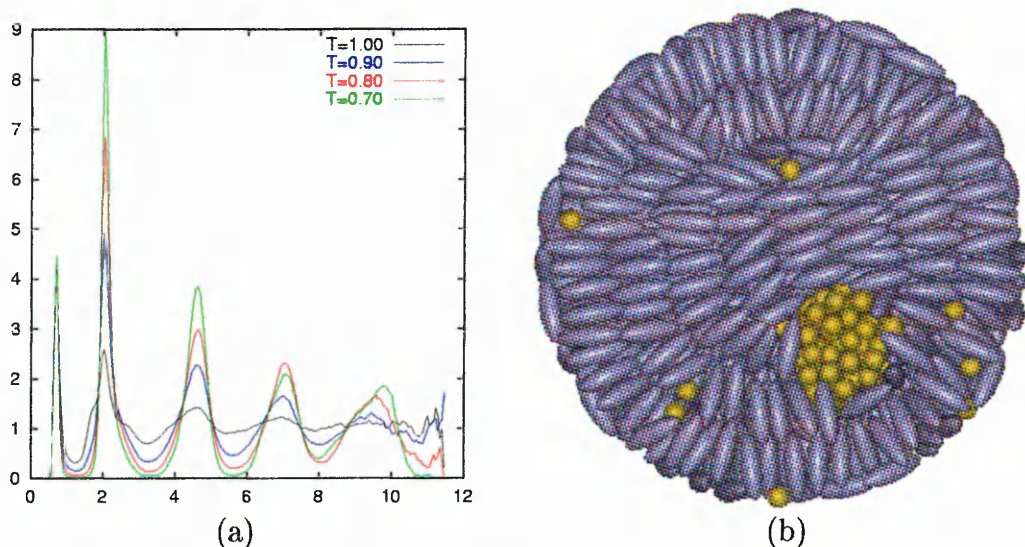
(a)   (b)

Figure 8.12: Rod probability density distributions calculated at $\rho = 0.32$ and anchoring $K_A = 3$ at different temperatures, (b) snapshot taken at $\rho = 0.32$ and $T = 0.70$.

increased as the temperature was decreased. This indicates that concentric shells of the radially aligned rods were established under cooling. The final configuration equilibrated at $T = 0.7$ for 1.8×10^6 MD time steps is shown in Fig. 8.12(b). It resembles the director field configuration shown in Fig. 8.6(a) with a droplet of spheres situated in one of the point defects. The homogeneity of the system was assessed by cluster analysis, and the resultant data are summarised in Tab. 8.8. The enlargement of the clusters indicates demixing at $T \approx 0.8$. Therefore, under

Temperature	1.00	0.90	0.80	0.70
Number of clusters	128	130	113	89
Single spheres	79	82	67	36
Largest cluster	9	11	44	86

Table 8.8: Cluster size distribution averaged over 2×10^5 MD time steps at $\rho = 0.32$ and different temperatures.

cooling from a homogeneous configuration shown in Fig. 8.11(b), the studied mixture underwent a phase separation at $T \approx 0.8$ and spherical particles segregated in the defect of the director field.

In summary, we have developed a model which can generate efficient potentials to

190

deal with large length-scale curved substrates. They provide more realistic descriptions of the surface anchoring when compared to the reviewed literature models. These potentials also allow both the sense and strength of the anchoring to be controlled independently. Here, exploratory simulations have shown that the bulk mixing-demixing behaviour of rod-sphere mixtures is different from that in the presence of curved substrates. The system structure can also be modified by the change in either the substrate's geometry or its preferred surface anchoring condition. In the cases when demixing does occur, spheres tend to accumulate at defect points. This process is found to take place more easily on cooling, whereas the entropy driven demixing, which occurs on compression, is much weaker.

Chapter 9

Conclusions and Future Work

In this Chapter, the principal results of this thesis are summarised and suggestions for future work are made.

9.1 Conclusions

The aim of this project, as specified in Chapter 1, was to use computer simulations of the Generalised Gay-Berne model to achieve greater understanding of the mechanisms and nature of LC phase behaviour in the presence of non-mesogenic additives. We have focused on the phase behaviour of binary mixtures of original Gay-Berne particles with small Lennard-Jones particles subject to different types of rod-sphere interaction potentials. From this, we have found that such mixtures exhibit fascinating and very rich phase behaviour which is particularly sensitive to the strength and symmetry of the rod-sphere interaction, as well as the concentration ratio.

Preliminary simulations of binary hard rod-sphere mixtures were conducted in Chapter 5 to investigate the purely entropic effects occurring in the system. The rods were modelled as Hard Gaussian Overlap particles of length to breadth ratio 3:1 and hard spheres with diameters equal to the breadths of the rods. Both the isotropic-nematic and mixing-demixing transitions were studied over the sphere concentration range

$0 \leq c_{sph} \leq 0.50$. An isotropic-nematic transition was observed at each sphere concentration simulated, this being found to occur at higher volume fractions as the sphere concentration was increased. At low sphere concentrations, the mixtures remained homogeneous even above the transition point and only started to demix under further compression. This suggests that the mixing entropy was high and maintained the mixture in its well-mixed state at moderate volume fractions ($f < 0.52$). At sphere concentration of about 50%, the density range of the mixed nematic phase was substantially reduced, despite the fact that the mixing entropy should be at its greatest at this concentration. The subsequent simulations of Gay-Berne and Lennard-Jones particles, which had the same shapes as the hard particles, were performed in this same density regime, so that, any possible demixing behaviour can be regarded to the attractive interactions.

Four types of mixtures, which differed from each other only by the interaction between unlike particles, were studied in Chapter 6 using both MD and MC techniques to build up their approximate phase diagrams. System (i), which had the original parameterisation of the Generalised Gay-Berne rod-sphere potential, exhibited strong demixing: the mixture components separated macroscopically at 10%, 20%, and 50% sphere concentrations. The anisotropy of the rod-sphere potential was inverted in system (ii) as that the end interaction was made 5 times as strong as the side interaction. This system showed similar behaviour to system (i) at 50/50 rod-sphere concentration ratio, whereas at low sphere concentrations it tended to form a micellar phase at low temperatures. This suggests that the structural properties of thermotropic LCs are more sensitive to additives that are more attracted to the end groups of LC molecules rather than to their sides. No supramolecular organisation was observed in either of these systems.

System (iii) exhibited a completely new type of phase behaviour. Here, the strength of the rod-sphere interaction had no orientational dependence, which resulted in enhancing the mixing properties. At 50/50 rod-sphere concentration ratio, this mixture exhibited neither isotropic-nematic nor mixing-demixing transitions. Instead, it underwent microphase separation at low temperatures and formed a bicontinuous,

relatively dynamic structure. At 30% sphere concentration, the rods underwent an isotropic-smectic transition under compression at low temperature and the spheres occupied the interlayer spacing, leading to a periodic structure. At lower sphere concentrations, no novel mesophases were seen.

The rod-sphere interaction in system (iv) was characterised by a very strong end attraction, which combined the calamatic and lyotropic LC properties, thereby, introducing possibilities of novel phase formation. At different concentrations of spheres, mixtures of type (iv) exhibited micellar, cubic and lamellar phases. All of these mesophases were found to posses supramolecular positional periodicity. The hexagonal phase, typical for surfactant-solvent systems, was not found for these mixtures. However, it was observed in Chapter 7 when a sufficiently strong field was applied to these bulk systems. In particular, both micellar and cubic phases transformed under a strong field to form a hexagonal array of channels of spheres. This process was found to be time reversible, i.e. at zero field, the hexagonal phase was not stable and system reverted back to its original structure. This opens up the prospects of experimental systems with similar properties which could form self-organising nanostructures with applications, for example, as field switchable membranes or display devices.

New potentials were developed in Chapter 8 to describe interactions with convex and concave surfaces to allow the study of colloid-LC and PDLC systems. The newly developed models, unlike those in the literature, provide more realistic descriptions of the surface anchoring. These potentials also allow both the sense and strength of the anchoring condition to be controlled independently. It was found in Chapter 8 that small spheres tended to accumulate at the defects of the director field. Another finding of these simulations was that colloidal particles with different types of anchoring may exhibit some self-organisation when dispersed together in a nematic LC. To our knowledge, only systems with a single type of colloidal particles (either with planar or homeotropic anchoring) have been studied up to date by experimentalists and theorists working on such systems.

9.2 Future Work

The work presented in this thesis has produced encouraging results and opened up several possible avenues for further research. These include computer simulations as well as theoretical and experimental studies.

The performed literature analysis has shown that, to date, mixtures of mesogenic and small spherical molecules have been simulated at molecular scale only in the hard core approximation. The current project, in which a rod-sphere mixture is considered as a mixture of Gay-Berne and Lennard-Jones particles is, therefore, novel. Due to the great number of independent model parameters, the work described in this report is largely preliminary, and there remain several directions for further investigation. The most interesting of these are to:

- study the effects of subtle changes to the system, such as variation of the Gay-Berne parameterisation used;

- study the effects of more significant changes to the system, such as the size of the spheres. Particularly, to study LC ordering in the presence of low concentrations of relatively large spherical particles;

- conduct a detailed analysis of the defects of the director field formed under various geometrical confinements;

- study LC-colloid and PDLC systems using different types of rod-sphere interaction potentials;

- study the cooperative effects of surface interactions and an applied field on the system structure. Both the cases of pure LCs and LC mixtures are of interest;

- investigate the dynamic properties of the structures observed as well as their stability;

- employ more advanced Monte Carlo methods to study the phase equilibria exhibited by these systems.

It is also vital to obtain a sound theoretical understanding of the parameters which control the formation of new phases in order for their behaviour to be optimised. Therefore, our work is expected to initiate some theoretical research in this field. Some progress can be made using density functional theory (DFT) which is an excellent tool for the predictive calculation of both phase behaviour and spatial structure in systems with well-specified microscopic interactions. DFT has been successfully applied to both thermotropic LCs [117] and amphiphiles [118], and it has been generalised to associating fluids as self-associating field theory (SAFT) [119]. SAFT is a powerful tool for studying systems which incorporate relatively strong interactions, hydrogen bonds, for example, similar to those of our system (iv). It also relates system behaviour to the intermolecular forces involved and can be tested against molecular simulations, if refinements to the theory are needed.

As was mentioned above, the competing interactions present in the systems studied here lead, in some cases, to complex self-assembled structures which could be switched or deformed by external fields. It is evident that a range of exciting new functional materials could be fabricated by real molecular systems exhibiting equivalent behaviour. For this reason, experimental research in this field is now being considered through a collaborative link with a Liquid Crystals and Advanced Materials Group at Hull University. Several starting points for this experimental research have been suggested, particular systems to be investigated being:

- systems with hydrogen bonding through a variety of common moieties such as hydroxyl, amino, carboxyl, amido;

- fluorocarbon-hydrocarbon systems;

- non-polar hydrocarbon systems which assemble through shape and conformational factors only.

The targeting of the materials have to be synthesised will be based on the dimensional constraints (e.g., length to breadth aspect ratios) provided by our simulation results. Through chemical design protocols, it should also be possible to vary the

relative strengths of the various inter-species interactions, the goal being to produce practical realisation of the novel phenomena discovered using our model systems.

Appendix A

Derivation of forces and torques

The explicit forms of the forces and the torques exerted on the particles are necessary to perform molecular dynamics simulations (Subsection 4.1.1). Provided the analytical expression of a potential is continuous it is possible to calculate the force as a gradient of this potential:

$$\mathbf{F}(\mathbf{r}) = -\nabla_{\mathbf{r}} U(\mathbf{r}). \tag{A.1}$$

In our models, the torques make sense only for anisotropic particles as there is no rotational degree of freedom for the spherical particles.

Within this Appendix, a brief overview of the methods used to deprive these explicit forms for the spherical Lennard-Jones and prolate Gay-Berne particles are given, followed by details of the implementation of these methods to the potentials describing interaction with curved surfaces.

A.1 Calculation of forces for single-site spherical particles

The spheres in our model interact via Lennard-Jones potential which depends only on separation r_{ij} between two particles i and j. Therefore, formula (A.1) can be

written as

$$\mathbf{F}_{ij} = -\frac{dU_{LJ}(r_{ij})}{dr_{ij}} \frac{\mathbf{r}_{ij}}{r_{ij}} = \frac{24\epsilon}{r_{ij}} \left[2 \left(\frac{\sigma}{r_{ij}} \right)^{12} - \left(\frac{\sigma}{r_{ij}} \right)^6 \right] \hat{\mathbf{r}}_{ij} \qquad (A.2)$$

If cut-off at distance r_c is applied, the potential between two spheres becomes

$$U_{SS}(r_{ij}) = \begin{cases} U_{LJ}(r_{ij}) - U_{LJ}(r_c) & (r_{ij} \leq r_c) \\ 0 & (r_{ij} > r_c) \end{cases} \qquad (A.3)$$

Since $U_{LJ}(r_c)$ is a constant, the cut-off does not affect the expression for forces.

A.2 Calculation of forces and torques for single-site anisotropic particles

Consider two single-site biaxial particles with centre of mass position vectors $\mathbf{r}_i$ for particle i and $\mathbf{r}_j$ for particle j. The intermolecular vector $\mathbf{r}_{ij}$ is given by $\mathbf{r}_{ij} = \mathbf{r}_j - \mathbf{r}_i$ and unit vectors $\hat{\mathbf{u}}_i$ and $\hat{\mathbf{u}}_j$ are parallel to the longest axis of the molecules as illustrated in Fig. A.1. The force exerted on the centre of mass of particle i is
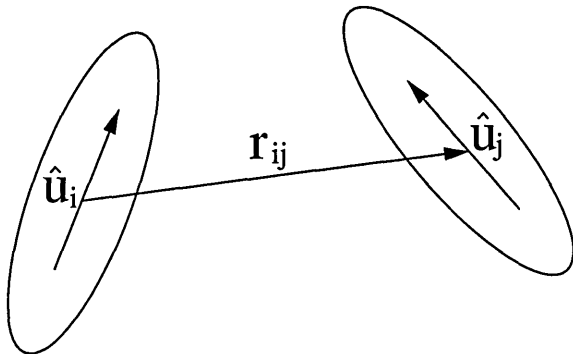

Figure A.1: Representation of interaction between two elongated particles.

denoted by $\mathbf{F}_{ij} = -\nabla_{\mathbf{r}_{ij}} U_{ij}$. Using the chain rule we obtain,

$$\mathbf{F}_{ij} = -\sum_{\mathbf{s}} \frac{\partial U_{ij}}{\partial (\mathbf{s} \cdot \mathbf{r}_{ij})} \nabla_{\mathbf{r}_{ij}} (\mathbf{s} \cdot \mathbf{r}_{ij}), \qquad (A.4)$$

where the notation for the sum indicates that all scalar products involving the intermolecular vector are considered, including $r_{ij} = (\hat{\mathbf{r}}_{ij} \cdot \mathbf{r}_{ij})$. Now,

$$\nabla_{\mathbf{r}_{ij}} (\mathbf{s} \cdot \mathbf{r}_{ij}) = \left(\frac{d(r_{ij}^x s^x)}{dr_{ij}^x}, \frac{d(r_{ij}^y s^y)}{dr_{ij}^y}, \frac{d(r_{ij}^z s^z)}{dr_{ij}^z} \right) = (s^x, s^y, s^z) = \mathbf{s}.$$

Therefore equation (A.4) becomes,

$$\mathbf{F}_{ij} = -\sum_{s} \frac{\partial U_{ij}}{\partial(\mathbf{s} \cdot \mathbf{r}_{ij})} \mathbf{s}. \tag{A.5}$$

According to the third Newton's law the force on particle j has the same magnitude as that acting upon molecule i and acts in the opposite direction.

The torque on particle i can be written [120] as:

$$\boldsymbol{\tau}_{ij} = -[\hat{\mathbf{u}}_i \times \nabla_{\hat{\mathbf{u}}_i} U_{ij}] = -\sum_{s} \frac{\partial U_{ij}}{\partial(\hat{\mathbf{u}}_i \cdot \mathbf{s})} [\hat{\mathbf{u}}_i \times \mathbf{s}], \tag{A.6}$$

where the notation implies that the sum is over all scalar products in which one vector, $\hat{\mathbf{u}}_i$, does not change its coordinates in the body-fixed frame while the other, $\mathbf{s}$, does so. We now apply equations (A.5) and (A.6) to the truncated and shifted Gay-Berne potential, considering it as a function of scalar products $r = \hat{\mathbf{r}}_{ij} \cdot \mathbf{r}_{ij}$, $a = \hat{\mathbf{u}}_i \cdot \mathbf{r}_{ij}$, $b = \hat{\mathbf{u}}_j \cdot \mathbf{r}_{ij}$, and $c = \hat{\mathbf{u}}_i \cdot \hat{\mathbf{u}}_j$,

$$U_{RR}(r, a, b, c) = 4\epsilon(r, a, b, c) \left[\left(\frac{\sigma_0}{r - \sigma(r, a, b, c) + \sigma_0} \right)^{12} - \left(\frac{\sigma_0}{r - \sigma(r, a, b, c) + \sigma_0} \right)^{6} \right] -$$
$$4\epsilon(r, a, b, c) \left[\left(\frac{\sigma_0}{r_c - \sigma(r, a, b, c) + \sigma_0} \right)^{12} - \left(\frac{\sigma_0}{r_c - \sigma(r, a, b, c) + \sigma_0} \right)^{6} \right].$$

The potential energy is shifted at a spherical cut-off distance, r_c, such that the potential at the cut-off is equal to zero, thus eliminating a discontinuity in the potential energy due to truncation. It should be noted that parameters ϵ and σ remain functions of r not r_c, being defined [6] as dependent upon scalar products of the form $\hat{\mathbf{r}}_{ij} \cdot \hat{\mathbf{u}}_i$, not $\mathbf{r}_{ij} \cdot \hat{\mathbf{u}}_i$. Indeed, the r dependence within ϵ and σ is used to normalise a and b, such that,

$$\hat{\mathbf{r}}_{ij} \cdot \hat{\mathbf{u}}_i = \frac{\mathbf{r}_{ij} \cdot \hat{\mathbf{u}}_i}{r} = \frac{a}{r} \neq \frac{\mathbf{r}_{ij} \cdot \hat{\mathbf{u}}_i}{r_c}.$$

Expression (A.5) for the rod-rod potential can be written as:

$$\mathbf{F}_{ij} = -\frac{\partial U_{RR}}{\partial r} \hat{\mathbf{r}}_{ij} - \frac{\partial U_{RR}}{\partial a} \hat{\mathbf{u}}_i - \frac{\partial U_{RR}}{\partial b} \hat{\mathbf{u}}_j \tag{A.7}$$

Similarly the torques may be evaluated by the expansion of equation (A.6), to give,

$$\boldsymbol{\tau}_{ij} = -\hat{\mathbf{u}}_i \times \left(\frac{\partial U_{RR}}{\partial a} \mathbf{r}_{ij} + \frac{\partial U_{RR}}{\partial c} \hat{\mathbf{u}}_j \right) \tag{A.8}$$

for particle i, and

$$\boldsymbol{\tau}_{ji} = -\hat{\mathbf{u}}_j \times \left(\frac{\partial U_{RR}}{\partial b} \mathbf{r}_{ij} + \frac{\partial U_{RR}}{\partial c} \hat{\mathbf{u}}_i \right) \tag{A.9}$$

for particle j. The explicit forms of all derivatives are given below.

$$\frac{\partial U_{RR}}{\partial r} = 4\epsilon \left[\frac{\mu \chi'}{\epsilon_2 r^3} \left(\frac{(a+b)^2}{1+\chi'c} + \frac{(a-b)^2}{1-\chi'c} \right) (A - A_c) - \frac{B}{\sigma_0} \right.$$
$$\left. - \frac{\sigma^3 \chi}{2\sigma_0^3 r^3} \left(\frac{(a+b)^2}{1+\chi c} + \frac{(a-b)^2}{1-\chi c} \right) (B - B_c) \right] \tag{A.10}$$

$$\frac{\partial U_{RR}}{\partial a} = 4\epsilon \left[-\frac{\mu \chi'}{\epsilon_2 r^2} \left(\frac{a+b}{1+\chi'c} + \frac{a-b}{1-\chi'c} \right) (A - A_c) \right.$$
$$\left. + \frac{\sigma^3 \chi}{2\sigma_0^3 r^2} \left(\frac{a+b}{1+\chi c} + \frac{a-b}{1-\chi c} \right) (B - B_c) \right] \tag{A.11}$$

$$\frac{\partial U_{RR}}{\partial b} = 4\epsilon \left[-\frac{\mu \chi'}{\epsilon_2 r^2} \left(\frac{a+b}{1+\chi'c} - \frac{a-b}{1-\chi'c} \right) (A - A_c) \right.$$
$$\left. + \frac{\sigma^3 \chi}{2\sigma_0^3 r^2} \left(\frac{a+b}{1+\chi c} - \frac{a-b}{1-\chi c} \right) (B - B_c) \right] \tag{A.12}$$

$$\frac{\partial U_{RR}}{\partial c} = 4\epsilon \left[(A - A_c) \left(\nu \epsilon_1^2 \chi^2 c + \frac{\mu \chi'^2}{2\epsilon_2 r^2} \left(\left(\frac{a+b}{1+\chi'c} \right)^2 - \left(\frac{a-b}{1-\chi'c} \right)^2 \right) \right) \right.$$
$$\left. - (B - B_c) \frac{\sigma^3 \chi^2}{4\sigma_0^3 r^2} \left(\left(\frac{a+b}{1+\chi c} \right)^2 - \left(\frac{a-b}{1-\chi c} \right)^2 \right) \right] \tag{A.13}$$

where

$$A = \left(\frac{\sigma_0}{r - \sigma(r,a,b,c) + \sigma_0} \right)^{12} - \left(\frac{\sigma_0}{r - \sigma(r,a,b,c) + \sigma_0} \right)^{6}$$

$$A_c = \left(\frac{\sigma_0}{r_c - \sigma(r,a,b,c) + \sigma_0} \right)^{12} - \left(\frac{\sigma_0}{r_c - \sigma(r,a,b,c) + \sigma_0} \right)^{6}$$

$$B = 12 \left(\frac{\sigma_0}{r - \sigma(r,a,b,c) + \sigma_0} \right)^{13} - 6 \left(\frac{\sigma_0}{r - \sigma(r,a,b,c) + \sigma_0} \right)^{7}$$

$$B_c = 12 \left(\frac{\sigma_0}{r_c - \sigma(r,a,b,c) + \sigma_0} \right)^{13} - 6 \left(\frac{\sigma_0}{r_c - \sigma(r,a,b,c) + \sigma_0} \right)^{7}$$

The explicit forms of the force and the torque exerted on Gay-Berne particle i by Lennard-Jones particle j can be evaluated in a similar way. To evaluate the force

equation (A.5) is applied to potential

$$U_{RS}(r,a) = 4\epsilon(r,a)\left[\left(\frac{\sigma_0}{r - \sigma(r,a) + \sigma_0}\right)^{12} - \left(\frac{\sigma_0}{r - \sigma(r,a) + \sigma_0}\right)^{6}\right] - $$
$$4\epsilon(r,a)\left[\left(\frac{\sigma_0}{r_c - \sigma(r,a) + \sigma_0}\right)^{12} - \left(\frac{\sigma_0}{r_c - \sigma(r,a) + \sigma_0}\right)^{6}\right],$$

which yields,

$$\mathbf{F}_{ij} = -\frac{\partial U_{RS}}{\partial r}\hat{\mathbf{r}}_{ij} - \frac{\partial U_{RS}}{\partial a}\hat{\mathbf{u}}_i. \tag{A.14}$$

The torque acting upon the rod is

$$\boldsymbol{\tau}_{ij} = -\hat{\mathbf{u}}_i \times \frac{\partial U_{RS}}{\partial a}\mathbf{r}_{ij} \tag{A.15}$$

Using expressions (4.33) and (4.34) for $\epsilon(r,a)$ and $\sigma(r,a)$ we can calculate the derivatives:

$$\frac{\partial U_{RS}}{\partial r} = 4\epsilon\left[\frac{2\mu\chi''a^2}{(1 - \chi''\frac{a^2}{r^2})r^3}(A - A_c) - \frac{\sigma^3\chi a^2}{\sigma_0^3 r^3}(B - B_c) - \frac{B}{\sigma_0}\right] \tag{A.16}$$

$$\frac{\partial U_{RS}}{\partial a} = 4\epsilon\left[\frac{2\mu\chi''a}{(1 - \chi''\frac{a^2}{r^2})r^2}(A_c - A) + \frac{\sigma^3\chi a}{\sigma_0^3 r^2}(B - B_c)\right] \tag{A.17}$$

A.3 Derivation of forces and torques exerted by a colloidal particle

In this Section, the forces and torques exerted by a colloidal particle on rods and spheres are calculated. Formulas (8.2) and (8.6) obtained in Section 8.1 are differentiated with respect to r to yield the explicit expressions of the forces in this model. Then the colloid-rod potential is analysed to obtain the explicit form of the torques exerted on the rods.

The derivative of colloid-sphere potential (8.2) with respect to r is:

$$\frac{U_{CS}(r)}{dr} = \epsilon_{CS}\left[-\frac{1}{5(r-R)^{10}} + \frac{1}{2(r-R)^4} + \frac{1}{40r(r-R)^8}\left(\frac{8}{r-R} - \frac{1}{r}\right) - \right.$$
$$\left. - \frac{1}{4r(r-R)^2}\left(\frac{2}{r-R} - \frac{1}{r}\right)\right]. \tag{A.18}$$

To obtain explicit expressions of the forces and torques exerted on the rod the derivatives of the colloid-rod potential (8.6) are calculated. Analogous to the previous Section we denote

$$r = \hat{\mathbf{r}} \cdot \mathbf{r}, \, a = \hat{\mathbf{u}} \cdot \mathbf{r}$$

and differentiate the potential $U_{CR}^{total}(\mathbf{r}, \hat{\mathbf{u}})$ with respect to r and a.

$$\frac{\partial U_{CR}^{total}(\mathbf{r}, \hat{\mathbf{u}})}{\partial r} = \frac{2\mu\chi'' a^2}{r^3(1 - \chi'' + \chi'' \frac{a^2}{r^2})} U_{CR}^{total}(\mathbf{r}, \hat{\mathbf{u}}) + \epsilon_{CR}\left(\frac{\partial \sigma_{CR}}{\partial r} - 1\right) X -$$
$$- \frac{\epsilon_{CR}}{4r^2(r - R - \sigma_{CR} + 1)^2}\left(1 - \frac{1}{10(r - R - \sigma_{CR} + 1)^{10}}\right) +$$
$$+ \epsilon_{CR}\frac{\partial \sigma_{CR}}{\partial r} X_c \qquad\qquad (A.19)$$

$$\frac{\partial U_{CR}^{total}(\mathbf{r}, \hat{\mathbf{u}})}{\partial a} = \epsilon_{CR}\frac{\partial \sigma_{CR}}{\partial a}(X - X_c), \qquad\qquad (A.20)$$

where

$$X = \left(\frac{1}{5(r - R - \sigma_{CR} + 1)^9} - \frac{1}{2(r - R - \sigma_{CR} + 1)^3}\right)\left(\frac{1}{r - R - \sigma_{CR} + 1} - \frac{1}{r}\right)$$

$$X_c = \left(\frac{1}{5(r_c - R - \sigma_{CR} + 1)^9} - \frac{1}{2(r_c - R - \sigma_{CR} + 1)^3}\right)\left(\frac{1}{r_c - R - \sigma_{CR} + 1} - \frac{1}{r_c}\right)$$

$$\frac{\partial \sigma_{CR}}{\partial r} = -\frac{\sigma_{CR}\chi a^2}{r^3}\frac{1}{(1 - \chi + \chi\frac{a^2}{r^2})}$$

$$\frac{\partial \sigma_{CR}}{\partial a} = \frac{\sigma_{CR}\chi a}{r^2}\frac{1}{(1 - \chi + \chi\frac{a^2}{r^2})}$$

The final expressions of the force and the torque exerted on the rod by the colloid can be obtained now by substituting these derivatives into formulas (A.14) and (A.15).

A.4 Derivation of forces and torques in PDLC model

The explicit forms of the forces and torques in the PDLC model developed in Section 8.2 are evaluated below.

The derivative of potential (8.8) with respect to h was found using the software package Mathematica [121]:

$$\frac{\partial U(h)}{\partial h} = \frac{-1}{40(R-h)^2} \left[\frac{h^2(10h^6 - 1) - R(R-h)(20h^6 - 8)}{h^{10}} \right.$$
$$\left. + \frac{2(5r_c^6 - 2)((R-h)^2 + R^2) + 5r_c^2(1 - 4r_c^6)}{r_c^{10}} \right]. \tag{A.21}$$

It must be noted that the force on the particle is equal to

$$\mathbf{F}_i = -\nabla_{\mathbf{r}_i} U(\mathbf{r}_i)\frac{\mathbf{r}_i}{r_i} = \frac{\partial U(h)}{\partial h}\frac{\mathbf{h}}{h},$$

not

$$\mathbf{F}_i = -\frac{\partial U(h)}{\partial h}\frac{\mathbf{h}}{h},$$

because $dr_i = -dh$. In order to differentiate the potential (8.9) U^{rod} is to be considered as a complex function

$$U^{rod} = \epsilon_{PR}(h, a)\, U(H(h, a), R_c(h, a)),$$

where $a = \mathbf{r}_i \cdot \hat{\mathbf{u}}_i$ as it was defined above. Therefore,

$$\frac{\partial U^{rod}}{\partial h} = \frac{\partial \epsilon_{PR}(h, a)}{\partial h} U(H, R_c) + \epsilon_{PR}(h, a)\left(\frac{\partial U(H, R_c)}{\partial H}\frac{\partial H}{\partial h} + \frac{\partial U(H, R_c)}{\partial R_c}\frac{\partial R_c}{\partial h} \right).$$

The expression for $\frac{\partial U(H, R_c)}{\partial H}$ has the form of (A.21) but depends on (H, R_c) rather than (h, r_c). The explicit forms of the other derivatives are given below.

$$\frac{\partial \epsilon_{PR}}{\partial h} = -\frac{\mu\,\epsilon_{PR}}{\left(1 - \chi'' + \chi''\frac{a^2}{(R-h)^2}\right)}\frac{2\chi''a^2}{(R-h)^3}$$

$$\frac{\partial U}{\partial R_c} = \frac{1}{R-h}\left[h(2R - h) - 2R_c(R - h) - R_c^2\right]\left(\frac{1}{R_c^5} - \frac{1}{R_c^{11}}\right)$$

$$\frac{\partial H}{\partial h} = 1 - \frac{\chi}{1-\chi}\frac{a^2}{\sigma(R-h)^3}$$

$$\frac{\partial R_c}{\partial h} = -\frac{\chi}{1-\chi}\frac{a^2}{\sigma(R-h)^3}.$$

In a similar way the derivative with respect to a are calculated:

$$\frac{\partial U^{rod}}{\partial a} = \frac{\partial \epsilon_{PR}(h, a)}{\partial a} U(H, R_c) + \epsilon_{PR}(h, a)\left(\frac{\partial U(H, R_c)}{\partial H}\frac{\partial H}{\partial a} + \frac{\partial U(H, R_c)}{\partial R_c}\frac{\partial R_c}{\partial a} \right),$$

where

$$\frac{\partial \epsilon_{PR}}{\partial a} = -\frac{\mu\,\epsilon_{PR}}{\left(1 - \chi'' + \chi''\frac{a^2}{(R-h)^2}\right)}\frac{2\chi''a}{(R-h)^2}$$

$$\frac{\partial H}{\partial a} = \frac{\partial R_c}{\partial a} = -\frac{\chi}{1-\chi}\frac{a}{\sigma(R-h)^2}.$$

Bibliography

[1] T. Kato, *Nature*, **295**, 2414 (2002)

[2] C. Tschieske, *J. Mat. Chem.*, **11** 2647 (2001)

[3] R. Lipowsky, *Structure and Dynamics of Membranes*, Elsevier (1995)

[4] M.P. Allen and D.J. Tildesley, *Computer Simulation of Liquids*, Clarendon Press (1987)

[5] R. Latham and D.J. Cleaver, *Chem. Phys. Letts.*, **330**, 7 (2000)

[6] J.G. Gay and B.J. Berne, *J. Chem. Phys.*, **74**, 3316 (1981)

[7] P.G. de Gennes and J. Prost, *The Physics of Liquid Crystals*, Clarendon Press, Oxford (1993)

[8] S. Chandrasekhar, *Liquid Crystals*, Cambridge University Press (1992)

[9] S. Chandrasekhar *et al.*, *Pramana*, **9**, 471 (1977)

[10] S. Singh, *Physics Reports*, **324** (2000)

[11] B. Wazynska, *Mol. Cryst. Liq. Cryst.*, **301** 391 (1997)

[12] J.W. Emsley, G.R. Luckhurst, P.J. Parsons, *Mol. Phys.*, **56** 767 (1985); P.E. Cladis, *Phys. Rev. A*, **23**, 2594 (1981)

[13] P.K. Mukherjee, *Current-Science*, **74** (11), 945 (1998)

[14] I.W. Hamley *et al.*, *J. Chem. Phys.*, **104**, 10046 (1996)

[15] A. Saupe, G. Enllert, *Mol. Cryst.*, **1**, 503 (1966)

[16] L. Onsager, *Ann. N. Y. Acad. Sci.,* **51**, 627 (1949)

[17] P.J. Flory, *Proc. R. Soc.*, **A234**, 73 (1956)

[18] W. Maier and A. Saupe, *Z Naturf (a)*, **13**, 564 (1958)

[19] P.G. de Gennes, *Mol. Cryst. Liq. Cryst.*, **12**, 193 (1971)

[20] M.C.J.M. Vissenberg, S. Stallinga, G. Vertogen, *Phys. Rev. E*, **55**, 4367 (1997)
P.K. Mukherjee, *Liq. Cryst.*, **24**, 519 (1998)

[21] H. Yurtseven, *Phase Transit.*, **53**, 75 Part A (1995)

[22] C.W. Oseen, *Trans. Faraday Soc.*, **29**, 883 (1933)
H. Zocher, *Trans. Faraday Soc.*, **29**, 945 (1933)

[23] F.C. Frank, *Disc. Faraday Soc.*, **25**, 19 (1958)

[24] J.L. Ericksen, *Arch. Rational Mech. Anal.*, **4**, 231 (1960)

[25] F.M. Leslie, *Quart. J. Mech. Appl. Math.*, **19**, 357 (1966)

[26] A.A. Sonin, *The Surface Physics of Liquid Crystals*, Gordon and Breach (1995)

[27] E.M. Terentjev, *Phys. Rev. E*, **56**, 5561 (1997)

[28] S. Asakura and F. Oosawa, *J. Polym. Sci.*, **33**, 183 (1958)

[29] Y. Mao, M.E. Cates, and H.N.W. Lekkerkerker, *J. Chem. Phys.*, **106**, 3721 (1997)

[30] K. Yaman, C. Jeppesen, and C.M. Marques, *Europhys. Lett*, **42**, 221 (1998)

[31] M. Schmidt, *Phys. Rev. E*, **63**, 050201 (2001)

[32] T. Koda, M. Numajiri, and S. Ikeda, *J. Phys. Soc. Jpn.*, **65**, 3551 (1996)

[33] Z. Dogic, D. Frenkel and S. Fraden, *Phys. Rev. E*, **62**, 3925 (2000)

[34] R. van Roij, B. Mulder, *Phys. Rev. E*, **54**, 6430 (1996)

[35] Y. Rosenfeld, *J. Chem. Phys*, **89**, 4271 (1989)

[36] H. Bosetti and A. Perera, *Phys. Rev. E*, **63**, 021206 (2001)

[37] A. Perera *et al.*, *Mol. Phys.*, **100**, 3409 (2002)

[38] M. Dijkstra and D. Frenkel, *Phys. Rev. Lett.*, **72**, 298 (1994)

[39] S.P. Meeker, W.C. Poon, J. Crain, E. Terentjev, *Phys. Rev. E*, **61**, 6083 (2000)

[40] CMBE Liquid Crystals, *http://www.nes.coventry.ac.uk/research/cmbe/liqurist.htm*

[41] P.G. Petrov and E.M. Terentjev, *Langmuir*, **17**, 2942 (2001)

[42] Bristol SPM Research, *http://spm.phy.bris.ac.uk/research/LiquidCrystals/AFM/*

[43] P.J. Collings and M. Hird, *Introduction to Liquid Crystals Chemistry and Physics*, Taylor & Francis (1997)

[44] I.W. Hamley, S. Garnett, G.R. Luckhurst, *J. Chem. Phys*, **104**, 10046 (1996)

[45] H. Nakamura, S.P. Meeker, Y. Taira, WCK Poon, J Crain, *Mol. Cryst. Liq. Cryst.*, **368**, 3935 (2001)

[46] P. Poulin, D.A. Witz *Phys. Rev. E*, **57**, 626 (1998)

[47] J. Loudet, P. Barois, and P. Poulin, *Nature*, **407**, 611 (2000)

[48] J. Yamamoto and H. Tanaka, *Nature*, **409**, 321 (2001)

[49] M. Adams and S. Fraden, *Biophys.J*, **74**, 669 (1998)

[50] M. Adams, Z. Dogic, S.L. Keller, and S. Fraden, *Nature*, **393**, 349 (1998)

[51] G.A. Vilegenthart, A. van Blaaderen, and H.N.W. Lekkerkerker, *Faraday Discuss.*, **112**, 1, (1999)

[52] T.W. Cheung, S.M. Fan, G.R. Luckhurst, D.L. Turner, *J. Chem. Soc. Faraday Trans.*, **93**, 3099 (1997)

[53] N. Metropolis, A.W. Rosenbluth, N.M. Rosenbluth, A.H. Teller and E. Teller, *J. Chem. Phys.*, **21**, 1087 (1953)

[54] M.P. Allen and M.R. Wilson, *J. Comp. Aided Mol. Des.*, **3**, 335 (1989)

[55] J.E. Vieillard-Baron, *Mol. Phys.*, **28**, 209 (1974)

[56] J. Kushick and B.J. Berne, *J. Chem. Phys.*, **64**, 1362 (1976)

[57] P.A. Lebwohl and G. Lasher, *Phys. Rev. A*, **6**, 426 (1972)

[58] U. Fabbri and C. Zannoni, *Molec. Phys.*, **58**, 763 (1986)

[59] R.Hashim, G.R. Luckhurst, and S. Romano, *Proc. R. Soc. Lond. A*, **429**, 323 (1990)

[60] D. Frenkel and R. Eppenga, *Phys. Rev. Lett.*, **49**, 1089 (1982)

[61] D. Frenkel, B.M. Mulder and J.P. Mctague, *Phys. Rev. Lett.*, **52**, 287 (1984)

[62] D. Frenkel and B.M. Mulder, *Mol. Phys.*, **55**, 1171 (1985)

[63] D. Frenkel, *Mol. Phys.*, **60**, 1 (1987)

[64] A. Stroobants, H.N.W. Lekkerkerker, D. Frenkel, *Phys. Rev. Lett.*, **57**, 1452 (1986)

[65] D. Frenkel, *J. Phys. Chem.*, **92**, 3280 (1988)

[66] J.A.C. Veerman and D. Frenkel, *Phys. Rev. A*, **41**, 3237 (1990)

[67] P.Bolhuis and D.Frenkel, *J. Chem. Phys.*, **106**, 666 (1997)

[68] M.N. Wilson, *Mol. Phys.*, **81**, 675 (1994)
D.C. Williamson and G. Jackson, *J. Chem. Phys.*, **108**, 10294 (1998)

[69] A. Stroobants, *Phys. Rev. Lett.*, **69**, 2388 (1992)
A. Stroobants, *J. Phys. Cond. Mat.*, **6**, A285 (1994)

[70] P.J. Camp, M.P. Allen, *Physica A*, **229**, 410 (1996)

[71] P.J. Camp, M.P. Allen, P.G. Bolhuis, D. Frenkel, *J. Chem. Phys.*, **106**, 9270 (1997)

[72] G.V. Paolini, G. Ciccotti, M. Ferrario, *Molec. Phys.*, **80**, 297 (1993)

[73] J. Corner, *Proc. Roy. Soc. Lond. A*, **192**, 275 (1948)

[74] B.J. Berne and P. Pechukas, *J. Chem. Phys.*, **56**, 4213 (1972)

[75] D.J. Adams, G.R. Luckhurst and R.W. Phippen, *Mol. Phys.*, **61**, 1575 (1987)

[76] E. de Miguel, L.F. Rull, M.K. Chalam and K.E. Gubbins, *Mol. Phys.*, **71**, 1223 (1990); *Mol. Phys.*, **72**, 593 (1991)

[77] E. de Miguel, L.F. Rull, M.K. Chalam, K. Gubbins, *Mol. Phys.*, **74**, 405 (1991)

[78] J.W. Emsley, G.R. Luckhurst, W.E. Palke, D.J. Tildesley, *Liq. Cryst.*, **11**, 519 (1992)

[79] G.R. Luckhurst, R.A. Stephens and R.W. Phippen, *Liq. Cryst.*, **8**, 451 (1990)

[80] G.R. Luckhurst and P.S.J. Simmonds, *Mol. Phys.*, **80**, 233 (1993)

[81] E. de Miguel, E. Martin del Rio, J.T. Brown and M.P. Allen, *J. Chem. Phys.*, **105**, 4234 (1996)

[82] J.T. Brown, M.P. Allen, E. Martin del Rio, E. de Miguel, *Phys. Rev. E*, **57**, 6685 (1998)

[83] M.A. Bates, G.R. Luckhurst, *J. Chem. Phys.*, **104**, 6696 (1996)

[84] H. Zewdie, *J. Chem. Phys.*, **108**, 2117 (1998)

[85] C.W. Cross and B.M. Fung, *J. Chem. Phys.*, **101**, 6839 (1994)

[86] J. Ilnytskyi and M.R. Wilson, *Comp. Phys. Com.*, **134**, 23 (2001)

[87] C.J. Adam, S.J Clark, J. Crain, *Proceedings of the SPIE. Int. Soc. for Opt. Eng.*, **3318** 171 (1998);

[88] R. Car and M. Parrinello, *Phys. Rev. Lett.*, **55**, 2471 (1985)

[89] R. Lukac, F.J. Vesely, *Mol. Cryst. Liq. Cryst.*, **262** 533 (1995)

[90] D.J. Cleaver *et al.*, *Phys. Rev. E*, **54**, 559 (1996)

[91] R.A. Bemrose *et al.*, *Mol. Phys.* **90**, 625 (1997);
Mol. Cryst. Liq. Cryst., **299**, 27 (1997)

[92] S.J. Mills and D.J. Cleaver, *Mol. Phys.*, **98**, 1379 (2000)

[93] S.D. Stoddard and J. Ford, *Phys. Rev. A*, **8**, 1504 (1973)

[94] W.C. Swope, H.C. Andersen, P.H. Berens and K.R. Wilson, *J. Chem. Phys.*, **76**, 637 (1982)

[95] J.A. Barker and R.O. Watts, *Chem. Phys. Lett.*, **3**, 144 (1969)

[96] E. de Miguel and E.M. del Rio, *J. Chem. Phys.*, **115**, 9072 (2001)

[97] E. de Miguel, *Phys. Rev. E*, **47**, 3334 (1993)

[98] M. Dijkstra, R. van Roij, R. Evans, *Phys. Rev. E*, **59**, 5744 (1999)

[99] A. Galindo, G. Jackson, and D.J. Photinos, *Chem. Phys. Lett.*, **325**, 631 (2000)

[100] M.D. Rintoul, S. Torquato, *J. Chem. Phys.*, **105**, 9258 (1996)

[101] W.H. Press, S.A. Teukolsky, W.T. Vetterling and B.P. Flannery, *Numerical Recipes in C*, Cambridge Press (1995)

[102] A.Z. Panagiotopoulos, *Mol. Phys.*, **61**, 813 (1988); *Mol. Phys.*, **63**, 527 (1988)

[103] I.W. Hamley, *Introduction to soft matter : polymers, colloids amphiphiles, and liquid crystals*, Wiley (2000)

[104] S.V. Lishchuk, C.M. Care and I. Halliday in preparation

[105] J. Ilnitskyi and M.R. Wilson, *Comp. Phys. Com.*, **134**, 23 (2001)

[106] M.P. Allen and D.J. Tildesley, *Computer Simulation in Chemical Physics*, Kluwer Academic Publishers (1993)

[107] M. Bender, P Holstein, D. Geschke, *Liq. Cryst.*, **28**, 1813 (2001)

[108] G.R. Luckhurst, *Mol. Cryst. Liq. Cryst.*, **347**, 365 (2000)

[109] D. Andrienko, G. Germano, and M.P.Allen, *Phys. Rev. E*, **63**, 041701 (2001)

[110] R. Yamamoto, *Phys. Rev. Lett.*, **87**, 075502 (2001)

[111] K. Good PhD thesis, Sheffield Hallam University (2001)

[112] J.L. Billeter, R.A. Pelcovits, *Phys. Rev. E*, **62**, 711 (2000)

[113] S.A. Langer, S.C. Glotzer, *Physica A*, **239**, 358 (1997)

[114] C. Chiccoli, P. Pasini, F. Semeria, and C. Zannoni, *Phys. Lett. A*, **150**, 311 (1990)

[115] R.K. Bharadwaj, T.J. Bunning, B.L. Farmer, *Liq. Cryst.*, **27**, 591 (2000)

[116] A.P. Emerson and C. Zannoni, *J. Chem. Soc. Faraday Trans.*, **91**, 3441 (1995)

[117] G. Cinacchi and F. Schmid, *J. Phys. Cond. Mat.*, **14**, 12223 (2002)

[118] C. M. Guerra *et al.*, *J. Chem. Phys.*, **109**, 1152 (1998)

[119] E.A. Muller and K.E. Gubbins, *Ind. Eng. Chem. Res.*, **40**, 2193 (2001)

[120] P.S.Y.Cheung, *Chem. Phys. Lett.*, **40**, 19 (1976)

[121] S. Wolfram, *Mathematica: A System for Doing Mathematics by Computer*, Addison Wesley (1991)